

<sup>1</sup> Study of Central Exclusive Production of  $\pi^+\pi^-$ ,  $K^+K^-$   
<sup>2</sup> and  $p\bar{p}$  Pairs in Proton-Proton Collisions at  $\sqrt{s} = 510$  GeV

<sup>3</sup> Tomáš Truhlář, Włodek Guryń, Michal Vranovský, and Jaroslav Bielčík  
<sup>4</sup> [Tomas.Truhlar@fjfi.cvut.cz](mailto:Tomas.Truhlar@fjfi.cvut.cz), [guryn@bnl.gov](mailto:guryn@bnl.gov), [vranomic@fjfi.cvut.cz](mailto:vranomic@fjfi.cvut.cz),  
<sup>5</sup> [jaroslav.bielcik@fjfi.cvut.cz](mailto:jaroslav.bielcik@fjfi.cvut.cz)

<sup>6</sup> August 1, 2025

<sup>7</sup> **Abstract**

<sup>8</sup> We report on the measurement of the  $pp \rightarrow ph^+h^-p$  ( $h = \pi, K, p$ ) central exclusive  
<sup>9</sup> production process in proton-proton collisions at the center-of-mass energy  $\sqrt{s} = 510$   
<sup>10</sup> GeV with the STAR detector at RHIC. At this energy, the process is dominated by a  
<sup>11</sup> double IPomeron exchange mechanism. The oppositely charged hadron pairs are mea-  
<sup>12</sup> sured within the central detector of STAR, the Time Projection Chamber, and the Time  
<sup>13</sup> of Flight detector. The hadron pairs are identified using the ionization energy loss and  
<sup>14</sup> the time of flight method. The forward scattered protons, which remain intact inside the  
<sup>15</sup> RHIC beam pipe after the collision, are measured in the Roman Pot system allowing the  
<sup>16</sup> verification of event's exclusivity. Differential fiducial cross sections within the STAR  
<sup>17</sup> acceptance are presented as function of the difference in the azimuthal angle between  
<sup>18</sup> the outgoing protons, hadron pair invariant mass and rapidity of the central system.  
<sup>19</sup> The STAR detector's acceptance is determined by pseudorapidity  $\eta$  of the centrally-  
<sup>20</sup> produced hadrons in the range  $|\eta| < 0.9$ . The invariant masses of the charged hadrons  
<sup>21</sup> pairs are measured up to about 3 GeV and the square of the four-momentum transfer  $t$   
<sup>22</sup> of the forward protons is in the range  $0.3 \text{ GeV}^2 < -t_1, -t_2 < 1.6 \text{ GeV}^2$ . The differential  
<sup>23</sup> fiducial cross sections of the forward protons as a function of the  $|t_1 + t_2|$  are also pre-  
<sup>24</sup> sented. All results for the  $\pi^+\pi^-$  pair are presented in three mass ranges. A comparison  
<sup>25</sup> with GRANITTI Monte Carlo predictions are also presented, where the spectra include  
<sup>26</sup> continuum and resonant contributions.



# **27** Contents

<b>28</b>	<b>List of Figures</b>	<b>xi</b>
<b>29</b>	<b>List of Tables</b>	<b>xiii</b>
<b>30</b>	<b>Basic analysis information</b>	<b>1</b>
<b>31</b>	<b>Introduction</b>	<b>1</b>
<b>32</b>	<b>1 Experimental setup</b>	<b>3</b>
33	1.1 Relativistic Heavy Ion Collider . . . . .	3
34	1.2 Solenoidal Tracker at RHIC . . . . .	3
35	1.3 Time Projection Chamber . . . . .	4
36	1.4 Time of Flight detector . . . . .	4
37	1.5 Beam-Beam Counter . . . . .	5
38	1.6 Zero-Degree Calorimeters . . . . .	5
39	1.7 Roman Pot system . . . . .	5
40	1.8 The forward proton track reconstruction algorithm . . . . .	7
<b>41</b>	<b>2 Data set and Quality Assurance</b>	<b>9</b>
42	2.1 Data format . . . . .	9
43	2.2 Reconstruction software . . . . .	9
44	2.3 Triggers . . . . .	10
45	2.4 RP alignment . . . . .	11
46	2.4.1 Elastic events . . . . .	11
47	2.4.2 Alignment based on the collinearity of elastic events . . . . .	12
48	2.5 Bad run list . . . . .	13
<b>49</b>	<b>3 Event Selection</b>	<b>15</b>
50	3.1 List of cuts . . . . .	15
51	3.2 RP tracks (C1) . . . . .	16
52	3.3 Primary vertex and its $z$ -position (C2, C3) . . . . .	17
53	3.4 TPC tracks (C4, C5) . . . . .	18

54	3.5 Exclusivity cut (C6) . . . . .	19
55	3.6 Particle identification . . . . .	21
56	<b>4 Backgrounds</b>	<b>25</b>
57	4.1 Exclusive background . . . . .	25
58	4.2 Non-exclusive background . . . . .	26
59	4.3 Non-exclusive background subtraction . . . . .	27
60	<b>5 Monte Carlo simulations</b>	<b>29</b>
61	5.1 Central embedding . . . . .	29
62	5.2 Simulation of the RP system . . . . .	30
63	5.2.1 Validation of the MC . . . . .	31
64	5.3 GRANITTI . . . . .	32
65	<b>6 Corrections</b>	<b>35</b>
66	6.1 Method of corrections application . . . . .	35
67	6.2 Trigger corrections . . . . .	35
68	6.2.1 DSM trigger bit corrections . . . . .	36
69	6.2.2 TOF trigger study . . . . .	38
70	6.2.3 RP trigger study . . . . .	39
71	6.2.4 Probability of retaining CEP event . . . . .	39
72	6.3 Roman Pot efficiency study . . . . .	41
73	6.3.1 Data-driven method . . . . .	41
74	6.3.2 Embedded MC method . . . . .	44
75	6.3.3 The detector efficiency . . . . .	44
76	6.3.4 The proton selection efficiency . . . . .	46
77	6.3.5 RP Fiducial volume . . . . .	47
78	6.4 TPC vertex reconstruction efficiency . . . . .	48
79	6.5 Central embedding . . . . .	49
80	6.5.1 TPC track acceptance, reconstruction and selection efficiency . . . . .	49
81	6.5.2 TOF acceptance, hit reconstruction and TPC track matching efficiency . . . . .	51
83	6.6 PID efficiency study . . . . .	52
84	6.7 TPC z-vertex cut C2 . . . . .	52
85	6.8 Exclusivity cut C6 . . . . .	54
86	6.9 Corrections to the luminosity . . . . .	58
87	<b>7 Systematic Uncertainties</b>	<b>61</b>
88	7.1 Summary of the systematic effects . . . . .	61
89	7.2 Systematic Uncertainties . . . . .	61

90	7.3 TPC combined efficiency correction . . . . .	63
91	7.4 TOF matching efficiency correction . . . . .	65
92	7.5 TPC vertex reconstruction . . . . .	65
93	<b>8 Results</b>	<b>67</b>
94	8.0.1 Differential fiducial cross sections . . . . .	67
95	8.0.2 Integrated fiducial cross sections . . . . .	76
96	<b>Appendices</b>	<b>77</b>
97	<b>A The m2TOF method</b>	<b>79</b>
98	<b>B Missing pT cut plots</b>	<b>81</b>
99	<b>C Good run list</b>	<b>83</b>
100	<b>D Bad run list</b>	<b>89</b>
101	<b>E The central embedding validation</b>	<b>93</b>
102	<b>F The validation of the simulation of the RP system</b>	<b>105</b>
103	<b>G The total TPC track efficiency</b>	<b>109</b>
104	<b>H The total TOF hit efficiency</b>	<b>117</b>
105	<b>I Data driven method to TOF efficiency</b>	<b>123</b>
106	I.1 Pre-selection of candidates . . . . .	123
107	I.2 Selection criteria . . . . .	126
108	I.3 Yield extraction and results . . . . .	127
109	I.4 Systematic errors . . . . .	128
110	<b>References</b>	<b>133</b>



# 111 List of Figures

112	1.1	Schematic view of STAR experiment . . . . .	4
113	1.2	Roman Pot Phase II* layout . . . . .	6
114	1.3	Roman pot vessels and SSD package . . . . .	7
115	1.4	A scheme of the forward proton track reconstruction algorithm . . . . .	8
116	2.1	Illustration of (in)elastic combination . . . . .	10
117	2.2	Collinearity distributions $\Delta\theta_{x,y}$ . . . . .	12
118	2.3	An example of TPC-TOF inefficiency . . . . .	14
119	2.4	$A < \eta >$ of good TPC-TOF tracks for all runs . . . . .	14
120	2.5	A probability of retaining CEP event as a function of instantaneous luminosity. . . . .	14
121	2.6	Difference between the fit and data in probability of retaining CEP event. . . . .	14
123	3.1	The RP fiducial volume. . . . .	17
124	3.2	$z$ -position of the primary vertex for CEP event candidates . . . . .	17
125	3.3	$N_{\text{hits}}^{\text{fit}}$ and $N_{\text{hits}}^{\langle dE/dx \rangle}$ for CEP event candidates . . . . .	18
126	3.4	$DCA(xy)$ and $DCA(z)$ for CEP event candidates . . . . .	18
127	3.5	$\eta - z_{\text{vtx}}$ for CEP event candidates . . . . .	19
128	3.6	$p_{\text{T}}^{\text{miss}}$ for $\pi^+\pi^-$ CEP event candidates . . . . .	20
129	3.7	Summary of CEP event selection . . . . .	20
130	3.8	$\langle dE/dx \rangle$ and $m_{\text{TOF}}^2$ of the central system . . . . .	21
131	4.1	An illustration of the most common cases of non-exclusive background sources. . . . .	26
132	4.2	Correlation between $m(\pi^+\pi^-)$ and $p_{\text{T}}^{\text{miss}}$ . . . . .	28
133	4.3	The corrected $m(\pi^+\pi^-)$ before the non-exclusive background subtraction. . . . .	28
134	4.4	The comparison $d\sigma dm(\pi^+\pi^-)$ for different projection range in the background subtraction method. . . . .	28
135	5.1	A comparison of the $N_{\text{hits}}^{\text{fit}}$ between the data and embedding. . . . .	30
136	5.2	The distance between reconstructed point and the fit for elastic events . . . . .	31

139	5.3	A generic diagram of central exclusive production of $\pi^+\pi^-$ . . . . .	32
140	5.4	The Durham QCD model of central exclusive production. . . . .	33
141	6.1	Total efficiencies of selected CEP events in $\pi^+\pi^-$ channel. . . . .	36
142	6.2	DSM trigger bits' efficiencies . . . . .	38
143	6.3	DSM trigger bits' efficiencies only for good runs. . . . .	38
144	6.4	The RP trigger efficiency in $p_x, p_y$ space . . . . .	40
145	6.5	A probability of retaining CEP event as a function of instantaneous luminosity. . . . .	41
147	6.6	Difference between the fit and data in probability of retaining CEP event.	42
148	6.7	Scheme of efficiency calculation for E1U . . . . .	42
149	6.8	The point reconstruction efficiency as the function of reconstructed track momenta. . . . .	43
151	6.9	The point reconstruction efficiency as the function of reconstructed track momenta for MC embedded with ZB. . . . .	45
153	6.10	The point reconstruction efficiency as the function of reconstructed track momenta for MC embedded with ZB. . . . .	46
155	6.11	Illustration of the TPC vertex reconstruction efficiency study. . . . .	49
156	6.12	Distribution of $\delta(\eta, \phi)$ between reconstructed tracks and matched true-level particles. . . . .	51
158	6.13	Pair identification efficiency and misidentification probability. . . . .	53
159	6.14	The distribution of $z_{\text{vtx}}$ for the CPT2noBBCL trigger with a single TOF vertex . . . . .	54
161	6.15	The distribution of the mean parameter of the normal distribution as a function of the fill number . . . . .	55
163	6.16	The distribution of the width parameter of the normal distribution as a function of the fill number . . . . .	55
165	6.17	The efficiency as a function of the fill number . . . . .	56
166	6.18	$p_x^{\text{miss}}$ for $\pi^+\pi^-$ CEP event candidate . . . . .	57
167	6.19	$p_y^{\text{miss}}$ for $\pi^+\pi^-$ CEP event candidate . . . . .	57
168	6.20	$p_T^{\text{miss}}$ for $\pi^+\pi^-$ CEP event candidate . . . . .	58
169	6.21	CEP $\pi^+\pi^-$ signal efficiency, purity and significance as a function of $p_T^{\text{miss}}$	59
170	7.1	Variation of the TPC track quality cuts on the fiducial differential exclusive $\pi^+\pi^-$ production cross section . . . . .	64
172	7.2	Variation of the TPC efficiency correction application on the fiducial differential exclusive $\pi^+\pi^-$ production cross section . . . . .	64
174	7.3	Variation of the TOF efficiency correction application on the fiducial differential exclusive $\pi^+\pi^-$ production cross section . . . . .	65

---

176	7.4 Variation of the TPC vertex quality cuts on the fiducial differential ex-	
177	clusive $\pi^+\pi^-$ production cross section . . . . .	66
178	8.1 Differential fiducial cross sections of hadron pairs as a function of $\Delta\varphi$ . .	68
179	8.2 Differential fiducial cross sections of pion, kaon, and proton pairs as a	
180	function of the invariant mass of the pair in two regions of $\Delta\varphi$ . . . . .	69
181	8.3 Differential fiducial cross sections of pion, kaon, and proton pairs as a	
182	function of the rapidity of the pair in two regions of $\Delta\varphi$ . . . . .	71
183	8.4 Differential fiducial cross sections of pion, kaon, and proton pairs as a	
184	function of the $ t_1 + t_2 $ in two regions of $\Delta\varphi$ . . . . .	73
185	8.5 Differential fiducial cross sections of pion pairs as a function of the $\Delta\varphi$ in	
186	three regions of the invariant mass of the pair . . . . .	74
187	8.6 Differential fiducial cross sections of pion pairs as a function of the $y$ in	
188	three regions of the invariant mass of the pair . . . . .	74
189	8.7 Differential fiducial cross sections of pion pairs as a function of the $ t_1 + t_2 $	
190	in three regions of the invariant mass of the pair . . . . .	75
191	A.1 Illustration of $m_{\text{TOF}}^2$ method . . . . .	79
192	B.1 $p_x^{\text{miss}}$ and $p_y^{\text{miss}}$ for $K^+K^-$ and $p\bar{p}$ CEP event candidates . . . . .	81
193	B.2 $p_{\text{T}}^{\text{miss}}$ for $K^+K^-$ and $p\bar{p}$ CEP event candidate . . . . .	82
194	B.3 $p_{\text{T}}^{\text{miss}}$ for $K^+K^-$ and $p\bar{p}$ CEP event candidates . . . . .	82
195	E.1 A comparison of the $z$ -position between the data and the true-level MC. . . . .	93
196	E.2 A comparison of the $m_{\text{TOF}}^2$ between the data and embedding. . . . .	94
197	E.3 A comparison of the $\eta$ a $\varphi$ between the data, the true-level MC and	
198	embedding. . . . .	95
199	E.4 A comparison of the $N_{\text{hits}}^{\langle dE/dx \rangle}$ and the $N_{\text{hits}}^{\text{fit}}$ between the data and em-	
200	bedding. . . . .	95
201	E.5 A comparison of the transverse momenta between the data, the true-level	
202	MC and embedding. . . . .	95
203	E.6 A comparison of the TOF path length between the data and the embedding. . . . .	96
204	E.7 A comparison of the $x$ and $y$ position between the data and embedding. . . . .	96
205	E.8 A comparison of the $n\sigma_{\pi^-}$ and $n\sigma_{\pi^+}$ between the data and embedding. . . . .	97
206	E.9 A comparison of the $dEdx$ between the data and embedding. . . . .	98
207	E.10 A comparison of the $dEdx$ between the data and embedding. . . . .	99
208	E.11 A comparison of the $dEdx$ between the data and embedding. . . . .	100
209	E.12 A comparison of the $dEdx$ between the data and embedding. . . . .	101
210	E.13 A comparison of the $dEdx$ between the data and embedding. . . . .	102
211	E.14 A comparison of the $dEdx$ between the data and embedding. . . . .	103

212	F.1	Cluster energy distributions for the data, embedding and pure MC . . . . .	105
213	F.2	Cluster length distributions for the data, embedding and pure MC . . . . .	106
214	F.3	Difference between the reconstructed scattering angles for the data, em- bedding and pure MC. . . . .	106
215	F.4	Number of clusters per RP for the data, embedding and pure MC . . . . .	107
217	G.1	The total TPC track efficiency as a function of the azimuthal angle $\varphi$ and the pseudorapidity $\eta$ . . . . .	109
219	G.2	The total TPC track efficiency as a function of the pseudorapidity $\eta$ . . . . .	110
220	G.3	The total TPC track efficiency as a function of the azimuthal angle $\varphi$ . . . . .	111
221	G.4	The total TPC track efficiency as a function of the transverse momenta $p_T$ . . . . .	112
222	G.5	The total TPC track efficiency as a function of the $z$ -position of the primary vertex $z_{\text{vtx}}$ . . . . .	113
224	G.6	The total TPC track efficiency as a function of the $z$ -position of the primary vertex $z_{\text{vtx}}$ and the pseudorapidity $\eta$ . . . . .	114
225	G.7	The average total TPC track efficiency as a function of the $z$ -position of the primary vertex $z_{\text{vtx}}$ and the pseudorapidity $\eta$ . . . . .	115
228	H.1	The total TOF track efficiency as a function of the azimuthal angle $\varphi$ and the pseudorapidity $\eta$ . . . . .	117
230	H.2	The total TOF track efficiency as a function of the pseudorapidity $\eta$ . . . . .	118
231	H.3	The total TOF track efficiency as a function of the azimuthal angle $\varphi$ . . . . .	119
232	H.4	The total TOF track efficiency as a function of the transverse momenta $p_T$ . . . . .	120
233	H.5	The total TOF track efficiency as a function of the $z$ -position of the primary vertex $z_{\text{vtx}}$ and the pseudorapidity $\eta$ . . . . .	121
235	H.6	The average total TOF track efficiency as a function of the $z$ -position of the primary vertex $z_{\text{vtx}}$ and the pseudorapidity $\eta$ . . . . .	122
237	I.1	An illustration of topological cuts used in the StUPCV0 class for V0 selection process. . . . .	124
239	I.2	Distribution of variable DCA between combinations of daughter particles in the pre-selection process. . . . .	125
241	I.3	Distribution of variable DCA from the inverted momentum of V0 candi- date to the beamline in the pre-selection process. . . . .	125
243	I.4	Distribution of variable decay length from pre-selection of candidates for TOF detector efficiency. . . . .	125
245	I.5	Distribution of variable pointing angle which is the cosine of angle be- tween reconstructed pair momentum and a vector between primary and secondary vertex. . . . .	125

248	I.6	Correlation plot of particle momentum and energy loss while traversing the TPC. . . . .	127
249	I.7	Correlation plot of $n\sigma$ plot for pions on the $x$ -axis and protons on the $y$ -axis. . . . .	127
250	I.8	Correlating distribution of decay length on the $x$ axis and pointing angle on the $y$ axis. . . . .	128
251	I.9	Distribution of $z$ coordinate position of vertex along the beamline. . . . .	128
252	I.10	Sketch of how $K_S^0$ yield is extracted using integration method. . . . .	129
253	I.11	Invariant mass of $\pi^+\pi^-$ pairs where at least one of the tracks has a match with Time of Flight detector. . . . .	130
254	I.12	Invariant mass of $\pi^+\pi^-$ pairs where both tracks have a match with Time of Flight detector. . . . .	130
255	I.13	Efficiency of TOF detector as a function of pseudorapidity. . . . .	130
256	I.14	Efficiency of TOF detector as a function of azimuthal angle $\varphi$ . . . . .	130
257	I.15	Efficiency of TOF detector as a function of transverse momentum. . . . .	130
258	I.16	Efficiency of TOF detector as a function of $z$ coordinate of vertex. . . . .	130
259	I.17	Histogram of data efficiency divided by the true MC sample w.r.t. pseu- dorapidity for evaluation of systematic error. . . . .	131
260	I.18	Histogram of data efficiency divided by the true MC sample w.r.t. az- imuthal angle for evaluation of systematic error. . . . .	131
261	I.19	Histogram of data efficiency divided by the true MC sample w.r.t. trans- verse momentum for evaluation of systematic error. . . . .	131
262	I.20	Histogram of data efficiency divided by the true MC sample w.r.t. vertex $z$ position for evaluation of systematic error. . . . .	131
263			
264			
265			
266			
267			
268			
269			
270			
271			



# <sup>272</sup> List of Tables

<sup>273</sup>	2.1	Central production trigger description . . . . .	10
<sup>274</sup>	2.2	Description of BBC trigger bit . . . . .	11
<sup>275</sup>	6.1	Description of DSM trigger bit corrections . . . . .	37
<sup>276</sup>	6.2	The average obtained RP efficiency for each branch . . . . .	43
<sup>277</sup>	6.3	The average obtained RP efficiency for each branch . . . . .	45
<sup>278</sup>	6.4	The average obtained RP efficiency for each branch . . . . .	47
<sup>279</sup>	6.5	The final total RP efficiency for each branch . . . . .	47
<sup>280</sup>	6.6	Summary of the parameters defining the fiducial volume. . . . .	48
<sup>281</sup>	7.1	Systematic uncertainties for the integrated fiducial cross section for CEP of $\pi^+\pi^-$ , $K^+K^-$ , and $p\bar{p}$ pairs. . . . .	63
<sup>283</sup>	8.1	The summary of resonances used in the calculation of GRANITTI pre- dictions. . . . .	68
<sup>285</sup>	8.2	Integrated fiducial cross sections of $\pi^+\pi^-$ , $K^+K^-$ , and $p\bar{p}$ pairs. . . . .	76
<sup>286</sup>	I.1	Table of results for Time of Flight detector efficiency. . . . .	128
<sup>287</sup>	I.2	Table of systematic errors for different variables obtained by comparing data to true MC sample. . . . .	129



289

# Basic analysis information

<b>Data set</b>	Run 17
<b>Production tag</b>	P20ic
<b>Library version</b>	L20c.
<b>Trigger IDs</b>	RP_CPT2noBBCL (570705)
<b>Embedding ids</b>	20222901 ( $\pi^+\pi^-$ ), 20222902 ( $K^+K^-$ ), 20222903 ( $p\bar{p}$ )

290      The goal of the analysis is to measure differential cross sections for CEP of  $\pi^+\pi^-$ ,  
291  $K^+K^-$ , and  $p\bar{p}$  pairs as functions of the azimuthal angle between the outgoing protons  
292 and two-hadron invariant mass inside a fiducial region. The fiducial region corresponds  
293 to the acceptance of the STAR detector and is determined by the central particles'  
294 transverse momenta and pseudorapidities as well as by the forward-scattered protons'  
295 momenta.



# <sup>296</sup> Introduction

<sup>297</sup> Measurement of Central Exclusive Production (CEP) in the Double IPomeron Exchange  
<sup>298</sup> (DIPE) process provides a unique opportunity to study the strong interaction described  
<sup>299</sup> by quantum chromodynamics (QCD). In the lowest order in QCD, the pomeron is de-  
<sup>300</sup> scribed as a pair of gluons. Thus, the DIPE provides a gluon-rich environment suitable  
<sup>301</sup> to study the production of glueballs, bound states consisting only of gluons. However,  
<sup>302</sup> the exact nature of the pomeron still remains elusive and the existence of a glueball has  
<sup>303</sup> not been unambiguously confirmed yet, despite its theoretical predictions. The experi-  
<sup>304</sup> mental confirmation of the existence of the glueball would be yet another strong support  
<sup>305</sup> for the validity of the QCD theory.

<sup>306</sup> CEP is a process where the colliding protons stay intact after the collision and  
<sup>307</sup> a central system is produced with quantum numbers of vacuum. Furthermore, the  
<sup>308</sup> produced system is well separated from the outgoing protons by large rapidity gaps. The  
<sup>309</sup> exclusive property of the process means that all particles in the final state are measured.  
<sup>310</sup> There are three possible mechanisms of CEP: double photon exchange, photoproduction,  
<sup>311</sup> and DIPE. The last one is expected to be dominant CEP mechanism at the Relativistic  
<sup>312</sup> Heavy Ion Collider (RHIC) energies. Hence, this work focuses on the CEP of two hadrons  
<sup>313</sup> produced through DIPE. The emphasis is on the production of  $\pi^+\pi^-$ ,  $K^+K^-$ , and  $p\bar{p}$   
<sup>314</sup> pairs. Although this process is topologically very simple, it is complex in theory and rich  
<sup>315</sup> in phenomena due to significant interference effects between resonance and continuum  
<sup>316</sup> production and significant re-scattering effects via additional interaction between the  
<sup>317</sup> protons.

<sup>318</sup> The data from the STAR experiment at RHIC allow us to perform such studies.  
<sup>319</sup> This was confirmed by the most recent results of the CEP in proton-proton collisions  
<sup>320</sup> at  $\sqrt{s} = 200$  GeV [1], the highest center-of-mass energies at which DIPE has been  
<sup>321</sup> measured with the detection of the outgoing protons. The STAR experiment is able  
<sup>322</sup> to measure both the central system and the forward-scattered protons. This gives us  
<sup>323</sup> complete control over the kinematics of the interaction and verification of its exclusivity.  
<sup>324</sup> The central system is mainly measured in the Time Projection Chamber (TPC) and in  
<sup>325</sup> the Time of Flight (TOF) systems and outgoing protons are detected in Roman Pot  
<sup>326</sup> detectors. The Roman Pot detectors are presented in the next chapter and the following

<sup>327</sup> chapters are dedicated to the analysis of the CEP of  $\pi^+\pi^-$ ,  $K^+K^-$ , and  $p\bar{p}$  pairs in  
<sup>328</sup> proton-proton collisions at  $\sqrt{s} = 510$  GeV.

329 **Chapter 1**

330 **Experimental setup**

331 The results reported here are based on the data collected by the STAR experiment [2] in  
332 proton–proton collisions at the center of mass energy  $\sqrt{s} = 510$  GeV at the Relativistic  
333 Heavy Ion Collider (RHIC) [3], [4]. The setup is the same as for  $\sqrt{s} = 200$  GeV and  
334 described in [1].

335 The following sections briefly describe RHIC, STAR, and the main detectors used in  
336 this analysis. The last section, Sec. 1.7, presents the detailed description of the Roman  
337 Pot system since it is not commonly used in STAR.

338 **1.1 Relativistic Heavy Ion Collider**

339 The RHIC is a versatile collider with two main programs: collisions of relativistic heavy  
340 ions and polarized protons with  $\sqrt{s}$  up to 510 GeV.

341 **1.2 Solenoidal Tracker at RHIC**

342 The Solenoidal Tracker at RHIC (STAR) is a general-purpose detector at RHIC. It was  
343 originally designed to study the strongly interacting matter at high temperatures and  
344 high energy densities, especially the properties of the quark-gluon plasma. It is a massive  
345 detector weighing about 1200 tons and consisting of many sub-detectors enclosed in 0.5  
346 Tesla solenoidal magnetic field parallel to the beam axis. The magnetic field is generated  
347 by solenoidal magnet covering full azimuthal angle and pseudorapidity  $|\eta| < 1$ . Since  
348 2000, when the STAR detector was launched, it has been continuously upgraded. The  
349 relevant setup for this analysis is the one installed in 2017, therefore, it is presented here.

350 Figure 1.1 shows the STAR detector with its sub-detectors, namely TPC [5] is the  
351 core of the STAR detector, TOF [6], the Beam-Beam Counter (BBC) [7], the Vertex  
352 Position Detector (VPD), and the Barrel Electromagnetic Calorimeter (BEMC). Fur-  
353 thermore, the STAR experiment includes forward systems: the Zero-Degree Calorimeters

354 (ZDC) [8], [9] and the Roman Pot (RP) system [10]. These sub-detectors are located  
 355 further down the beam line and they are particularly important for the CEP analysis,  
 356 especially the RP system. In the following sections, the sub-detectors are briefly  
 357 described.

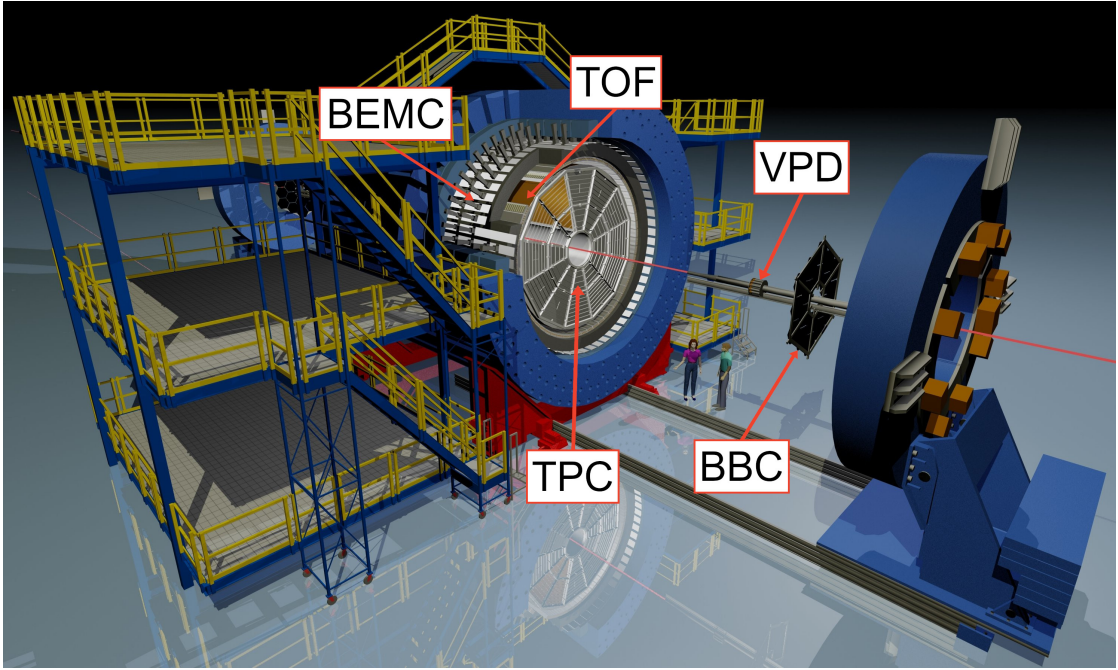


Figure 1.1: The schematic view of the STAR experiment. Main sub-detectors, including the TPC, the TOF, the BBC, the VPD and the BEMC are highlighted.

### 358 1.3 Time Projection Chamber

359 The TPC is the main detector in STAR and plays a significant role in this analysis.  
 360 It is a gaseous detector providing both tracking information and the average ionization  
 361 energy loss per unit length  $\langle dE/dx \rangle$  for each track. The momentum reconstruction and  
 362  $\langle dE/dx \rangle$  allow identification of charged particles. The particle identification is described  
 363 in Sec. 3.6. It is of cylindrical shape with the length of 4.2 m, the inner radius of 0.5 m  
 364 and the outer radius of 2 m. The TPC has full azimuthal coverage and pseudorapidity  
 365 coverage  $|\eta| < 1.0$ .

### 366 1.4 Time of Flight detector

367 The TOF is a cylindrical shell around the TPC extending the PID capabilities of the  
 368 TPC for particles with momenta up to  $\sim 3$  GeV. The TOF is composed of adjacent  
 369 Multi-gap Resistive Plate Chambers (MRPC). There are 120 trays, each consisting of  
 370 32 MRPC modules, covering the full azimuthal angle and the pseudorapidity  $|\eta| < 0.9$ .

371 It is a fast timing detector with a time resolution between 60 – 100 ps. Therefore, it  
372 is often used in the trigger system of the STAR experiment to select charged particle  
373 multiplicities. For the CEP events, it is crucial for triggering on low multiplicity events  
374 in the TPC. Moreover, it helps to discriminate in-time TPC tracks from different bunch  
375 crossings (out-of-time pile-up).

376 **1.5 Beam-Beam Counter**

377 The BBC is an array of plastic scintillator detectors designed to detect high- $\eta$  particles  
378 produced in the forward direction. The BBC consists of two identical detectors placed at  
379  $\pm 3.74$  m from the interaction point (IP). The location of the BBC can be seen in Fig. 1.1.  
380 Each detector is made up of 36 hexagonal scintillator tiles, 18 small ones, covering a  
381 pseudorapidity range of  $2.1 < |\eta| < 3.3$  and 18 large ones, covering  $3.3 < |\eta| < 5.0$ ,  
382 respectively. For the CEP events, it is used as a rapidity gap veto, to ensure the rapidity  
383 gaps between the central produced system and forward-scattered protons.

384 **1.6 Zero-Degree Calorimeters**

385 ZDC's main function is to measure particles produced in the forward direction (at near  
386 zero degree angle). They are placed on each side of the IP at the distance of 18 m from  
387 the IP. The ZDCs are placed directly in line with the STAR beam pipe behind the dipole  
388 magnets, which deflect charged particles. They are sensitive to the neutrons produced in  
389 the forward direction and are used in this analysis as one of the detectors to determine  
390 CEP topology.

391 **1.7 Roman Pot system**

392 The RP system is used to detect and measure forward protons scattered at very small  
393 angles (few mrad), whose trajectories are contained in the accelerator beam pipe. For  
394 that purpose, the STAR experiment was upgraded with the RP system previously used  
395 by the PP2PP experiment [10]. Two RP stations were installed on each side of the IP  
396 at a distance of 15.8 m and 17.6 m from the IP. The location of the RPs, the top and  
397 side views, and the coordinate system are shown schematically in Fig. 1.2.

398 The RP stations were placed behind the DX magnet, the RHIC-lattice dipole mag-  
399 net closest to the IP, hence allowing the measurement of the momentum vector of the  
400 scattered protons at the detection point. Because of the symmetry of the RHIC rings,  
401 the fields in the DX magnets on both sides of the IP are identical at the  $10^{-3}$  level.  
402 The RP layout ensures that no special beam conditions were needed to operate the RP  
403 detectors.

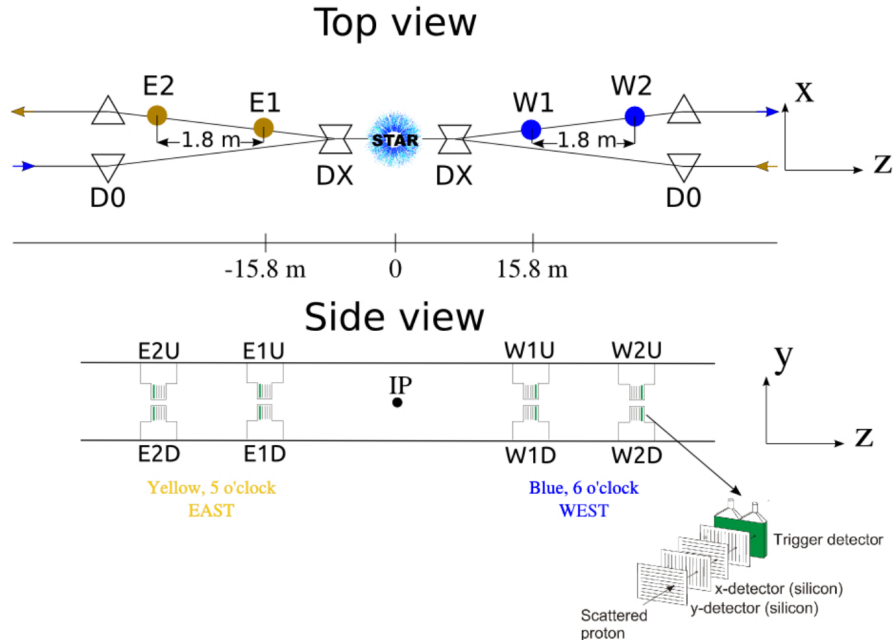


Figure 1.2: The layout of the RP setup at STAR (not to scale) for measuring forward protons. Top ( $x, z$ ) and side ( $y, z$ ) views are shown. Two sets of RPs, labeled (W1, W2) and (E1, E2) were installed between the DX and D0 magnets, at 15.8 m and 17.6 m, on either side of the IP. The detector package has transverse size  $5 \times 8 \text{ cm}^2$  and a depth 3.5 cm. The Si sensor is  $400 \mu\text{m}$  thick, while the trigger scintillator is 5 mm thick. The strips in the Si detectors are  $\approx 100 \mu\text{m}$  wide. Two dipole magnets, DX and D0, which bend the beams into and out of the IP, are also shown. Top view with highlighted Roman Pot stations E1, E2, W1, W2 and dipole magnets DX, D0. Side view with depicted Roman Pots. Taken from Ref. [11].

404     Each RP station has two movable RP vessels: one above and one below the beam  
 405 pipe. An RP vessel is illustrated in Fig. 1.3 (left) with the main parts highlighted. A  
 406 window is made of  $300 \mu\text{m}$  thick stainless steel to minimize the amount of material  
 407 where the traversing proton can be scattered before being measured in SSDs. The  
 408 rectangular profile of the RP vessel enables one to vertically approach the detector to  
 409 the beam. The typical distance between the beam and the RP is between  $2 - 3$  cm  
 410 during data collection. Each stainless steel RP vessel houses a Silicon Strip Detector  
 411 (SSD) package and a scintillation counter. The SSD package is shown in Fig. 1.3 (right)  
 412 and consists of four SSDs measuring the position of the proton in the  $x - y$  plane, two  
 413 measuring  $x$ - coordinates, and two measuring  $y$ - coordinates. Having two RP stations  
 414 on each side allowed momentum reconstruction of scattered protons. The scintillation  
 415 counter was used to trigger on forward protons. Each trigger counter was read out by  
 416 two photomultipliers. The stainless steel vessel separates the detector package from the  
 417 machine vacuum, allowing the package to operate at normal atmospheric pressure.

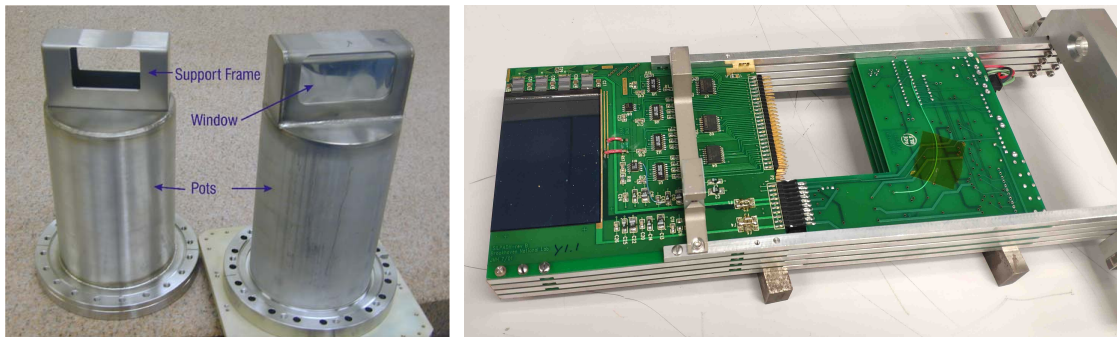


Figure 1.3: The Roman pot vessels and the SSD package. Left: a photo of the two Roman Pots vessels, taken from Ref. [10]. Main parts are indicated. Right: a photo of the Silicon Strip Detector package, taken by myself.

418     There is an RP naming convention that denotes the position of each RP. The RP  
 419 names are in the following format: side of the IP (E or W), station (1 or 2), and  
 420 orientation (U or D). For example, the first RP located on the west side of the IP above  
 421 the beam line is called W1U. Moreover, the RP system is divided into four branches (EU,  
 422 ED, WU, and WD), in which proton tracks can be reconstructed. A branch is composed  
 423 of two RP on the same side and with the same orientation (U or D). For example, the  
 424 EU branch is composed of E1U and E2U RPs.

## 425    1.8 The forward proton track reconstruction algorithm

426     The proton reconstruction algorithm forms tracks from signal in each SSD plane. Fig. 1.4  
 427 illustrates the forward track reconstruction algorithm. First, the signal is read in each  
 428 plane, and the signal from adjacent strips in the same plane forms a cluster. The cluster

is the smallest structure that is stored in the *star-upcDst* framework. The clusters are paired from two planes that measure the same coordinate in the hit. From the hits, a point is reconstructed in a RP. Subsequently, a track is formed from two points. If there is an additional cluster in the plane, the additional hit is formed. Hence, an additional track is also formed. Therefore, all possible tracks are reconstructed, and the "true" track is indistinguishable from the others. Thus, in this and also in other analyses at STAR, exactly one RP track on each side is required (cut C1).

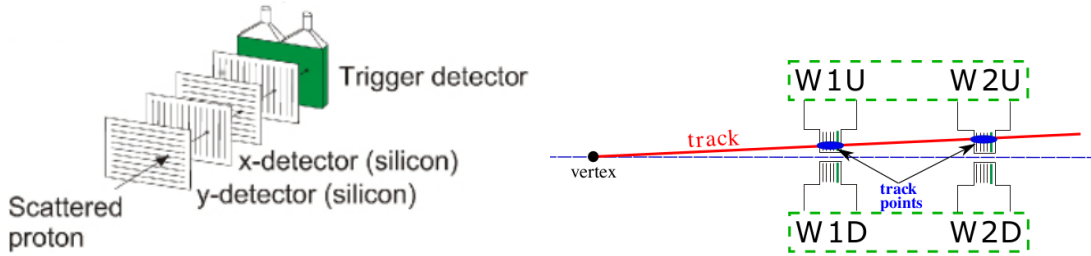


Figure 1.4: An illustration of the forward proton track reconstruction algorithm. The left part illustrates a formation of clusters and subsequent hit in a RP when a proton traverse through. The right one depicts the west branches of the RP system and the reconstruction of a RP track in WU branch from two hits in W1U and W2U.

436 **Chapter 2**

437 **Data set and Quality Assurance**

438 **2.1 Data format**

439 In 2017 between February 12 and May 30, the STAR experiment collected data on  $pp$   
440 collisions at  $\sqrt{s} = 510$  GeV. However, the standard picoDst format is not suitable for  
441 this analysis since it does not contain the information about outgoing protons from the  
442 Roman Pot detectors. Thus, a *star-upcDst* framework was developed to simplify the  
443 analyzes related to forward and ultra-peripheral collisions (UPC) physics.

444 To estimate the efficiency of reconstruction of the TPC vertex and to study the  
445 efficiency of TOF matching using  $K_S^0$  particles, global tracks must be used. The original  
446 *star-upcDst* framework contained only the primary tracks. Hence, it was extended by  
447 including preselected global tracks from the standard picoDst format. The *star-upcDst*  
448 framework description files (C++ headers, etc.) can be found in the code repository [12].

449 **2.2 Reconstruction software**

450 Raw data was processed with STAR libraries in versions SL20c. The following BFC  
451 options were used in the reconstruction: *DbV20200225*, *pp2017a*, *StiCA*, *btof*, *mtd*,  
452 *mtdCalib*, *pp2pp*, *PicoVtxDefault*, *UseBTOFmatchOnly*, *VFStoreX*, *fmsDat*, *fmsPoint*,  
453 *fpsDat*, *BEmcChkStat*, *OSpaceZ2*, *OGridLeakFull*, *-evout*, *-hitfilt*

454 Main attention should be put on the option *useBTOFmatchOnly* which forced the  
455 vertexing algorithm to form vertices only from the global TPC tracks matched with  
456 hits in the TOF system. This solution was found to yield significantly larger signal  
457 reconstruction efficiency (vertexing efficiency) and better resolutions. It is also worth  
458 mentioning that the TOF matching in the vertex algorithm uses different TOF match  
459 definition than is normally used, see [13].

460 **2.3 Triggers**

461 The following CPT triggers were collected: CPT2noBBCL (570705), CPT2 (570701),  
 462 CPT2 (570711). The definitions of triggers are summarized in Tab. 2.1. Triggers  
 463 were formed from the conditions combined by logical AND (`&&`). After all, only  
 464 the CPT2noBBCL trigger is used in this study. It consisted of two conditions, each  
 465 containing a signal in at least one RP on each side of the STAR central detector in  
 466 the (in)elastic combination of RP stations. The elastic and inelastic combinations are  
 467 sketched in Fig. 2.1. The signal ensures the presence of at least two forward-scattered  
 468 protons. Furthermore, a veto was imposed on a simultaneous signal in the other combi-  
 nation, which could come from either proton dissociation or pile-up events.

Condition	CPT2noBBCL 570705	CPT2 570701	CPT2 570711
Elastic combination in RP	–	+	–
Inelastic combination in RP	+	–	+
Number of TOF hits > 1	+	+	+
Number of TOF hits > 10	–	–	–
Hit in BBC east	–	–	–
Hit in BBC west	–	–	–
Hit in BBC Large east	–	–	x
Hit in BBC Large west	–	–	x
Hit in ZDC east	–	–	–
Hit in ZDC west	–	–	–

Table 2.1: Description of central production trigger. Symbols “+”, “–”, and “x” stand for a requirement, a veto, and not used, respectively.

469

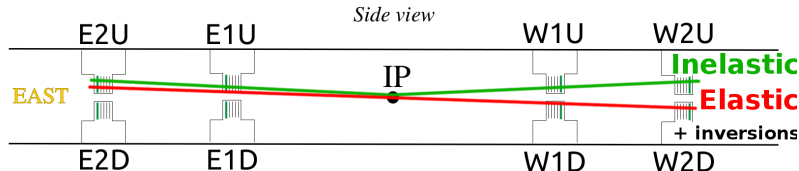


Figure 2.1: An illustration of the inelastic and the elastic combinations of reconstructed tracks in RP stations. The “+ inversions” denotes the possibility of the (in)elastic signal in (ED-WD) ED-WU branch combinations.

470 Next, at least two hits in the TOF were required to ensure two in-time tracks in the  
 471 TPC. To reject a high multiplicity event, a veto on TOF hits ( $\leq 10$ ) was imposed. A  
 472 veto on any signal in small or large BBC tiles or ZDCs on any side of the STAR central  
 473 detector was used to ensure the double-gap topology typical of CEP events.

474 A valid RP signal, measured in the scintillation trigger counter, had to be within  
 475 the TAC window ( $200 < \text{TAC} < 1750$  TAC) and the ADC signal be greater than 30  
 476 ADC. The TAC window and the ADC threshold were also used for CPT2 (570711).  
 477 CPT2 (570701) was taken as the first CPT trigger with the same trigger settings as in

478 2015: the wider TAC window ( $100 < \text{TAC} < 2500$  TAC) and the higher ADC threshold  
 479 of 100 ADC. A valid signal in BBC (both small and large) was defined using good hit  
 480 logic. First, a good hit in a channel was required to have an ADC value greater than  
 481 a threshold ( $\text{ADC}_{\text{Min}}$ ) while the corresponding TAC value greater than  $\text{TAC}_{\text{Min}}$  and  
 482 less than  $\text{TAC}_{\text{Max}}$ . Then, the ADC values of all good hit channels were summed and  
 483 compared with a threshold  $\text{ADC}_{\text{Sum}}$ . The threshold values are summarized in Tab. 2.2.  
 484 The setting of  $\text{ADC}_{\text{Sum}}$  equal to  $\text{ADC}_{\text{Min}}$  simplified the definition of a valid signal in  
 485 BBC to the requirement of a good hit at least in one channel. A valid signal in ZDC  
 486 had to be within the TAC window ( $500 < \text{TAC} < 2700$  TAC) and had to have an ADC  
 487 value greater than 25 ADC in at least one of the three photomultiplier tubes.

	BBC Small	BBC Large
$\text{ADC}_{\text{Min}}$	20	50
$\text{TAC}_{\text{Min}}$	100	100
$\text{TAC}_{\text{Max}}$	2400	2500
$\text{ADC}_{\text{Sum}}$	20	50

Table 2.2: Description of BBC trigger bit for both BBC Small and Large tiles.

## 488 2.4 RP alignment

489 To be able to measure protons with very small scattering angles, RPs must be placed  
 490 very close to the beam ( $\sim$  cm). In this vicinity, RP cannot be permanently mounted  
 491 due to a very high background, especially during beam injections that could resolved in  
 492 radiation damage of the detectors.

493 The RPs are placed in the safe position about 9 cm from the beam line. Once the  
 494 beam is stable, RPs are moved closer to the beam. RPs are kept between 2 – 3 cm  
 495 from the beam during the data taking. The movement is read by the Linear Variable  
 496 Differential Transformer (LVDT). The position is needed to reconstruct the positions  
 497 of the hits of protons in RPs, especially in  $y$ -positions, where the movement of RPs.  
 498 Therefore, an alignment procedure is needed to obtain the true positions.

499 The alignment procedure consists of two steps. First, the  $y$ -position of the first strip  
 500 in RP is obtained from the LVDT readings, and the hits positions are calculated in the  
 501 lab frame. Second, the collinearity of elastic scattering tracks is used to cross-check the  
 502 alignment corrections from LVDTs. The first is done during the track reconstruction.  
 503 The second is further described in the next section.

### 504 2.4.1 Elastic events

505 The schematic view of the elastic event can be seen in Fig. 2.1. The elastic event is  
 506 characterized by two collinear tracks on each side of the IP and a lack of signal on the

other detectors. The collinear tracks are such that all of their reconstructed points lie on the same straight line.

The elastic triggers 570709 and 570719 are used for this study. Exactly two tracks are required in one of the elastic combinations: East-Up - West-Down or East-Down - West-Up. The same good quality RP criteria are applied as in the main analysis C1. The uniqueness of reconstructed tracks is required - one and only one reconstructed point (3/4 planes) in each RP and no points in the another elastic combination in the same event. Moreover, the collinearity cut and distance cut are applied. The collinearity is defined as

$$\Delta\theta_x = \theta_x^W - \theta_x^E < 3\sigma_0 \text{ and } \Delta\theta_y = \theta_y^W - \theta_y^E < 3\sigma_0, \quad (2.1)$$

where  $\theta_{x,y}^{W,E}$  are the reconstructed scattering angles on the West (W) and East (E) side in  $x - z$  and  $y - z$  planes. The  $\sigma_x^0 \approx \sigma_y^0 = \sigma_0 = 130 \mu\text{rad}$  is the Gaussian width of the collinearity distribution see Fig. 2.2. The  $\sigma_0$  is consistent with the beam angular divergence.

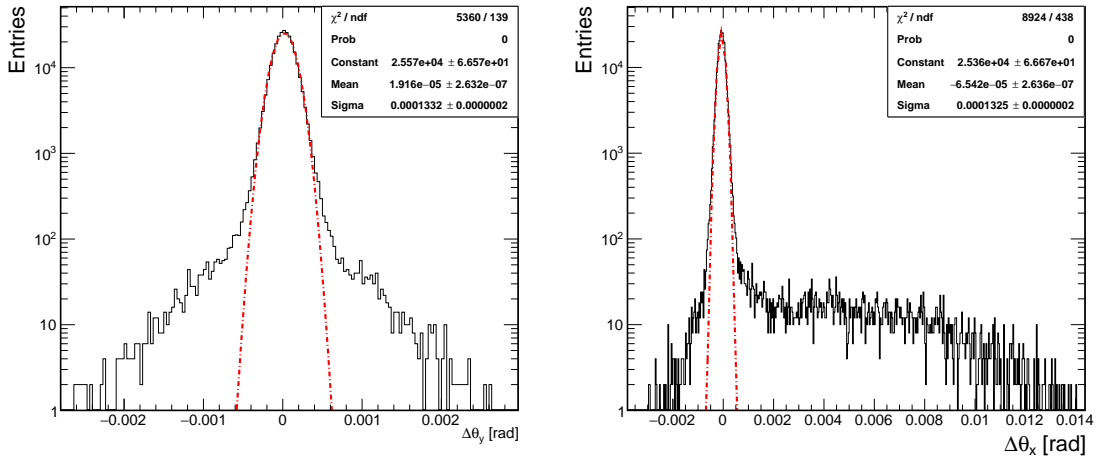


Figure 2.2: Collinearity distributions, the difference of scattering angles  $\theta_{x,y}$  in in  $x - z$  (left) and  $y - z$  (right) plane, respectively. The red dot-dashed lines illustrate the Gaussian fit.

#### 2.4.2 Alignment based on the collinearity of elastic events

Alignment corrections are obtained using reconstructed elastic events. It is the same procedure as it was already performed in elastic analysis [11] on a different data set.

In each elastic event, the four reconstructed points are corrected to the position of RP based on the LVDT readout on the MuDst level. In elastic events, the four points should be on a straight line in a global coordinate reference system. Hence, they are fitted by a 3D straight line. To calculate RP alignment corrections for each run, the average distance between the fit and the position of point is calculated for each RP:

529

$$\langle \Delta X_{\text{RP}} \rangle = \frac{1}{N_{\text{events}}} \sum_{i=1}^{N_{\text{events}}} (X_{i,\text{RP}} - X_{i,\text{Fit}}) \quad (2.2)$$

530

$$\langle \Delta Y_{\text{RP}} \rangle = \frac{1}{N_{\text{events}}} \sum_{i=1}^{N_{\text{events}}} (Y_{i,\text{RP}} - Y_{i,\text{Fit}}), \quad (2.3)$$

531 where  $X_{i,\text{RP}}$  and  $Y_{i,\text{RP}}$  are the reconstructed point positions and  $X_{i,\text{Fit}}$  and  $Y_{i,\text{Fit}}$  are the  
532 fitted line position in the  $i$ -th event of the run in the given RP.

533 The obtained corrections are applied to correct the position of reconstructed points.  
534 Then, the alignment process is repeated with new strip positions. Finally, the average  
535 correction over all runs of  $20 \pm 10 \mu\text{m}$  is obtained. Although the average correction is at  
536 the resolution level, it cannot be neglected. The alignment is validated by comparison  
537 with MC in Sec. 5.2.1.

## 538 2.5 Bad run list

539 This section describes techniques used to identify bad runs for the CEP analysis. In total,  
540 there are 2851 runs in the upcDst files. Of which 1997 runs contain the CPT2noBBCL  
541 trigger. The good and bad run list can be seen in Appendix C and Appendix D.

542 The run 18097004 is excluded from the analysis, as it contains at least one inactive  
543 RP. Inactive RPs were held away from the proton acceptance, about 9 cm from the  
544 beam. Thus, inactive RPs can simply be identified on the basis of LVDT readings.

545 RPs are very sensitive detectors. To ensure their safety, they are only moved to  
546 active data-taking area when the beam is stable. Hence, RPs are not used in the first  
547 and last runs of each fill. Therefore, these runs do not contain the CPT2noBBCL trigger  
548 and are excluded from the analysis. In total, 359 runs are excluded.

549 To identify inefficiency of TPC or TOF, a correlation plot of pseudorapidity  $\eta$  and  
550 azimuthal angle  $\varphi$  is studied for all good TPC-TOF tracks for each run. Several runs  
551 are identified with a missing TPC or TOF sector, see Fig. 2.3. To identify them, a  
552 distribution of average pseudorapidity  $\langle \eta \rangle$  of all good TPC-TOF tracks over each run  
553 is fitted by a Gaussian function; see Fig. 2.4. For each run outside the  $\pm 9\sigma$  range, the  
554  $\eta - \varphi$  correlation plot is studied separately. In this way, 174 runs are marked as bad  
555 runs, corresponding to approximately 5.8 % of CEP candidates.

556 The next 39 runs are excluded due to nonphysical values of instantaneous luminosity  
557 ( $\sim 0.017\%$  CEP candidates lost) and 459 runs show lower trigger efficiencies, see Sec. 6.2.  
558 They are also marked as bad runs ( $\sim 3.04\%$  CEP candidates lost).

559 Figure 2.5 depicts the probability of retaining the CEP event described in Sec. 6.2.4.  
560 Several runs strongly deviate from the overall trend illustrated by the blue line. The

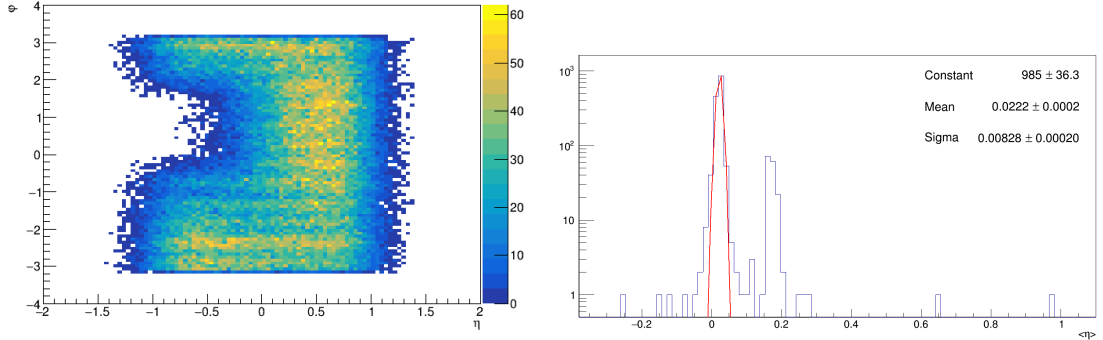


Figure 2.3: The map of TPC tracks matched with TOF hits in  $\eta - \varphi$  space for run 18094064.

Figure 2.4: An average pseudorapidity  $\langle \eta \rangle$  for each run for all good TPC-TOF tracks. The red line illustrates the Gaussian fit with its parameters displayed in the upper right corner of the figure.

561 iterative method was developed to identify the runs that deviate from the overall trend.  
 562 The difference between the data and the overall trend (fit from the previous iteration) is  
 563 calculated, see Fig. 2.6. The obtained distribution is fitted by the Gaussian function. For  
 564 all runs within the  $\pm 4\sigma$  range, the probability of retaining the CEP event as a function  
 565 of instantaneous luminosity was plotted and fitted by the exponential function  $a \times e^{-bL}$ .  
 566 The obtained fit parameters are used to estimate the overall trend. The method is  
 567 repeated until the fit parameters are stable. All runs outside the  $\pm 4\sigma$  range are marked  
 568 as bad runs.

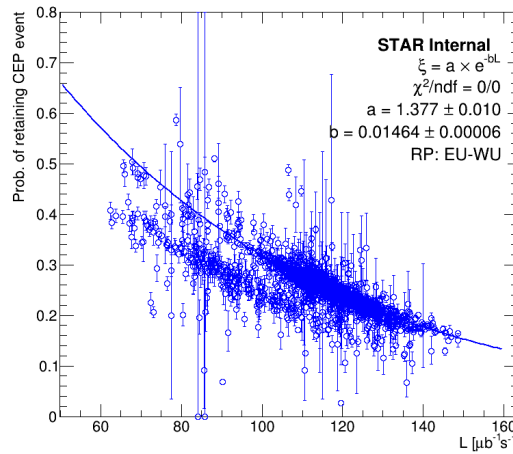


Figure 2.5: A probability of retaining CEP event as a function of instantaneous luminosity. The blue line illustrates the fit from the previous iteration. The iteration method is described in the text.

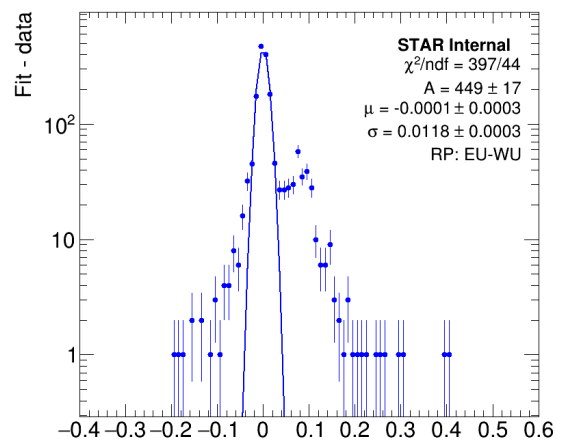


Figure 2.6: Difference between the fit of the probability of retaining CEP event as a function of instantaneous luminosity and the data. The blue line depicts the Gaussian fit.

569 **Chapter 3**

570 **Event Selection**

571 This chapter presents the selection cuts used for signal extraction. In Sec. 3.1, a list  
572 summarizing all selection criteria is introduced in Sec. 3.1. The subsequent sections are  
573 devoted to the detailed description of each cut.

574 **3.1 List of cuts**

575 To select CEP event candidates, the following cuts are applied:

576 C1 Exactly two good quality RP tracks inside the  $p_x, p_y$  fiducial region are found,  
577 where  $p_x, p_y$  are components of the transverse momenta of forward-scattered pro-  
578 tons:

579 C1.1 Good quality RP tracks have at least three out of four SSDs used in its  
580 reconstruction in each RP.

581 C1.2 Transverse momenta of RP tracks are within the  $p_x, p_y$  fiducial region of high  
582 geometrical acceptance defined in Sec. 6.3.5 by Eq. 6.8.

583 C1.3 There is exactly one RP track satisfying conditions above on each side of the  
584 IP.

585 C2 Exactly one primary vertex with a TPC track matched with a TOF hit is required.

586

587 C3 The  $z$ -position of the primary vertex is within  $\pm 100$  cm from the IP.

588 C4 Exactly two opposite-sign primary good quality TPC tracks matched with valid  
589 TOF hits are required:

590 C4.1 Tracks have sufficient momentum to reach TOF:  $p_T > 0.25$  GeV.

591 C4.2 Tracks must satisfy good quality criteria:

$$592 \quad N_{\text{hits}}^{\text{fit}} \geq 20 \text{ and } N_{\text{hits}}^{\langle dE/dx \rangle} \geq 15. \quad (3.1)$$

593 C4.3 Tracks are required to have good match to the primary vertex:

$$594 \quad |DCA(z)| < 1 \text{ cm and } |DCA(xy)| < 1.5 \text{ cm}. \quad (3.2)$$

595 C4.4 Tracks must be matched with valid TOF hits.

596 C4.5 There have to be exactly two tracks satisfying the above cuts.

597 C4.6 The total charge of tracks must be zero.

598 C5 Tracks have to be inside the kinematic range defined by Eq. 3.3 in  $\eta - z_{\text{vtx}}$  phase  
599 space:

$$600 \quad \begin{aligned} \eta &< -\frac{1}{250}z_{\text{vtx}} + 0.9, \\ \eta &> -\frac{1}{250}z_{\text{vtx}} - 0.9, \\ |\eta| &< 0.9. \end{aligned} \quad (3.3)$$

601

602 C6 The missing (total) transverse momenta of all tracks (TPC and RP)  $p_T^{\text{miss}}$  must be  
603 less than 120 MeV.

## 604 3.2 RP tracks (C1)

605 Only RP tracks with at least three out of four planes per RP used in the track re-  
606 construction are considered. Due to the very high single plane efficiency ( $> 99\%$ ), RP  
607 tracks with fewer hits are considered as background. Although planes have very high  
608 efficiencies, some planes were damaged during the data-taking. Hence, there were peri-  
609 ods during the data-taking, when there were only three active planes per RP until the  
610 damaged plane was replaced. Therefore, only three out of four planes are required.

611 To select candidates for the CEP events, exactly one RP track on each side satisfying  
612 the cut C1.1 is required. Furthermore, reconstructed protons must have transverse  
613 momenta ( $p_x, p_y$ ) inside a fiducial volume, defined in Sec. 6.3.5 by Eq. 6.8 to ensure  
614 high reconstruction and selection efficiency. The fiducial volume can be seen in Fig. 3.1,  
615 where it is drawn with black solid lines. The fiducial volume has been estimated based  
616 on the RP efficiency study Sec. 6.3 to reach a compromise between signal statistics and  
617 systematic uncertainties of RP efficiency.

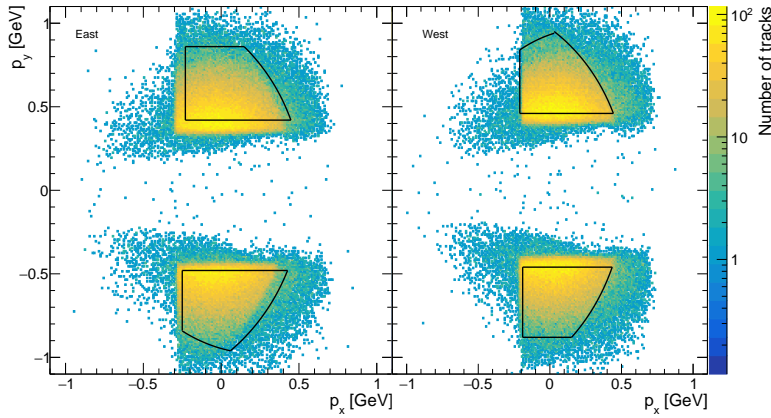


Figure 3.1: The RP fiducial volume shown with black solid lines on top of the combined distributions of forward protons' momenta  $p_y$  vs.  $p_x$  reconstructed with the East and West RP stations.

### 618 3.3 Primary vertex and its $z$ -position (C2, C3)

619 The primary vertex is a vertex associated to at least one TPC track matched with a valid  
 620 hit in TOF. A valid TOF hit is reconstructed from neighboring MRCP modules with  
 621 valid signals. A signal is valid when it exceeds the threshold and is within the predefined  
 622 time window. The vertex is reconstructed using the vertex finding algorithm [14], [15].  
 623 In the presented data set, the beamline constraint was used. It forces vertex to be  
 624 reconstructed at the  $(x, y)$  position of the beamline trajectory at given  $z$ . Furthermore,  
 625 the option *useBTOFmatchOnly* was used which forced the vertexing algorithm to form  
 626 vertices only from the global TPC tracks which are matched with hits in the TOF system.

627 Exactly one primary vertex is required to reject events with more than one inelastic  
 628 interaction per bunch crossing. In addition, the vertex must be placed within  $\pm 100$  cm  
 629 along the  $z$ -axis. Events outside the range have lower acceptance. Hence, they are  
 630 rejected. Figure 3.2 shows  $z$ -position of the primary vertices for CEP event candidates.  
 631 The black dot-dashed lines illustrate the cut C3.

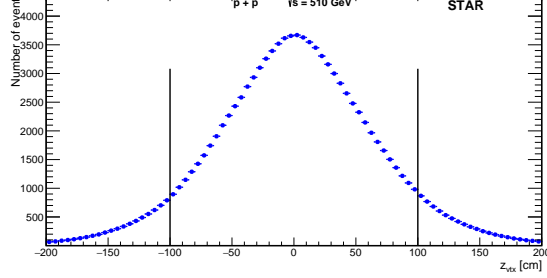


Figure 3.2: The distribution of the  $z$ -position of the primary vertex for CEP event candidates. Black lines depict the applied cut.

632 **3.4 TPC tracks (C4, C5)**

633 In the central state, only tracks matching a valid TOF hits are considered. The TOF  
 634 requirement ensures the selection of in-time tracks originating from the triggered bunch  
 635 crossing. In addition, the time-of-flight extend particle identification abilities that are  
 636 explained in Sec. 3.6. Therefore, tracks are required to have enough transverse momenta  
 637 to reach the TOF,  $p_T > 250$  MeV. Moreover, standard STAR good quality track criteria  
 638 are imposed to achieve good momentum and an average ionization energy loss per unit  
 639 length ( $\langle dE/dx \rangle$ ) resolution. Namely, a minimum of 20 hits in the TPC used for the  
 640 track reconstruction ( $N_{\text{hits}}^{\text{fit}} \geq 20$ ) and a minimum of 15 hits in the TPC used to calculate  
 641  $\langle dE/dx \rangle$  ( $N_{\text{hits}}^{\langle dE/dx \rangle} \geq 15$ ) are required. Figure 3.3 shows distributions of  $N_{\text{hits}}^{\text{fit}}$  and  
 642  $N_{\text{hits}}^{\langle dE/dx \rangle}$  of CEP event candidates.

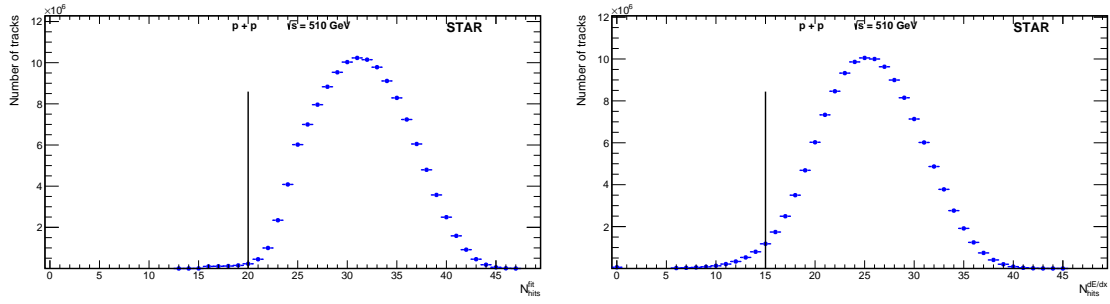


Figure 3.3: Distributions of number of hits in the TPC used for the track reconstruction  $N_{\text{hits}}^{\text{fit}}$  (left) and number of hits in the TPC used to calculate the energy loss  $N_{\text{hits}}^{\langle dE/dx \rangle}$  (right) for CEP event candidates. Black lines indicate applied cuts.

643 In addition, only tracks with good match to the primary vertex are further analyzed.  
 644 A track has a good match to the vertex if its distance of closest approach ( $DCA$ ) to the  
 645 vertex in the transverse plane ( $DCA(xy)$ ) is less than 1.5 cm and in the  $z$ -direction  
 646 ( $DCA(z)$ ) is smaller than 1.0 cm. Figure 3.4 shows the distributions of  $DCA(xy)$  and  
 647  $DCA(z)$  of the candidates for the CEP event with the imposed criteria highlighted by  
 648 black lines.

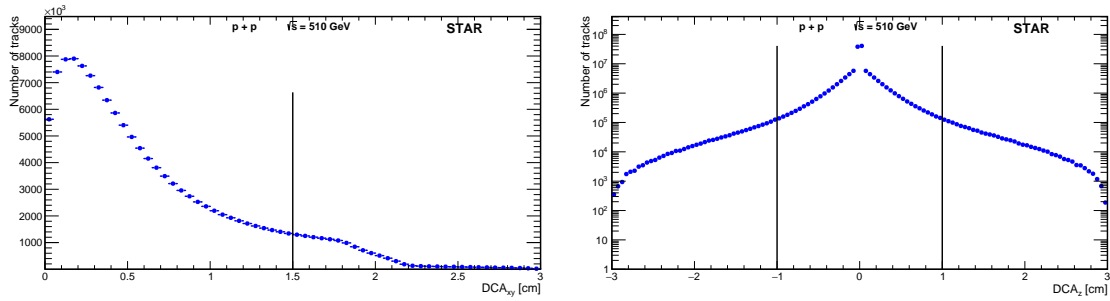


Figure 3.4: Distances of closest approach of track and the primary vertex in the transverse plane  $DCA(xy)$  (left) and in the  $z$ -direction  $DCA(z)$  (right) for CEP event candidates. Black dot-dashed lines depict applied cuts.

649 To select CEP event candidates, only events with exactly two tracks satisfying the  
 650 above criteria and with opposite charge are considered. To ensure high geometrical  
 651 acceptance and efficiency, the tracks are also required to have pseudorapidity within the  
 652 fiducial range defined by Eq. 3.3. The fiducial range can be seen in Fig. 3.5 where it is  
 653 illustrated by black lines.

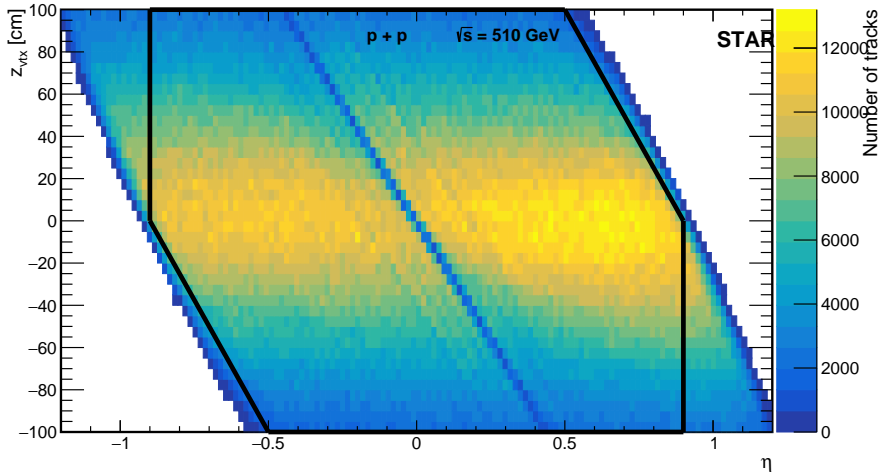


Figure 3.5: Correlation between pseudorapidity  $\eta$  and  $z$ -position of the primary vertex for CEP event candidates. The fiducial range is illustrated by black lines.

### 654 3.5 Exclusivity cut (C6)

655 The exclusivity cut represents the most important cut used in this analysis to select the  
 656 CEP event candidates. The missing transverse momentum is defined as the transverse  
 657 momentum of the sum of momenta of all the measured particles:

$$658 \quad p_T^{\text{miss}} := |(\vec{p}_p + \vec{p}_{h+} + \vec{p}_{h-} + \vec{p}_p)_T|. \quad (3.4)$$

659 It can be calculated only thanks to the detection and reconstruction of the forward-  
 660 scattered protons in RP detectors,

661 For CEP processes,  $p_T^{\text{miss}}$  should be equal to zero due to four-momentum conservation.  
 662 The distribution of  $p_T^{\text{miss}}$  can be seen in Fig. 3.6. The peak at the beginning of the  
 663 distribution comes from the exclusive events. Hence, the cut C6 ( $p_T^{\text{miss}} < 120$  MeV)  
 664 illustrated by the black dot-dashed line is used to select the CEP event candidates. The  
 665 figure is fully described in Sec. 6.8.

666 Figure 3.7 captures the entire event selection. Each bin represents event candidates  
 667 passing all the previous criteria. To select CEP event candidates, all presented criteria  
 668 plus the particle identification described in the next section are applied. In total, there  
 669 are 86008  $\pi^+\pi^-$ , 2454  $K^+K^-$ , and 225  $p\bar{p}$  CEP event candidates.

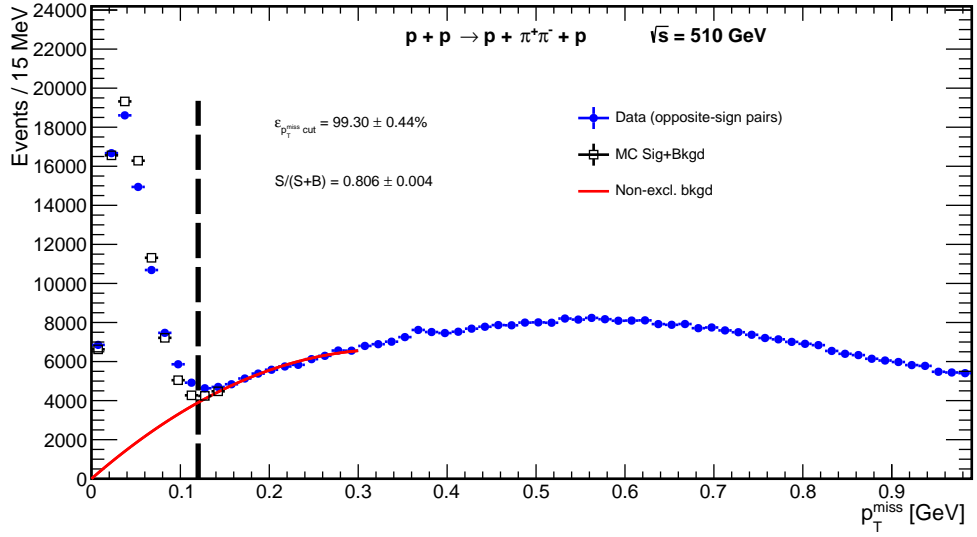


Figure 3.6: The distribution of the missing transverse momentum for  $\pi^+\pi^-$  CEP event candidates with used cut illustrated by the black dot-dashed line.

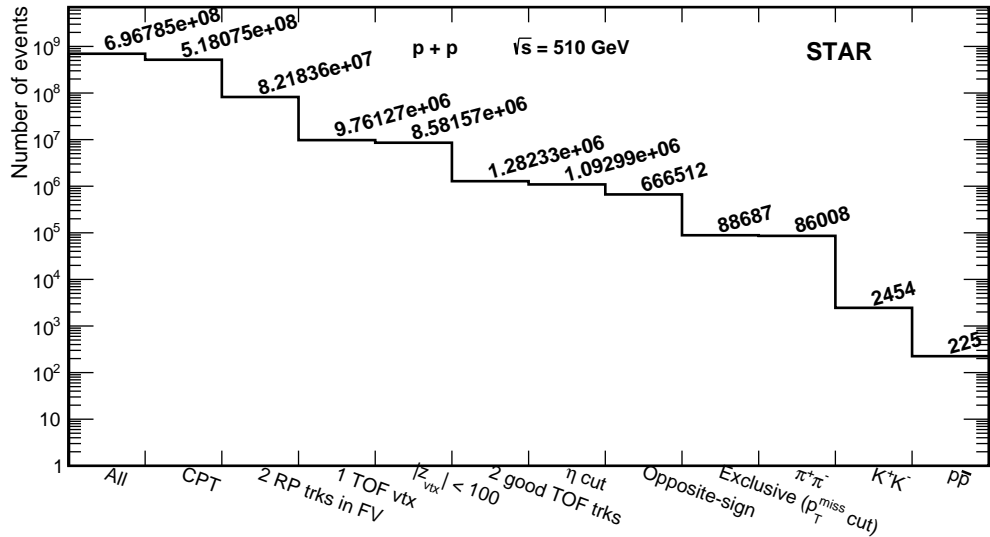


Figure 3.7: The summary of CEP event selection. Each bin represents data-sample satisfying all previous criteria. The size of each data-sample is shown by the number in the upper part.

### 670 3.6 Particle identification

671 The particle identification is based on the combined information from the TPC, the  
 672 average ionization energy loss per unit length ( $\langle dE/dx \rangle$ ), and the time of hit detection  
 673 in TOF. In DIPE, only pairs of hadrons of the same type can be produced. Therefore, the  
 674 combined information is used to identify the pairs of hadrons:  $\pi^+\pi^-$ ,  $K^+K^-$ , and  $p\bar{p}$ .  
 675 For this purpose, a pair hypothesis is introduced:

$$676 \chi_{\langle dE/dx \rangle}^2(XX) := (n\sigma_{X+})^2 + (n\sigma_{X-})^2, \quad (3.5)$$

677 where  $n\sigma_X$  is the number of standard deviations between the measured and the theo-  
 678 retical energy loss for a given particle  $X$  ( $X$  stands for  $\pi$ ,  $K$  or  $p$ ) at a given momentum  
 679 and it is defined as:

$$680 n\sigma_X := \frac{\ln \frac{\langle dE/dx \rangle}{\langle dE/dx \rangle_X^{\text{cal.}}}}{R_{\langle dE/dx \rangle}}, \quad (3.6)$$

681 where  $\langle dE/dx \rangle$  is an energy loss per unit length measured by the TPC,  $\langle dE/dx \rangle_X^{\text{cal.}}$  is  
 682 a calculated mean energy loss per unit length for a given particle  $X$  calculated using  
 683 the Bichsel function [16] and  $R_{\langle dE/dx \rangle}$  is the TPC resolution. In STAR,  $R_{\langle dE/dx \rangle}$  is  
 684 approximately 7%. Hence, PID based on  $\langle dE/dx \rangle$  is feasible for particles with momenta  
 685 between 100 MeV and 1 GeV. Figure 3.8 (left) shows the  $\langle dE/dx \rangle$  of charged particles  
 686 as a function of their momentum. Pions, kaons, and protons are clearly seen.

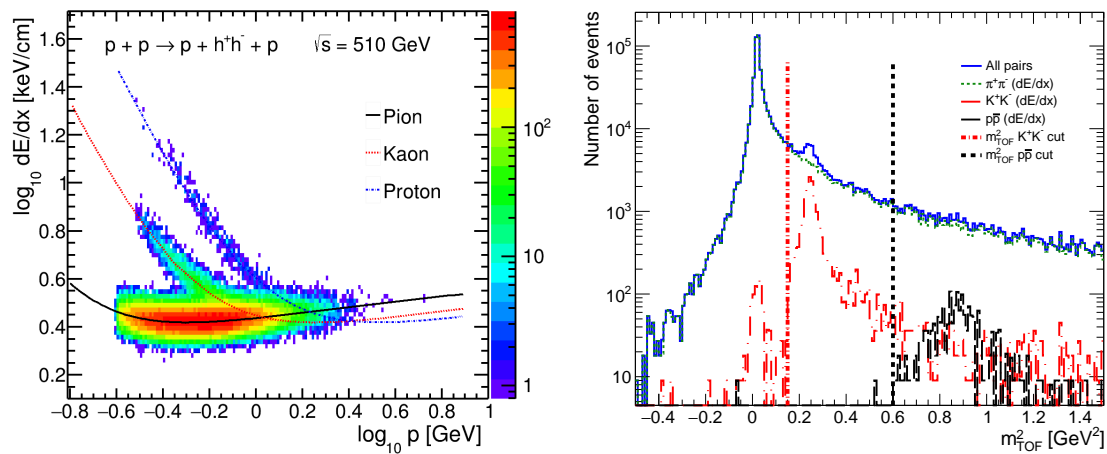


Figure 3.8: Left: the energy loss  $\langle dE/dx \rangle$  of central charged particles as a function of their momentum for CEP event candidates. Coloured curves illustrate expected values for pions, kaons, and protons. Right: distributions of invariant mass squared  $m_{\text{TOF}}^2$  of pions, kaons, and protons. Particle type is identified solely based on  $\langle dE/dx \rangle$  information. Applied PID cuts are highlighted by dot-dashed lines.

687 To extent the PID capabilities of the  $\langle dE/dx \rangle$  method, the TOF information is used.  
 688 However, the standard method, the inverse particle velocity  $1/\beta$ , cannot be used in CEP

events due to lack of the starting time of the collision  $t_0$ . The  $t_0$  is typically reconstructed from fragments of dissociated beam particles detected in the Vertex Position Detector (VPD). In CEP events, there is no signal in VPD since the initial protons remain intact after the collision. Instead, a  $m_{\text{TOF}}^2$  method is used. It is based on elimination of the starting time by assuming that both central tracks, originating from the same vertex, have the same mass. See [Appendix A](#) for details. The  $m_{\text{TOF}}^2$  distributions of pions, kaons, and protons, identified solely based on  $\langle dE/dx \rangle$  information, can be seen in [Fig. 3.8](#) (right). Although peaks close to particles invariant mass squared values are seen, pions misidentified as kaons are also seen. Due to the resolution effects, negative, non-physical values can also be seen.

Particle pairs are identified on the basis of the following hypothesis to minimize exclusive background in kaons and protons samples. First, the proton pair hypothesis is checked:

$$\chi_{\langle dE/dx \rangle}^2(pp) < 9 \text{ \& } m_{\text{TOF}}^2 > 0.6 \text{ \& } \chi_{\langle dE/dx \rangle}^2(KK) > 9 \text{ \& } \chi_{\langle dE/dx \rangle}^2(\pi\pi) > 9, \quad (3.7)$$

where the first two terms  $\chi_{\langle dE/dx \rangle}^2(pp) < 9 \text{ \& } m_{\text{TOF}}^2 > 0.6$  select proton pairs and the rest rejects pions and kaons. If the pair is not identified as proton pair, the kaon hypothesis is verified:

$$\chi_{\langle dE/dx \rangle}^2(KK) < 9 \text{ \& } m_{\text{TOF}}^2 > 0.15 \text{ \& } \chi_{\langle dE/dx \rangle}^2(pp) > 9 \text{ \& } \chi_{\langle dE/dx \rangle}^2(\pi\pi) > 9, \quad (3.8)$$

where again the first two terms select kaon pairs and the rest reject protons and pions. If neither of the proton nor the kaon hypothesis is satisfied, the pion pair is assumed and its hypothesis is checked:

$$\chi_{\langle dE/dx \rangle}^2(\pi\pi) < 12. \quad (3.9)$$

In order to study systematic uncertainty, the additional set of cuts are introduced, namely the looser and tighter cuts. The looser cut uses the  $\chi_{\langle dE/dx \rangle}^2(hh) < 12$  condition instead of  $\chi_{\langle dE/dx \rangle}^2(hh) < 9$  in [Eq. 3.7](#) and in [Eq. 3.8](#). The values for the cuts  $m_{\text{TOF}}^2$  are 0.1 and 0.55 GeV<sup>2</sup> for the kaon and proton hypotheses, respectively. The pion hypothesis [Eq. 3.9](#) is changed to  $\chi_{\langle dE/dx \rangle}^2(\pi\pi) < 15$ . The tighter cut uses the  $\chi_{\langle dE/dx \rangle}^2(hh) < 7$  condition instead of  $\chi_{\langle dE/dx \rangle}^2(hh) < 9$  in [Eq. 3.7](#) and in [Eq. 3.8](#). The values for the cuts  $m_{\text{TOF}}^2$  are 0.2 and 0.7 GeV<sup>2</sup> for the kaon and proton hypotheses, respectively. The pion hypothesis [Eq. 3.9](#) is changed to  $\chi_{\langle dE/dx \rangle}^2(\pi\pi) < 9$ .

Although this PID technique is designed to minimize misidentification of pion pairs as kaon or proton pairs, the restriction of fiducial space is needed to ensure high track reconstruction efficiency, see [Sec. 6.5.1](#), and high pair identification efficiency, see [Sec. 6.6](#).

722 The fiducial space is defined as:

723  $p_T(\pi) > 0.25 \text{ GeV}, \quad (3.10)$

724  $p_T(K) > 0.3 \text{ GeV} \& \min(p_T(K^+), p_T(K^-)) < 0.7 \text{ GeV}, \quad (3.11)$

726  $p_T(p) > 0.4 \text{ GeV} \& \min(p_T(p), p_T(\bar{p})) < 1.1 \text{ GeV}. \quad (3.12)$



728

# Chapter 4

729

## Backgrounds

730 In this chapter, sources of background and their quantitative determination are discussed  
731 and presented.

732 There are two main sources of background: **exclusive** and **non-exclusive** back-  
733 ground.

734

### 4.1 Exclusive background

735 Exclusive background corresponds to events that meet all the selection criteria but are  
736 misidentified. The probability of misidentification is studied together with the efficiency  
737 of the PID described in Sec. 6.6. The fiducial phase space of the measurement is con-  
738 strained to maintain high pair identification efficiency and low probability of misidenti-  
739 fication.

740 The size of the exclusive background is estimated from the transverse momenta of the  
741 hadrons ( $p_T^{\max}, p_T^{\min}$ ) and the PID efficiency described in Sec. 6.6. The measured distri-  
742 bution of the transverse momenta of the hadrons ( $p_T^{\max}, p_T^{\min}$ ) for each pair is propagated  
743 through the PID efficiency and the probability of misidentification to obtain samples of  
744 (in)correctly identified particles. Then, the samples are compared and the amount of  
745 exclusive background is estimated to be less than 1 %. Therefore, the exclusive back-  
746 ground can be neglected. It should be mentioned that the measured distribution of the  
747 transverse momenta of the particles ( $p_T^{\max}, p_T^{\min}$ ) is biased by the identification of the  
748 particles. Hence, a MC should be used to properly represent the true sample. However,  
749 the bias primarily affects data with high  $p_T^{\min}$  and therefore, will not significantly affect  
750 the estimated size of the exclusive background, as the amount of data decreases with  
751 increasing  $p_T^{\min}$ .

<sup>752</sup> **4.2 Non-exclusive background**

<sup>753</sup> The main background contribution arises from non-exclusive events imitating the topology  
<sup>754</sup> of CEP of  $h^+h^-$ : two forward protons, two oppositely charged central tracks, and  
<sup>755</sup> large rapidity gaps. Figure 4.1 depicts the most common cases of non-exclusive background:

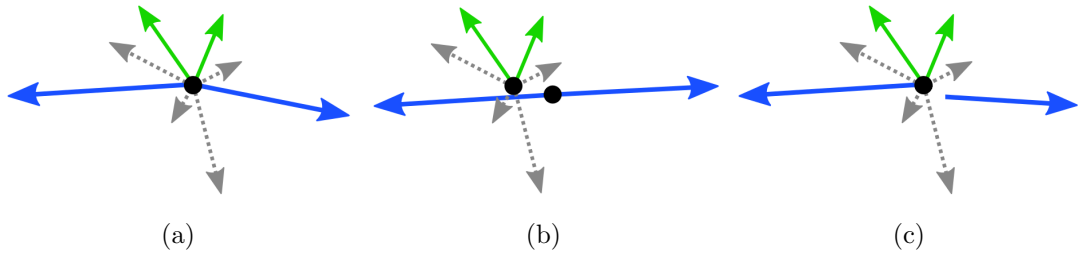


Figure 4.1: An illustration of the most common cases of non-exclusive background sources: central diffraction event with some particles not detected (a), elastic proton-proton scattering event with pile-up inelastic interaction in the central region (b), and single diffraction with a proton originating from beam halo (c). The arrows represent forward scattered protons (blue), detected particles in the central system (green), and undetected particles (dashed gray). Black circles signature primary interaction vertices.

<sup>756</sup>

<sup>757</sup> **1. Central Diffraction:**

<sup>758</sup> - it is the same process as CEP but with a higher number of particles produced,  
<sup>759</sup> which can mimic the CEP of  $h^+h^-$  if some particles are not detected. The central  
<sup>760</sup> diffraction is illustrated in Fig. 4.1a.

<sup>761</sup> **2. Accidental coincidences (pile-up):**

<sup>762</sup> - there can be an accidental coincidence between the forward and central system.  
<sup>763</sup> One of them is the overlap of elastic scattering with another inelastic interaction  
<sup>764</sup> in the central system illustrated in Fig. 4.1b.  
<sup>765</sup> - it can also be an overlap of a single diffraction with a proton originating from  
<sup>766</sup> the beam halo shown in Fig. 4.1c.

<sup>767</sup> In general, the source of non-exclusive background events is the combination of  
<sup>768</sup> sources discussed above. For example, there can be an accidental coincidences of central  
<sup>769</sup> diffraction when some particles are not detected including the forward-scattered protons  
<sup>770</sup> that are interchanged with the protons from the beam halo. Although the reconstruc-  
<sup>771</sup> tion efficiency of the RP system is high, its geometrical acceptance is limited. Therefore,  
<sup>772</sup> some protons can easily miss the RP system and thus may not be reconstructed. Then,  
<sup>773</sup> the missed protons can be interchanged with the protons from the beam halo.

### 774 4.3 Non-exclusive background subtraction

775 The method of non-exclusive background subtraction is based on the missing transverse  
 776 momentum defined in [Eq. 3.4](#). Due to four-momentum conservation, the transverse  
 777 momentum of the sum of all measured particles is equal to zero. Therefore, the missing  
 778 transverse momentum should also be equal to zero.

779 In the non-exclusive background, there are always particles that are not coming from  
 780 the same primary interaction vertex or particles that are not detected. Hence, the total  
 781 missing transverse momentum should deviate from zero.

782 The distribution of the total missing transverse momentum ( $p_T^{\text{miss}}$ ) can be seen  
 783 in [Fig. 6.20](#). The peak at the beginning of the distribution corresponds to the exclusive  
 784 events. The peak deviates from zero due to finite resolution. In [Sec. 6.8](#), the figure is  
 785 fully described along with the determination of the size of non-exclusive background.

786 To study the shape of non-exclusive background as a function of a given observable,  
 787 the following method is used. The method is described for the invariant mass of  $\pi^+\pi^-$   
 788 pairs ( $m(\pi^+\pi^-)$ ), but it works for any observable.

- 789 1. Firstly, the correlation between  $m(\pi^+\pi^-)$  and  $p_T^{\text{miss}}$  is plotted with the same binning  
 790 as the  $m(\pi^+\pi^-)$  distribution.
- 791 2. Then,  $p_T^{\text{miss}}$  is projected into  $m(\pi^+\pi^-)$  in the range from 160 to 220 MeV. The  
 792 range is selected to be as close as possible to the signal region and at the same time  
 793 outside the signal region. The exclusivity cut [C6](#) is set to 120 MeV. Its efficiency  
 794 is about 99 %. The shape of the background, in this case as the function of mass,  
 795 in the selected range is assumed to be the same as in the signal region.
- 796 3. The obtained background distribution is normalized to the expected background  
 797 size determined in [Sec. 6.8](#).
- 798 4. Finally, the normalized background distribution is subtracted from the  $m(\pi^+\pi^-)$   
 799 separately for each bin of the distribution.

800 The correlation between  $m(\pi^+\pi^-)$  and  $p_T^{\text{miss}}$  is plotted in [Fig. 4.2](#). The red dot-dash  
 801 line represents the selected range and the black dot-dash line represent exclusivity cut.  
 802 Figure [4.3](#) shows the invariant mass of pion pairs,  $m(\pi^+\pi^-)$ , with the non-exclusive  
 803 background before the background subtraction.

804 The systematic uncertainty of the non-exclusive background subtraction is studied  
 805 by varying the range of the projection: from 170 to 210 MeV (smaller range) and from  
 806 140 to 250 MeV (wider range). The subtraction is performed for all ranges: smaller,  
 807 nominal, and wider range. Then, the differential cross sections for CEP of  $\pi^+\pi^-$  pairs  
 808 as a function  $m(\pi^+\pi^-)$  are compared. Figure [4.4](#) shows ratios of the differential cross

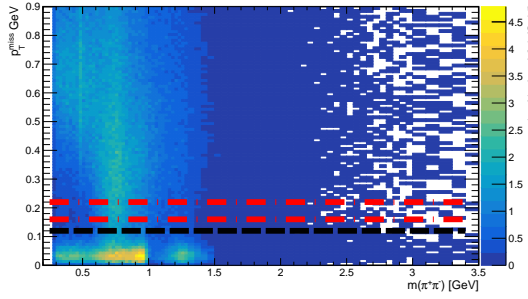


Figure 4.2: The correlation between corrected invariant mass of pion pairs and missing transverse momentum. The red dot-dash lines highlight the region for the projection and the black dot-dash line depicts the exclusivity cut.

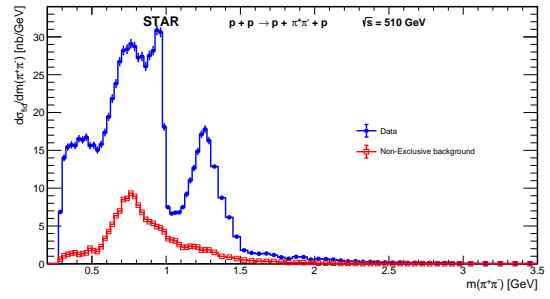


Figure 4.3: The corrected invariant mass of pion pairs before the non-exclusive background subtraction with the non-exclusive background also shown.

sections for each range to the nominal one. The uncertainty is taken as the average of absolute deviations for each bin separately. The weighted mean of uncertainties of the background subtraction in the invariant mass distribution of  $\pi^+\pi^-$ ,  $K^+K^-$ , and  $p\bar{p}$  pairs are 0.4%, 0.8%, and 3.3%, respectively. The inverse variance of statistical uncertainty in each bin is used as the weight. Moreover, there is another source coming from the normalization that is common for all the bins.

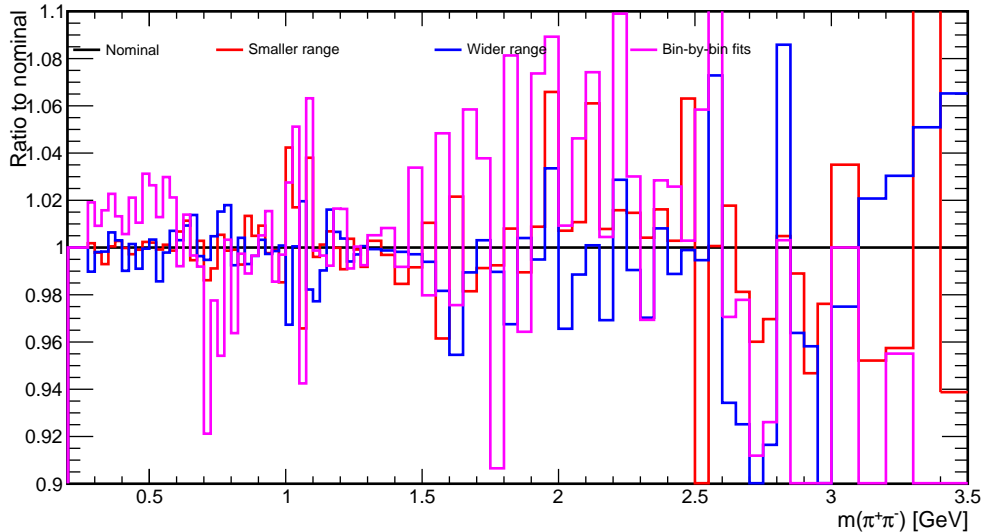


Figure 4.4: The comparison of the differential cross sections for CEP of  $\pi^+\pi^-$  pairs as a function of their invariant mass  $m(\pi^+\pi^-)$  after the subtraction of non-exclusive background obtained with different projection ranges.

# <sup>815</sup> Chapter 5

## <sup>816</sup> Monte Carlo simulations

<sup>817</sup> This chapter describes the MC tools developed and used in this analysis. The first section  
<sup>818</sup> ([Sec. 5.1](#)) contains the description of the embedding of central particles used to determine  
<sup>819</sup> reconstruction, selection, and matching efficiencies. The next section ([Sec. 5.2](#)) presents  
<sup>820</sup> the simulation of the forward detectors used to determine the reconstruction and selec-  
<sup>821</sup> tion efficiencies and the fiducial volume of the RP. The last section ([Sec. 5.3](#)) discusses  
<sup>822</sup> the GRANIIITI model that is compared with the measured fiducial cross sections.

### <sup>823</sup> 5.1 Central embedding

<sup>824</sup> The particles were generated and embedded in pairs of  $\pi^+\pi^-$ ,  $K^+K^-$  and  $p\bar{p}$  with the  
<sup>825</sup> following setup:

- <sup>826</sup> • one million  $\pi^+\pi^-$ , half a million  $K^+K^-$ , and half a million  $p\bar{p}$  events,
- <sup>827</sup> • a flat distribution of  $z$ -position of vertices in the range:  $|z_{\text{vtx}}| < 100$  cm,
- <sup>828</sup> • a flat distribution of azimuthal angles:  $-\pi < \varphi < \pi$  in radians,
- <sup>829</sup> • a flat distribution in the pseudorapidity,  $-1.0 < \eta < 1.0$ ,
- <sup>830</sup> • a flat distribution in transverse momenta:  $0.15 < p_T < 1.0$  GeV (80 % of particles)  
<sup>831</sup> and  $1.0 < p_T < 2.5$  GeV (20 % of particles)

<sup>832</sup> The tracks are placed at the same vertex, where the coordinates of the vertex  $x$  and  $y$   
<sup>833</sup> are selected according to the beamline constraint. The vertex itself is not reconstructed  
<sup>834</sup> in the embedding. Hence, only the global particles are studied.

<sup>835</sup> The generated embedding sample is validated by comparing several variables be-  
<sup>836</sup> tween the true-level MC, embedding, and CEP data. The comparison can be seen in  
<sup>837</sup> [Appendix E](#). The good agreement between all the samples validates the embedding.  
<sup>838</sup> Although, there are some clear discrepancies between few variables, e.g.  $z_{\text{vtx}}, p_T, \dots$

These differences are created intentionally since the goal is to get enough statistics in the whole phase space. Therefore, flat non-physical distributions are used in the embedding setup described above. The most important discrepancy is at the beginning of the  $N_{\text{hits}}^{\text{fit}}$  distribution shown in Fig. 5.1. The discrepancy resolves in slightly higher systematic uncertainty, see Sec. 7.3, compared to only  $N_{\text{hits}}^{(dE/dx)}$ . However, the final systematic uncertainty is still acceptable. Therefore, no additional tuning of the of  $N_{\text{hits}}^{\text{fit}}$  is performed.

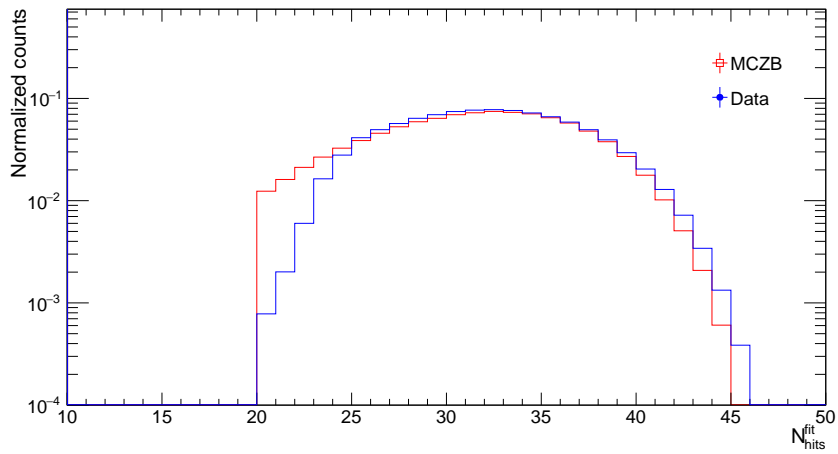


Figure 5.1: A comparison of the number of hits in the TPC used for the track reconstruction ( $N_{\text{hits}}^{\text{fit}}$ ) between the CEP  $\pi^+\pi^-$  event candidates (Data) and reconstructed tracks in the embedding sample (MCZB).

## 5.2 Simulation of the RP system

The official simulation tool of the STAR detector, called STARsim, does not include the RP system. Hence, a dedicated tool for precise simulation of the RP detectors was prepared with Geant4. A tool called *ppSim* was designed and prepared by the Cracow group and it was already used for several publications [1], [17]. It contains a detailed implementation of the beam line and RP detectors, position, and readout behavior. Furthermore, collider elements including magnets and the spatial distribution of their fields are also implemented. Therefore, *ppSim* includes full implementation of the beam line elements, the background contribution from the scattered protons interacting with the material in front of the RPs, and non-working readout chips.

To reproduce all the effects of the collision environment in the reconstruction of the simulated signal, the embedding of the *ppSim* output in the real ZB events has been implemented. The embedding is performed at the level of reconstructed clusters, combining those from the *ppSim* and ZB events. Overlapping clusters are merged and new lengths, energies, and positions are calculated. New points and tracks are reconstructed from the new collection of clusters based on the track reconstruction algorithm.

### 5.2.1 Validation of the MC

Although all relevant quantities such as the number of clusters, their lengths, and energies are compared, only the projection method is discussed in this section as it captures the overall aspects of the forward track reconstruction. The complete validation is described in [Appendix F](#).

The projection method is based on elastic events discussed in [Sec. 2.4.1](#) where the distance between the reconstructed point and the elastic collinear line, the fit of all four points, is calculated. The distance is calculated for each point and for each coordinate. [Fig. 5.2](#) depicts the distance for each coordinate and for each RP. All distributions are centered around zero, with the same spread for data and MC as expected. Without the RP alignment discussed in [Sec. 2.4](#), the distributions would be displaced from zero. Therefore, *ppSim* is able to reconstruct the forward-scattered proton with the same resolution as in the data.

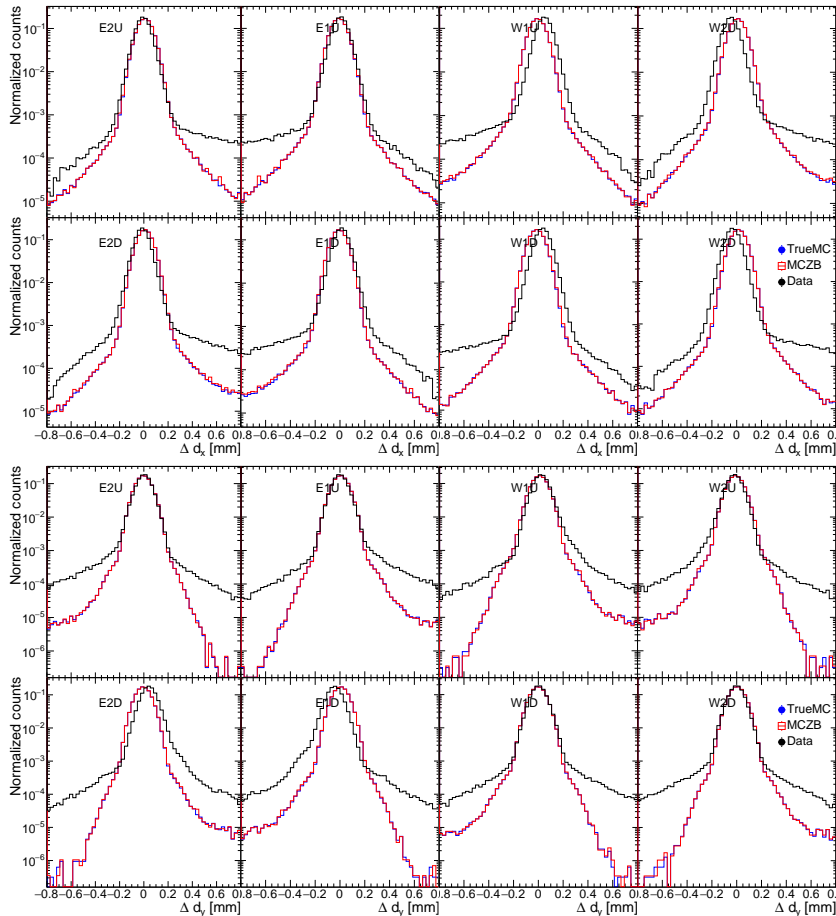


Figure 5.2: The distance between reconstructed point in the given RP and the fit between all four reconstructed points for elastic events. The distance is plotted for each RP and each coordinate. The  $x$ -coordinate is in the top figure and the  $y$ -one in the bottom one. The distance is compared between three data samples: measured data, pure MC, and MC embedded with ZB events.

875 **5.3 GRANIITTI**

876 This section describes a Monte Carlo event generator called GRANIITTI [18]. In this  
 877 analysis, the results are compared with the newest version of GRANIITTI v. 1.090  
 878 available at the moment. This version includes CEP resonance couplings also tuned to  
 879 the latest STAR CEP results at  $\sqrt{s} = 200$  GeV [1].

880 GRANIITTI is designed for high-energy diffraction with a focus on central exclu-  
 881 sive production. The generator includes all the interactions relevant for CEP, namely,  
 882 photon-photon, photon-pomeron, and pomeron-pomeron interactions. Furthermore,  
 883 GRANIITTI includes the Durham QCD model [19] and the tensor pomeron model [20].  
 884 Therefore, it can combine a full parametric resonance spectrum with a continuum pro-  
 885 duction. Furthermore, significant interference effects between resonance and continuum  
 886 production are considered, as they are implemented at the amplitude level. A generic  
 887 diagram of the central exclusive production of  $\pi^+\pi^-$  is shown as the combination of  
 888 continuum and resonance production at the level of the scattering amplitude in Fig. 5.3.  
 889 Scattering amplitudes are calculated based on Regge theory in the non-perturbative  
 890 domain of strong interactions. Although some perturbative QCD, quantum electrodyn-  
 891 namics and electroweak processes are included as well.

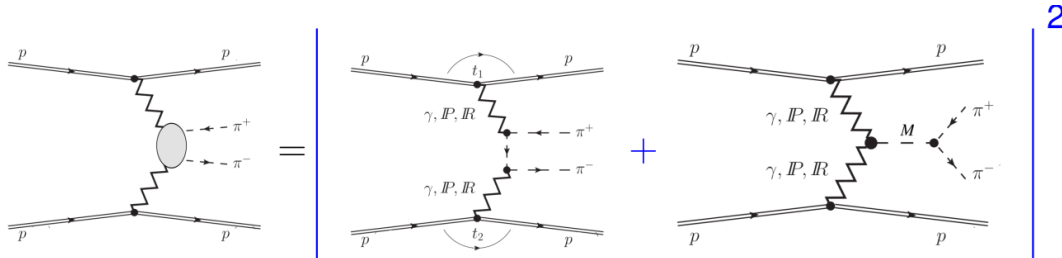


Figure 5.3: A generic diagram of central exclusive production of  $\pi^+\pi^-$  as combination of continuum and resonance production at the scattering amplitude level.

892 GRANIITTI combines up-to-date phenomenological models and approaches [20]–  
 893 [22]. The eikonal pomeron model [23] is used to generate elastic scattering events and  
 894 the screening loop for central production. The screening loop takes into account the  
 895 significant rescattering (absorption) effects via additional interaction between the pro-  
 896 tons and/or hadron-proton interactions. The absorption is embedded in the so-called  
 897 Survival Factor depending on the collision energy. At RHIC and LHC energies, the  
 898 suppression factor can be up to 5 and 10, respectively. The common approach for the  
 899 screening loop is used. The same approach is used in the Dime [24] and SuperChic [25]  
 900 event generators.

901 The resonance and continuum contributions from the pomeron-pomeron interaction  
 902 are also included. The continuum is based on generalizing the amplitudes of the meson  
 903 pair described in [24], [26]. The contribution from resonance production, interfering with

904 the continuum, is described by relativistic Breit-Wigner poles

$$905 \quad \Delta_{\text{BW}}^{\text{R}}(m^2) = \frac{1}{m_{\text{R}}^2 - m^2 - im_{\text{R}}\Gamma}, \quad (5.1)$$

906 where  $m_{\text{R}}$  and  $\Gamma$  is pole mass and pole width, respectively. The pomeron spin is taken to  
 907 be  $J = 0$  for the production of scalar or tensor meson resonances and to be  $J = 1$  for the  
 908 production of pseudoscalars, where results from [27] are used to accelerate calculations.  
 909 The resonance production couplings for three or four body decays are free complex  
 910 parameters. The couplings  $\mathcal{M}_D$  for two-body decays ( $M_{\text{R}} \rightarrow m_1 + m_2$ ) are calculated  
 911 from the branching ratios and the standard partial decay width formula

$$912 \quad \Gamma_i = \frac{|\mathcal{M}_D|^2 \sqrt{\lambda(M_{\text{R}}^2, m_1^2, m_2^2)}}{16\pi M_{\text{R}}^3 S}, \quad (5.2)$$

913 where  $\lambda$  is the standard Källen (triangle) function [28] and  $S$  is the statistical symme-  
 914 try factor. Known branching ratios are taken from the Particle Data Group [29] and  
 915 unknown branching ratios (e.g. some  $f$ -mesons) are estimated.

916 The Durham QCD model is also used for the transition region from the low-mass  
 917 Regge domain to the QCD domain. In particular, the numerical gluon loop with spin-  
 918 parity projection and a generalized gluon-parton distribution function transformation  
 919 is used. Figure 5.4 illustrates the Durham QCD model of central exclusive production.  
 920 The eikonal screening  $\Omega$  is also depicted.

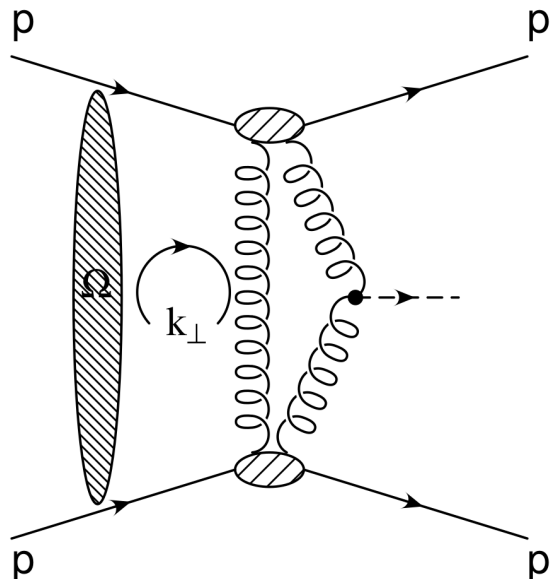


Figure 5.4: The Durham QCD model of central exclusive production with eikonal screening  $\Omega$ . Taken from Ref. [18].

921 GRANITTI also includes an implementation of the tensor pomeron model. The

model provides a description of a two-body continuum production of pseudoscalar pairs, vector meson pairs and baryon pairs. Furthermore, resonance production is also provided and implemented in GRANIITI, namely scalar resonances  $f_0$ , pseudoscalar resonances  $\eta, \eta'$ , vector mesons  $\rho^0(770)$  and  $\phi(1020)$  via photoproduction and  $f_2$  tensor mesons. The user is able to select the tensor pomeron model or the one introduced earlier for continuum and/ or resonance production.

928 **Chapter 6**

929 **Corrections**

930 In this chapter, the methodology of correcting data to the hadron-level cross sections is  
931 described.

932 **6.1 Method of corrections application**

933 In order to measure the cross section, several corrections are applied independently of  
934 all kinematic variables, affecting only the normalization. A differential cross section in  
935 every bin of measured quantity of interest,  $q$ , have been calculated according to [Eq. 6.1](#):

$$\frac{d\sigma}{dq}(q) = \frac{1}{\Delta q} \times \frac{N^w(q) - N_{\text{bkgd}}^w(q)}{L_{\text{int}}^{\text{eff}}}, \quad (6.1)$$

936 where  $N^w(q)$  and  $N_{\text{bkgd}}^w(q)$  are the weighted numbers of observed and background events  
937 in the given bin, where the weight is the inverse total efficiency calculated as the product  
938 of all efficiencies for the given event.  $\Delta q$  is the width of the bin, and  $L_{\text{int}}^{\text{eff}}$  is the effective  
939 integrated luminosity defined as:

$$L_{\text{int}}^{\text{eff}} = \sum_{\text{run}} L_{\text{int}}^{\text{run}} \times \epsilon_{\text{veto}}(L_{\text{inst}}^{\text{run}}), \quad (6.2)$$

940 where  $\epsilon_{\text{veto}}(L_{\text{inst}}^{\text{run}})$  is the probability of retaining the CEP event as a function of  
941 the instantaneous luminosity,  $L_{\text{inst}}^{\text{run}}$ , discussed in [Sec. 6.2.4](#) and  $L_{\text{int}}^{\text{run}}$  is the integrated  
942 luminosity for the given run.

943 **6.2 Trigger corrections**

944 This section describes the trigger corrections. The trigger itself was already described  
945 and discussed in [Sec. 2.3](#). Since CPT2noBBCL trigger is one of the most complicated  
946 triggers at STAR, its efficiency corrections are divided into following studies: the DSM

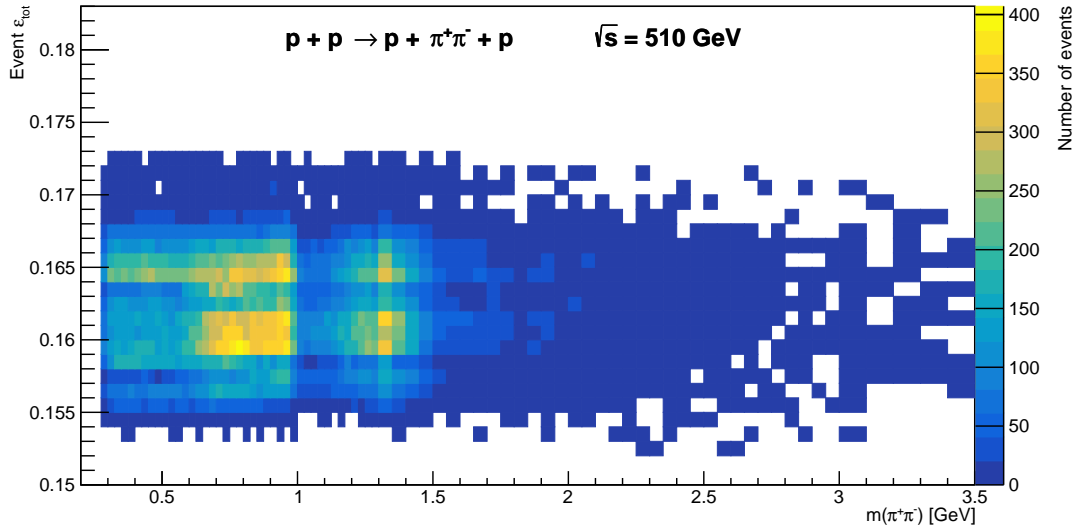


Figure 6.1: Distribution of total efficiencies assigned to selected CEP events in  $\pi^+\pi^-$  channel.

949 trigger bit corrections, the TOF trigger study, the RP trigger study and the probability  
 950 of retaining the event.

### 951 6.2.1 DSM trigger bit corrections

952 The trigger bits are summarized and discussed in Sec. 2.3 and Tab. 2.1. The CPT2noBBC1  
 953 trigger is triggered only when all of its trigger bits are set to the corresponding values:  
 954 triggered or vetoed. Data from detectors are processed through the Data Storage and  
 955 Manipulation (DSM) boards and a Trigger Control Unit (TCU). This subsection studies  
 956 the probability of setting each trigger bit to a required value.

957 The trigger bits are studied in two data sets. The first one is formed from ZB events  
 958 without additional conditions. The second represents CEP-like events. It is formed from  
 959 ZB events with only one TOF vertex (cut C2) and exactly two primary good quality  
 960 TOF-matched TPC tracks (cut C4). The DSM trigger bit correction is calculated as  
 961 the ratio of the number of events *passed* to the *total* number of events. The sample  
 962 *total* is composed of events that meet the DSM trigger definition described in Sec. 2.3.  
 963 Events forming sample *passed* have to meet the same trigger definition and also must  
 964 have corresponding value of the DSM bit. Table 6.1 summarizes the definitions of the  
 965 samples. The BBC Large ADC<sub>Sum</sub> in the *star-upcDst* framework is defined differently  
 966 from the TCU described in Sec. 2.3. It is defined in the same way as BBC Small, that is,  
 967 the good hit in a channel is required to have  $ADC > 20$  and  $100 < TAC < 2400$  instead  
 968 of  $ADC > 50$  and  $100 < TAC < 2500$ . Although the *star-upcDst* definition is not the  
 969 same, it is sufficient for this study.

Condition	Sample <i>total</i>	Sample <i>passed</i>
Elastic hits in RP	$200 < TAC < 1750 \&\& ADC > 30$	$total \&\& RPET$ bit set
Inelastic veto in RP	$TAC >= 1750 \parallel TAC <= 200 \&\& ADC <= 30$	$total \&\& RPIT$ bit unset
Elastic veto in RP	$TAC >= 1750 \parallel TAC <= 200 \&\& ADC <= 30$	$total \&\& RPET$ bit unset
Inelastic hits in RP	$200 < TAC < 1750 \&\& ADC > 30$	$total \&\& RPIT$ bit set
Number of TOF hits $> 1$	$TOF \text{ multiplicity} > 1$	$total \&\& TOF(1)$ bit set
Number of TOF hits $\leq 10$	$TOF \text{ multiplicity} \leq 10$	$total \&\& TOF(10)$ bit unset
No hit in BBC east	$ADC_{SUM} \leq 20$	$total \&\& BBCE$ bit unset
No hit in BBC west	$ADC_{SUM} \leq 20$	$total \&\& BBCW$ bit unset
No hit in BBC Large east	$ADC_{SUM} \leq 50$	$total \&\& BBCLE$ bit unset
No hit in BBC Large west	$ADC_{SUM} \leq 50$	$total \&\& BBCLW$ bit unset
No hit in ZDC east	$TAC \leq 500 \parallel TAC \geq 2700 \parallel ADC_i \leq 25$	$total \&\& ZDCE$ bit unset
No hit in ZDC west	$TAC \leq 500 \parallel TAC \geq 2700 \parallel ADC_i \leq 25$	$total \&\& ZDCW$ bit unset

Table 6.1: Description of the samples used in DSM trigger bit correction study. The detailed bit definition is described in Sec. 2.3. Symbols “ $\&\&$ ” and “ $\parallel$ ” stand for logical AND and OR, respectively. The sample *passed* is formed using the same condition as the sample *total* plus addition requirement on DSM bit. The  $ADC_{SUM}$  for BBC Large is redefined in the text above.

970     Fig. 6.2 and Fig. 6.3 illustrate the DSM trigger bits' efficiencies calculated from two  
 971 sets of runs: all runs including runs marked as bad runs and only good runs. In addition,  
 972 the DSM trigger bits' efficiencies are studied for two data samples: ZB events with no  
 973 additional conditions and ZB CEP-like events. Lower efficiencies were found to come  
 974 mainly from bad runs. Moreover, in good runs, the efficiencies are consistent between  
 975 data sets. The DSM efficiencies are nearly 100%. Hence, DSM corrections are neglected.

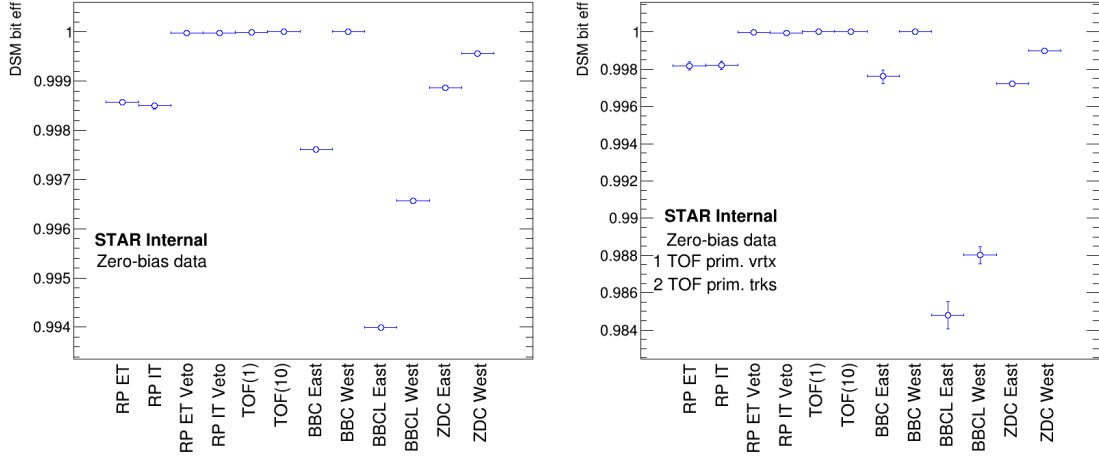


Figure 6.2: The DSM trigger bits' efficiencies calculated from ZB events with no additional conditions (left) and from ZB CEP-like events (right) for all (good and bad) runs.

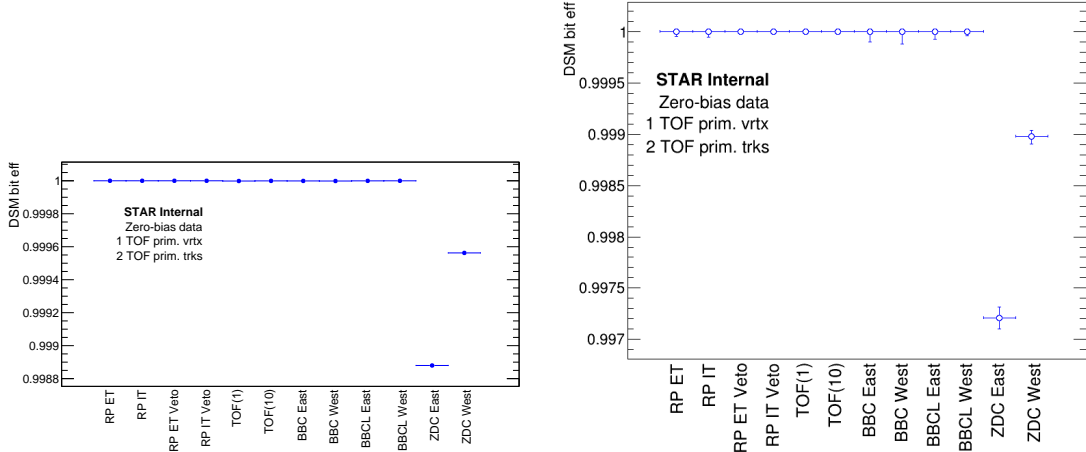


Figure 6.3: The DSM trigger bits' efficiencies calculated from ZB events with no additional conditions (left) and from ZB CEP-like events (right) only for good runs.

### 976     6.2.2 TOF trigger study

977     The CPT2noBBCL trigger required the TOF multiplicity greater than one. The effi-  
 978 ciency correction is estimated using the ZB data. Events with exactly 1 TOF vertex  
 979 (cut C2) and exactly 2 primary good quality TOF-matched TPC tracks (cut C4)) are

used to calculate this efficiency defined as a probability of the DSM TOF bit set on in a selected set of events:

$$\epsilon_{TOF}^{trig} = \frac{\# \text{events with TOF(1) bit and 1 TOF vertex and 2 TOF tracks}}{\# \text{events with 1 TOF vertex and 2 TOF tracks}}. \quad (6.3)$$

There are 342590 ZB events with 1 TOF vertex and 2 primary good quality TOF-matched TPC tracks. 341336 events also have the TOF(1) DSM bit set on. Therefore, the TOF trigger efficiency is  $99.64 \pm 0.01\%$  and can be neglected.

### 6.2.3 RP trigger study

The CPT2noBBCL trigger contains only events triggered by the coincidence of valid PMT signals. Hence, any malfunction of the PMT counter can lead to the loss of a good CEP event. The RP trigger efficiency  $\epsilon_{RP}^{trig}$  is studied in the ZB data sample for the elastic and inelastic combinations separately. The efficiency is defined by Eq. 6.4 as the ratio of the number of events reconstructed with the silicon detector and confirmed by the corresponding DSM bit in the ZB data sample. The same proton reconstruction as in the main analysis is used.

$$\epsilon_{RP}^{trig} = \frac{\# \text{events with 1 good proton on each side and RP DSM bit}}{\# \text{events with 1 good proton on each side}}. \quad (6.4)$$

For the elastic bit (RP\\_ET), the efficiency is  $\epsilon_{RP}^{trig} = 14241/14398 = 98.91 \pm 0.09\%$  and for the inelastic bit (RP\\_IT) is  $\epsilon_{RP}^{trig} = 832/839 = 99.2 + 0.3 - 0.4\%$ . Since the efficiencies are the same within the uncertainties, the combined elastic and inelastic efficiency was calculated  $\epsilon_{RP}^{trig} = 15073/15237 = 98.92 + 0.08 - 0.09\%$ . When comparing the efficiency with the other efficiencies, it can be neglected.

Figure 6.4 illustrates the efficiency of the RP trigger in the  $p_x, p_y$  space. The black lines represent the fiducial volume defined in Sec. 6.3.5 by Eq. 6.8. The RP trigger efficiency is consistent through all RP stations and in the whole fiducial volume.

### 6.2.4 Probability of retaining CEP event

The definition of the CPT2noBBCL trigger includes many vetoes that ensure the CEP topology. However, if even one detector fires, the event is lost, regardless of whether it fires due to pile-up, multiple interactions per bunch crossing, or random noise in the detector. The probability of retaining CEP event combines both the online and offline vetoes. The online vetoes are part of trigger definition, namely in TOF, RP, BBC small, BBC large, and ZDC detectors. The offline veto comes from the requirement of one TOF vertex (cut C2). The probability is calculated using the ZB data sample for each

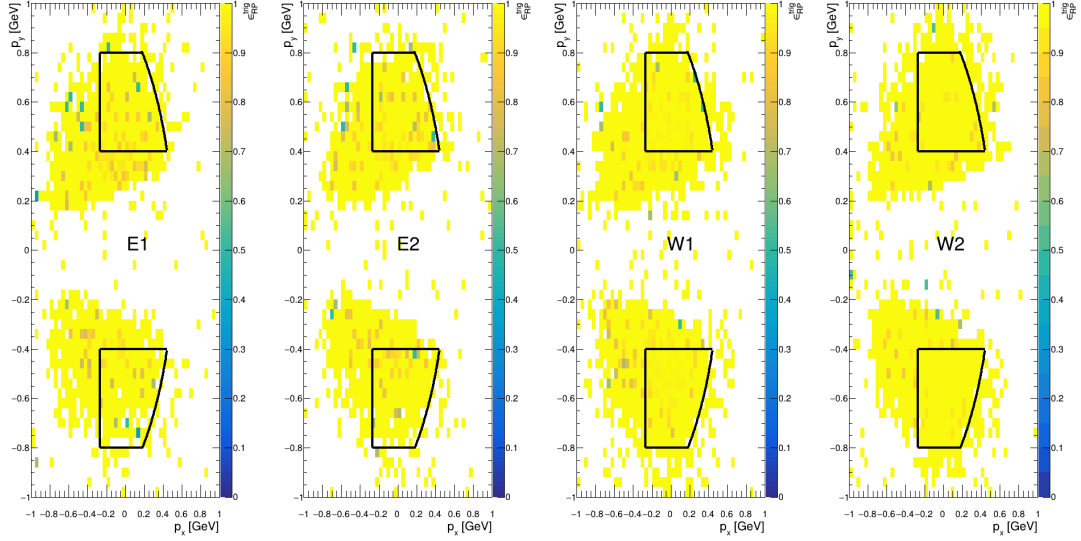


Figure 6.4: The RP trigger efficiency in  $p_x, p_y$  space. The black lines depicts the fiducial volume defined in Sec. 6.3.5 by Eq. 6.8.

1011 combination of east and west RP branches. The probability is defined by formula below:

$$P_{b_E, b_W} = \frac{\text{#events without signal in BBC-S, BBC-L, ZDC, paired RP branches, without TOF vertices and with TOF mult } \leq 10}{\text{#events in the run}}, \quad (6.5)$$

1013 where paired RP branches are the other RP branches than  $b_E, b_W$ .

1014 Since the pile-up is proportional to the instantaneous luminosity  $L_{\text{inst}}^{\text{run}}$  delivered by  
 1015 the accelerator, the probability is studied as a function of instantaneous luminosity.  
 1016 Figure 6.5 shows the results for each combination of the east and west RP branches.  
 1017 The results are almost identical, as the acceptance of triggers in all branches is similar  
 1018 and the RP trigger veto is not dominant.

1019 The probability of retaining CEP event should behave similar to the probability of  
 1020 lack of any interaction in the bunch crossing given by the Poisson distribution:

$$Pois(0; \mu) = \frac{\mu^0}{0!} \times e^{-\mu} = e^{-\mu}. \quad (6.6)$$

1021 Hence, the data points are fitted with the exponential function  $a \times e^{-b\mu}$ . The differ-  
 1022 ence between the fit and the data points for each combination of branches is depicted  
 1023 in Fig. 6.6. It is observed that the difference is independent of the choice of the branch  
 1024 combination. Therefore, the final probability of retaining the CEP event is independent  
 1025 of the choice of the branch combination, and it is calculated by Eq. 6.7 which is used to  
 1026 correct the measured data.

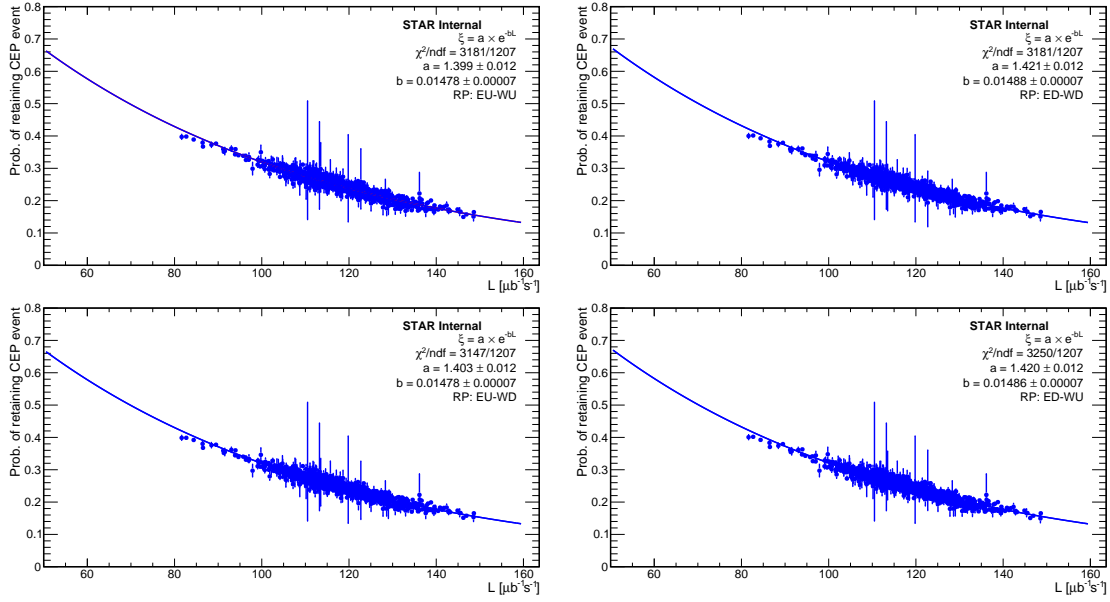


Figure 6.5: A probability of retaining CEP event as a function of instantaneous luminosity for each RP branch combination.

$$P_{\text{retain}}^{\text{CEP}} = 1.42 \times \exp(-0.01488 \times L_{\text{inst}}^{\text{run}}) \pm 0.01. \quad (6.7)$$

### 6.3 Roman Pot efficiency study

In this section, the RP efficiency study is discussed. The first subsection (Sec. 6.3.1) presents the data-driven method and its drawbacks. The next one (Sec. 6.3.2) focuses on an embedded MC developed to overcome the drawbacks of the data-driven method. The following two subsections present the RP efficiencies. The first (Sec. 6.3.4) is devoted to the efficiency of measuring a proton in a RP and the second (Sec. 6.3.4) to the probability that the reconstructed RP track will be selected. The last subsection (Sec. 6.3.5) is dedicated to the fiducial volume of RP in the  $p_x, p_y$  space.

#### 6.3.1 Data-driven method

The data-driven method is based on elastic events. The elastic events are characterized by two proton collinear tracks. The tracks are collinear if the difference in their scattering angle is small, namely the collinearity cut  $\Delta\theta_{x,y} < 3\sigma$ , where  $\sigma = 130 \mu\text{rad}$ , discussed in Sec. 2.4.1, is used.

The goal is to look for an event corresponding to an elastic event. The method is demonstrated on the study of E1U. There is only one possible scenario, signal in the east-upper branch (E2U and E1U) and west-lower branch (W1D and W2D). The efficiency

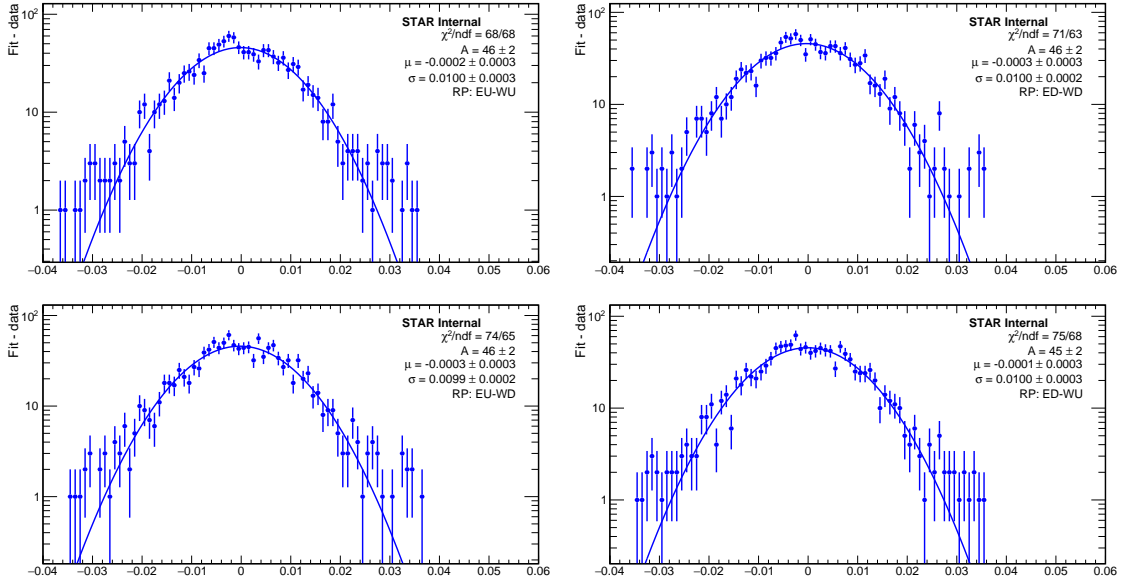


Figure 6.6: Difference between the fit of the probability of retaining CEP event as a function of instantaneous luminosity and the data.

study of E1U is illustrated in Fig. 6.7. The method goes as follows:

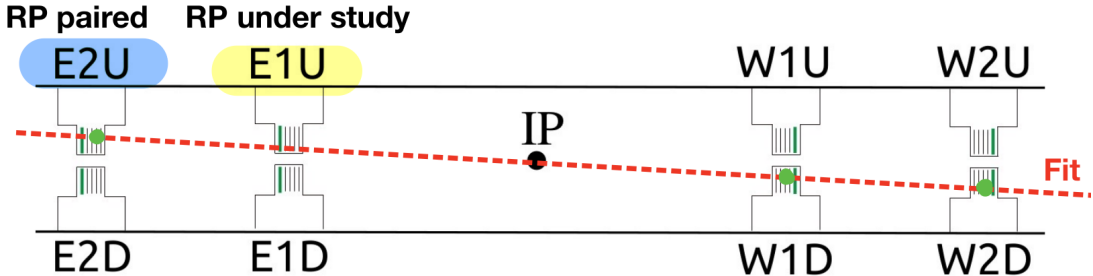


Figure 6.7: An illustration of efficiency calculation for E1U, highlighted with yellow colour and denoted as "RP under study". The second RP in the same branch, E2U is called "RP paired" and is highlighted with blue colour. The red dashed line illustrates a fit of three known points in E2U, W1D, and W2D.

1045

1046 1. Find an event with only one reconstructed point per E2U, W1D, and W2D. No  
1047 reconstructed point is allowed in the remaining RPs (E2D, E1D, W2U, and W1U).

1048

1049 2. Form a track based on the three points found in E2U, W1D, and W2D. The track  
1050 does not correspond to any real particle. It is a straight line where the proton  
1051 tracks should lie on. However, the line is called track. This notation is taken from  
1052 the elastic analysis [17].

1053 3. The track has to pass the criteria for elastic events defined in Sec. 2.4.1.

- 1054 4. Events that satisfy all the above criteria form sample called *Total*.
- 1055 5. In the RP under study (E1U), exactly one point is required. Furthermore, the  
1056 point must be close to the fit. The distance  $d$  in the  $x - y$  plane should be equal  
1057 to or less than 12 mm.
- 1058 6. Events satisfying all the above criteria form sample called *Passed*. The efficiency  
1059 is number of *Passed* over *Total* using TEfficiency class in ROOT.

1060 The efficiencies are studied as a function of track momenta ( $p_x, p_y$ ) for each branch  
1061 separately, see Fig. 6.8. cross section for elastic events drops rapidly with the increasing  
1062 scattering angle. Therefore, there is a lack of statistic on the edges of the detectors and  
1063 the geometry acceptance in  $p_x - p_y$  phase space has to be limited to ensure low efficiency  
1064 uncertainties. The limitation is illustrated by the black solid rectangles. Within the  
1065 limitation, the average obtained efficiencies are summarized in Tab. 6.2.

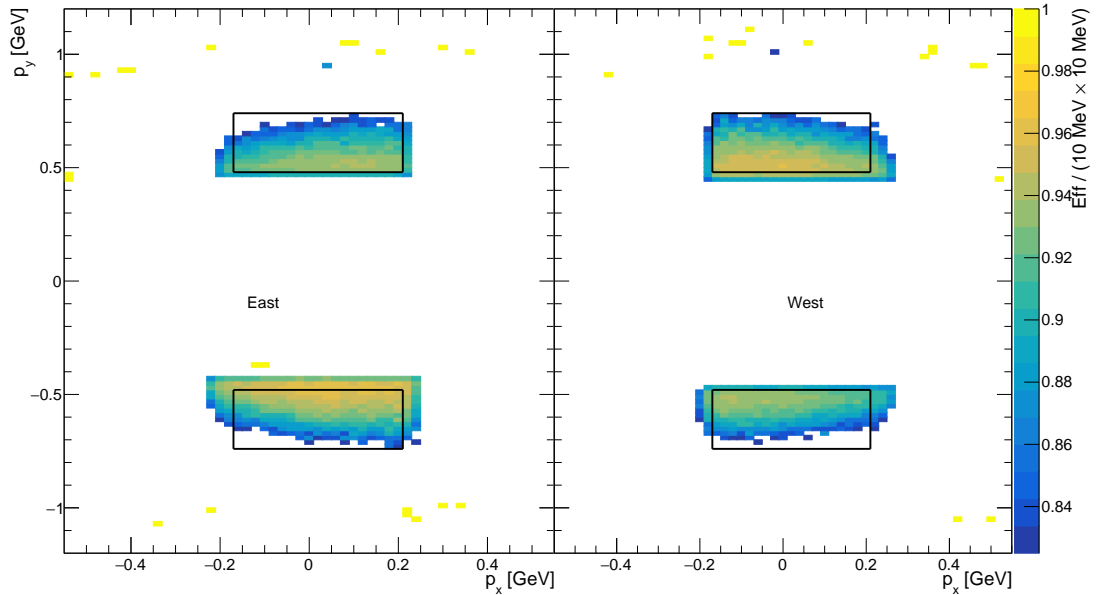


Figure 6.8: The point reconstruction efficiency as the function of reconstructed track momenta  $p_x, p_y$  studied separately for each branch. The black solid rectangle depicts the acceptance limitation of the data-driven methodlimitation.

Branch	efficiency
EU	(96.8 ± 0.7) %
ED	(95.6 ± 0.8) %
WU	(97.0 ± 0.6) %
WD	(96.4 ± 0.7) %

Table 6.2: The average obtained RP efficiency for each branch in limited elastic acceptance in  $p_x - p_y$  phase space.

1066        The obtained efficiencies cannot be used in CEP analysis because of limited geometry  
 1067        acceptance. The geometry acceptance of elastic events is limited by the collinearity  
 1068        constraint and the fact that RPs are not centered around the beam. Geometry accept-  
 1069        ance for CEP events can be seen in Fig. 3.1. The acceptance is clearly larger than the  
 1070        acceptance of elastic events used in the data-driven method. Since about 50 % of CEP  
 1071        candidates have at least one RP outside the elastic acceptance, a full MC simulation of  
 1072        the RPs and the beam pipe embedded with ZB data is needed to calculate the efficiencies  
 1073        outside the elastic acceptance. The presented efficiencies are used as validation of the  
 1074        MC approach.

### 1075        6.3.2 Embedded MC method

1076        The embedded MC method is developed to calculate the total efficiency of the RP and  
 1077        to overcome the acceptance limitation of the data-driven method discussed above. The  
 1078        MC simulation of the RP detectors and its quality assurance is described in Sec. 5.2.

1079        The total RP efficiency is calculated as a probability that a single good quality RP  
 1080        track (satisfying cuts C1.1, C1.3 and C1.2) matched with the true-level primary forward  
 1081        proton is reconstructed and selected in the given branch.

1082        There are two parts of the total RP efficiency: the detector efficiency and the proton  
 1083        selection efficiency. The first describes the probability that the proton is measured and  
 1084        reconstructed in RPs. Any detector malfunction will reduce its efficiency. The second  
 1085        denotes the probability that the reconstructed proton will be selected by the proton  
 1086        reconstruction algorithm. Any additional background from pile-up or noise will lower  
 1087        the proton selection efficiency.

### 1088        6.3.3 The detector efficiency

1089        To validate the MC method, the detector efficiency is compared with the data-driven  
 1090        results discussed in Sec. 6.3.1. Since any additional pile-up or background is mostly  
 1091        rejected by the 1<sup>st</sup> step of the data-driven method described in Sec. 6.3.1, the data-  
 1092        driven method mainly described the detector efficiency.

1093        First, the same method as in Sec. 6.3.1 is used on pure MC and MC embedded with  
 1094        ZB data. It should be noted that the same vetoes are applied on ZB data as are used  
 1095        in the CPT2noBBC trigger Sec. 2.3. Namely, the vetoes on BBC and ZDC signal, and  
 1096        the TOF multiplicity are required together with only one of (in)elastic combinations  
 1097        in RP trigger. Furthermore, no TPC-TOF vertex is allowed to emulate the offline  
 1098        veto (cut C2). The point reconstruction efficiency as a function of the reconstructed  
 1099        track momenta  $p_x, p_y$  for the MC embedded with ZB data is depicted in Fig. 6.9. The  
 1100        solid black rectangle depicts the acceptance limitation of the data-driven method. The  
 1101        average obtained RP efficiencies for each branch in limited acceptance for pure MC, MC

1102 embedded with ZB data, and for the data-driven method are summarized in Tab. 6.3.  
 1103 The efficiencies obtained from pure MC are the highest, and the efficiencies obtained  
 1104 from the data-driven method are the lowest, as expected. In general, the efficiencies are  
 1105 in agreement within  $2\sigma$ . This small discrepancy between the MC and the data-driven  
 1106 method is overcome by the next method.

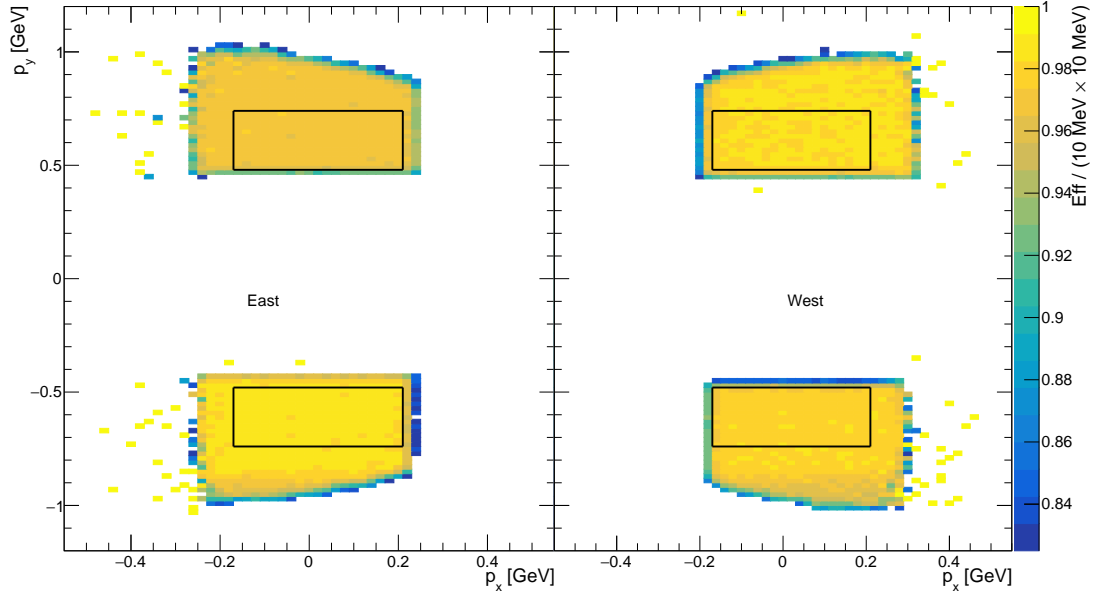


Figure 6.9: The point reconstruction efficiency as the function of reconstructed track momenta  $p_x, p_y$  for MC embedded with ZB studied separately for each branch. The black solid rectangle depicts the acceptance limitation.

Branch	$\varepsilon_{MC}$	$\varepsilon_{MCZB}$	$\varepsilon_{Data}$
EU	$(99.0 \pm 0.1) \%$	$(98.6 \pm 0.1) \%$	$(96.8 \pm 0.7) \%$
ED	$(98.6 \pm 0.2) \%$	$(97.0 \pm 0.3) \%$	$(95.6 \pm 0.8) \%$
WU	$(99.0 \pm 0.1) \%$	$(98.4 \pm 0.2) \%$	$(97.0 \pm 0.6) \%$
WD	$(98.8 \pm 0.2) \%$	$(98.2 \pm 0.2) \%$	$(96.4 \pm 0.7) \%$

Table 6.3: The average obtained RP efficiency for each branch in limited elastic acceptance in  $p_x - p_y$  phase space for pure MC ( $\varepsilon_{MC}$ ) and MC embedded with ZB data ( $\varepsilon_{MCZB}$ ) samples. The efficiencies obtained by the data-driven method ( $\varepsilon_{Data}$ ) are showed as well for the comparison.

1107 To overcome the acceptance limitation of the data-driven method, the following  
 1108 method is used. The point reconstruction efficiency for the given branch,  $\varepsilon^{\text{branch}}$ , is  
 1109 calculated as the probability that a single good quality RP track (satisfying cuts C1.1,  
 1110 C1.3, and C1.2) matched with a true-level primary forward proton is reconstructed in  
 1111 the given branch. The procedure is following:

- 1112 1. Exactly one point in the RP paired is required. These events formed a set *Total*.  
 1113 This condition is used to reproduce the 1<sup>st</sup> step of the data-driven method.

- 1114     2. The nominal RP track selection algorithm is used to find a single good quality track  
 1115     in the given branch. If exactly one such track is found, it is additionally checked if  
 1116     it matches with the true-level primary proton. The distance in the  $p_x - p_y$  space  
 1117     between the track is required to be less than 80 MeV.
- 1118     3. Events that passed the above criteria formed the set *Passed*.
- 1119     4. The efficiency is number of *Passed* over *Total* using TEfficiency class in ROOT.

1120     It should be noted that the momentum components ( $p_x, p_y$ ) are taken after the initial  
 1121     smearing of the momenta, taking into account the effect of the beam angular divergence.  
 1122     The true-level momenta are used for both data sets to minimize the bin migration effect.  
 1123     The results are summarized in Tab. 6.4. The limitation of the data-driven method  
 1124     is overcome, as can be seen in Fig. 6.10. The pure MC gives the highest efficiencies as  
 1125     expected. The efficiencies from the MC embedded sample and the data-driven method  
 1126     agree within uncertainties and their difference is negligible compared to the proton se-  
 1127     lection efficiency discussed below.

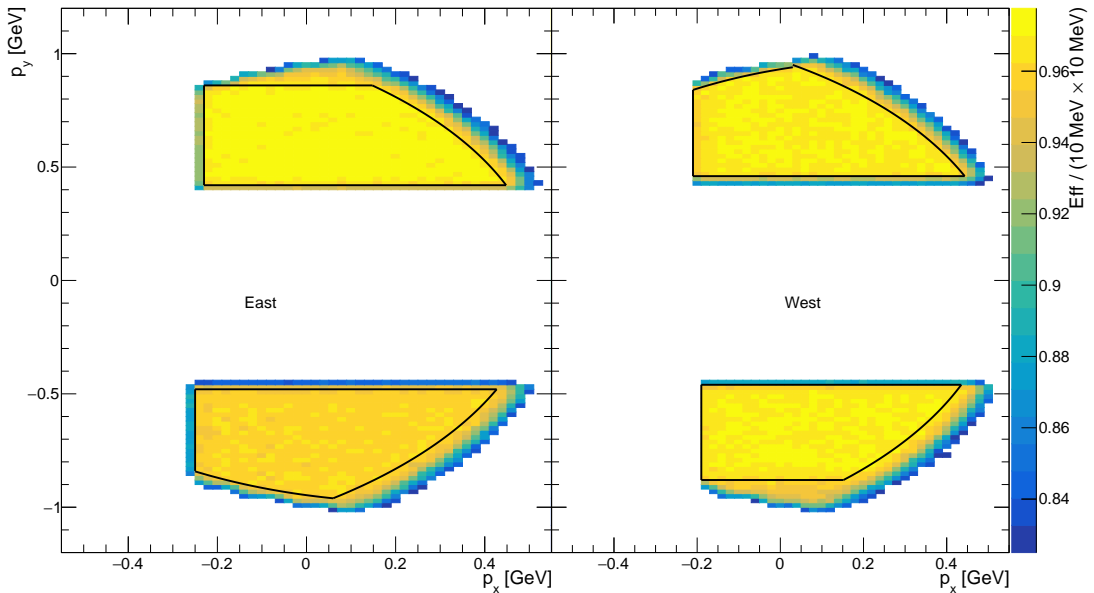


Figure 6.10: The point reconstruction efficiency as the function of reconstructed track momenta  $p_x, p_y$  for MC embedded with ZB studied separately for each branch. The black solid lines depicts the fiducial space.

### 1128     6.3.4 The proton selection efficiency

1129     Any additional proton in the same branch will lower the efficiency of proton selection.  
 1130     Therefore, the requirement of exactly one point in the RP paired is dropped to study  
 1131     the total RP efficiency, the detector efficiency, and the proton selection efficiency. Thus,

Branch	$\varepsilon_{\text{MC}}$	$\varepsilon_{\text{MCZB}}$	$\varepsilon_{\text{Data}}$
EU	(98.0 $\pm$ 0.2) %	(97.1 $\pm$ 0.2) %	(96.8 $\pm$ 0.7) %
ED	(97.7 $\pm$ 0.2) %	(95.6 $\pm$ 0.3) %	(95.6 $\pm$ 0.8) %
WU	(98.0 $\pm$ 0.2) %	(97.0 $\pm$ 0.2) %	(97.0 $\pm$ 0.6) %
WD	(97.9 $\pm$ 0.2) %	(97.0 $\pm$ 0.3) %	(96.4 $\pm$ 0.7) %

Table 6.4: The average obtained RP efficiency for each branch in  $p_x - p_y$  fiducial space for pure MC ( $\varepsilon_{\text{MC}}$ ) and MC embedded with ZB data ( $\varepsilon_{\text{MCZB}}$ ) samples obtained a MC technique. The efficiencies obtained by the data-driven method ( $\varepsilon_{\text{Data}}$ ) are showed as well for the comparison.

the previous method without the 1<sup>st</sup> step is reproduced for the MC embedded sample as it best describes the true efficiency of the RP.

To account for run-by-run variations, efficiency is studied as an average efficiency in the  $p_x, p_y$  phase space for each run. The final total RP efficiency for a given branch is determined as the mean of the obtained average efficiencies, with the systematic uncertainty estimated from the width of the distribution of these average efficiencies. The final total RP efficiencies, along with their systematic uncertainties, are summarized in Tab. 6.5.

Branch	$\varepsilon_{\text{Branch}}^{\text{RP}}$
EU	(89.8 $\pm$ 1.4) %
ED	(87.0 $\pm$ 2.1) %
WU	(89.6 $\pm$ 1.3) %
WD	(89.2 $\pm$ 1.8) %

Table 6.5: The final total RP efficiency ( $\varepsilon_{\text{Branch}}^{\text{RP}}$ ) for each branch obtained by the MC technique on MC embedded sample. The errors represent the systematic uncertainty that is much larger than the statistical one.

### 6.3.5 RP Fiducial volume

The analysis of the forward proton is limited to the envelope in  $p_x, p_y$  space called the fiducial volume. Sometimes it can also be referenced as fiducial region. The fiducial volume is used to compromise high geometrical acceptance, high RP tracking and selecting efficiency, and low systematic uncertainties. Therefore, the following fiducial volume is chosen:

$$\begin{aligned}
 & |y| > p_y^{\text{Min}} \text{ and } x > p_x^{\text{Min}} \\
 & (x + p_x^{\text{Center}})^2 + y^2 < R^2 \\
 & y > 0 \quad \text{for EU and WU and } y < 0 \quad \text{for ED and WD} \\
 & |y| < p_y^{\text{Max}} \quad \text{for EU and WD} \\
 & (x + \bar{p}_x^{\text{Center}})^2 + y^2 < \bar{R}^2 \quad \text{for ED and WU,}
 \end{aligned} \tag{6.8}$$

<sup>1147</sup> where the parameters are summarized in [Tab. 6.6](#).

	EU	ED	WU	WD
$p_x^{\text{Min}} (\text{GeV})$	-0.23	-0.25	-0.21	-0.19
$p_y^{\text{Min}} (\text{GeV})$	0.42	0.48	0.46	0.46
$p_y^{\text{Max}} (\text{GeV})$	0.86	0.84	0.84	0.88
$p_x^{\text{Center}} (\text{GeV})$	0.64	0.7	0.6	0.7
$R^2 (\text{GeV}^2)$	1.36	1.5	1.3	1.5
$\bar{p}_x^{\text{Center}} (\text{GeV})$	0.0	-0.25	-0.28	0.0
$\bar{p}_x^{\text{Max}} (\text{GeV})$	0.0	0.06	0.03	0.0
$\bar{R}^2 (\text{GeV}^2)$	0.0	0.959	0.946	0.0

Table 6.6: Summary of the parameters defining the fiducial volume.

<sup>1148</sup> The fiducial volume is chosen to maximize the  $p_x, p_y$  phase space while simultaneously  
<sup>1149</sup> maintaining a small systematic uncertainty in the RP efficiency. The primary motivation  
<sup>1150</sup> for using a different fiducial volume for each branch stems from the condition  $|y| > p_y^{\text{Min}}$ .  
<sup>1151</sup> Most of the statistics are concentrated at low  $p_y^{\text{Min}}$  because the cross section decreases  
<sup>1152</sup> with increasing scattering angle, which corresponds to higher  $p_y^{\text{Min}}$ . However, as  $p_y^{\text{Min}}$   
<sup>1153</sup> decreases, the probability of detecting protons from the beam halo increases due to  
<sup>1154</sup> proximity to the beam. Consequently, it is crucial to minimize  $p_y^{\text{Min}}$  for each branch  
<sup>1155</sup> independently to maximize statistics while maintaining high RP efficiency.

## <sup>1156</sup> 6.4 TPC vertex reconstruction efficiency

<sup>1157</sup> The primary objective of this study is to determine the efficiency of TPC vertex recon-  
<sup>1158</sup> struction.

<sup>1159</sup> The analysis requires global tracks that are not accessible in the *star-upcDst* ([Sec. 2.1](#)),  
<sup>1160</sup> data format used for the main analysis. Hence, global tracks from the STAR picoDst  
<sup>1161</sup> files are used. However, the picoDst format includes only events with one primary ver-  
<sup>1162</sup> tex. To avoid bias, the analysis focuses on events with multiple interactions per bunch  
<sup>1163</sup> crossing.

<sup>1164</sup> The idea is to find an event with a primary vertex (selected by the picoDst algorithm)  
<sup>1165</sup> and an additional vertex candidate similar to the CEP vertex. The method is based on  
<sup>1166</sup> the key assumption that the efficiency of reconstructing the second vertex is the same  
<sup>1167</sup> as that of the first vertex.

<sup>1168</sup> The methodology involves identifying events with two TOF matched tracks forming a  
<sup>1169</sup> CEP vertex candidate with an addition primary vertex selected by the picoDst algorithm.  
<sup>1170</sup> The criteria follow those used in the main analysis ([C4](#)):

- <sup>1171</sup> • Distance of closest approach (DCA) to the primary vertex (selected by the picoDst  
<sup>1172</sup> algorithm) greater than 10 cm to minimize the bias from the primary vertex.

- Good quality criteria (C4.2):  $N_{\text{hits}}^{\text{fit}} \geq 20$  and  $N_{\text{hits}}^{\langle dE/dx \rangle} \geq 15$ .
- The tracks have to have enough momenta to reach TOF:  $p_T > 0.2$  GeV (C4.1).
- The tracks must match valid TOF hits (C4.4).
- There must be exactly two tracks satisfying the cuts above (C4.5).
- The total charge of the tracks must be zero (C4.6).

The vertex candidates found are checked against the *star-upcDst* data format, see Sec. 2.1 for details. Vertex reconstruction is efficient if the vertex candidate is found in the *star-upcDst*. The efficiency is studied as a function of the DCA of the tracks ( $\text{DCA}_{\text{Part}}$ ) and the DCA of the candidate to the beam line ( $\text{DCA}_{\text{Beam}}$ ) see Fig. 6.11.

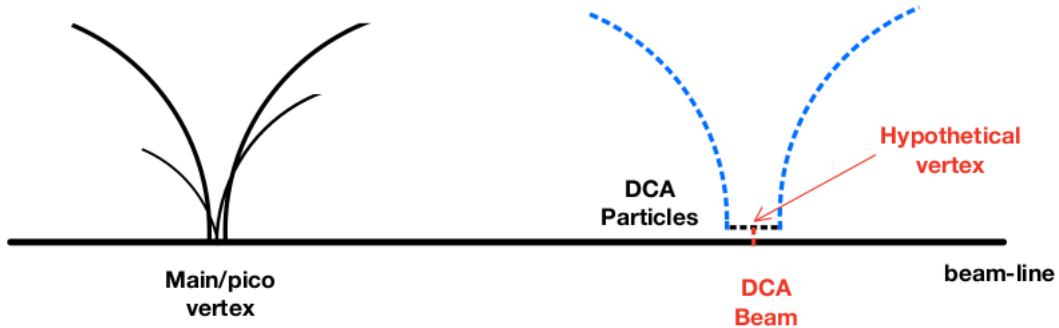


Figure 6.11: An illustration of the TPC vertex reconstruction efficiency study. The main primary vertex selected by picoDst algorithm is depicted by black solid lines along with the vertex candidate ("Hypothetical vertex") formed by blue dashed lines. The DCA between tracks and beam line is shown as well.

There are 23750 out of 26496 good vertices formed by tracks satisfying  $\text{DCA}_{\text{Part}} < 1.5$  cm,  $\text{DCA}_{\text{Beam}} < 0.8$  cm, and  $|\text{vertex}_z^{\text{Candidate}}| < 100$  cm. Hence, the efficiency of the TPC vertex reconstruction is 89.6. The good quality primary vertex criteria ( $\text{DCA}_{xy}$  and  $\text{DCA}_z$ ) are defined in Sec. 3.4.

## 6.5 Central embedding

This section describes the analysis of simulated data embedded in ZB data, called embedding, to determine the TPC and TOF detector efficiency and the PID efficiency. The embedding sample and its validation are described in Sec. 5.1.

### 6.5.1 TPC track acceptance, reconstruction and selection efficiency

The TPC track acceptance, reconstruction, and selection efficiencies are studied together as the total TPC efficiency. The total TPC efficiency is calculated by tracking how many

1193 MC particles are properly reconstructed and how many of them are lost. Technically,  
 1194 the method for the total TPC efficiency can be described as follows:

- 1195 1. True-level particles, generated by MC, are selected. The particles form *set A*.
- 1196 2. Each particle in *set A* is checked if there is a good reconstructed global TPC track  
 1197 associated with the particle.
- 1198 3. All particles from *set A* associated with a reconstructed global particle form *set B*.
- 1199 4. An efficiency is calculated as the ratio of histograms of the true level quantities  
 1200 (such as  $p_T$ ,  $\eta$  or  $z_{\text{vtx}}$ ) for particles from *set B* and particles from *set A*:

$$1201 \varepsilon_{\text{TPC}}^{ID}(p_T, \eta, z_{\text{vtx}}) = \frac{(p_T, \eta, z_{\text{vtx}}) \text{ histogram for given particle from } \textit{set } B}{(p_T, \eta, z_{\text{vtx}}) \text{ histogram for given particle from } \textit{set } A}, \quad (6.9)$$

1202 where  $\varepsilon_{\text{TPC}}^{ID}$  represents a single particle efficiency for the given particle ID e.g.  $\pi^+$  as a  
 1203 function of the given quantity.

1204 Firstly, the *idTruth* and the *qaTruth* should be described here before the association  
 1205 between a true level and a reconstructed particle can be defined.

1206 During simulation, full access is given to the state of the simulated particles. As a  
 1207 particle propagates through the simulation of the STAR detector (STARsim), hits in  
 1208 sensitive layers are formed. The hit represents a position where the particle deposited  
 1209 an energy. Each hit stores the information about the particle depositing the energy as  
 1210 the *idTruth* of the hit.

1211 The reconstructed tracks contain two truth variables: the *idTruth* and the *qaTruth*.  
 1212 The first represents an ID of the simulated true-level particle sharing more than half  
 1213 of its hits with the reconstructed track. The second describes the percentage of hits  
 1214 provided by the simulated true-level particle.

1215 The standard STAR criteria for the association of the reconstructed global track with  
 1216 a particle generated at the true level are a valid *idTruth* and the *qaTruth* higher than  
 1217 95 %. In this analysis, the additional requirement on the distance between the track and  
 1218 the particle in  $\eta - \varphi$  is imposed to minimize the number of fake tracks:  $\delta(\eta, \varphi) < 0.15$ ,  
 1219 where the distance between the track and the particle in the  $\eta - \varphi$  space is defined by:

$$1220 \delta(\eta, \varphi) = \sqrt{(\eta^{\text{true}} - \eta^{\text{reco}})^2 + (\varphi^{\text{true}} - \varphi^{\text{reco}})^2}, \quad (6.10)$$

1221 where  $\eta^{\text{true}}, \eta^{\text{reco}}$  are pseudorapidities of the true-level particle and the reconstructed  
 1222 track and  $\varphi^{\text{true}}, \varphi^{\text{reco}}$  are azimuthal angles of the true-level particle and the reconstructed  
 1223 track. The distance  $\delta(\eta, \varphi)$  with the applied cut can be seen in Fig. 6.12. The value of  
 1224 the cut 0.15 is chosen to be small to reduce number of fake tracks but not too small to  
 1225 keep high number of good tracks. The same procedure with the same 0.15 value was  
 1226 used in the previous study at 200 GeV [1].

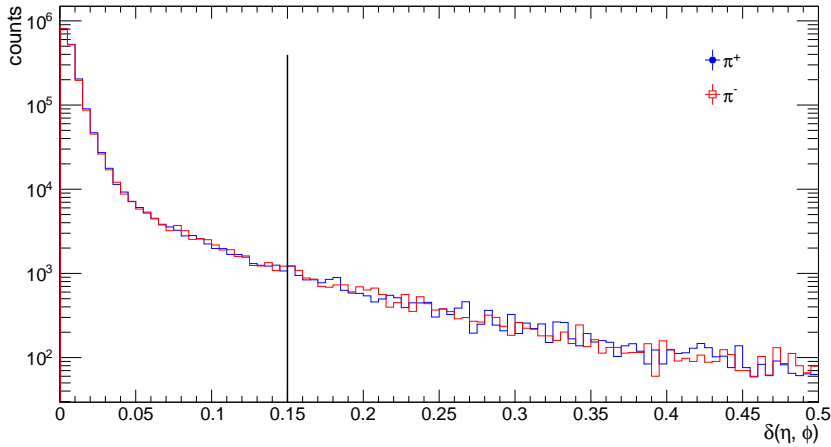


Figure 6.12: Distribution of the distance between reconstructed tracks and matched true-level particles (using standard matching) in the  $\eta - \phi$  space. The vertical black line indicates the used cut value of 0.15.

The total TPC efficiency as a function of  $p_T, \eta, \varphi$ , and  $z_{\text{vtx}}$  can be seen in [Appendix G](#).

The efficiencies are applied as a function of  $p_T, \eta, z_{\text{vtx}}$ . Different binnings of the  $(p_T, \eta, z_{\text{vtx}})$  space were compared leading to a change of  $< 1\%$ .

### [6.5.2 TOF acceptance, hit reconstruction and TPC track matching efficiency](#)

The TOF acceptance, hit reconstruction, and TPC track matching to a TOF hit efficiency was studied altogether as total TOF efficiency. Technically, the method for the total TPC efficiency is following:

1. TPC reconstructed tracks matched to true-level particles are selected. The tracks form *set A*.
2. Each particle in *set A* is checked if it has a TOF match. All MC particles are generated as "in-time" particles. Hence, they should generate a TOF hit when and if they reach the TOF. All matched tracks form *set B*.
3. The efficiency is calculated as the ratio of the histograms of the quantities of tracks (such as  $p_T, \eta$  or  $z_{\text{vtx}}$ ) for particles from *set B* and particles from *set A*:

$$\varepsilon_{\text{TOF}}^{ID}(p_T, \eta, z_{\text{vtx}}) = \frac{(p_T, \eta, z_{\text{vtx}}) \text{ histogram for given particle from } \textit{set B}}{(p_T, \eta, z_{\text{vtx}}) \text{ histogram for given particle ID from } \textit{set A}}. \quad (6.11)$$

The total TOF efficiency as a function of  $p_T, \eta, \varphi$ , and  $z_{\text{vtx}}$  can be seen in [Appendix H](#).

The Geant simulation of the TOF detector has not yet been fully implemented. Especially, merging of TOF hits from ZB data and the MC simulation is missing. However,

the TOF embedding is still useful in our case as we are interested solely in the TOF information from the MC simulation and we focus on low multiplicity events where a TOF background (number of TOF hits in ZB data) is small from the definition. Hence, the probability that a background TOF hit would be merged/ mixed with the MC simulated hit is negligible.

The average total TOF efficiencies for  $\pi^+$ ,  $\pi^-$ ,  $K^+$ ,  $K^-$ ,  $p$ , and  $\bar{p}$  are 63.4 %, 63.3 %, 60.0 %, 58.8 %, 58.8 %, and, 59.2 %, respectively. The efficiencies are applied as a function of  $p_T$ ,  $\eta$ ,  $z_{\text{vtx}}$ . Different binnings of the  $(p_T, \eta, z_{\text{vtx}})$  space were compared and the average change was added to the systematic uncertainties.

## 6.6 PID efficiency study

The efficiency of particle identification is studied as a function of the transverse momenta of the particles ( $p_T^{\max}, p_T^{\min}$ ). The particle identification efficiency  $\epsilon_X$  and the probability of misidentification  $\lambda_{X \rightarrow Y}$  are calculated for each particle type ( $X, Y = \pi, K, p$ ) using the pair selection criteria Eq. 3.9-3.7 discussed in Sec. 3.6.

$$\epsilon_X(p_T^{\max}, p_T^{\min}) = \frac{N_{\text{reco}X}^{\text{true}X}(p_T^{\max}, p_T^{\min})}{N_{\text{true}X}(p_T^{\max}, p_T^{\min})}, \quad (6.12)$$

$$\lambda_{X \rightarrow Y}(p_T^{\max}, p_T^{\min}) = \frac{N_{\text{reco}Y}^{\text{true}X}(p_T^{\max}, p_T^{\min})}{N_{\text{true}X}(p_T^{\max}, p_T^{\min})}, \quad (6.13)$$

where  $N_{\text{true}X}$  is number of true  $XX$  pairs in the embedding,  $N_{\text{reco}X}^{\text{true}X}$  is number of  $XX$  pairs correctly identified as  $XX$  pairs and  $N_{\text{reco}Y}^{\text{true}X}$  is number of  $XX$  pairs misidentified as  $YY$  pairs. The embedding itself is discussed in Sec. 5.1.

Figure 6.13 presents the result as a function of the maximum and minimum true transverse momenta of particles in the pair ( $p_T^{\max}, p_T^{\min}$ ). The clear motivation for the restriction of the fiducial space is seen. Hence, the fiducial space is limited by Eq. 3.10-3.12 to preserve high pair identification efficiency and also to keep low systematic uncertainty. The restriction is also illustrated by the black lines in Fig. 6.13. The obtained efficiencies for each particle type are used to correct the data.

## 6.7 TPC z-vertex cut C2

TPC z-vertex cut (C2) removes the specific range of  $z$ -positions of the primary vertices from the analysis. Thus, it reduces the accepted luminosity with respect to that delivered by the collider. To account for this loss, we assume that the distribution of  $z_{\text{vtx}}$  of all primary interactions follows a normal distribution ( $\mathcal{N}$ ), then the efficiency of the cut C2 is described by:

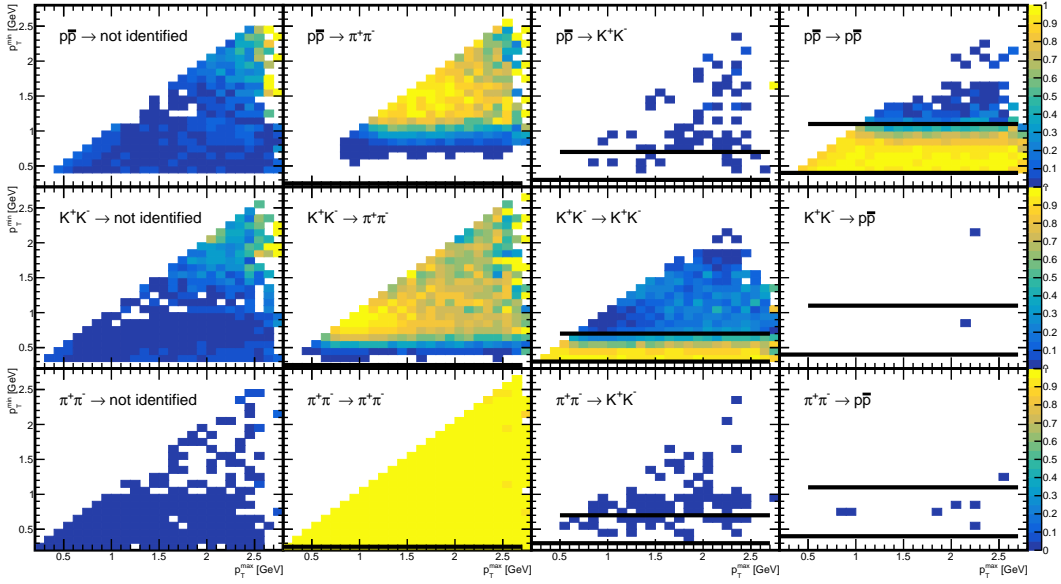


Figure 6.13: Pair identification efficiency and misidentification probability as a function of maximum and minimum true particles' transverse momenta of particles in the pair ( $p_T^{\max}, p_T^{\min}$ ) for  $\pi^+\pi^-$ ,  $K^+K^-$  and  $p\bar{p}$ . The first row of figures illustrates true samples of  $p\bar{p}$  pairs, categorized as follows from left to right: not identified, misidentified as  $\pi^+\pi^-$  pairs, misidentified as  $K^+K^-$  pairs, and correctly identified as  $p\bar{p}$  pairs. The second row depicts the true samples of  $K^+K^-$  pairs, while the third row presents the  $\pi^+\pi^-$  pairs. The results are obtained from the central embedding discussed in Sec. 6.5.

$$1278 \quad \epsilon_{z_{\text{vtx}}}^{\text{fit}} = \int_{z_{\text{vtx}}^{\text{Min}}}^{z_{\text{vtx}}^{\text{Max}}} \mathcal{N}(z_{\text{vtx}}; \mu, \sigma) dz_{\text{vtx}} = \frac{1}{2} \left[ \text{Erf} \left( \frac{z_{\text{vtx}}^{\text{Max}} - \mu}{\sqrt{2}\sigma} \right) - \text{Erf} \left( \frac{z_{\text{vtx}}^{\text{Min}} - \mu}{\sqrt{2}\sigma} \right) \right] \quad (6.14)$$

1279 where  $z_{\text{vtx}}^{\text{Max}}$  and  $z_{\text{vtx}}^{\text{Min}}$  are the maximum and minimum value of the longitudinal position of the vertex accepted in the analysis, and the parameters  $\mu$  and  $\sigma$  represent the 1280 mean and standard deviation of the normal distribution. The Erf is the error function 1281 defined as:

$$1283 \quad \text{Erf}(x) = \frac{2}{\sqrt{\pi}} \int_0^x e^{-t^2} dt. \quad (6.15)$$

1284 Since the shape and position of  $z_{\text{vtx}}$  can vary on the fill-by-fill basis, the real parameters 1285 of the  $z_{\text{vtx}}$  distribution are studied separately for each single fill.

1286 The distribution of  $z_{\text{vtx}}$  is studied only for the CPT2noBBCL trigger with a single 1287 TOF vertex. This distribution for the fill 20734 is shown in Fig. 6.14. The distribution 1288 is fitted with the Gaussian function in the range  $z_{\text{vtx}} \in [-120 \text{ cm}, 120 \text{ cm}]$ . The fit 1289 parameters ( $\mu$  and  $\sigma$ ) obtained from each fill are plotted as a function of the fill number, 1290 see in Figs. 6.15 and 6.16. Figure 6.17 shows the efficiency as a function of the fill 1291 number. Because the distribution of  $z_{\text{vtx}}$  does not fully follow the normal distribution,

1292 the second method is developed.

1293 For each fill, the efficiency is calculated as:

$$1294 \quad \epsilon_{z_{\text{vtx}}}^{\text{data}} = \frac{\int_{z_{\text{vtx}}^{\text{Min}}}^{z_{\text{vtx}}^{\text{Max}}} z_{\text{vtx}} dz_{\text{vtx}}}{\int_{-200}^{200} z_{\text{vtx}} dz_{\text{vtx}}}. \quad (6.16)$$

1295 The difference between the two methods ( $\epsilon_{z_{\text{vtx}}}^{\text{fit}} - \epsilon_{z_{\text{vtx}}}^{\text{data}}$ ) is independent of a fill number,  
 1296 as can be seen in Fig. 6.17. Therefore, the average of the two efficiencies is used to correct  
 1297 the data and the systematic uncertainty is estimated as half of the difference between  
 1298  $\epsilon_{z_{\text{vtx}}}^{\text{fit}}$  and  $\epsilon_{z_{\text{vtx}}}^{\text{data}}$ . Hence, the systematic uncertainty is 1.1 % independent on a fill.

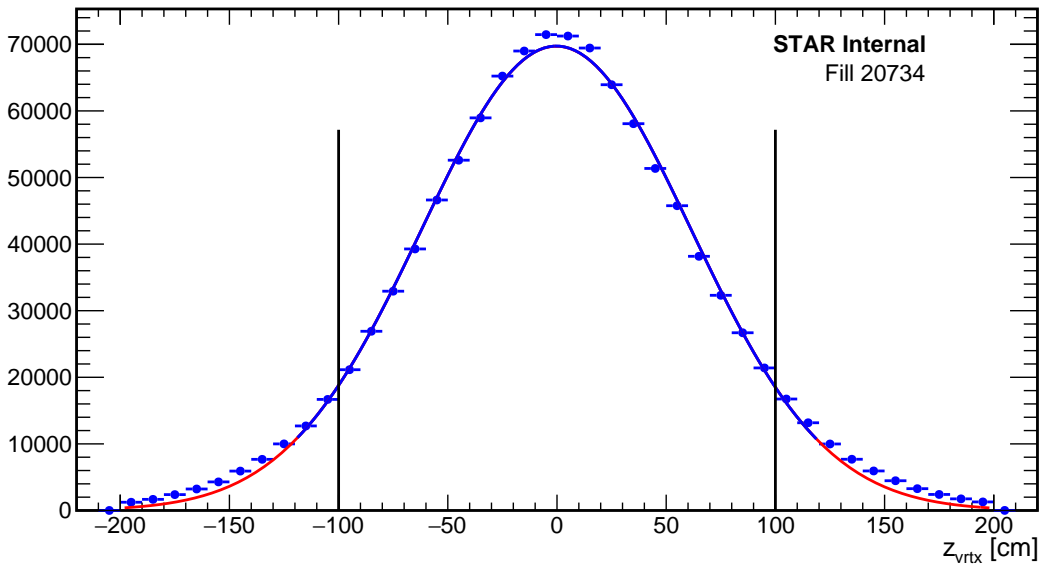


Figure 6.14: The distribution of  $z_{\text{vtx}}$  for the CPT2noBBCL trigger with a single TOF vertex together with the fit of normal distribution (solid blue) extended outside the range of the fit (solid red).

## 1299 6.8 Exclusivity cut C6

1300 The resolution of the total transverse momentum ( $\sigma(p_T^{\text{miss}})$ ) is a combination of the  
 1301 resolution of the forward protons and the central system. The most significant is the  
 1302 resolution of the forward proton ( $\sigma_{p_{x,y}}^{\text{proton}}$ ) formed by the RP resolution and the beam  
 1303 angular divergence. In Run 17, the beam angular divergence is  $90 \mu\text{rad}$ . For a 255 GeV  
 1304 beam, such divergence results in smearing of the transverse momentum components for  
 1305  $\sigma_{\text{divergence}} = 255 [\text{GeV}] \times 90 \times 10^{-6} = 22.950 [\text{MeV}] \approx 23 [\text{MeV}]$ . The RP resolution  
 1306 is obtained by fitting the difference between the generated and reconstructed proton

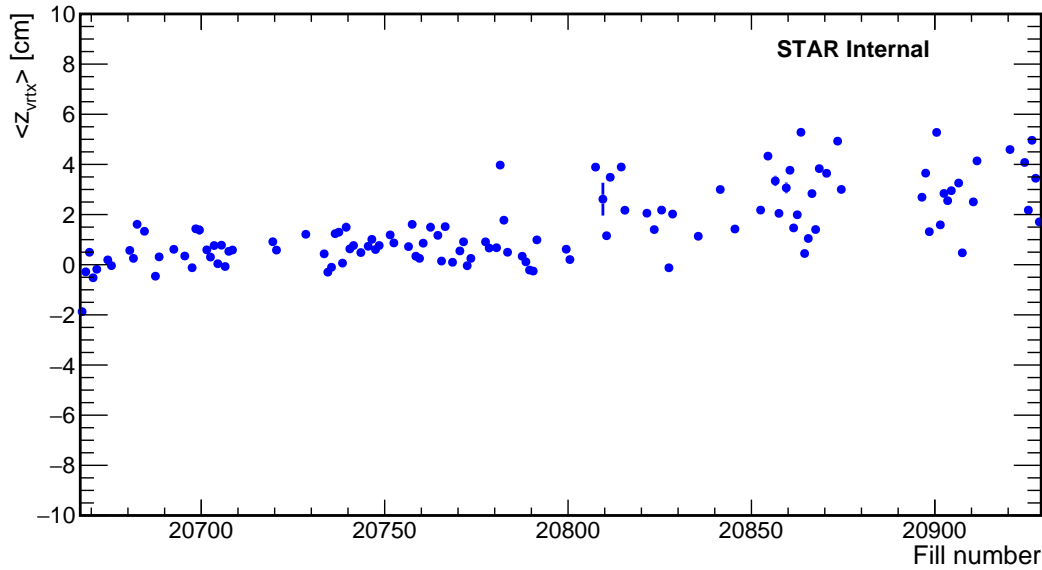


Figure 6.15: The distribution of the mean parameter of the normal distribution, obtained from a fit of normal distribution to  $z_{\text{vtx}}$  distribution in a range [-120 cm, 120 cm] for each RHIC fill, as a function of the fill number.

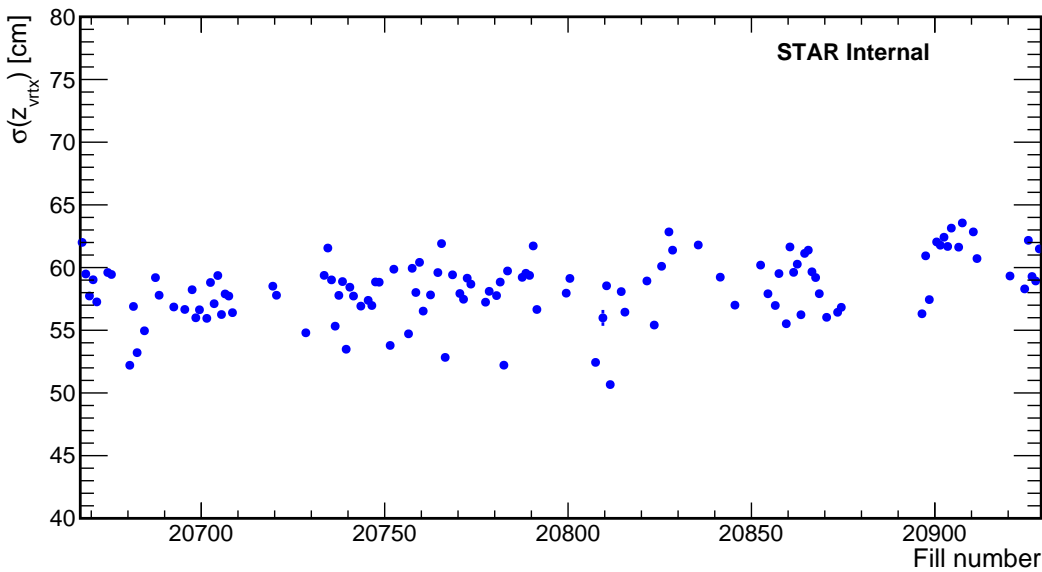


Figure 6.16: The distribution of the width parameter of the normal distribution, obtained from a fit of normal distribution to  $z_{\text{vtx}}$  distribution in a range [-120 cm, 120 cm] for each RHIC fill, as a function of the fill number.

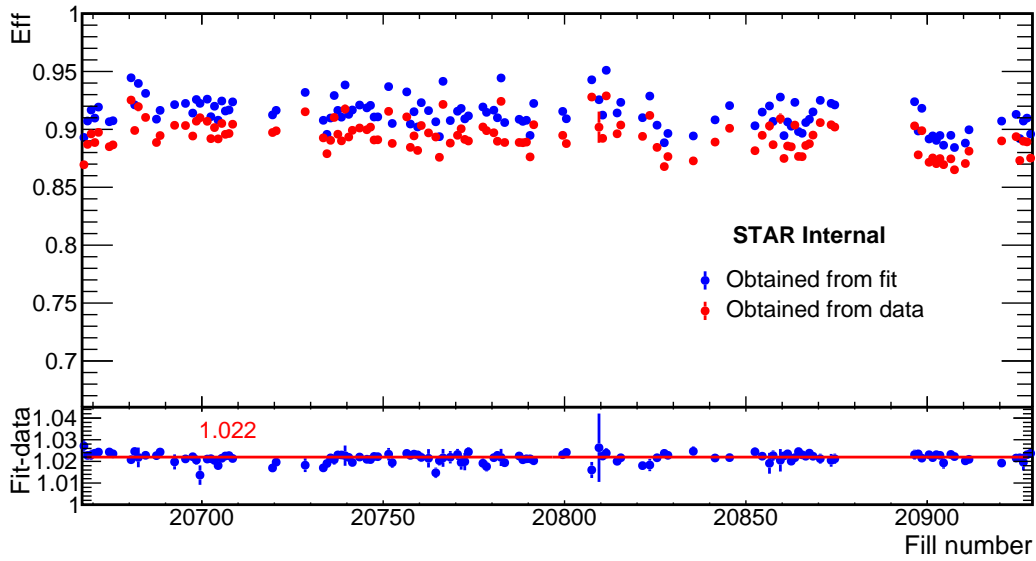


Figure 6.17: The efficiency as a function of the fill number. The difference between two method is plotted in the bottom panel together with the fit of the constant function  $\epsilon_{z_{\text{vtx}}}^{\text{fit}} - \epsilon_{z_{\text{vtx}}}^{\text{data}} = 1.022$ .

1307 momenta, and it is equal to  $\sigma_{RP} \approx 10$  MeV. The following equations estimate  $\sigma(p_T^{\text{miss}})$ .

$$1308 \quad \sigma_{p_{x,y}}^{\text{proton}} = \sqrt{\sigma_{\text{divergence}}^2 + \sigma_{RP}^2} = \sqrt{23^2 + 10^2} \approx 25 \text{ MeV} \quad (6.17)$$

$$1309 \quad \sigma(p_x^{\text{miss}}) = \sqrt{\sum_{\text{particles}} \sigma^2} > \sqrt{2 * (\sigma_{p_{x,y}}^{\text{proton}})^2} = \sqrt{2} * \sigma_{p_{x,y}}^{\text{proton}} \approx 35.4 \text{ MeV} \quad (6.18)$$

$$1310 \quad \sigma(p_T^{\text{miss}}) = \sigma(p_x^{\text{miss}}) > 35.4 \text{ MeV} \quad (6.19)$$

1311 Figures 6.18 and 6.19 shows distributions of the missing momentum in  $x$  and  $y$   
 1312 coordinates for  $\pi^+\pi^-$  CEP event candidates fitted by a Gaussian (signal) and second  
 1313 degree polynomial (background). The obtained Gaussian widths agree well with the  
 1314 proton resolution derived in Eq. 6.18.

1315 The MC distribution of the missing momentum is generated using the parame-  
 1316 ters (mean and width) obtained from the fits of the  $p_x^{\text{miss}}$  and  $p_y^{\text{miss}}$  distributions in  
 1317 Figs. 6.18 and 6.19. The MC distribution is scaled to the number of CEP events. The  
 1318 number is acquired by integrating the data (unlike-sign pairs) from 0.0 up to 140 MeV  
 1319 and subtracting the non-exclusive background. The background sample is estimated  
 1320 by fitting the second degree polynomial with the constant term equal to zero. The  
 1321 distribution  $p_T^{\text{miss}}$  is shown in Fig. 6.20.

1322 The efficiency of the  $p_T^{\text{miss}}$  cut is determined as the relative size of the exclusive  
 1323 sample for the data and MC below the  $p_T^{\text{miss}}$  cut. The efficiency as a function of the  
 1324 exclusivity cut thresholds is illustrated in Fig. 6.21 along with purity ( $S/(S+B)$ ) and  
 1325 significance ( $S/\sqrt{S+B}$ ). The  $p_T^{\text{miss}}$  cut equal to 120 MeV is chosen to balance the high

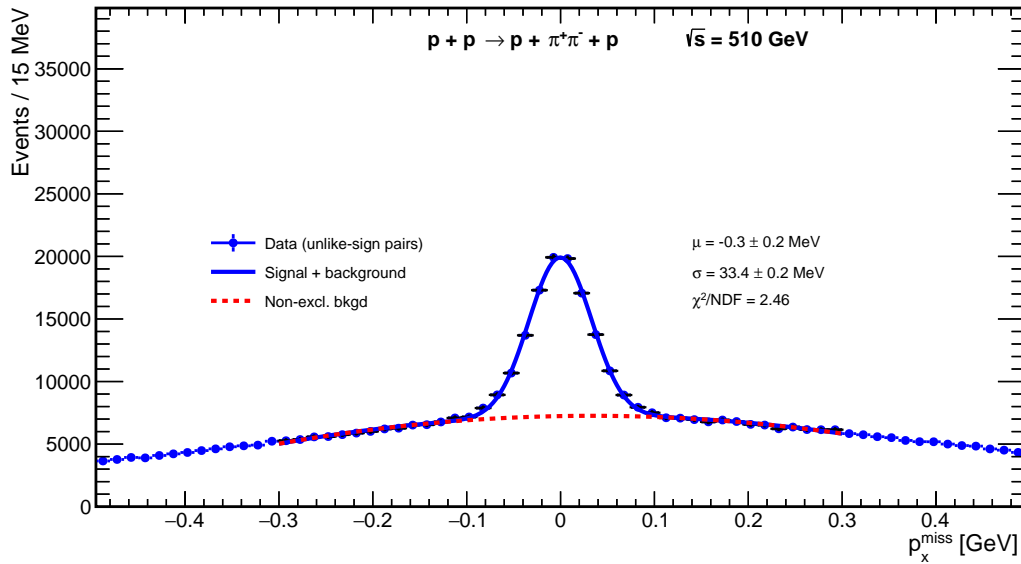


Figure 6.18: The distribution of the missing momentum in  $x$  coordinate for  $\pi^+\pi^-$  CEP event candidates fitted by a Gaussian and second degree polynomial.

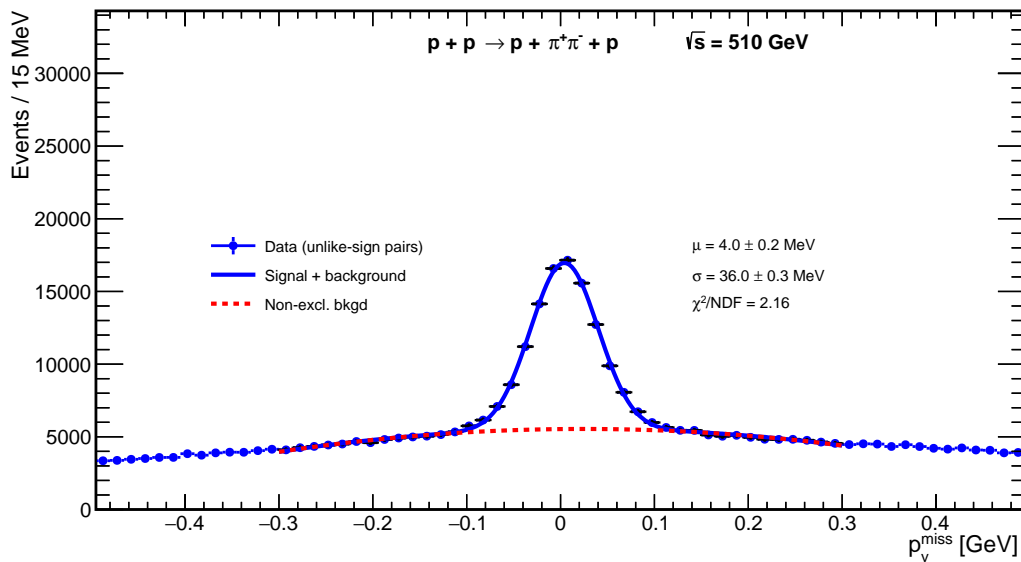


Figure 6.19: The distribution of the missing momentum in  $y$  coordinate for  $\pi^+\pi^-$  CEP event candidates fitted by a Gaussian and second degree polynomial.

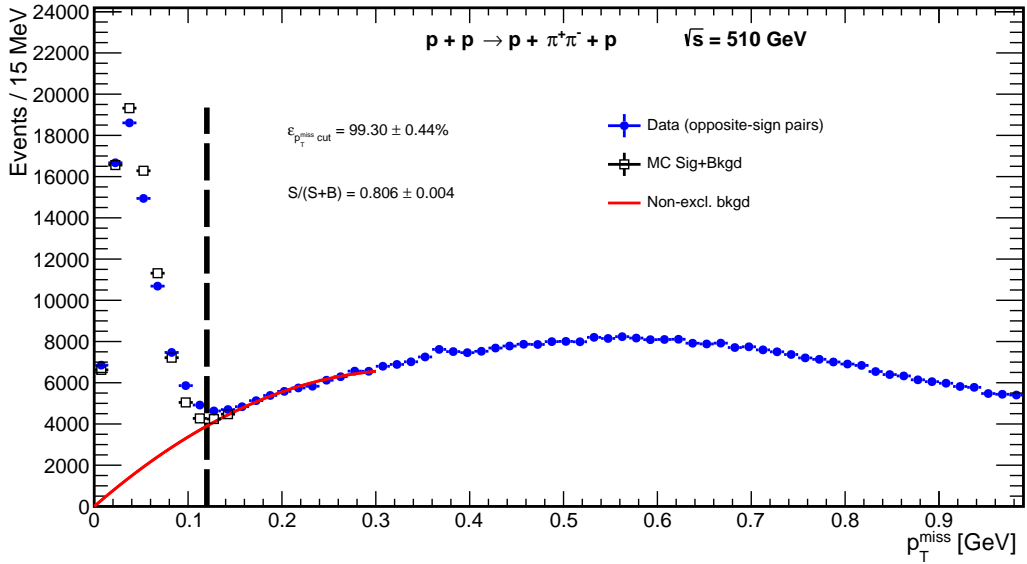


Figure 6.20: The distribution of the missing transverse momentum  $p_T^{\text{miss}}$  for  $\pi^+\pi^-$  CEP event candidates. The exclusivity cut is illustrated by the black dot-dashed line. The MC signal generated parameters from the fits in  $p_x^{\text{miss}}$  and  $p_y^{\text{miss}}$  is shown together with the non-exclusive background estimated by fitting the second degree polynomial with the constant term equal to zero. The sizes of obtained CEP samples from the  $p_T^{\text{miss}}$ ,  $p_x^{\text{miss}}$  and  $p_y^{\text{miss}}$  distributions are depicted as well.

efficiency and high purity of the final sample. The systematic uncertainty is estimated as the difference between the efficiencies obtained from the MC and the data. Hence, the final efficiency is  $\epsilon_{p_T^{\text{miss}} \text{cut}} = 99.3 \pm 0.4\%$ . Figures for kaons and protons can be seen in Appendix B.

## 6.9 Corrections to the luminosity

The nominal luminosity of the CPT2noBBCL trigger is  $142 \text{ pb}^{-1}$ . The value is already scaled for the dead time of the trigger, but it has to be scaled for the fraction of analyzed events since some data may be lost during data production. The number of analyzed triggers is given in the second bin of the histogram shown in Fig. 3.7. In Ref. [30], it was found that the luminosity has to be corrected by -2.6%, since the used ZDC cross section is 2.6% smaller than the correct value. The luminosity has to be also corrected for the probability of retaining the CEP event presented in Sec. 6.2.4. Hence, the integrated luminosity defined in Eq. 6.2 is  $121 \pm 4 \text{ pb}^{-1}$  and the effective integrated luminosity defined in Eq. 6.2 is  $25.6 \pm 1.1 \text{ pb}^{-1}$ .

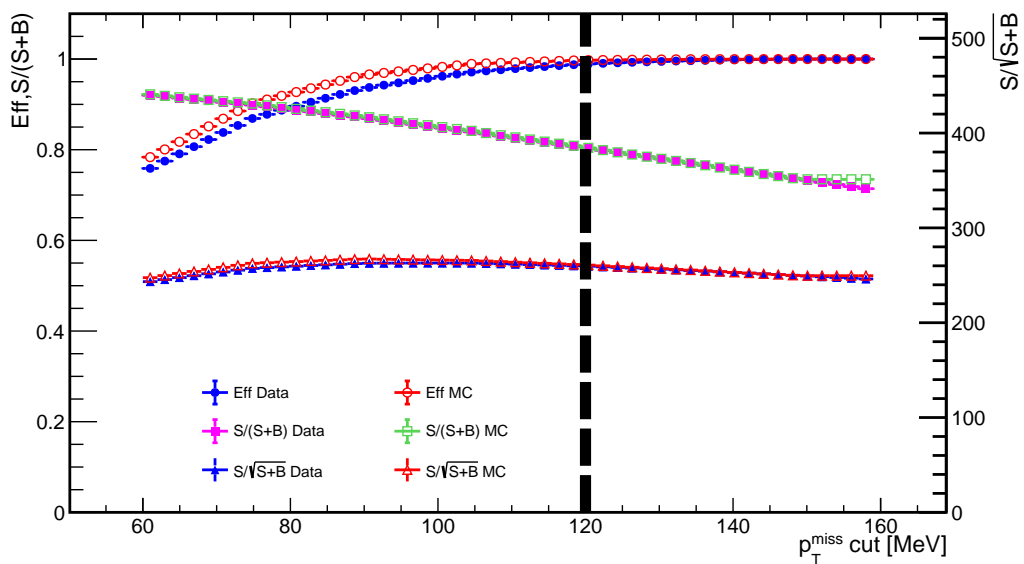


Figure 6.21: CEP  $\pi^+\pi^-$  signal efficiency, purity ( $S/(S+B)$ ) and significance ( $S/\sqrt{S+B}$ ) as a function of the exclusivity cut thresholds for data and MC.



1340

# Chapter 7

1341

## Systematic Uncertainties

1342 This chapter summarizes various sources of systematic uncertainties considered in this  
1343 analysis. The next section presents a summary of sources of systematic uncertainties.  
1344 The last two sections are dedicated to studies of systematic uncertainties of TPC and  
1345 TOF.

1346

### 7.1 Summary of the systematic effects

1347

### 7.2 Systematic Uncertainties

1348 In this section, we describe how systematic uncertainties were obtained. We find that  
1349 only the background subtraction systematic uncertainty is bin dependent. All other  
1350 systematic uncertainties are not bin dependent. The following systematic uncertainties  
1351 are evaluated for each presented distribution separately:

1352 1. **Background subtraction:** the systematic uncertainty related to the non-exclusive  
1353 background subtraction discussed in [chapter 4](#). It is studied by varying the range  
1354 of the projection: from 170 to 210 MeV (smaller range) and from 140 to 250 MeV  
1355 (wider range). The subtraction is performed for the ranges described previously.  
1356 The obtained fiducial differential cross sections for CEP of  $h^+h^-$  pairs as a function  
1357  $m(h^+h^-)$  are compared with the nominal one. The uncertainty is taken as  
1358 the average of absolute deviations for each bin separately. There is another source  
1359 of the systematic uncertainty, which is due to the statistical uncertainty of the size  
1360 of the non-exclusive background sample. This uncertainty is common for all the  
1361 bins. The weighted mean of uncertainties of the background subtraction in the  
1362 invariant mass distribution of  $\pi^+\pi^-$ ,  $K^+K^-$ , and  $p\bar{p}$  pairs are 0.4%, 0.8%, and  
1363 3.3%, respectively. Only this systematic uncertainty is bin dependent.

1364 2. **RP efficiency correction:** the systematic uncertainty associated with the RP  
1365 efficiency corrections for a single proton is studied from run-by-run variations in

1366 each RP branch separately. An average variation is approximately 1.5% for a single  
 1367 proton resulting in the total RP systematic uncertainty on the fiducial differential  
 1368 cross sections to be 2.4%.

- 1369     3. **TPC efficiency correction:** the uncertainty is studied by varying the TPC track  
 1370 selection criteria ( $N_{\text{hits}}^{\text{fit}}$  and  $N_{\text{hits}}^{(dE/dx)}$ ) and applying the TPC efficiency corrections  
 1371 corresponding to the given set of selection criteria. The obtained fiducial differen-  
 1372 tial cross sections are compared with the cross section calculated with corrections  
 1373 as described in [chapter 6](#). The typical uncertainties on the fiducial differential cross  
 1374 sections are  $^{+7}_{-4}\%$ ,  $^{+7}_{-4}\%$ , and  $^{+4}_{-4}\%$  for  $\pi^+\pi^-$ ,  $K^+K^-$ , and  $p\bar{p}$  pairs, respectively.
- 1375     4. **TOF efficiency correction:** the uncertainty is studied by comparing the cor-  
 1376 rections obtained from the embedding and the data-driven tag-and-probe method  
 1377 based on  $K_S^0 \rightarrow \pi^+\pi^-$  decays. The difference between the embedding and the  
 1378 tag-and-probe method is found to be about 1.0% per a single track. In addition,  
 1379 the corrections from the embedding are calculated as function of ( $p_T$ ,  $\eta$ ,  $z_{\text{vtx}}$ ) with  
 1380 different binning applied. The obtained fiducial differential cross sections are com-  
 1381 pared with the cross section calculated with corrections as described in [chapter 6](#).  
 1382 This method of applying the TOF matching efficiency corrections leads to an ad-  
 1383 dition uncertainty. The typical total TOF uncertainty on the fiducial differential  
 1384 cross sections is  $^{+1}_{-2}\%$  for  $\pi^+\pi^-$ ,  $K^+K^-$ , and  $p\bar{p}$  pairs.
- 1385     5. **TPC vertex reconstruction:** the systematic uncertainty is determined by vary-  
 1386 ing the good primary vertex criteria ( $DCA_{xy}$  and  $DCA_z$ ) and applying the TPC  
 1387 vertex reconstruction efficiency corrections corresponding to the given set of vertex  
 1388 criteria. The uncertainty on the fiducial differential cross section is  $^{+2.6}_{-1.0}\%$ .
- 1389     6. **TPC z-vertex criterion:** the uncertainty is calculated as half of the difference  
 1390 between the two methods used. The systematic uncertainty is determined to be  
 1391 independent of the fill and is 1.1%.
- 1392     7. **Exclusivity  $p_T^{\text{miss}}$  cut:** the systematic uncertainty is 0.4% as the difference be-  
 1393 tween efficiencies obtained from MC and data samples.
- 1394     8. **Particle identification:** the uncertainty is studied by varying the pair identifica-  
 1395 tion criteria. The typical change of  $< 1\%$ ,  $^{+4}_{-5}\%$  and  $^{+4}_{-5}\%$  in the fiducial differen-  
 1396 tial cross section is observed for  $\pi^+\pi^-$ ,  $K^+K^-$ , and  $p\bar{p}$  pairs, respectively. This change  
 1397 results from applying looser and tighter identification criteria and correcting for the  
 1398 corresponding PID efficiency. The looser condition uses the  $\chi^2_{(dE/dx)}(h^+h^-) < 12$   
 1399 condition instead of  $\chi^2_{(dE/dx)}(h^+h^-) < 9$  in [Eq. 3.7](#) and in [Eq. 3.8](#). The values  
 1400 for the cuts  $m_{\text{TOF}}^2$  are 0.1 and 0.55 GeV<sup>2</sup> for the kaon and proton hypotheses,  
 1401 respectively. The pion hypothesis [Eq. 3.9](#) is changed to  $\chi^2_{(dE/dx)}(\pi^+\pi^-) < 15$ . The

tighter cut uses the  $\chi^2_{\langle dE/dx \rangle}(h^+h^-) < 7$  condition instead of  $\chi^2_{\langle dE/dx \rangle}(h^+h^-) < 9$  in Eq. 3.7 and in Eq. 3.8. The values for the cuts  $m_{\text{TOF}}^2$  are 0.2 and 0.7 GeV<sup>2</sup> for the kaon and proton hypotheses, respectively. The pion hypothesis Eq. 3.9 is changed to  $\chi^2_{\langle dE/dx \rangle}(\pi^+\pi^-) < 9$ .

9. **The luminosity uncertainty.** There are two parts of the luminosity uncertainty: luminosity calibration based on van der Meer scans **vanderMeer:1968zz** and the probability of retaining a CEP event, dependent on instantaneous luminosity. The first, contributes to the integrated luminosity uncertainty and is 5% [31]. The second, is evaluated to be 4%. Thus, the total uncertainty on effective integrated luminosity Eq. 6.2 is 6.4%. This systematic vertical scale uncertainty is not plotted on the results.

Systematic uncertainties for the integrated fiducial cross sections for CEP of  $\pi^+\pi^-$ ,

$K^+K^-$ , and  $p\bar{p}$  pairs are shown in Tab. 7.1.

Particle species	$\delta_{\text{syst}}/\sigma_{\text{fid}} [\%]$				Total
	TPC	TOF	RP	Other	
$\pi^+\pi^-$	+7 -4	+1 -2	2.4	+3 -2	+8 -5
$K^+K^-$	+7 -4	+1 -2	2.4	+5 -4	+9 -7
$p\bar{p}$	+4 -4	+1 -2	2.4	+5 -4	+7 -6

Table 7.1: Typical systematic uncertainties for the integrated fiducial cross section for CEP of  $\pi^+\pi^-$ ,  $K^+K^-$ , and  $p\bar{p}$  pairs. The numbers represent the relative systematic uncertainty of the integrated fiducial cross section in percentage.

### 7.3 TPC combined efficiency correction

The TPC efficiency is solely based on MC simulation and its quality of modeling of the quantities used to select TPC tracks. Since the vertexing algorithm is not part of the MC simulation, the quantities of global tracks are studied, namely the number of hits in the TPC used for the track reconstruction ( $N_{\text{hits}}^{\text{fit}}$ ) and the number of hits in the TPC used to calculate  $\langle dE/dx \rangle$  ( $N_{\text{hits}}^{\langle dE/dx \rangle}$ ). The obtained cross section should be independent of the choice of the minimum number of hits. Hence, the analysis is repeated with a different choice of the minimum number of hits and corrected by the corresponding set of corrections. The nominal set of cuts is described in Sec. 3.4 and corresponds to  $N_{\text{hits}}^{\text{fit}} \geq 20$  and  $N_{\text{hits}}^{\langle dE/dx \rangle} \geq 15$ . The tight and loose sets correspond to  $N_{\text{hits}}^{\text{fit}} \geq 22, 17$  and  $N_{\text{hits}}^{\langle dE/dx \rangle} \geq 17, 12$ , respectively. The obtained cross sections are compared with the nominal cross sections in Fig. 7.1.

The most significant difference can be seen for  $N_{\text{hits}}^{\text{fit}}$  that comes from the discrepancy

between the data and the MC at the beginning of the  $N_{\text{hits}}^{\text{fit}}$  distribution, see Fig. 5.1.

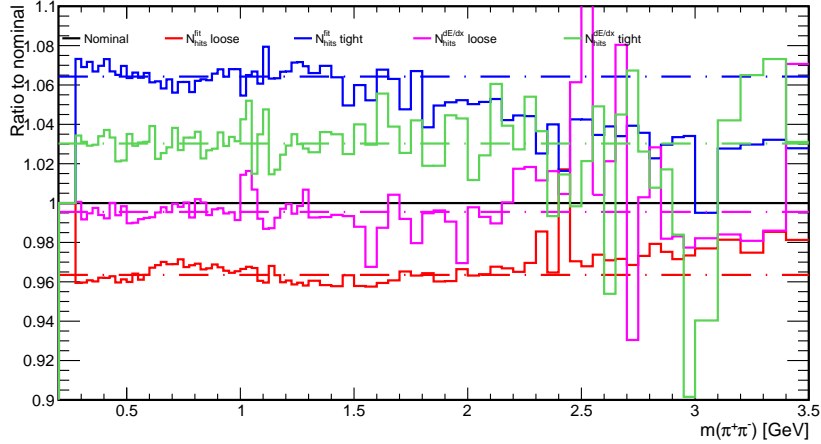


Figure 7.1: A comparison of different results obtained by variation of the TPC track quality cuts on the fiducial differential exclusive  $\pi^+\pi^-$  production cross section as a function of the invariant mass of  $\pi^+\pi^-$ . Dot-dashed horizontal lines represent an average ratio for a modified cut shown in the same color.

1429 Hence, the average deviation for  $N_{\text{hits}}^{\text{fit}}$  is used to determine the uncertainty to be  $^{+5.5\%}_{-3.3\%}$ .

1430 The next source of uncertainty is the method of applying the efficiency correction.  
 1431 Due to the insufficient statistic, it is not possible to differentiate the correction into the  
 1432 full phase space, i.e. to make the correction as a function of  $p_T, \varphi, \eta$ , and  $z$ -position of  
 1433 the vertex. Therefore, different methods of correction application are compared. The  
 1434 comparison can be seen in Fig. 7.2. The average deviation is about 0.5% and can be  
 1435 neglected. Therefore, the total uncertainty on the fiducial differential cross section is  
 1436 determined to be  $^{+5.5\%}_{-3.3\%}$ .

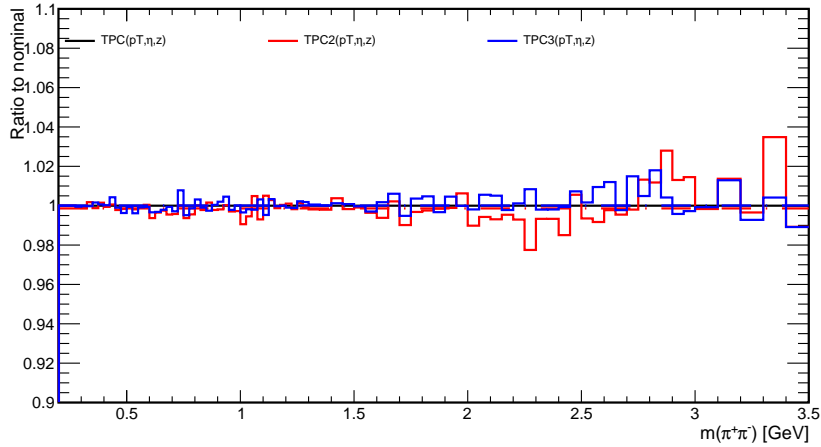


Figure 7.2: A comparison of different results obtained by variation of the TPC track efficiency corrections application on the fiducial differential exclusive  $\pi^+\pi^-$  production cross section as a function of the invariant mass of  $\pi^+\pi^-$ . Dot-dashed horizontal lines represent an average ratio for a modified cut shown in the same color.

## <sup>1437</sup> 7.4 TOF matching efficiency correction

<sup>1438</sup> The uncertainty is studied by comparison of the MC method with a data-driven tag&probe  
<sup>1439</sup> method based on  $K_S^0$  particles in the  $\pi^+\pi^-$  channel. This comparison is performed by  
<sup>1440</sup> Michal Vranovsky from CTU and it is summarized in [Appendix I](#). The average TOF  
<sup>1441</sup> efficiency for  $\pi^+$ ,  $\pi^-$  obtained by the tag&probe method is  $(62.5 \pm 0.9(\text{stat}) \pm 1.0(\text{sys}))$   
<sup>1442</sup> %. The difference is found to be within 1.0% for a single track. In addition, different  
<sup>1443</sup> methods of how TOF corrections are applied are compared in [Fig. 7.3](#). The largest  
<sup>1444</sup> deviation is  $^{+4.8\%}_{-1.0\%}$ . Hence, the total uncertainty on the fiducial cross section amounts  
<sup>1445</sup>  $^{+5.0\%}_{-1.8\%}$ .

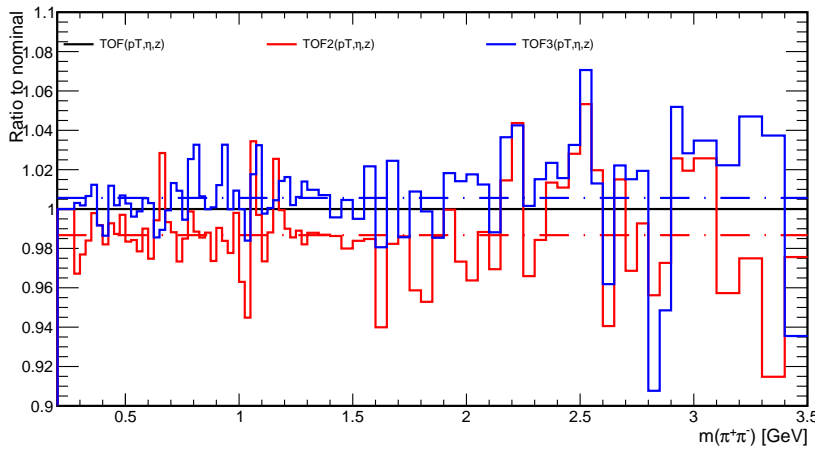


Figure 7.3: A comparison of different results obtained by variation of the TOF efficiency corrections application on the fiducial differential exclusive  $\pi^+\pi^-$  production cross section as a function of the invariant mass of  $\pi^+\pi^-$ . Dot-dashed horizontal lines represent an average ratio for a modified cut shown in the same color.

## <sup>1446</sup> 7.5 TPC vertex reconstruction

<sup>1447</sup> The systematic uncertainty is determined by varying the good primary vertex criteria  
<sup>1448</sup> ( $DCA_{xy}$  and  $DCA_z$ ) and applying the TPC vertex reconstruction efficiency correc-  
<sup>1449</sup> tions corresponding to the given set of vertex criteria. The nominal criteria are defined  
<sup>1450</sup> in [Sec. 3.4](#) and are of  $DCA_{xy} < 1.5$  cm and  $DCA_z < 1.0$  cm. The values are varied  
<sup>1451</sup> to obtain four addition sets:  $DCA_z$  loose ( $DCA_z < 1.5$ ),  $DCA_z$  tight ( $DCA_z < 0.8$ ),  
<sup>1452</sup>  $DCA_{xy}$  loose ( $DCA_{xy} < 2.0$ ), and  $DCA_{xy}$  tight ( $DCA_{xy} < 1.25$ ). The efficiency corre-  
<sup>1453</sup> tion is calculated for each set as described in [Sec. 6.4](#). There are 24252, 23033, 23758,  
<sup>1454</sup> and 23274 out of 26496 good vertices resolving in the efficiency corrections of 91.5%,  
<sup>1455</sup> 86.9%, 89.7%, and 87.8%, respectively. The obtained cross sections are compared with  
<sup>1456</sup> the nominal cross sections in [Fig. 7.4](#). The uncertainty in the fiducial differential cross  
<sup>1457</sup> section is calculated as the average difference for loose and tight sets separately and it

$_{1458}$  is  $^{+2.6\%}_{-1.0\%}$ .

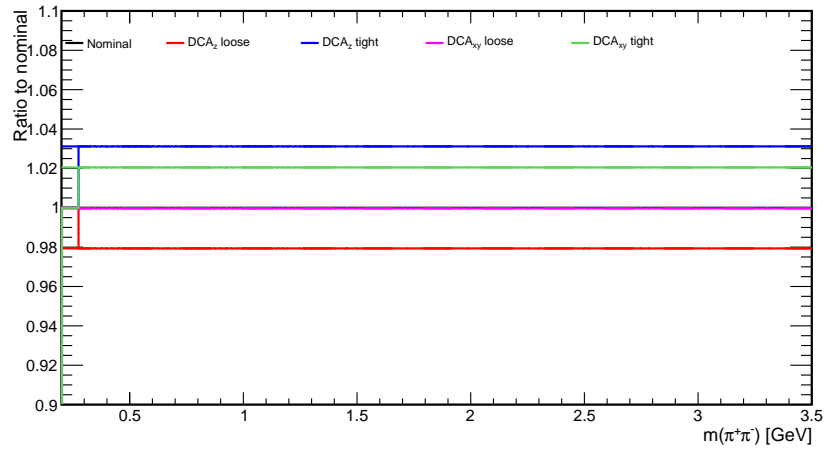


Figure 7.4: A comparison of different results obtained by variation of the TPC vertex quality cuts on the fiducial differential exclusive  $\pi^+\pi^-$  production cross section as a function of the invariant mass of  $\pi^+\pi^-$ .

1459

# Chapter 8

1460

## Results

1461 In this chapter, the results on differential fiducial cross sections and the integrated fidu-  
1462 cial cross sections are presented. The fiducial volume of the measurement is common for  
1463 all the presented results and it is defined in ?? for the protons in the RPs, and depending  
1464 the specific central hadronic state in [Eq. 3.3](#), and Equations [3.10–3.12](#).

1465

### 8.0.1 Differential fiducial cross sections

1466 In this section, differential fiducial cross sections are presented and compared with pre-  
1467 dictions from GRANIIITI [\[18\]](#). GRANIIITI is an MC event generator designed for  
1468 high energy diffraction with focus on the CEP. It combines up-to-date phenomenological  
1469 models and approaches [\[20\]–\[22\]](#). GRANIIITI is the only model that includes a full  
1470 parametric resonant spectrum, continuum production with significant interference ef-  
1471 fects between them. In this analysis, the newest version of GRANIIITI v. 1.090 is used,  
1472 which was tuned to the latest STAR CEP results at  $\sqrt{s} = 200$  GeV **Graniitti2023**, [\[1\]](#).

1473 [Fig. 8.1](#) shows the differential fiducial cross sections for CEP of  $\pi^+\pi^-$ ,  $K^+K^-$ , and  
1474  $p\bar{p}$  pairs as a function of the difference between azimuthal angles of the forward protons  
1475  $\Delta\varphi$ . Strong suppression close to  $\Delta\varphi = 90^\circ$  is due to the limited azimuthal acceptance in  
1476 RP detector system. The acceptance naturally divides the phase space into two ranges of  
1477  $\Delta\varphi$ , where different IPomeron dynamics and absorption effects are expected. Therefore,  
1478 GRANIIITI predictions were produced separately for each  $\Delta\varphi$  region:  $\Delta\varphi > 90^\circ$  and  
1479  $\Delta\varphi < 90^\circ$ .

1480 GRANIIITI predictions are calculated including both continuum (Cont.) and reso-  
1481 nance (Res.) contributions. The resonances used in the model are summarized in [Tab. 8.1](#).  
1482 Subsequently, the predictions are scaled to match the integrated cross section in each  
1483  $\Delta\varphi$  region. If the scaling is within 10% no scaling is applied. Moreover, the pure contin-  
1484 uum is shown without scaling applied for  $\pi^+\pi^-$  and  $K^+K^-$  pairs and with scaling for  
1485  $p\bar{p}$  pairs. The hadron pairs are smeared based on the  $p_T$  resolution and the same fiducial  
1486 criteria on forward protons and central hadron as described in [chapter 3](#) are applied.

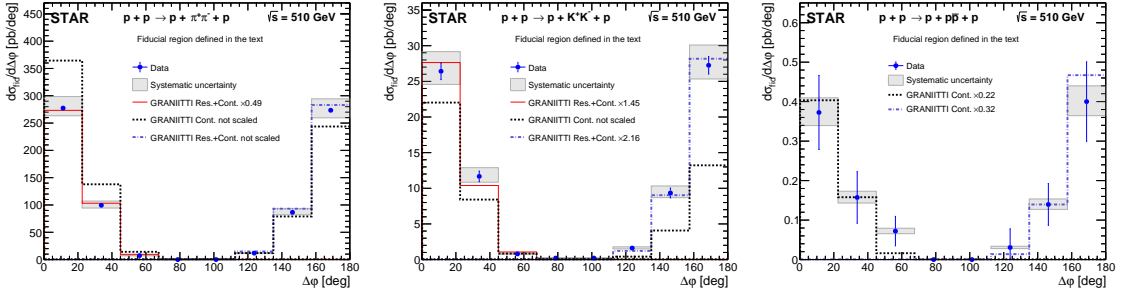


Figure 8.1: Differential fiducial cross sections of  $\pi^+\pi^-$  (left),  $K^+K^-$  (middle) and  $p\bar{p}$  (right) pairs as a function  $\Delta\varphi$  of the forward scattered protons measured in the fiducial volume explained in the text. Data are shown as solid blue points with error bars representing the statistical uncertainties. The systematic uncertainties are shown as gray boxes. The scale uncertainty on the vertical axis due to the effective integrated luminosity is 6.4% and is not shown. Predictions from MC model GRANITTI are shown separately for each  $\Delta\varphi$  region along with the normalization factor.

Particle species	$\Delta\varphi < 90^\circ$ and $\Delta\varphi > 90^\circ$
$\pi^+\pi^-$	$f_0(980)$ , $f_2(1270)$ , and $f_0(1710)$
$K^+K^-$	$f_0(980)$ , $f_0(1500)$ , $f_2(1525)$ , and $f_0(1710)$
$p\bar{p}$	only continuum

Table 8.1: The summary of resonances used in the calculation of GRANITTI predictions for CEP of  $\pi^+\pi^-$ ,  $K^+K^-$ , and  $p\bar{p}$  pairs in two regions of the difference in azimuthal angles  $\Delta\varphi$  of the forward scattered protons:  $\Delta\varphi > 90^\circ$  and  $\Delta\varphi < 90^\circ$ .

1487     Fig. 8.2 shows differential fiducial cross sections of  $\pi^+\pi^-$ ,  $K^+K^-$ , and  $p\bar{p}$  pairs as a  
1488     function of the invariant mass of the pair in two  $\Delta\varphi$  regions measured within the STAR  
1489     acceptance in proton-proton collisions at  $\sqrt{s} = 510$  GeV. GRANITTI predictions are  
1490     shown as well.

1491     In the  $\pi^+\pi^-$  invariant mass distribution in both  $\Delta\varphi$  regions, expected features seen  
1492     in previous CEP [1], [32], [33] and central production [34] measurements are observed: a  
1493     sharp drop at about 1 GeV attributed to the quantum mechanical negative interference  
1494     of  $f_0(980)$  with the continuum contribution, and a peak consistent with the  $f_2(1270)$ . A  
1495     clear difference between the two  $\Delta\varphi$  regions can be seen. In  $\Delta\varphi < 90^\circ$ , an enhancement  
1496     at low invariant mass and a suppression of  $f_2(1270)$  are observed. Above  $m(\pi^+\pi^-) > 1.5$   
1497     GeV, there are no significant structures in the cross section, which generally decreases  
1498     with increasing invariant mass. Evidence of structures at 1.7 and 1.9 GeV in  $\Delta\varphi < 90^\circ$   
1499     can be seen. The first one can be attributed to  $f_0(1710)$  resonance that was considered as  
1500     a “pure” glueball candidate [35]. Moreover, there is no peak around the mass  $m(\pi^+\pi^-) \sim$   
1501     0.8 GeV that could be attributed to the  $\rho(770)$  meson. Hence, the contributions from  
1502     photoproduction and Reggeons exchanges should be insignificant.

1503     Although GRANITTI had to be scaled to match the data, the shape with the main  
1504     features is described quite well. There are few differences: the higher cross section above

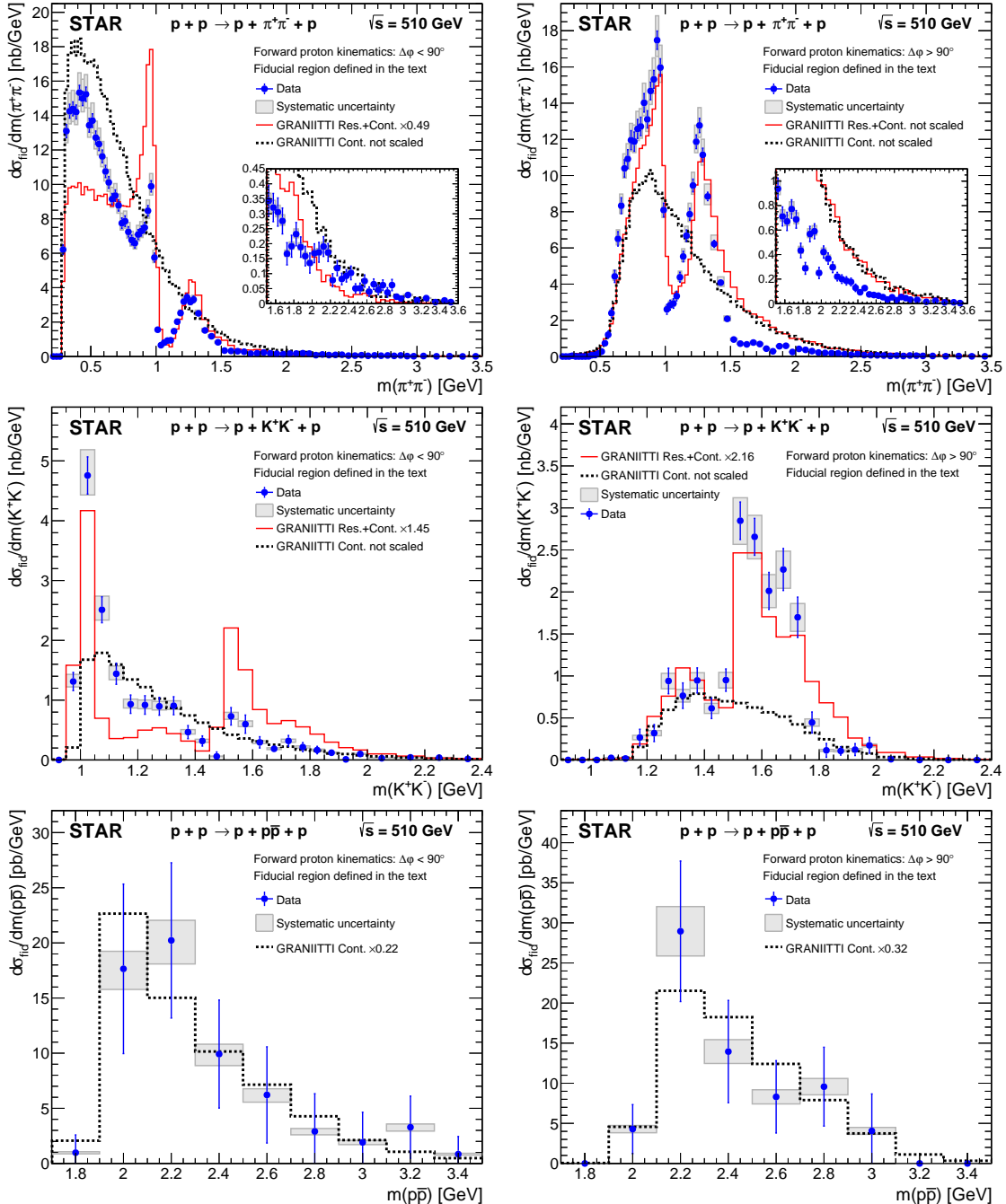


Figure 8.2: Differential fiducial cross sections of  $\pi^+\pi^-$  (top),  $K^+K^-$  (middle), and  $p\bar{p}$  (bottom) pairs as a function of the invariant mass of the pair in two regions of the difference in azimuthal angles  $\Delta\phi$  of the forward scattered protons:  $\Delta\phi < 90^\circ$  (left) and  $\Delta\phi > 90^\circ$  (right), measured in the fiducial volume explained in the text. Data are shown as solid blue points with error bars representing the statistical uncertainties. The systematic uncertainties are shown as gray boxes. The scale uncertainty on the vertical axis due to the effective integrated luminosity is 6.4% and is not shown. Predictions from MC model GRANITI are shown separately for each  $\Delta\phi$  region along with the normalization factor.

1505     $m(\pi^+\pi^-) > 1.5$  GeV in  $\Delta\varphi > 90^\circ$  and more pronounced  $f_0(980)$  resonance in  $\Delta\varphi < 90^\circ$ .  
 1506    Also, the enhancement at the invariant mass at about 500 MeV could be attributed to  
 1507    the  $f_0(500)$  resonance. However, that contribution to the mass spectrum would have to  
 1508    be tuned in GRANIIITI.

1509    In the invariant mass of  $K^+K^-$  pairs, a strong dependence of differential fiducial cross  
 1510    sections on the azimuthal separation between forward protons ( $\Delta\varphi < 90^\circ, \Delta\varphi > 90^\circ$ )  
 1511    is observed. In particular, a strong enhancement at low invariant mass in  $\Delta\varphi < 90^\circ$ .  
 1512    Based on the comparison with GRANIIITI, the enhancement is attributed solely to the  
 1513     $f_0(980)$  resonance contribution.

1514    This is the first observation of  $f_0(980)$  production in  $K^+K^-$  channel. This is be-  
 1515    cause the experimental setup allows for the detection of states close to the production  
 1516    threshold, particularly in the region of large transverse momentum. The next possible  
 1517    resonance would be  $\varphi(1020)$  meson produced via the photoproduction process. How-  
 1518    ever, the contribution from this process is not significant as in the earlier conclusion that  
 1519    photoproduction and Reggeon exchanges are not significant in  $\pi^+\pi^-$  channel.

1520    For  $\Delta\varphi > 90^\circ$ , two structures are seen at about 1.3 and 1.5 GeV. In GRANIIITI, the  
 1521    broad structure around 1.3 GeV is due to the acceptance cut off of the  $K^+K^-$  continuum  
 1522    invariant mass distribution at the lower masses, while the peak at  $\sim 1.5$  GeV can be  
 1523    explained by  $f_0(1500), f_2(1525)$ . There is also a possible peak at  $\sim 1.7$  GeV, which  
 1524    could be due to  $f_0(1710)$  resonance. Also a possible enhancement at  $m(K^+K^-) \sim 1.975$   
 1525    GeV is seen.

1526    For  $\Delta\varphi < 90^\circ$ , peaks at the 1 GeV and 1.5 GeV are seen. They correspond to  
 1527     $f_0(980)$  and ( $f_0(1500), f_2(1525)$ ) resonances. Also, a dip at  $m(K^+K^-) \lesssim 1.5$  GeV. The  
 1528    dip can be explained as due the negative interference of  $f_0(1500)$  with the continuum  
 1529    production. Also, an enhancement corresponding to  $f_0(1710)$  is seen.

1530    Data do not support the presence of the  $f_2(1270)$  resonance and GRANIIITI repro-  
 1531    duces the invariant mass spectrum quite well without the  $f_2(1270)$ .

1532    The differential fiducial cross sections of  $p\bar{p}$  pairs do not show any significant reso-  
 1533    nances or any notable  $\Delta\varphi$  asymmetry except for a possible dip at  $m(p\bar{p}) \sim 3.0$  GeV  
 1534    for  $\Delta\varphi < 90^\circ$ . Hence, it is compared with the GRANIIITI predictions based solely on  
 1535    continuum contributions. An enhancement at the level of  $1\sigma$  at  $m(p\bar{p}) \sim 2.2$  GeV for  
 1536     $\Delta\varphi > 90^\circ$  is seen. It was also observed at the same level at  $\sqrt{s} = 200$  GeV [1].

1537    Fig. 8.3 shows differential fiducial cross sections of  $\pi^+\pi^-$ ,  $K^+K^-$ , and  $p\bar{p}$  pairs as a  
 1538    function of the pair rapidity in two  $\Delta\varphi$  regions. The GRANIIITI predictions are shown  
 1539    as well with the same scaling as in the invariant mass distributions. In general, the  
 1540    shapes of the measured distributions are well described by the GRANIIITI predictions  
 1541    and show the same behavior as at  $\sqrt{s} = 200$  GeV [1].

1542    Fig. 8.4 shows differential fiducial cross sections of  $\pi^+\pi^-$ ,  $K^+K^-$ , and  $p\bar{p}$  pairs as a  
 1543    function of the absolute value of the sum of the squares of the four-momentum transfer

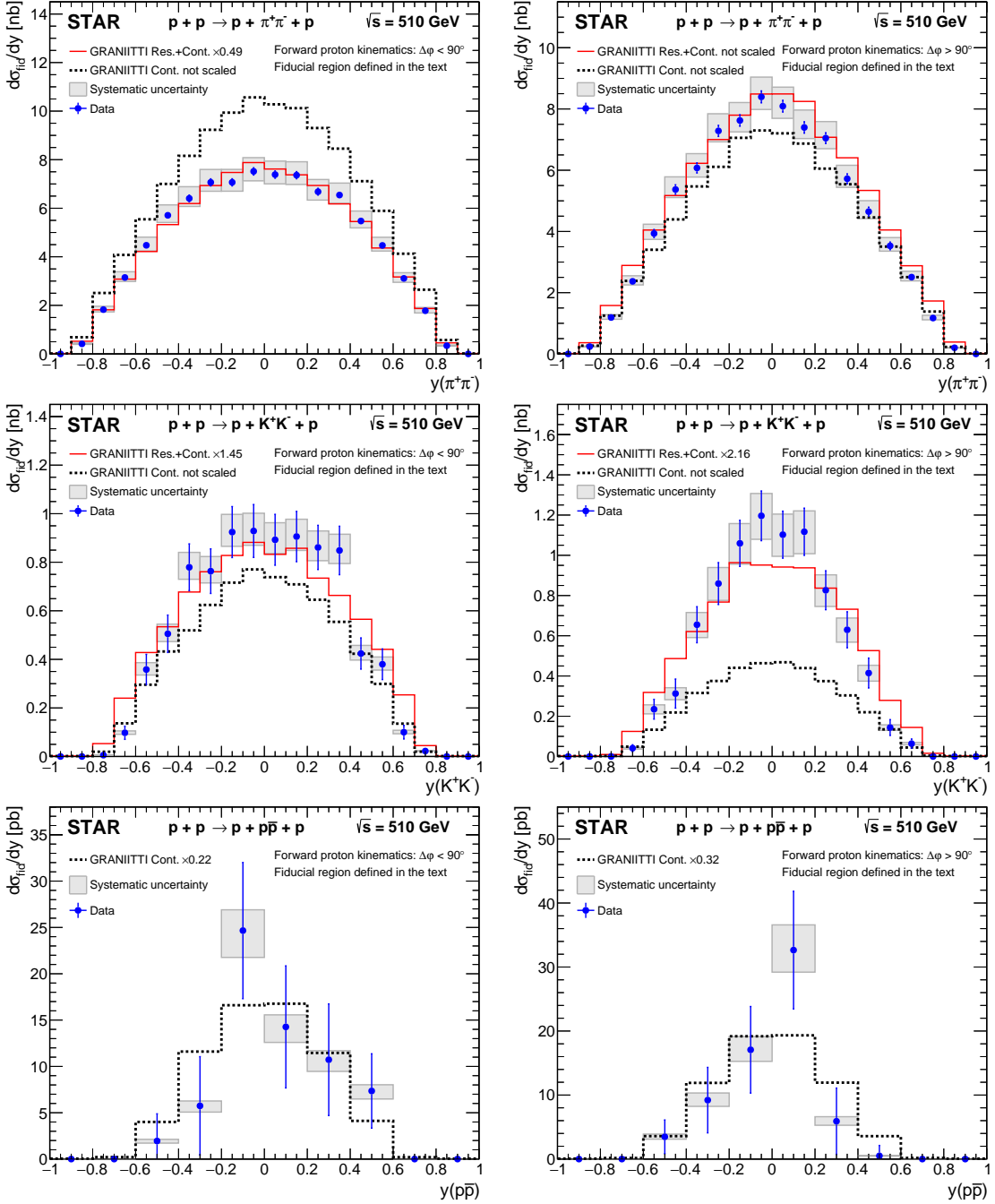


Figure 8.3: Differential fiducial cross sections of  $\pi^+\pi^-$  (top),  $K^+K^-$  (middle), and  $p\bar{p}$  (bottom) pairs as a function of the pair rapidity in two regions of the difference in azimuthal angles  $\Delta\phi$  of the forward scattered protons:  $\Delta\phi < 90^\circ$  (left) and  $\Delta\phi > 90^\circ$  (right), measured in the fiducial volume explained in the text. Data are shown as solid blue points with error bars representing the statistical uncertainties. The systematic uncertainties are shown as gray boxes. The scale uncertainty on the vertical axis due to the effective integrated luminosity is 6.4% and is not shown. Predictions from MC model GRANITTI are shown separately for each  $\Delta\phi$  region along with the normalization factor.

of the forward protons ( $|t_1 + t_2|$ ) in two  $\Delta\varphi$  regions. GRANIIITI predictions are shown as well. The same scaling as in the invariant mass distributions is applied. The shapes of the measured distributions are strongly affected by the fiducial cuts applied to the forward scattered protons. In general, the shapes are well described by the GRANIIITI predictions in  $\Delta\varphi < 90^\circ$  while the distributions in  $\Delta\varphi > 90^\circ$  are slightly shifted to the higher values. The shapes are similar to those observed at  $\sqrt{s} = 200$  GeV [1].

The large statistics of the  $\pi^+\pi^-$  sample enables a more detailed study. The differential fiducial cross sections are studied in three characteristic ranges of the invariant mass of the pair:  $m(\pi^+\pi^-) < 1$  GeV,  $1 \text{ GeV} < m(\pi^+\pi^-) < 1.5$  GeV and  $m(\pi^+\pi^-) > 1.5$  GeV. The first region is considered to be dominant by continuum production. The second is dominant by resonant production, namely by  $f_2(1270)$ .

[Fig. 8.5](#) shows differential fiducial cross sections of  $\pi^+\pi^-$  pairs as a function of the difference in azimuthal angles ( $\Delta\varphi$ ) of the forward scattered protons in three ranges of the  $\pi^+\pi^-$  pair invariant mass. GRANIIITI predictions are shown as well. The strong suppression close to  $\Delta\varphi = 90^\circ$  is due to the limited azimuthal acceptance in RP detector system. The differential fiducial cross sections in  $\Delta\varphi > 90^\circ$  in the first range of the  $\pi^+\pi^-$  pair invariant mass is suppressed due to the to the STAR TPC acceptance. The same suppression was observed also at  $\sqrt{s} = 200$  GeV [1]. In the other ranges, suppressions of differential fiducial cross sections in  $\Delta\varphi < 90^\circ$  are seen. The suppression in the middle range was also seen at  $\sqrt{s} = 200$  GeV [1] and is also predicted by GRANIIITI calculations assuming only continuum contribution. In the last range, the GRANIIITI predicts the same asymmetry as seen in the data.

[Fig. 8.6](#) shows differential fiducial cross sections of hadron  $\pi^+\pi^-$  pairs as a function of the pair rapidity in three ranges of the  $\pi^+\pi^-$  pair invariant mass and in two  $\Delta\varphi$  regions. GRANIIITI predictions are shown as well. The GRANIIITI predictions describe well the shapes of measured differential fiducial cross sections in both  $\Delta\varphi$  regions and in all three ranges of the  $\pi^+\pi^-$  pair invariant mass. The measured shapes are similar to those observed at  $\sqrt{s} = 200$  GeV [1].

[Fig. 8.7](#) shows differential fiducial cross sections of  $\pi^+\pi^-$  pairs as a function of  $|t_1 + t_2|$  in three ranges of the  $\pi^+\pi^-$  pair invariant mass and in two  $\Delta\varphi$  regions. GRANIIITI predictions are shown as well. The GRANIIITI predictions describe well the shapes of measured differential fiducial cross sections in  $\Delta\varphi < 90^\circ$  in all three ranges of the  $\pi^+\pi^-$  pair invariant mass. In  $\Delta\varphi > 90^\circ$ , the GRANIIITI prediction matches the data only for the higher invariant masses while the predictions are shifted to the higher values of  $|t_1 + t_2|$  for the first two ranges. The measured shapes are comparable to those observed at  $\sqrt{s} = 200$  GeV [1]. The higher range of  $|t_1 + t_2|$  is due to higher momentum of the forward protons compared to that at  $\sqrt{s} = 200$  GeV [1].

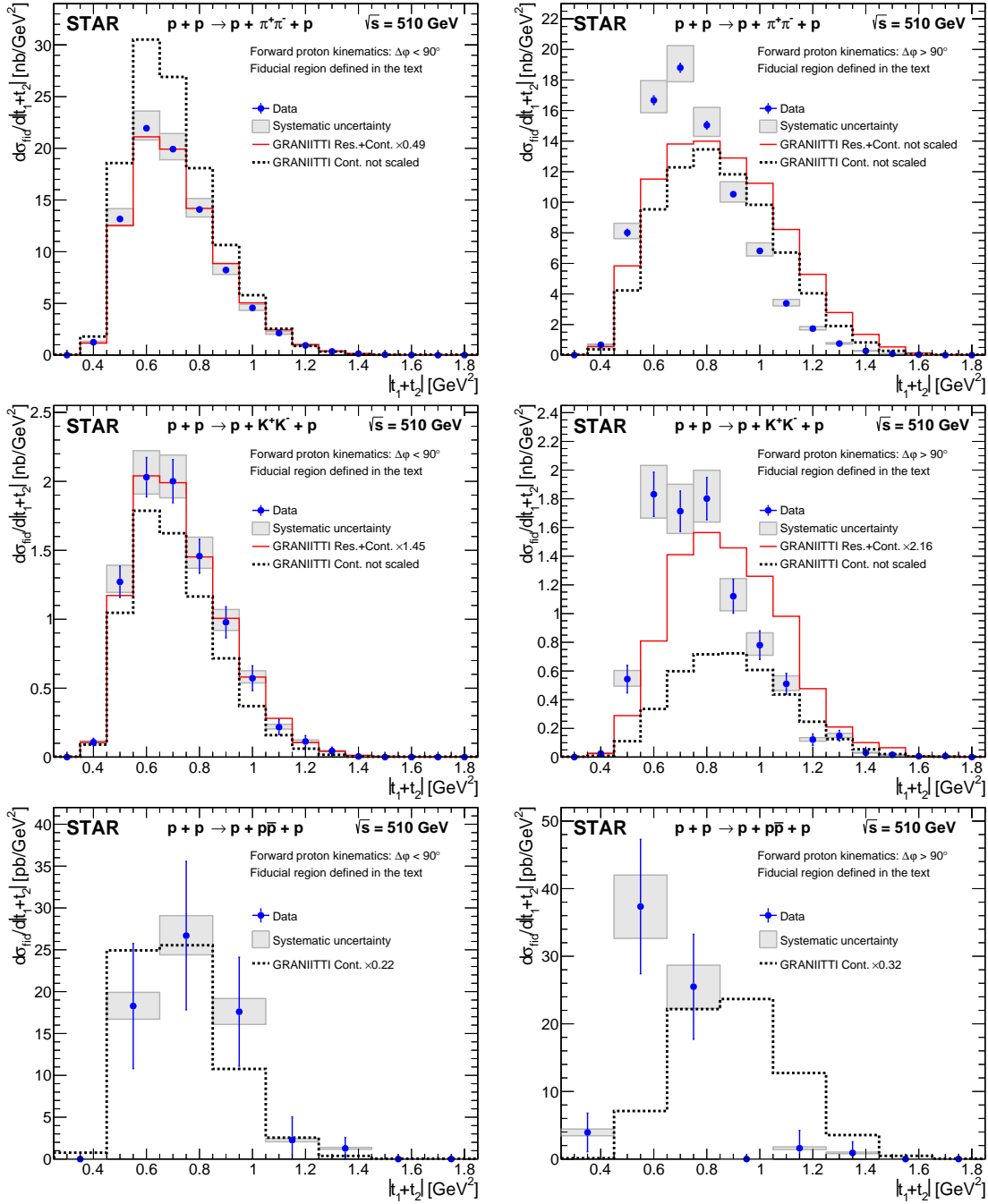


Figure 8.4: Differential fiducial cross sections for CEP of  $\pi^+\pi^-$  (top),  $K^+K^-$  (middle), and  $p\bar{p}$  (bottom) pairs as a function of the absolute value of the sum of the squares of the four-momentum transfer of the forward protons in two regions of the difference in azimuthal angles  $\Delta\phi$  of the forward scattered protons:  $\Delta\phi < 90^\circ$  (left) and  $\Delta\phi > 90^\circ$  (right), measured in the fiducial volume explained in the text. Data are shown as solid blue points with error bars representing the statistical uncertainties. The systematic uncertainties are shown as gray boxes. The scale uncertainty on the vertical axis due to the effective integrated luminosity is 6.4% and is not shown. Predictions from MC model GRANITTI are shown separately for each  $\Delta\phi$  region along with the normalization factor.

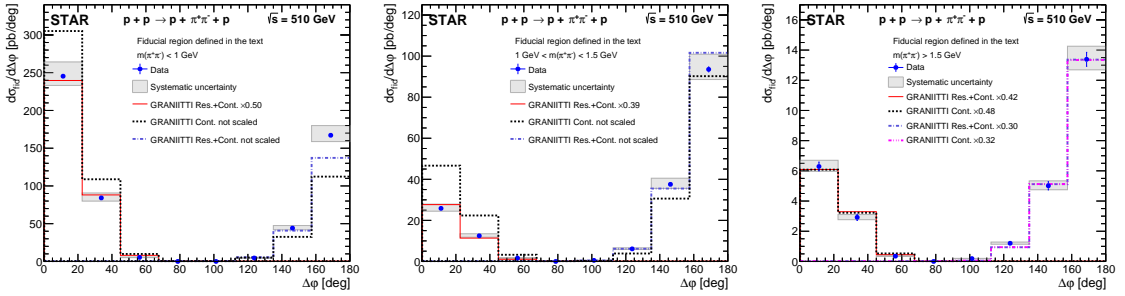


Figure 8.5: Differential fiducial cross sections of  $\pi^+\pi^-$  pairs as a function of the difference in azimuthal angles  $\Delta\varphi$  of the forward scattered protons in three ranges of the  $\pi^+\pi^-$  pair invariant mass:  $m(\pi^+\pi^-) < 1 \text{ GeV}$  (left),  $1 \text{ GeV} < m(\pi^+\pi^-) < 1.5 \text{ GeV}$  (middle) and  $m(\pi^+\pi^-) > 1.5 \text{ GeV}$  (right), measured in the fiducial volume explained in the text. Data are shown as solid blue points with error bars representing the statistical uncertainties. The systematic uncertainties are shown as gray boxes. The scale uncertainty on the vertical axis due to the effective integrated luminosity is 6.4% and is not shown. Predictions from MC model GRANITTI are shown separately for each  $\Delta\varphi$  region along with the normalization factor.

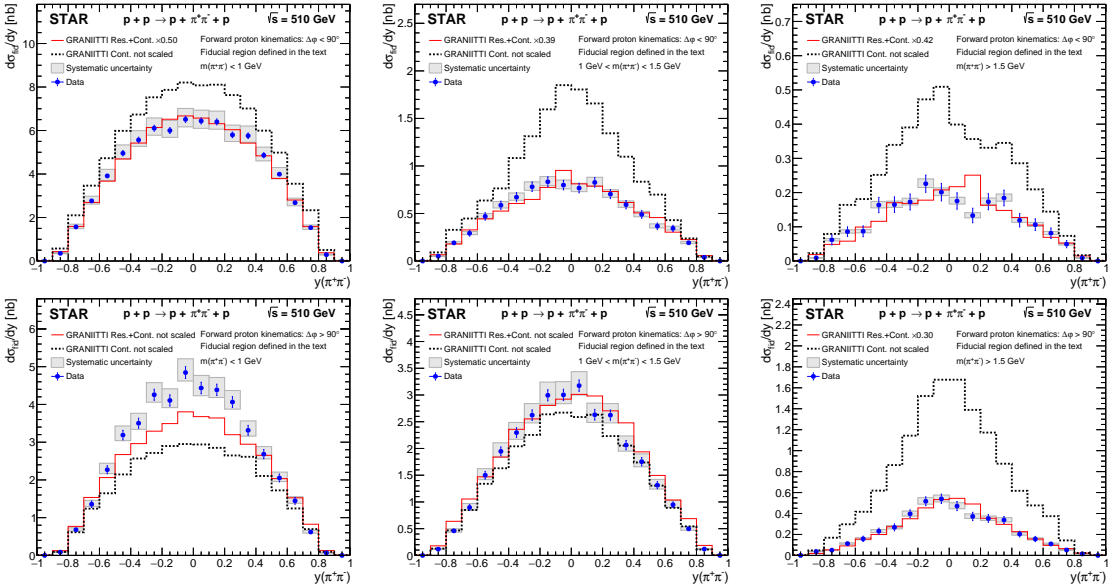


Figure 8.6: Differential fiducial cross sections of  $\pi^+\pi^-$  pairs as a function of the pair rapidity in three ranges of the  $\pi^+\pi^-$  pair invariant mass:  $m(\pi^+\pi^-) < 1 \text{ GeV}$  (left),  $1 \text{ GeV} < m(\pi^+\pi^-) < 1.5 \text{ GeV}$  (middle) and  $m(\pi^+\pi^-) > 1.5 \text{ GeV}$  (right) and into two regions of the difference in azimuthal angles  $\Delta\varphi$  of the forward scattered protons:  $\Delta\varphi < 90^\circ$  (top) and  $\Delta\varphi > 90^\circ$  (bottom), measured in the fiducial volume explained in the text. Data are shown as solid blue points with error bars representing the statistical uncertainties. The systematic uncertainties are shown as gray boxes. The scale uncertainty on the vertical axis due to the effective integrated luminosity is 6.4% and is not shown. Predictions from MC model GRANITTI are shown separately for each  $\Delta\varphi$  region along with the normalization factor.

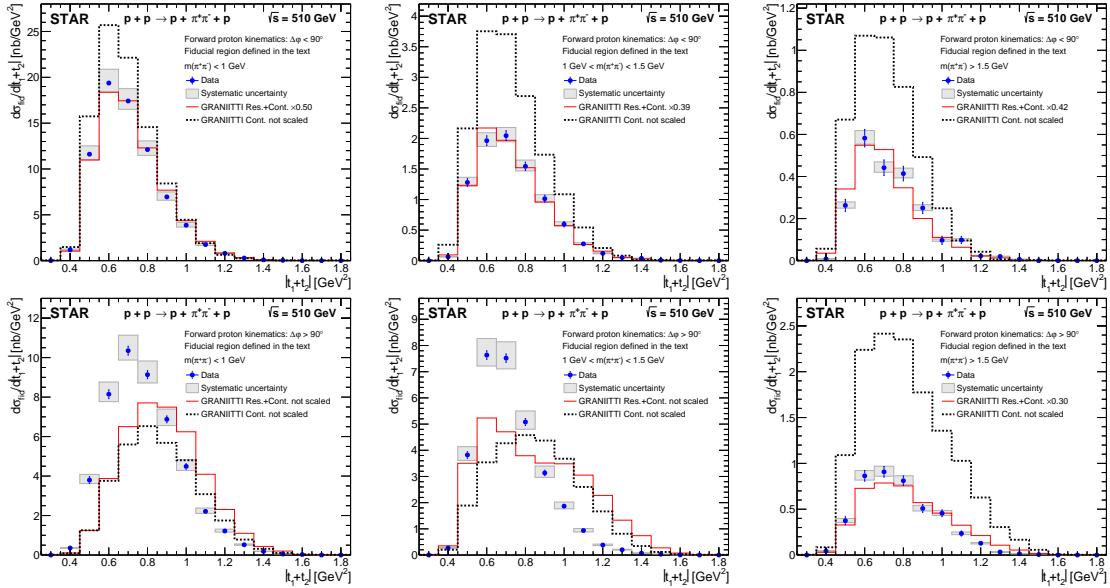


Figure 8.7: Differential fiducial cross sections of  $\pi^+\pi^-$  pairs as a function of the absolute value of the sum of the squares of the four-momentum transfer of the forward protons in three ranges of the  $\pi^+\pi^-$  pair invariant mass:  $m(\pi^+\pi^-) < 1$  GeV (left),  $1 \text{ GeV} < m(\pi^+\pi^-) < 1.5 \text{ GeV}$  (middle) and  $m(\pi^+\pi^-) > 1.5 \text{ GeV}$  (right) and into two regions of the difference in azimuthal angles  $\Delta\phi$  of the forward scattered protons:  $\Delta\phi < 90^\circ$  (top) and  $\Delta\phi > 90^\circ$  (bottom), measured in the fiducial volume explained in the text. Data are shown as solid blue points with error bars representing the statistical uncertainties. The systematic uncertainties are shown as gray boxes. The scale uncertainty on the vertical axis due to the effective integrated luminosity is 6.4% and is not shown. Predictions from MC model GRANITI are shown separately for each  $\Delta\phi$  region along with the normalization factor.

<sup>1581</sup> **8.0.2 Integrated fiducial cross sections**

<sup>1582</sup> The integrated fiducial cross sections of  $\pi^+\pi^-$ ,  $K^+K^-$ , and  $p\bar{p}$  pairs, measured in the  
<sup>1583</sup> fiducial volume explained in the text above, are calculated separately for two regions of  
<sup>1584</sup> the difference in azimuthal angles  $\Delta\varphi$  of the forward scattered protons:  $\Delta\varphi > 90^\circ$  and  
<sup>1585</sup>  $\Delta\varphi < 90^\circ$ . The results are presented in Tab. 8.2.

Particle species	Unit	$\sigma_{\text{fid}} \pm \delta_{\text{stat}} \pm \delta_{\text{syst}}$	
		$\Delta\varphi < 90^\circ$	$\Delta\varphi > 90^\circ$
$\pi^+\pi^-$	nb	$8.68 \pm 0.04^{+0.64}_{-0.43}$	$8.42 \pm 0.04^{+0.64}_{-0.41}$
$K^+K^-$	pb	$879 \pm 27^{+78}_{-57}$	$868 \pm 28^{+81}_{-84}$
$p\bar{p}$	pb	$13.9 \pm 1.4^{+0.8}_{-1.3}$	$14.4 \pm 1.5^{+1.1}_{-1.1}$

Table 8.2: Integrated fiducial cross sections for CEP of  $\pi^+\pi^-$ ,  $K^+K^-$ , and  $p\bar{p}$  pairs measured in the fiducial volume explained in the text. Integrated cross sections are presented into two regions of the difference in azimuthal angles  $\Delta\varphi$  of the forward scattered protons:  $\Delta\varphi > 90^\circ$  and  $\Delta\varphi < 90^\circ$ . Statistical and systematic uncertainties are provided for each cross section.

# Appendices



<sub>1587</sub> **Appendix A**

<sub>1588</sub> **The m<sub>TOF</sub><sup>2</sup> method**

<sub>1589</sub> The  $m_{\text{TOF}}^2$  method is a substitute for the standard TOF method to extend the PID  
<sub>1590</sub> capabilities of the  $\langle dE/dx \rangle$  method of TPC. The standard TOF method is based on the  
<sub>1591</sub> inverse velocity of the particles  $1/\beta$  that cannot be calculated in CEP events due to the  
<sub>1592</sub> lack of the starting time of the collision  $t_0$ .

<sub>1593</sub> The  $m_{\text{TOF}}^2$  method assumes that both central tracks, originating from the same  
<sub>1594</sub> vertex, are of the same type. This is a natural expectation for CEP events. The scheme  
<sub>1595</sub> of the method is shown in Fig. A.1, where  $L_{1,2}$  is the length of the track and  $t_{1,2}$  is the  
<sub>1596</sub> time of track detection in TOF. Using  $L_{1,2}$ ,  $t_{1,2}$  and the momenta of the particles  $p_{1,2}$ ,  
<sub>1597</sub> one can calculate the squared mass  $m_{\text{TOF}}^2$ .

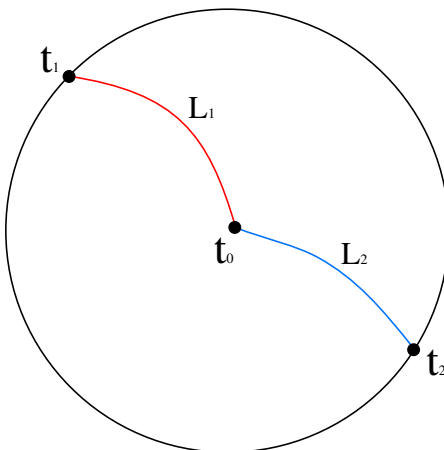


Figure A.1: An illustration of the  $m_{\text{TOF}}^2$  method. The black circle represents the TOF system and the blue and red curves depict two central tracks produced in the same vertex.  $L_1$  and  $L_2$  are lengths of the first and the second tracks, respectively.  $t_0$  is the time of the collisions and  $t_{1,2}$  are times, when the first and the second particles are detected in the TOF system, respectively.

1598 The following equations can be written based on the Fig. A.1:

$$1599 \quad t_1 - t_0 = L_1 \sqrt{1 + \frac{m_1^2}{p_1^2}} \text{ and } t_2 - t_0 = L_2 \sqrt{1 + \frac{m_2^2}{p_2^2}}. \quad (\text{A.1})$$

1600 To eliminate the unknown time  $t_0$ , the time difference is calculated:

$$1601 \quad \Delta t := t_1 - t_2 = L_1 \sqrt{1 + \frac{m_1^2}{p_1^2}} - L_2 \sqrt{1 + \frac{m_2^2}{p_2^2}}. \quad (\text{A.2})$$

1602 Since particles of the same type are assumed, they also have the same masses  $m_1 =$   
1603  $m_2 = m_{\text{TOF}}$ . Then, a quadratic equation for  $m_{\text{TOF}}^2$  can be written in the following form:

$$1604 \quad \mathcal{A} \cdot (m_{\text{TOF}}^2)^2 + \mathcal{B} \cdot m_{\text{TOF}}^2 + \mathcal{C} = 0, \quad (\text{A.3})$$

1605 where

$$1606 \quad \mathcal{A} = -2 \frac{L_1^2 L_2^2}{p_1^2 p_2^2} + \frac{L_1^4}{p_1^4} + \frac{L_2^4}{p_2^4}, \quad (\text{A.4})$$

$$1607 \quad \mathcal{B} = -2 L_1^2 L_2^2 \left( \frac{1}{p_1^2} + \frac{1}{p_2^2} \right) + 2 \frac{L_1^4}{p_1^4} + 2 \frac{L_2^4}{p_2^4} - 2(\Delta t)^2 \left( \frac{L_1^2}{p_1^2} + \frac{L_2^2}{p_2^2} \right), \quad (\text{A.5})$$

$$1609 \quad \mathcal{C} = (\Delta t)^4 - 2(\Delta t)^2 (L_1^2 + L_2^2) + L_1^4 + L_2^4 - 2 L_1^2 L_2^2. \quad (\text{A.6})$$

1611 Finally,  $m_{\text{TOF}}^2$  can be calculated as:

$$1612 \quad m_{\text{TOF}}^2 = \frac{-B + \sqrt{B^2 - 4AC}}{2A}. \quad (\text{A.7})$$

1613 Only the positive root of the quadratic equation is taken into account since the other  
1614 one has non-physical meaning.

<sup>1615</sup> **Appendix B**

<sup>1616</sup> **Missing pT cut plots**

<sup>1617</sup> Figures for kaons and protons relevant for the efficiency of the  $p_T^{\text{miss}}$  cut discussed  
<sup>1618</sup> in Sec. 6.8 are presented here.

<sup>1619</sup> The distributions of the missing momentum in the  $x$  and  $y$  coordinates for  $K^+K^-$  and  
<sup>1620</sup>  $p\bar{p}$  pairs identified as candidates for CEP events can be seen in Fig. B.1. The distributions  
<sup>1621</sup> are fitted by a Gaussian (signal) and a second degree polynomial (background).

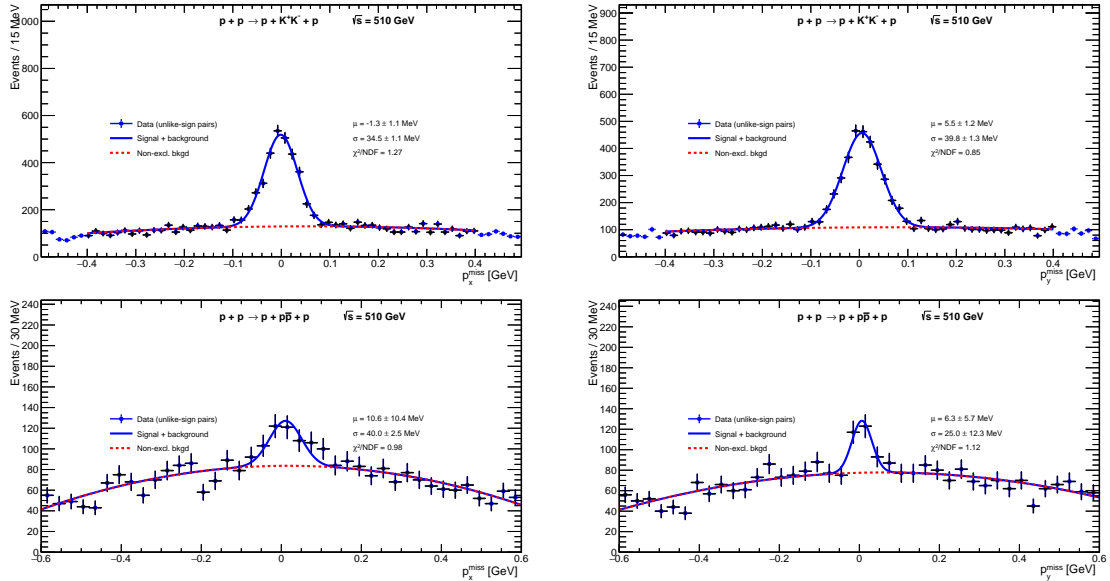


Figure B.1: The distribution of the missing momentum in  $x$  (left) and  $y$  (right) coordinate for  $K^+K^-$  (top) and  $p\bar{p}$  (bottom) CEP event candidates fitted by a Gaussian and second degree polynomial.

<sup>1622</sup> The  $p_T^{\text{miss}}$  distributions are depicted in Fig. B.3.

<sup>1623</sup> The efficiencies, the purity ( $S/(S+B)$ ), and the significance ( $S/\sqrt{S+B}$ ) as a function  
<sup>1624</sup> of the exclusivity cut thresholds can be seen in Fig. B.3.

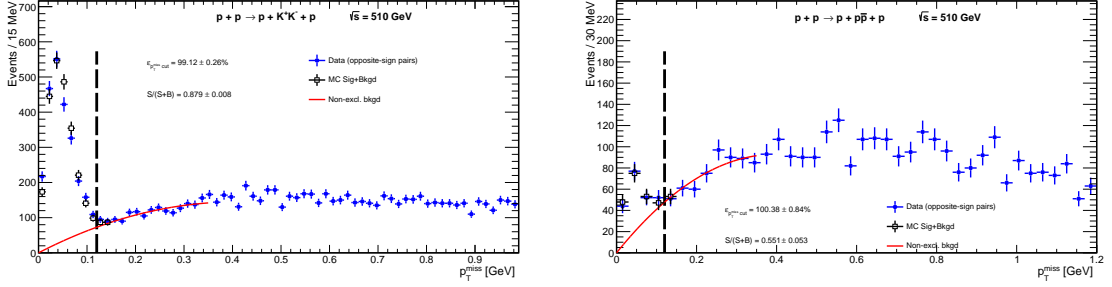


Figure B.2: The distribution of the missing transverse momentum for  $K^+K^-$  (left) and  $p\bar{p}$  (right) CEP event candidates with used exclusivity cut illustrated by the black dot-dashed line.

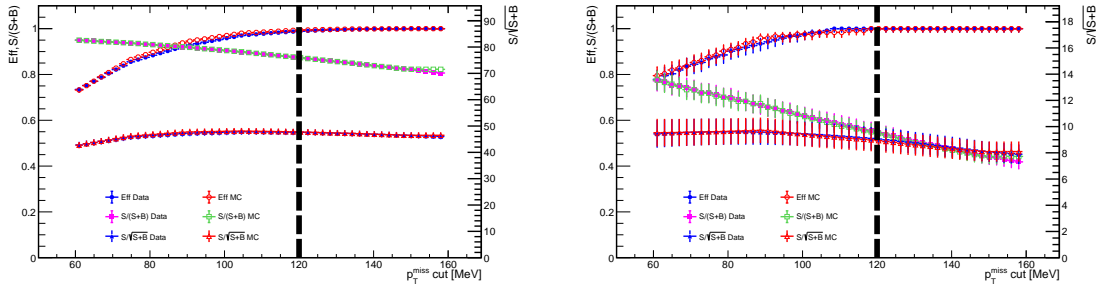


Figure B.3: The distribution of the missing transverse momentum for  $K^+K^-$  (left) and  $p\bar{p}$  (right) CEP event candidates with used exclusivity cut illustrated by the black dot-dashed line.

<sup>1625</sup> **Appendix C**

<sup>1626</sup> **Good run list**

<sup>1627</sup> 18083026, 18083029, 18083030, 18083031, 18083043, 18083047, 18083064, 18083065,  
<sup>1628</sup> 18083066, 18083067, 18083069, 18083070, 18083071, 18083072, 18083073, 18083074,  
<sup>1629</sup> 18083075, 18083077, 18084003, 18084004, 18084005, 18084007, 18084008, 18084009,  
<sup>1630</sup> 18084021, 18084022, 18084023, 18084027, 18084028, 18084029, 18084030, 18084031,  
<sup>1631</sup> 18084032, 18084036, 18084037, 18084038, 18084040, 18084041, 18084042, 18084046,  
<sup>1632</sup> 18084048, 18084049, 18084052, 18084053, 18084054, 18084056, 18084058, 18084059,  
<sup>1633</sup> 18084061, 18084062, 18085001, 18085011, 18085012, 18085013, 18085014, 18085015,  
<sup>1634</sup> 18085017, 18085018, 18085019, 18085020, 18085021, 18085022, 18085023, 18085024,  
<sup>1635</sup> 18085025, 18085026, 18085034, 18085035, 18085037, 18085039, 18085040, 18085041,  
<sup>1636</sup> 18085042, 18085043, 18085044, 18085045, 18085046, 18085047, 18085049, 18085050,  
<sup>1637</sup> 18085051, 18085052, 18085054, 18085055, 18085057, 18085058, 18085060, 18085061,  
<sup>1638</sup> 18086003, 18086004, 18086005, 18086006, 18086015, 18086016, 18086017, 18086021,  
<sup>1639</sup> 18086024, 18086026, 18086027, 18086028, 18086030, 18086033, 18086034, 18086041,  
<sup>1640</sup> 18086052, 18086053, 18086054, 18087003, 18087004, 18087006, 18087007, 18087009,  
<sup>1641</sup> 18087010, 18087011, 18087012, 18087043, 18087044, 18087046, 18087047, 18087048,  
<sup>1642</sup> 18087049, 18087051, 18087052, 18087053, 18087055, 18087056, 18087057, 18087058,  
<sup>1643</sup> 18087059, 18087060, 18087061, 18087062, 18087063, 18087067, 18088002, 18088003,  
<sup>1644</sup> 18088004, 18088005, 18088006, 18088007, 18088016, 18088017, 18088040, 18088041,  
<sup>1645</sup> 18088042, 18089006, 18089007, 18089008, 18089009, 18089010, 18089011, 18089013,  
<sup>1646</sup> 18089014, 18089015, 18089017, 18089018, 18089054, 18089063, 18089065, 18090001,  
<sup>1647</sup> 18090003, 18090004, 18090005, 18090006, 18090007, 18090008, 18090009, 18090010,  
<sup>1648</sup> 18090011, 18090012, 18090013, 18090014, 18090020, 18090021, 18090022, 18090023,  
<sup>1649</sup> 18090024, 18090025, 18090026, 18090047, 18090056, 18090057, 18090060, 18090061,  
<sup>1650</sup> 18090062, 18090063, 18090064, 18090066, 18090071, 18090072, 18090073, 18091002,  
<sup>1651</sup> 18091005, 18091006, 18091007, 18091009, 18091010, 18091011, 18091012, 18091013,  
<sup>1652</sup> 18091014, 18091015, 18091016, 18091017, 18091019, 18091026, 18091027, 18091029,  
<sup>1653</sup> 18091030, 18091031, 18091032, 18091033, 18091034, 18091035, 18091037, 18091038,

---

1654 18091039, 18091047, 18091048, 18091049, 18091050, 18091052, 18091053, 18091054,  
 1655 18091055, 18091056, 18091057, 18092002, 18092006, 18092007, 18092008, 18092015,  
 1656 18092016, 18092017, 18092018, 18092019, 18092020, 18092021, 18092023, 18092024,  
 1657 18092028, 18092054, 18092062, 18092063, 18092064, 18092068, 18092069, 18092070,  
 1658 18092071, 18092072, 18092074, 18092078, 18092079, 18092085, 18092086, 18092100,  
 1659 18092101, 18092102, 18093001, 18093002, 18093003, 18093005, 18093006, 18093008,  
 1660 18093010, 18093011, 18093013, 18093014, 18093015, 18093016, 18093017, 18093023,  
 1661 18093027, 18093028, 18093029, 18093030, 18093031, 18093033, 18093034, 18093035,  
 1662 18093039, 18093041, 18093042, 18095055, 18095056, 18095057, 18095058, 18096001,  
 1663 18096002, 18096003, 18096006, 18096007, 18096009, 18096010, 18096011, 18096012,  
 1664 18096013, 18096014, 18096015, 18097008, 18097009, 18097010, 18097011, 18097012,  
 1665 18097037, 18097038, 18097039, 18097040, 18097041, 18097042, 18097065, 18098001,  
 1666 18098002, 18098008, 18098009, 18098010, 18098011, 18098012, 18098014, 18098015,  
 1667 18098016, 18098020, 18098022, 18098023, 18098028, 18098029, 18098030, 18098031,  
 1668 18098032, 18098033, 18098035, 18098036, 18098037, 18098038, 18098039, 18098040,  
 1669 18098041, 18098042, 18098043, 18098044, 18098048, 18098049, 18098053, 18098054,  
 1670 18098055, 18099003, 18099006, 18099007, 18099010, 18099011, 18099012, 18099013,  
 1671 18099014, 18099015, 18099017, 18099018, 18099019, 18099025, 18099026, 18099027,  
 1672 18099028, 18099031, 18099032, 18099033, 18099034, 18099036, 18099037, 18099038,  
 1673 18099041, 18099042, 18099047, 18100001, 18100002, 18100003, 18100004, 18100008,  
 1674 18100010, 18100011, 18100013, 18100015, 18100017, 18100018, 18100023, 18100025,  
 1675 18100027, 18100029, 18100033, 18100034, 18100044, 18100045, 18100046, 18100048,  
 1676 18100049, 18100050, 18100051, 18100052, 18100054, 18100055, 18100056, 18100057,  
 1677 18100058, 18100059, 18101004, 18101006, 18101007, 18101008, 18101010, 18101012,  
 1678 18101016, 18101017, 18101018, 18101019, 18101020, 18101021, 18101022, 18101027,  
 1679 18101028, 18101029, 18101030, 18101031, 18101032, 18101036, 18101037, 18101038,  
 1680 18101039, 18101040, 18101041, 18101042, 18101043, 18101044, 18101045, 18101046,  
 1681 18101047, 18101057, 18102001, 18102002, 18102003, 18102004, 18102005, 18102007,  
 1682 18102008, 18102010, 18102011, 18102012, 18102013, 18102014, 18102016, 18102017,  
 1683 18102018, 18102021, 18102023, 18103001, 18103003, 18103009, 18103015, 18103017,  
 1684 18103020, 18103021, 18103056, 18103057, 18103058, 18103060, 18104001, 18104002,  
 1685 18104003, 18104004, 18104005, 18104010, 18104011, 18104012, 18104013, 18104014,  
 1686 18104015, 18104016, 18104017, 18104019, 18104020, 18104022, 18104023, 18104025,  
 1687 18104026, 18104027, 18104036, 18104037, 18104038, 18104039, 18104040, 18104041,  
 1688 18104043, 18104044, 18104045, 18104047, 18104048, 18105002, 18105012, 18105013,  
 1689 18105014, 18105015, 18105017, 18105018, 18105019, 18105020, 18105022, 18105023,  
 1690 18105024, 18105028, 18105030, 18105031, 18105040, 18105041, 18105042, 18105044,  
 1691 18105045, 18105046, 18105048, 18105049, 18105051, 18105053, 18105054, 18105055,  
 1692 18105056, 18106009, 18106011, 18106021, 18106023, 18106024, 18106031, 18106032,

1693 18106034, 18106035, 18106038, 18106046, 18106048, 18106056, 18106057, 18106058,  
1694 18106059, 18106065, 18106066, 18106067, 18106069, 18107026, 18107027, 18107028,  
1695 18107031, 18107040, 18107043, 18107044, 18108007, 18108010, 18108020, 18108022,  
1696 18108026, 18108028, 18108031, 18108037, 18108038, 18108039, 18108053, 18108082,  
1697 18108085, 18108087, 18108088, 18108089, 18108090, 18108092, 18108102, 18109001,  
1698 18109008, 18109009, 18109024, 18109025, 18109026, 18109027, 18109032, 18109037,  
1699 18109056, 18109057, 18109058, 18110001, 18110002, 18110004, 18110005, 18110016,  
1700 18110017, 18110018, 18110019, 18110021, 18111006, 18111007, 18111008, 18111009,  
1701 18111010, 18111011, 18111012, 18111013, 18111014, 18111015, 18111016, 18111019,  
1702 18111020, 18111022, 18111032, 18111033, 18111034, 18111035, 18111036, 18111038,  
1703 18111039, 18111040, 18111042, 18111045, 18111050, 18111054, 18111055, 18112001,  
1704 18112002, 18112003, 18112005, 18112006, 18112007, 18112008, 18112009, 18112010,  
1705 18112029, 18112030, 18112031, 18112032, 18112033, 18112034, 18112038, 18112039,  
1706 18112040, 18112041, 18112042, 18112043, 18112048, 18112049, 18113001, 18113002,  
1707 18113003, 18113004, 18113012, 18113013, 18113014, 18113015, 18113016, 18113017,  
1708 18113019, 18113027, 18113028, 18113029, 18113031, 18113032, 18113033, 18113034,  
1709 18113035, 18113037, 18113038, 18113040, 18113041, 18113049, 18113051, 18113052,  
1710 18113053, 18113054, 18113055, 18113057, 18113058, 18113060, 18113061, 18114007,  
1711 18114008, 18114009, 18114010, 18114011, 18114012, 18114052, 18114053, 18114054,  
1712 18114055, 18114056, 18114057, 18114059, 18114060, 18114061, 18115001, 18115002,  
1713 18115003, 18115004, 18115005, 18115006, 18115007, 18115013, 18115014, 18115015,  
1714 18115020, 18115022, 18115023, 18115026, 18115027, 18115028, 18115029, 18116004,  
1715 18116005, 18116036, 18116045, 18116046, 18116047, 18116048, 18117001, 18117002,  
1716 18117003, 18117008, 18117009, 18117010, 18117012, 18117023, 18117024, 18117025,  
1717 18117026, 18117027, 18117028, 18117076, 18117077, 18117078, 18117079, 18118001,  
1718 18118002, 18118004, 18118007, 18118008, 18118009, 18118010, 18118011, 18118016,  
1719 18118017, 18118019, 18118020, 18118021, 18118025, 18118026, 18118027, 18119020,  
1720 18119022, 18119024, 18119026, 18119028, 18119029, 18119044, 18119045, 18119046,  
1721 18119047, 18120001, 18120003, 18120004, 18120006, 18120007, 18120008, 18120009,  
1722 18120010, 18120014, 18120015, 18120017, 18120018, 18120020, 18120030, 18120032,  
1723 18120033, 18120034, 18120035, 18120036, 18120038, 18120039, 18120046, 18120047,  
1724 18120048, 18120051, 18120052, 18120066, 18120068, 18121004, 18121010, 18121011,  
1725 18121012, 18121013, 18121014, 18121015, 18121016, 18121018, 18121020, 18121022,  
1726 18121024, 18121025, 18121028, 18121029, 18121030, 18121031, 18121032, 18121033,  
1727 18122014, 18122025, 18122026, 18122027, 18122028, 18122029, 18122030, 18123004,  
1728 18123005, 18123006, 18123007, 18123011, 18123012, 18123013, 18123014, 18123016,  
1729 18123017, 18123026, 18124016, 18124021, 18124022, 18124023, 18124024, 18124025,  
1730 18124026, 18124027, 18124028, 18125017, 18125025, 18125027, 18125029, 18125030,  
1731 18125031, 18125048, 18125049, 18125050, 18125051, 18125052, 18125053, 18125056,

1732 18125057, 18125058, 18126001, 18126002, 18126003, 18127013, 18127038, 18127039,  
1733 18127041, 18127042, 18127046, 18127048, 18127066, 18127083, 18127086, 18127087,  
1734 18127088, 18127089, 18127090, 18127091, 18128001, 18128002, 18128003, 18128004,  
1735 18128005, 18128006, 18128007, 18128008, 18128009, 18128010, 18128011, 18128012,  
1736 18128018, 18128020, 18128021, 18128022, 18128023, 18128028, 18128029, 18128030,  
1737 18128031, 18128032, 18128033, 18128034, 18128052, 18128053, 18128054, 18128056,  
1738 18128057, 18128058, 18129005, 18129006, 18129007, 18129008, 18129009, 18129013,  
1739 18129014, 18129015, 18129016, 18129017, 18129018, 18129019, 18129036, 18129039,  
1740 18129045, 18129049, 18129050, 18129051, 18129052, 18129053, 18129054, 18129055,  
1741 18129105, 18129107, 18129108, 18129109, 18129110, 18129111, 18129112, 18129113,  
1742 18129114, 18130001, 18130002, 18130003, 18130005, 18130006, 18130007, 18130008,  
1743 18130009, 18130010, 18130011, 18130012, 18130020, 18130021, 18130022, 18130023,  
1744 18130026, 18130028, 18130031, 18130032, 18130035, 18130036, 18130092, 18130094,  
1745 18130095, 18130096, 18130097, 18130098, 18131001, 18131002, 18131003, 18131004,  
1746 18131010, 18131011, 18131012, 18131013, 18131015, 18131016, 18131017, 18131018,  
1747 18131019, 18131020, 18131021, 18131022, 18131095, 18131096, 18131097, 18131098,  
1748 18132011, 18132012, 18132013, 18132022, 18132024, 18132025, 18132026, 18132032,  
1749 18138027, 18138029, 18138030, 18138031, 18138036, 18138037, 18139002, 18139003,  
1750 18139004, 18139005, 18139011, 18139012, 18139017, 18139019, 18139020, 18139021,  
1751 18139022, 18139033, 18139034, 18139035, 18139036, 18139037, 18139038, 18139039,  
1752 18139041, 18139042, 18139043, 18139061, 18139063, 18139064, 18139066, 18139067,  
1753 18140001, 18140002, 18140003, 18140008, 18140010, 18140011, 18140012, 18140019,  
1754 18140020, 18140021, 18140022, 18140023, 18140024, 18140025, 18140027, 18140028,  
1755 18140029, 18140030, 18140034, 18140036, 18140037, 18140039, 18140040, 18140041,  
1756 18140054, 18140055, 18140056, 18140057, 18140058, 18140059, 18140060, 18141001,  
1757 18141002, 18141003, 18141007, 18141008, 18141011, 18141012, 18141013, 18141015,  
1758 18141016, 18141017, 18141019, 18141027, 18141030, 18141031, 18141032, 18141033,  
1759 18141034, 18141035, 18141036, 18141037, 18141038, 18141039, 18141040, 18141041,  
1760 18141042, 18141043, 18141044, 18141045, 18141046, 18141067, 18142001, 18142002,  
1761 18142005, 18142019, 18142020, 18142021, 18142022, 18142023, 18142024, 18142025,  
1762 18142026, 18142027, 18142029, 18142030, 18142031, 18142032, 18142033, 18142036,  
1763 18142037, 18142038, 18142039, 18142040, 18142059, 18142060, 18142066, 18142067,  
1764 18142068, 18142069, 18142082, 18142083, 18143003, 18143005, 18143006, 18143007,  
1765 18143008, 18143009, 18143011, 18143012, 18143032, 18143033, 18143034, 18143035,  
1766 18143036, 18143037, 18143038, 18143039, 18143040, 18143041, 18143042, 18143043,  
1767 18143044, 18143045, 18143046, 18143058, 18144001, 18144002, 18144003, 18144005,  
1768 18144006, 18144007, 18144010, 18144011, 18144012, 18144014, 18144015, 18146003,  
1769 18146004, 18146005, 18146007, 18146008, 18146009, 18146010, 18146011, 18146012,  
1770 18146020, 18146021, 18146022, 18146024, 18146025, 18146026, 18146027, 18146028,

<sub>1771</sub> 18146030, 18146043, 18146045, 18146046, 18146047, 18146048, 18146049, 18147001,  
<sub>1772</sub> 18147002, 18147003, 18147005, 18147006, 18147008, 18147009, 18147010, 18147012,  
<sub>1773</sub> 18147013, 18147014, 18147025, 18147026, 18147035, 18147036, 18147037, 18147038,  
<sub>1774</sub> 18147039, 18147042, 18147043, 18147044, 18147045, 18147046, 18147048, 18147049,  
<sub>1775</sub> 18148002, 18148005, 18148006, 18148008, 18148009, 18148010, 18148011, 18148012,  
<sub>1776</sub> 18148013, 18148014, 18148015, 18148016, 18148017, 18148019, 18148020, 18148022,  
<sub>1777</sub> 18148023, 18148031, 18148032, 18148033, 18148034, 18148035, 18148037, 18148038,  
<sub>1778</sub> 18148039, 18148045, 18148046, 18148047, 18148048



<sub>1779</sub> **Appendix D**

<sub>1780</sub> **Bad run list**

<sub>1781</sub> The run 18097004 is marked as bad because all RP detectors were inactive.

<sub>1782</sub> Following runs are excluded from good run list since their instantaneous luminosities  
<sub>1783</sub> have nonphysical values: 18058012, 18062053, 18062054, 18063034, 18063092, 18063093,  
<sub>1784</sub> 18063094, 18063095, 18063096, 18076016, 18077014, 18083049, 18083053, 18085016,  
<sub>1785</sub> 18086057, 18092030, 18092031, 18092032, 18092033, 18092035, 18092036, 18092038,  
<sub>1786</sub> 18092056, 18092076, 18092087, 18092093, 18093051, 18094009, 18094012, 18094029,  
<sub>1787</sub> 18094033, 18095013, 18106042, 18118022, 18127054, 18127081, 18136026, 18144008.

<sub>1788</sub> Runs strongly deviating from the overall trend of probability of retaining CEP  
<sub>1789</sub> event, Sec. 6.2.4, are also excluded: 18085056, 18087008, 18089012, 18089055, 18090027,  
<sub>1790</sub> 18090058, 18090059, 18090070, 18091003, 18091008, 18091025, 18091028, 18091040,  
<sub>1791</sub> 18091051, 18091058, 18091059, 18092001, 18092022, 18092065, 18093012, 18093024,  
<sub>1792</sub> 18093025, 18093038, 18098017, 18098034, 18099004, 18099005, 18100009, 18100016,  
<sub>1793</sub> 18100053, 18101005, 18101011, 18101033, 18101034, 18102009, 18102024, 18103016,  
<sub>1794</sub> 18103018, 18103023, 18104018, 18104046, 18105021, 18105029, 18105043, 18105047,  
<sub>1795</sub> 18106013, 18106033, 18106044, 18106045, 18106068, 18107042, 18108029, 18108036,  
<sub>1796</sub> 18108083, 18108084, 18108091, 18109002, 18110020, 18111021, 18111041, 18111047,  
<sub>1797</sub> 18111051, 18112037, 18116006, 18118003, 18119021, 18119030, 18119032, 18119055,  
<sub>1798</sub> 18120005, 18120037, 18123025, 18125028, 18127080, 18127084, 18128024, 18128025,  
<sub>1799</sub> 18128035, 18128051, 18128059, 18131094, 18138008, 18138011, 18139001, 18140013,  
<sub>1800</sub> 18140026, 18143001, 18143002, 18147004, 18147007, 18149010, 18084050, 18084051,  
<sub>1801</sub> 18085002, 18085038, 18086022, 18087054, 18091004, 18092025, 18092026, 18093026,  
<sub>1802</sub> 18094005, 18094006, 18094013, 18094016, 18094021, 18094030, 18094036, 18094037,  
<sub>1803</sub> 18094050, 18098007, 18098013, 18098019, 18101035, 18105039, 18106054, 18107030,  
<sub>1804</sub> 18112036, 18120044, 18121008, 18121009, 18121017, 18121023, 18122011, 18122016,  
<sub>1805</sub> 18122017, 18122018, 18122019, 18122020, 18122021, 18122022, 18122023, 18127079,  
<sub>1806</sub> 18129044, 18132042, 18134006, 18134009, 18134047, 18135055, 18136013, 18136042,  
<sub>1807</sub> 18136044, 18136045, 18136046, 18136047, 18136048, 18136050, 18136051, 18137004,

1808 18137005, 18137006, 18147011

1809 The following runs are marked as bad runs due to higher TPC or TOF inefficiency:  
 1810 18119019, 18132061, 18132064, 18132065, 18133001, 18133002, 18133003, 18133004,  
 1811 18133005, 18133006, 18133007, 18133008, 18133009, 18133010, 18133012, 18133017,  
 1812 18133041, 18133042, 18133043, 18133044, 18133045, 18133046, 18133047, 18133048,  
 1813 18133049, 18133050, 18133051, 18134002, 18134003, 18134004, 18134005, 18134012,  
 1814 18134013, 18134014, 18134015, 18134017, 18134019, 18134034, 18134035, 18134037,  
 1815 18134038, 18134040, 18134042, 18134043, 18134044, 18134045, 18134046, 18134048,  
 1816 18134049, 18134050, 18134051, 18135003, 18135004, 18135005, 18135007, 18135008,  
 1817 18135009, 18135010, 18135011, 18135012, 18135013, 18135014, 18135026, 18135027,  
 1818 18135028, 18135031, 18135033, 18135034, 18135035, 18135036, 18135037, 18135038,  
 1819 18135039, 18135050, 18135052, 18135053, 18135054, 18135056, 18135057, 18135059,  
 1820 18135060, 18135061, 18135062, 18135063, 18135064, 18135065, 18136001, 18136002,  
 1821 18136009, 18136010, 18136011, 18136012, 18136014, 18136015, 18136016, 18136017,  
 1822 18136018, 18136019, 18136020, 18136021, 18136022, 18136023, 18136024, 18136034,  
 1823 18136036, 18136037, 18136040, 18136041, 18136049, 18136052, 18137008, 18137009,  
 1824 18137010, 18137011, 18137012, 18137013, 18137014, 18137015, 18137016, 18137017,  
 1825 18137018, 18137019, 18137027, 18137028, 18137029, 18142041, 18092005, 18094011,  
 1826 18094015, 18094019, 18094035, 18094051, 18094052, 18094053, 18094054, 18094057,  
 1827 18094058, 18094059, 18094062, 18094064, 18094065, 18094066, 18094068, 18094069,  
 1828 18094070, 18094076, 18094077, 18094078, 18094079, 18094080, 18095001, 18095002,  
 1829 18095003, 18095004, 18095005, 18095006, 18095007, 18095008, 18095009, 18095010,  
 1830 18095011, 18095012, 18095013, 18095014, 18095017, 18095018, 18095019, 18095022,  
 1831 18095023, 18095024, 18085009, 18106006.

1832 The following runs are marked because the alignment correction could not be calculated for them: 18115016, 18115018, 18115019, 18083048, 18118018, 18119018, 18128055,  
 1833 18129037, 18129038, 18134038, 18134043, 18134044, 18134045, 18134046, 18087013,  
 1834 18087014, 18087015, 18087016, 18087017, 18087018, 18136012, 18087019, 18087020,  
 1835 18087021, 18087022, 18087023, 18137028, 18138004, 18138005, 18138006, 18138007,  
 1836 18138009, 18138010, 18087024, 18138012, 18138013, 18139014, 18140009, 18142041,  
 1837 18088008, 18088009, 18148054, 18148061, 18148062, 18148063, 18148064, 18088010,  
 1838 18148067, 18148068, 18148069, 18149002, 18149003, 18149004, 18149005, 18149006,  
 1839 18149008, 18088011, 18149009, 18149012, 18149019, 18149020, 18149021, 18149022,  
 1840 18088012, 18149025, 18149026, 18149027, 18149028, 18149029, 18149030, 18088013,  
 1841 18088014, 18088015, 18089064, 18091018, 18092003, 18092004, 18092005, 18092014,  
 1842 18092036, 18094015, 18094035, 18094066, 18095007, 18095010, 18095013, 18097044,  
 1843 18097049, 18097051, 18097052, 18097054, 18098006, 18104021, 18085009, 18083045,  
 1844 18106006, 18106008, 18106036, 18107005, 18108006.

1846 Several other runs were excluded from the good run list because there are too short

<sup>1847</sup> runs without any CPT2noBBCL trigger or with too few events: 18083041, 18122040,  
<sup>1848</sup> 18114002, 18094032, 18122039, 18094002, 18133053, 18148007, 18137007, 18089005.



1849 **Appendix E**

1850 **The central embedding validation**

1851 The validation of the central embedding discussed in Sec. 5.1 is described here. For the  
1852 sake of brevity, only the embedding of the  $\pi^+\pi^-$  sample (MCZB) is presented. It is  
1853 compared with the true-level information (TrueMC) and with the CEP sample (Data),  
1854 where they are comparable. For example in Fig. E.1, a comparison of the  $z$ -position of  
1855 the primary vertex for CEP event candidates and of the true-level position of the vertex  
1856 in the embedding is shown. However, the vertex is not reconstructed in the embedding,  
1857 since only the global tracks are studied. Therefore, only the true level and the data  
1858 information is presented. On the other hand, some information is not accessible on the  
1859 true level, e.g.  $N_{\text{hits}}^{\langle dE/dx \rangle}$  is accessible only for reconstructed tracks. The same criteria as  
1860 in the main analysis described in chapter 3 are used when applicable.

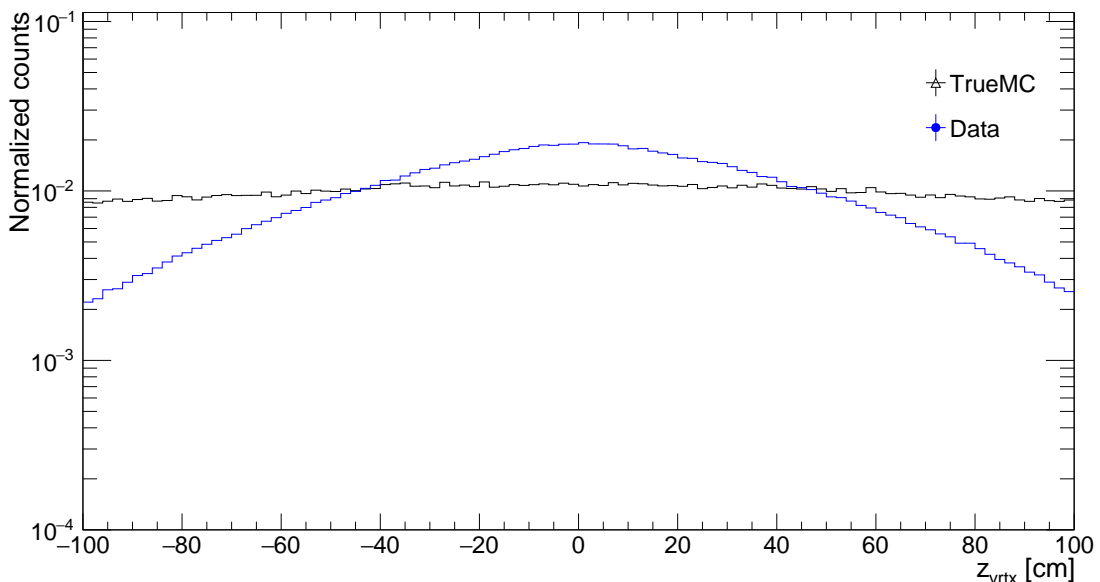


Figure E.1: A comparison of the  $z$ -position of the primary vertex for CEP event candidates (Data) and of the true-level position of the vertex in the embedding (TrueMC).

1861 Typically, there are three things that we get out of the TOF detector: a match with a

1862 TPC track, TOF time, and path length, where the first one is necessary of the other two.  
 1863 The second represents the time between the collision and the detection of the particle in  
 1864 the TOF. So, it is the time it takes the particle to get from the vertex to the detector.  
 1865 The length of the trajectory of the particle from the vertex to the TOF is called path  
 1866 length. In the simulation, the time and the path length are calculated. However, in the  
 1867 data, the time of the collision/ vertex is missing as already discussed in Sec. 3.6. The  
 1868 TOF time stored in the data represents an inner TOF timer. Its values cycle through  
 1869 a range from 0 to 51k. The values are still useful for us since we are interested only in  
 1870 the difference of time, see Appendix A for more details. Hence, the TOF time between  
 1871 the data and embedding cannot be compared directly but can be analyzed thought the  
 1872  $m_{\text{TOF}}^2$  distribution, see Fig. E.2.

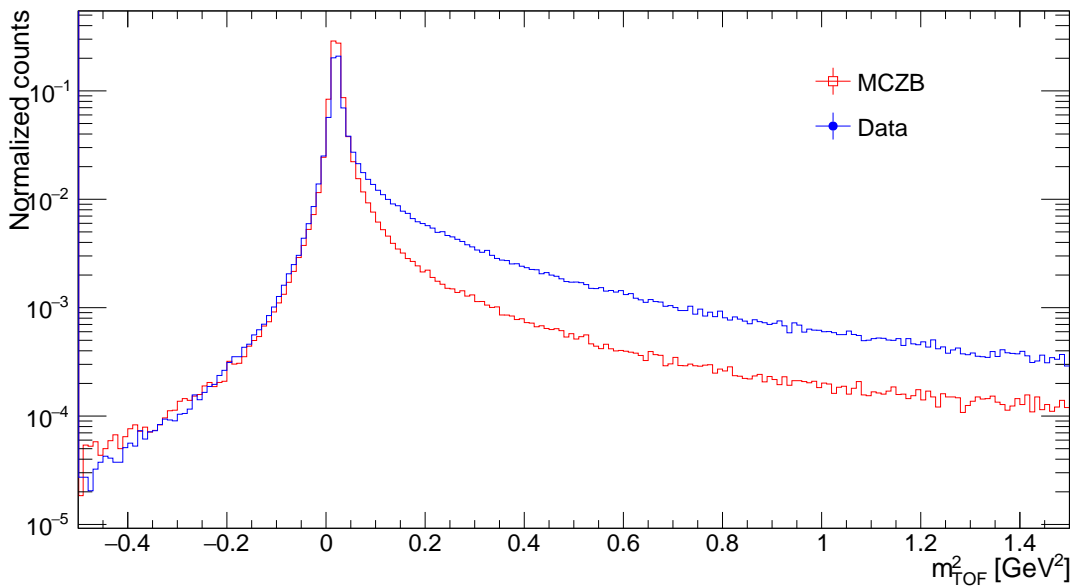


Figure E.2: A comparison of the invariant mass squared ( $m_{\text{TOF}}^2$ ) between the CEP event candidates (Data) and reconstructed tracks in the embedding (MCZB).

1873 A comparison of pseudorapidity ( $\eta$ ) and azimuthal angle ( $\varphi$ ) between the CEP event  
 1874 candidates, reconstructed tracks in the embedding, and the true-level MC information  
 1875 is depicted in Fig. E.3.

1876 A comparison of the number of hits in the TPC used to calculate the energy loss  
 1877 ( $N_{\text{hits}}^{\langle dE/dx \rangle}$ ) and the number of hits in the TPC used to reconstruct the track ( $N_{\text{hits}}^{\text{fit}}$ )  
 1878 between the candidates of the CEP events and the reconstructed tracks in the embedding  
 1879 can be seen in Fig. E.4.

1880 A comparison of the transverse momenta between the CEP event candidates, re-  
 1881 constructed tracks in the embedding, and the true-level MC information is depicted  
 1882 in Fig. E.5.

1883 A comparison of the TOF path length between the CEP event candidates and the

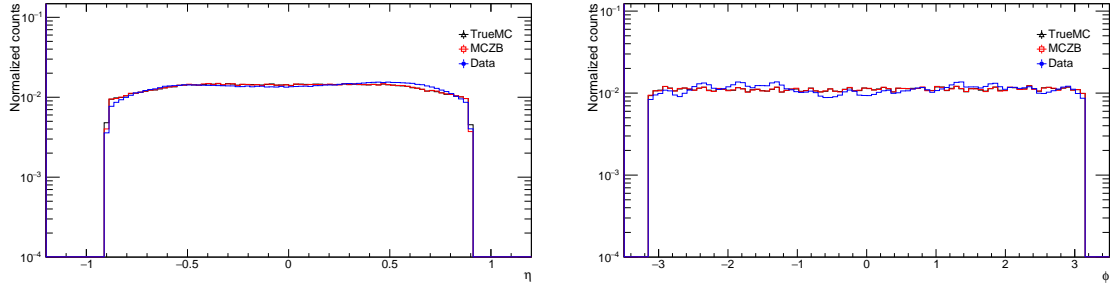


Figure E.3: A comparison of the pseudorapidity ( $\eta$ , left) and the azimuthal angle ( $\varphi$ , right) between the CEP event candidates (Data), reconstructed tracks in the embedding (MCZB) and the true-level MC information (TrueMC).

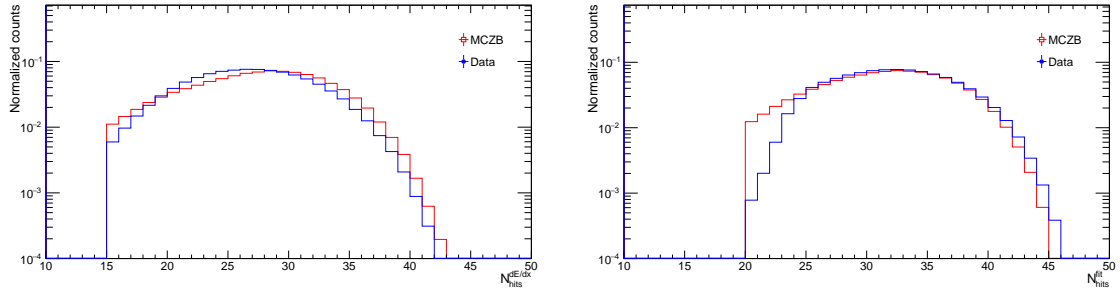


Figure E.4: A comparison of the number of hits in the TPC used to calculate the energy loss ( $N_{\text{hits}}^{(dE/dx)}$ , left) and the number of hits in the TPC used for the track reconstruction ( $N_{\text{hits}}^{\text{fit}}$ , right) between the CEP event candidates (Data) and reconstructed tracks in the embedding (MCZB).

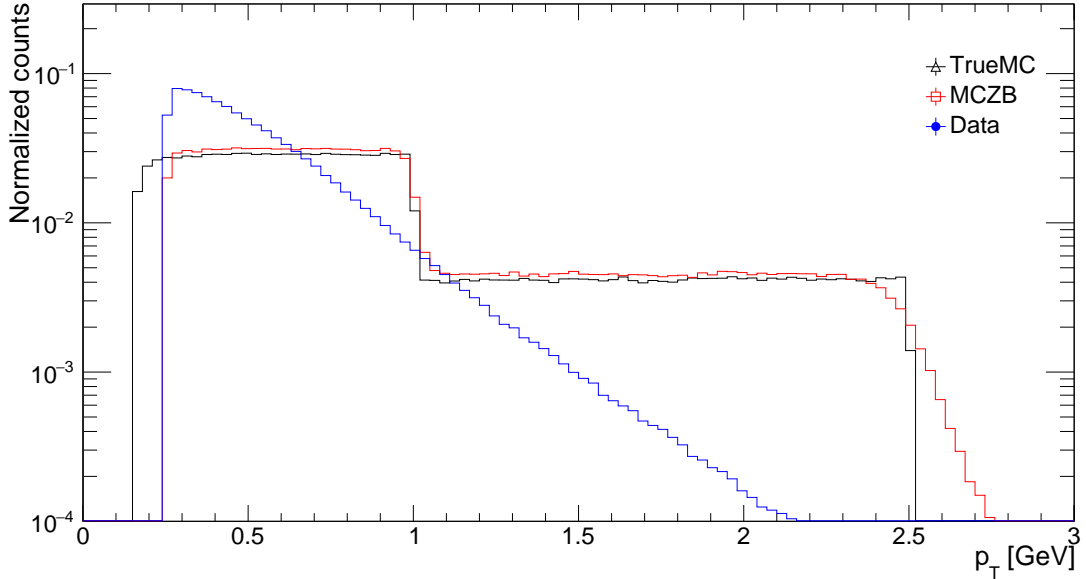


Figure E.5: A comparison of the transverse momenta between the CEP event candidates (Data), reconstructed tracks in the embedding (MCZB) and the true-level MC information (TrueMC).

1884 reconstructed tracks in the embedding is illustrated in Fig. E.6.

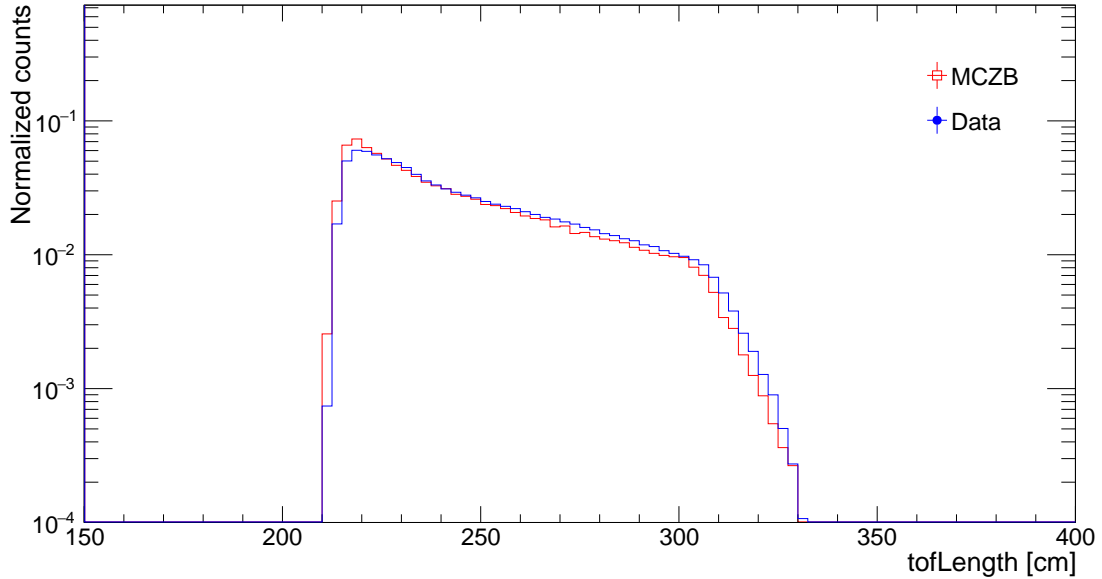


Figure E.6: A comparison of the TOF path length between the CEP event candidates (Data) and reconstructed tracks in the embedding (MCZB).

1885 A comparison of the positions  $x$  and  $y$  of the primary vertex for the candidates for  
1886 the CEP events and the position of the vertex at the true level in the embedding is  
1887 shown in Fig. E.7.

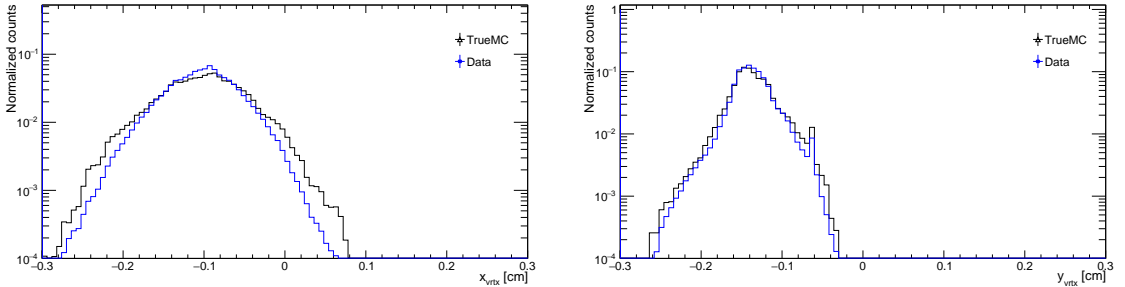


Figure E.7: A comparison of the  $x$  (left) and  $y$  (right) position of the primary vertex for CEP event candidates (Data) and of the true-level position of the vertex in the embedding (TrueMC).

1888 We have already demonstrated that  $m_{\text{TOF}}^2$  can be reproduced in the embedding.  
1889 However, to demonstrate that the embedding sample can be used for the PID study, the  
1890 energy loss ( $\langle dE/dx \rangle$ ) and the number of standard deviations between the measured and  
1891 theoretical energy loss  $n\sigma_X$  must be compared. Comparisons of  $n\sigma_{\pi^-}$  and  $n\sigma_{\pi^+}$  between  
1892 the candidates of the CEP events and the reconstructed tracks in the embedding are  
1893 shown in Fig. E.8. The distributions have the same width and are slightly shifted. The  
1894 shift is taken into account in the systematic uncertainty of the PID.

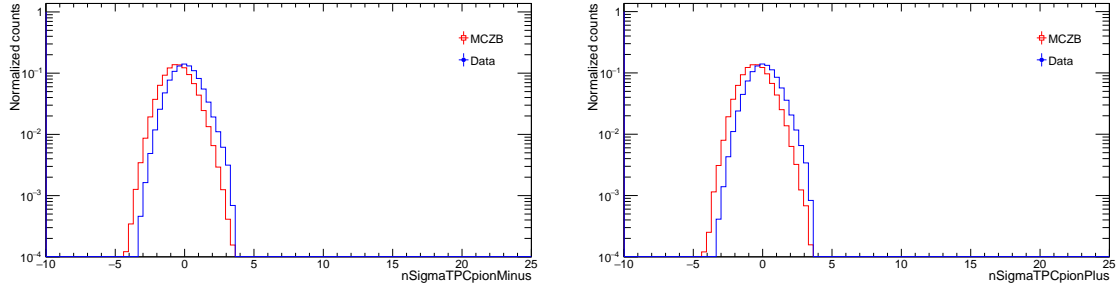


Figure E.8: A comparison of the number of standard deviations between the measured and the theoretical energy loss for  $\pi^-$  ( $n\sigma_{\pi^-}$ , left) and  $\pi^+$  ( $n\sigma_{\pi^+}$ , right) between the CEP event candidates (Data) and reconstructed tracks in the embedding (MCZB).

1895        The energy loss ( $\langle dE/dx \rangle$ ) of the particle is dependent on its momentum. Thus,  
 1896        the comparison of energy loss ( $\langle dE/dx \rangle$ ) between the CEP event candidates and the  
 1897        reconstructed tracks in the embedding is differentiated into different  $p_T$  bins and can be  
 1898        seen in Fig. E.9 – Fig. E.14. The embedding does not contain the same number of pairs  
 1899        as the data as discussed in Sec. 5.1. Therefore, the amplitudes of the peaks cannot be  
 1900        compared. There is a good agreement between the widths of the peaks in each  $p_T$  bin,  
 1901        so the embedding can be used for the PID study.

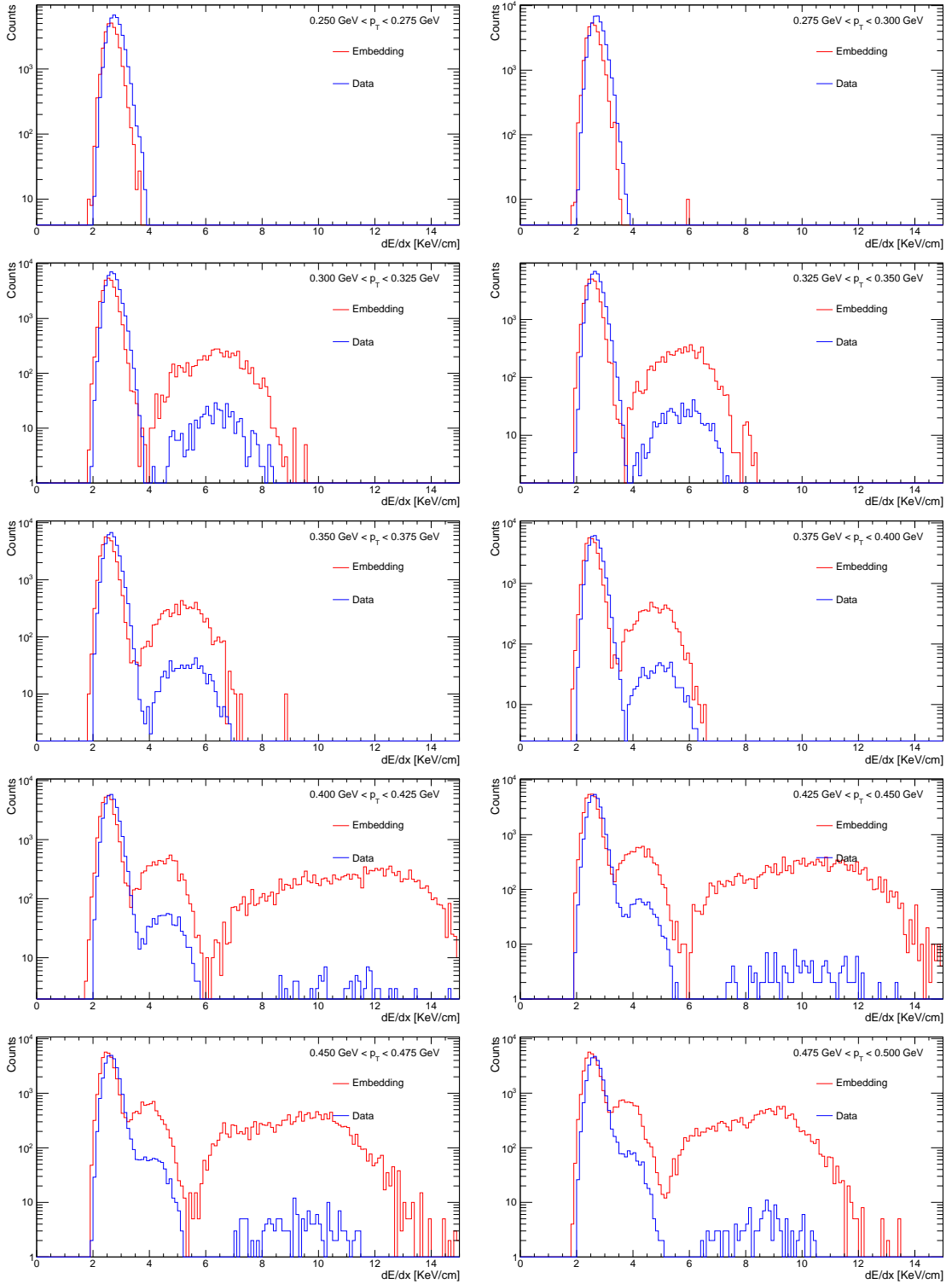


Figure E.9: A comparison of the energy loss ( $\langle dE/dx \rangle$ ) between the CEP event candidates and reconstructed tracks in the embedding for  $\pi^+, K^+, p$  differentiated into different  $p_T$  bins.

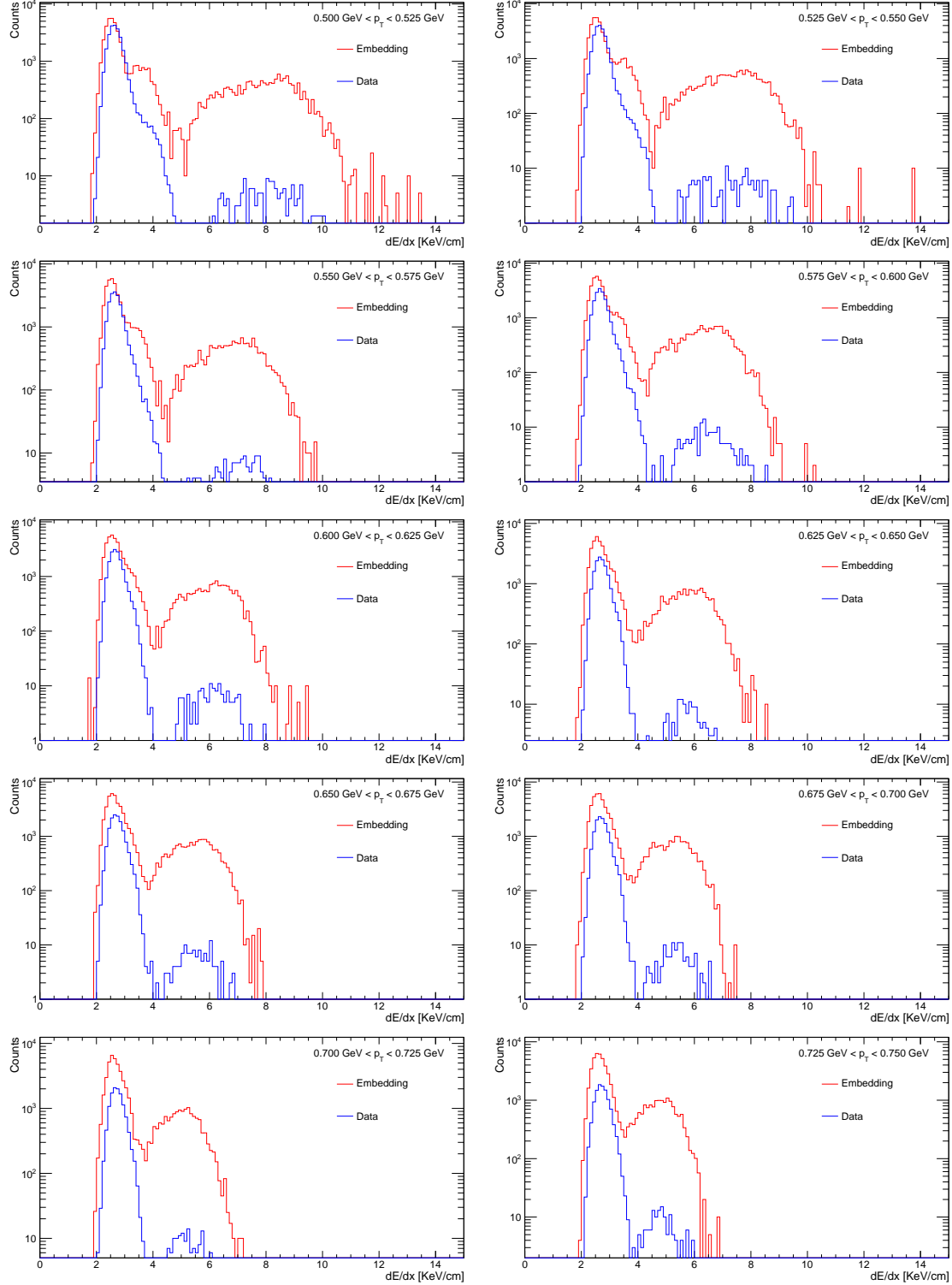


Figure E.10: A comparison of the energy loss ( $\langle dE/dx \rangle$ ) between the CEP event candidates and reconstructed tracks in the embedding for  $\pi^+, K^+, p$  differentiated into different  $p_T$  bins.

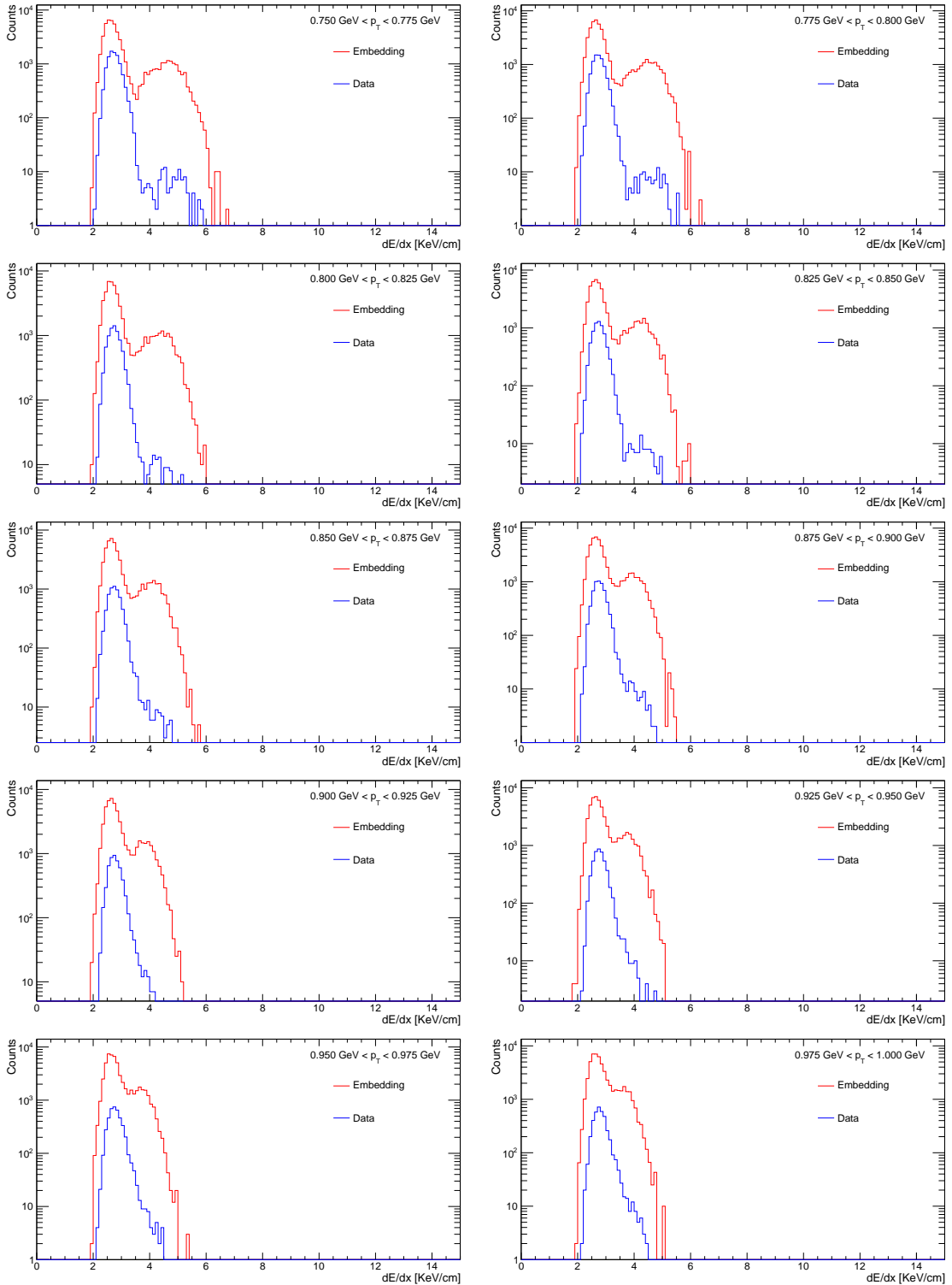


Figure E.11: A comparison of the energy loss ( $\langle dE/dx \rangle$ ) between the CEP event candidates and reconstructed tracks in the embedding for  $\pi^+, K^+, p$  differentiated into different  $p_T$  bins.

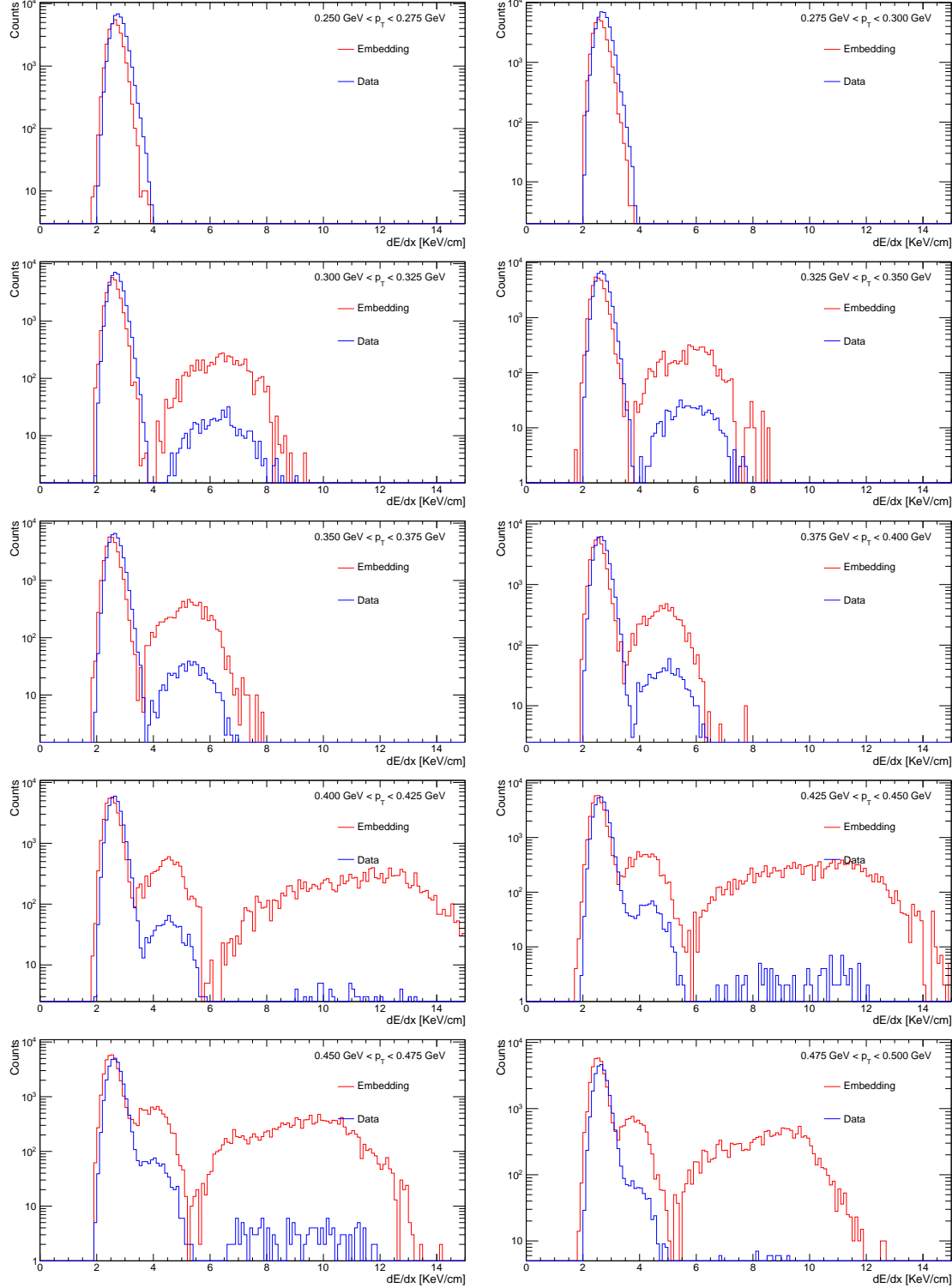


Figure E.12: A comparison of the energy loss ( $\langle dE/dx \rangle$ ) between the CEP event candidates and reconstructed tracks in the embedding for  $\pi^-$ ,  $K^-$ ,  $\bar{p}$  differentiated into different  $p_T$  bins.

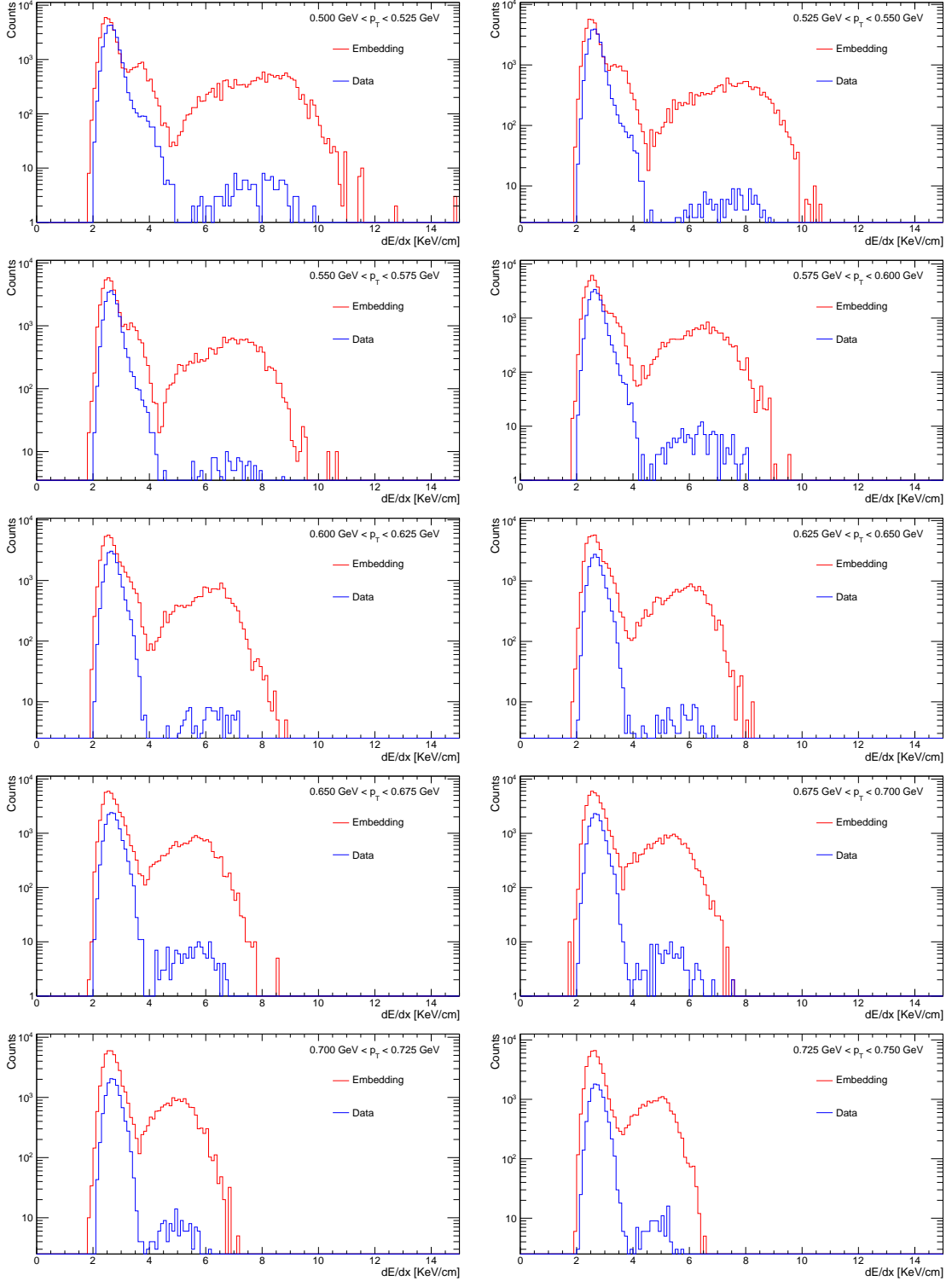


Figure E.13: A comparison of the energy loss ( $\langle dE/dx \rangle$ ) between the CEP event candidates and reconstructed tracks in the embedding for  $\pi^-$ ,  $K^-$ ,  $\bar{p}$  differentiated into different  $p_T$  bins.

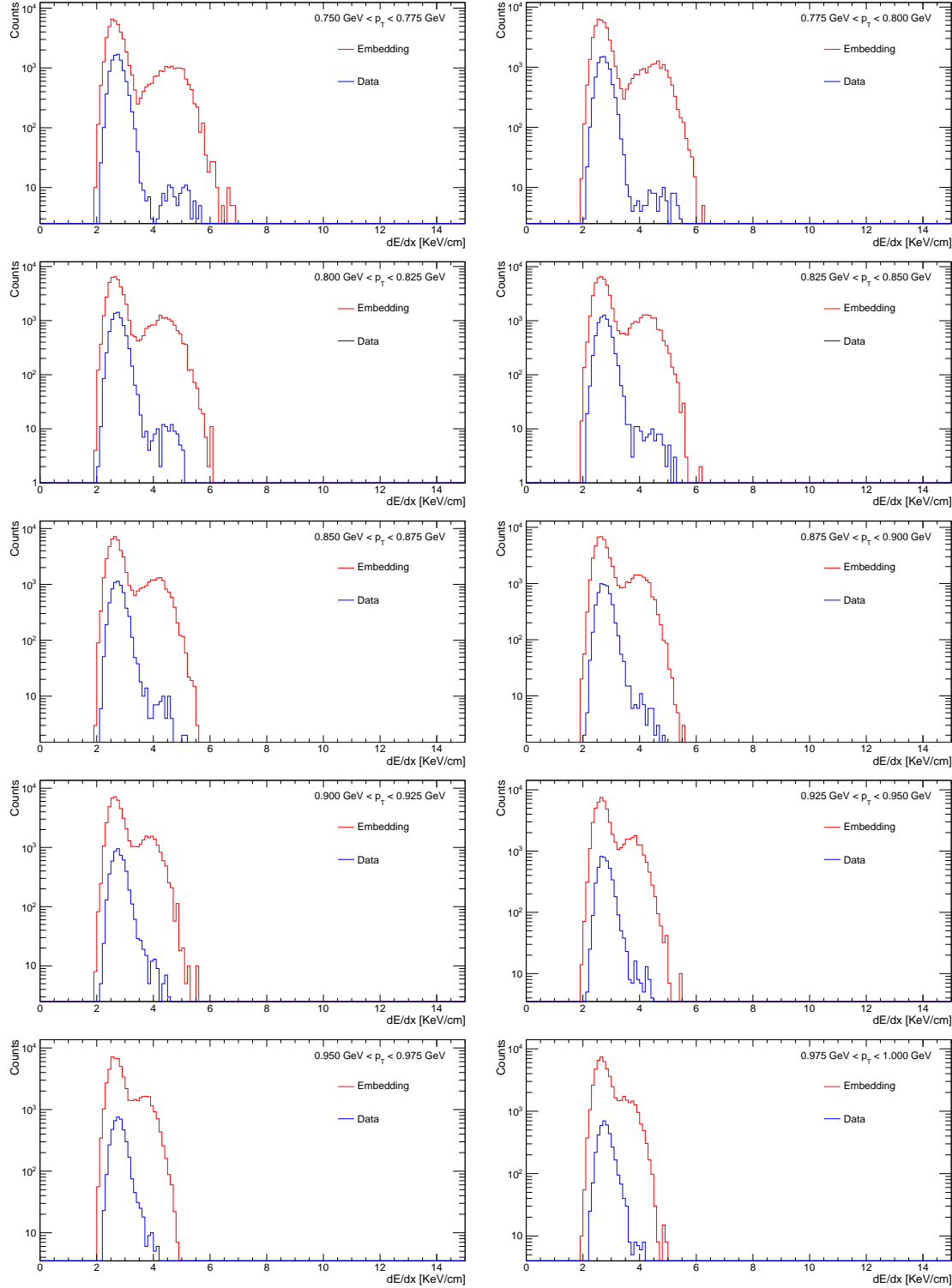


Figure E.14: A comparison of the energy loss ( $\langle dE/dx \rangle$ ) between the CEP event candidates and reconstructed tracks in the embedding for  $\pi^-$ ,  $K^-$ ,  $\bar{p}$  differentiated into different  $p_T$  bins.



1902 **Appendix F**

1903 **The validation of the simulation  
1904 of the RP system**

1905 The distributions of the cluster energy in the ADC counts after pedestal subtraction and  
 1906 cluster length plotted for each RP and for the data, the embedding and pure MC can  
 1907 be seen in Fig. F.1 and in Fig. F.2, respectively. The distribution of the cluster energy  
 1908 shows two significant peaks. The first at 10 ADC and the second at 40 ADC. The first  
 1909 corresponds to background hits, and the second one to the signal.

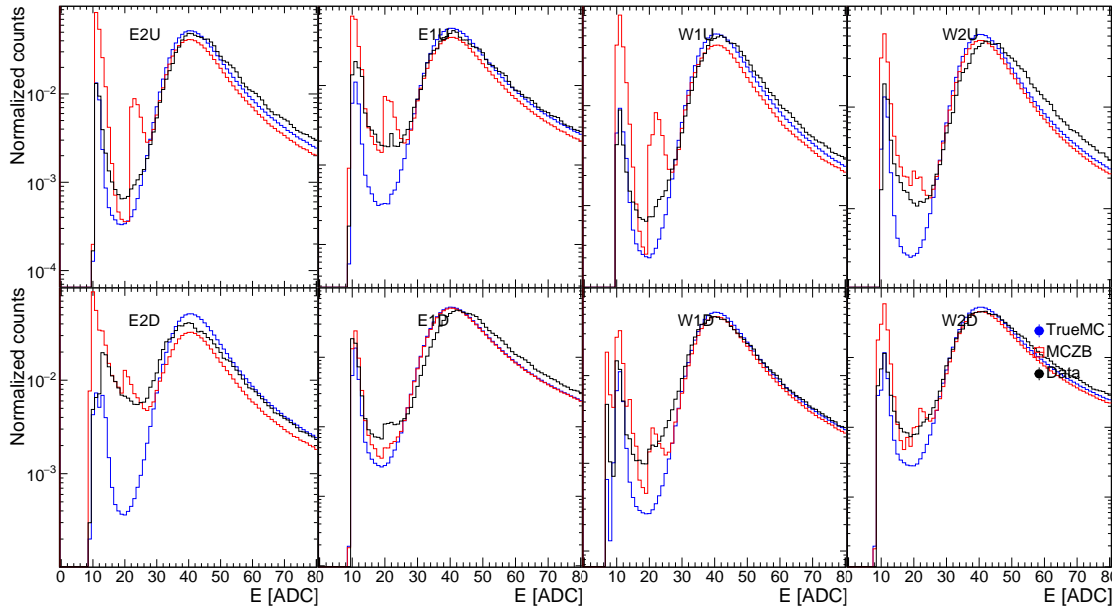


Figure F.1: Cluster energy distributions in ADC counts after pedestal subtraction plotted for each RP and for the data, embedding and pure MC.

1910 The RP resolution is studied through the collinearity of elastic events. The collinear-  
 1911 ity is defined as the difference between the reconstructed scattering angles on the West  
 1912 and East side for elastic events, see Sec. 2.4.1. The difference between the reconstructed

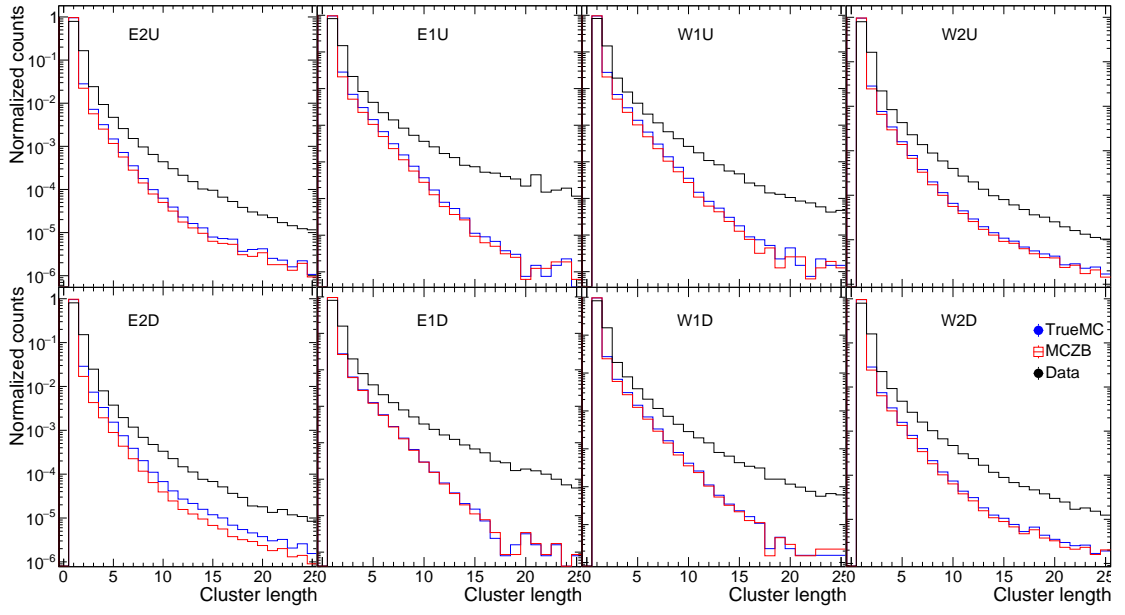


Figure F.2: Cluster length distributions plotted for each RP and for the data, embedding and pure MC.

scattering angles for the data, embedding and pure MC is illustrated in Fig. F.3. The distributions agree well in the signal region ( $-390\mu\text{rad}$ ;  $390\mu\text{rad}$ ).

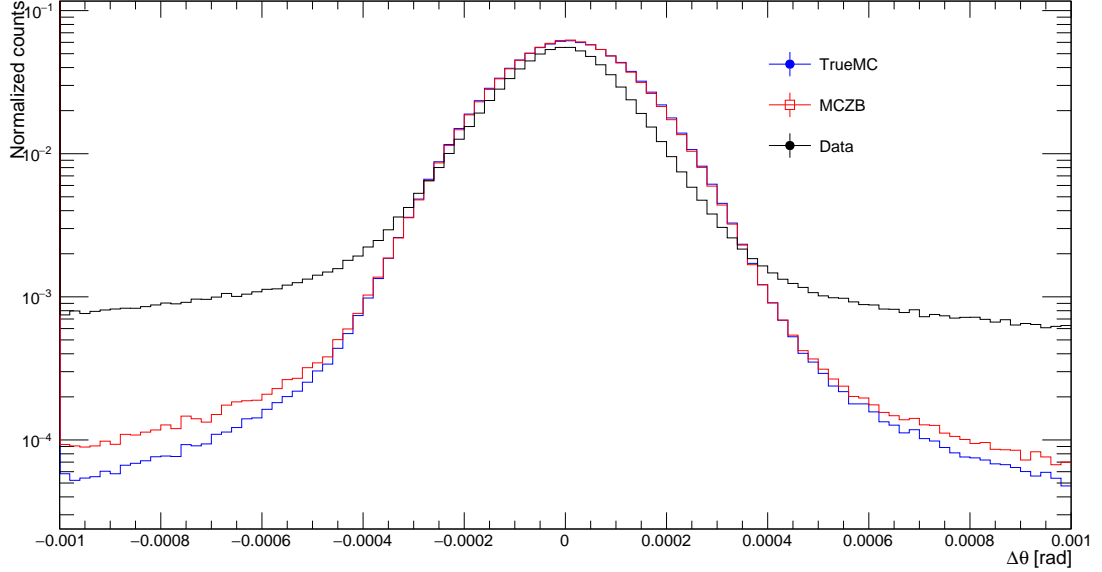


Figure F.3: Difference between the reconstructed scattering angles for the data, embedding and pure MC.

The distributions of the number of clusters per RP for the data, the embedding, and the pure MC are shown in Fig. F.4. Great agreement can be seen between the samples, especially for the region where the signal is expected. The reconstruction of

the track (cut C1.1) requires at least three out of four planes per RP. Therefore, a two-peak structure is formed. The first peak corresponds to the events without a signal in the given RP. Hence, the signal is reconstructed in the other branch on the given side. The second peak consists of events with the reconstructed point in the given RP.

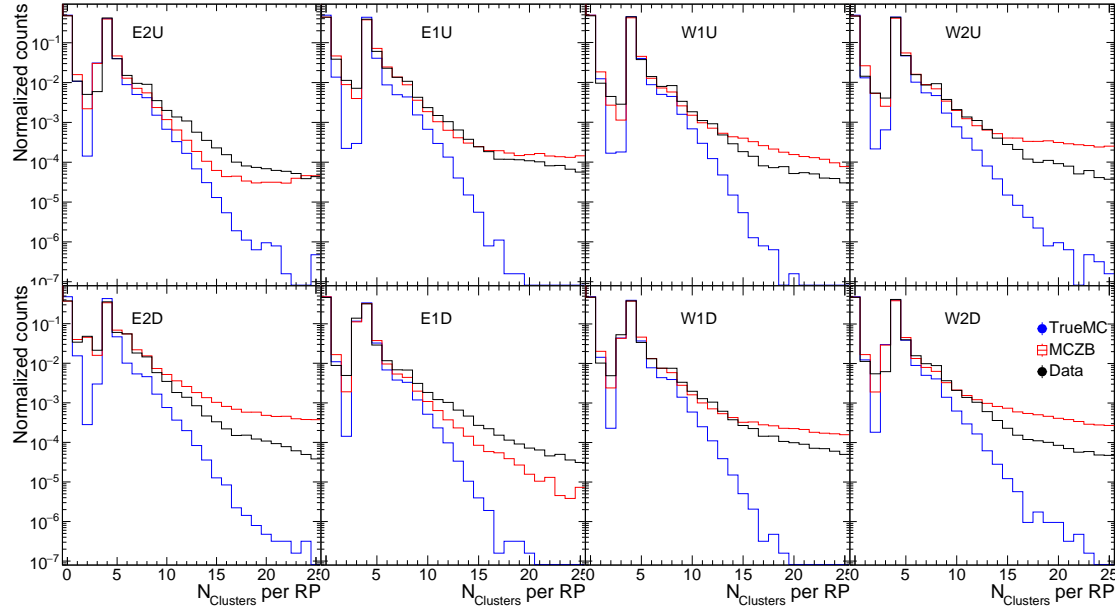


Figure F.4: Distributions of number of clusters per RP for the data, embedding and pure MC.



1922 Appendix G

1923 The total TPC track efficiency

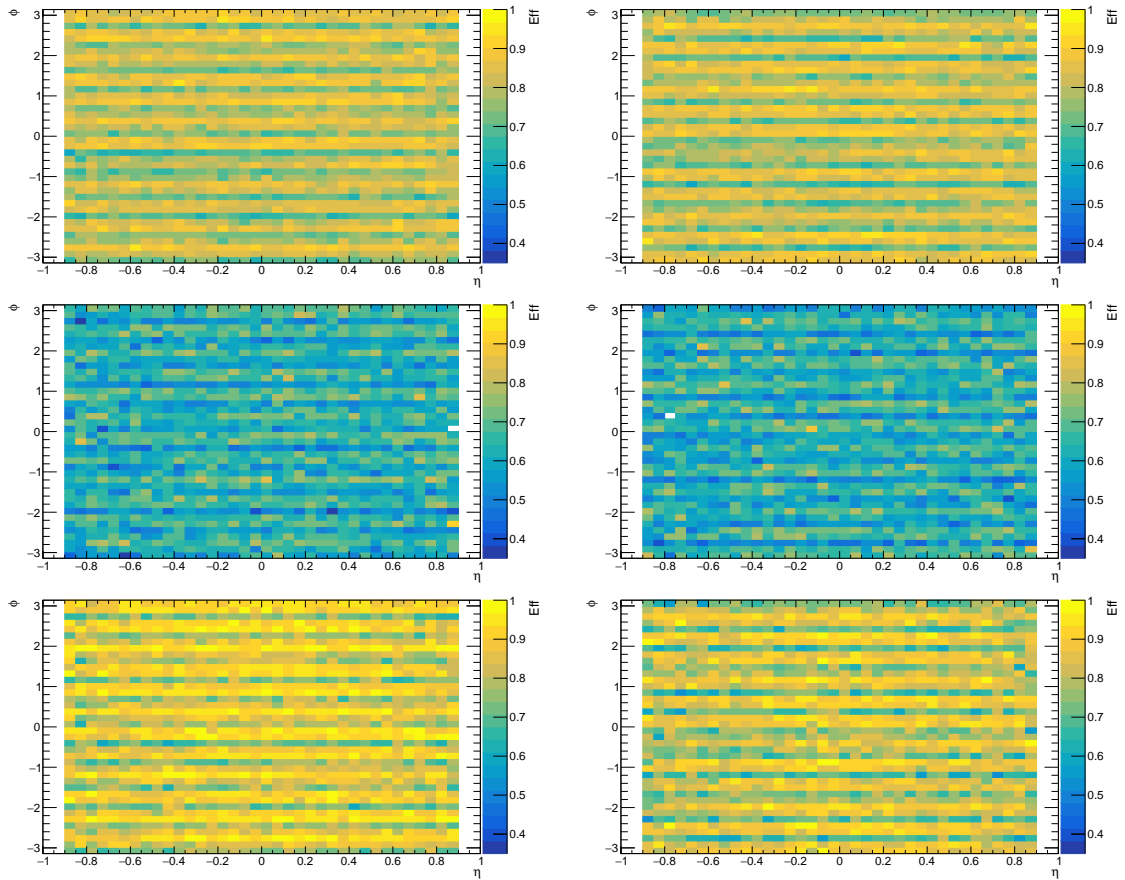


Figure G.1: The total TPC track efficiency for  $\pi^+$  (top left),  $\pi^-$  (top right),  $K^+$  (middle left),  $K^-$  (middle right), and  $p$  (bottom left), and  $\bar{p}$  (bottom right) as a function of the azimuthal angle  $\varphi$  and the pseudorapidity  $\eta$ .

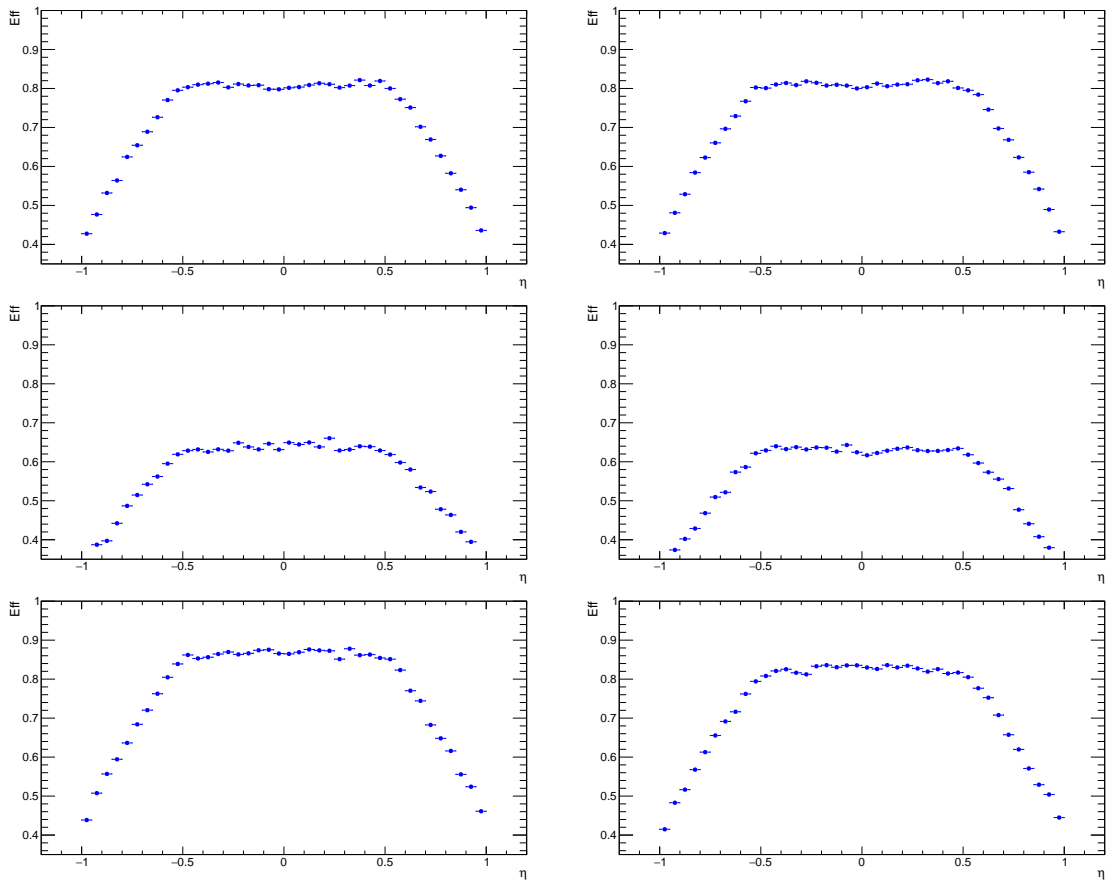


Figure G.2: The total TPC track efficiency for  $\pi^+$  (top left),  $\pi^-$  (top right),  $K^+$  (middle left),  $K^-$  (middle right), and  $p$  (bottom left), and  $\bar{p}$  (bottom right) as a function of the pseudorapidity  $\eta$ .

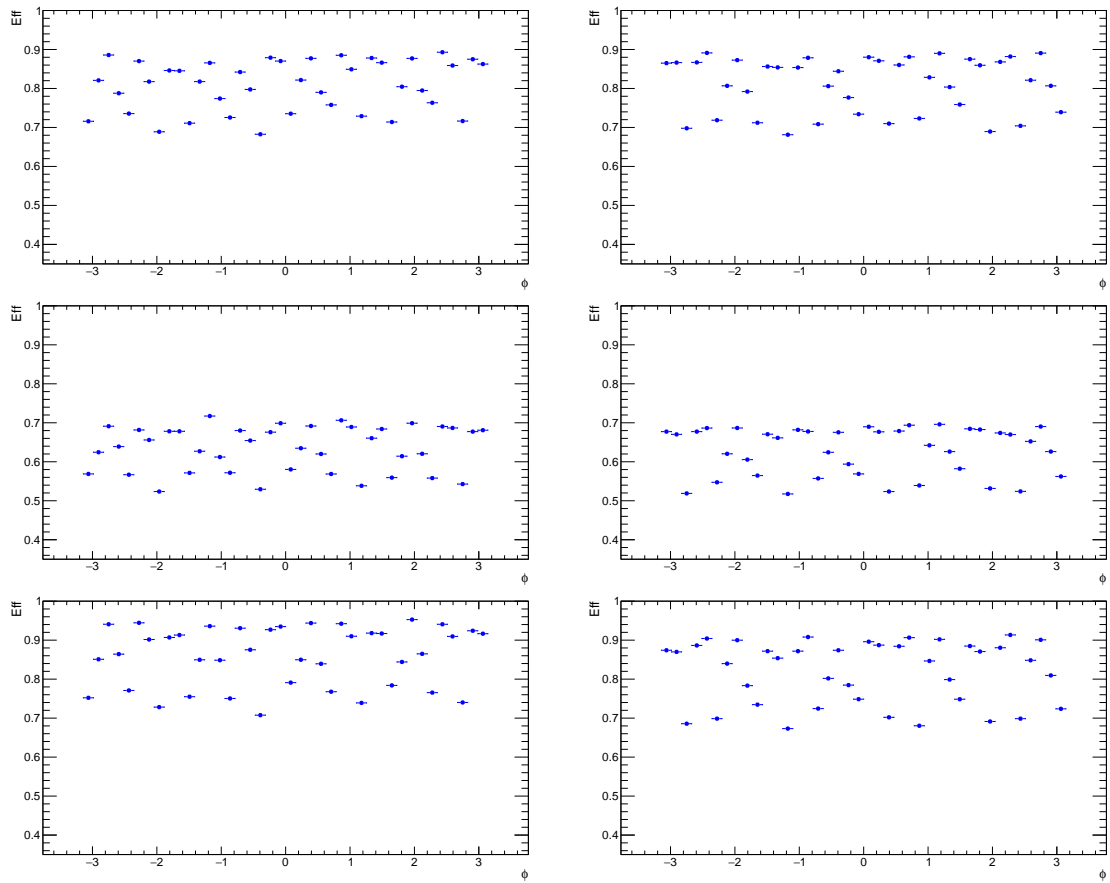


Figure G.3: The total TPC track efficiency for  $\pi^+$  (top left),  $\pi^-$  (top right),  $K^+$  (middle left),  $K^-$  (middle right), and  $p$  (bottom left), and  $\bar{p}$  (bottom right) as a function of the azimuthal angle  $\varphi$ .

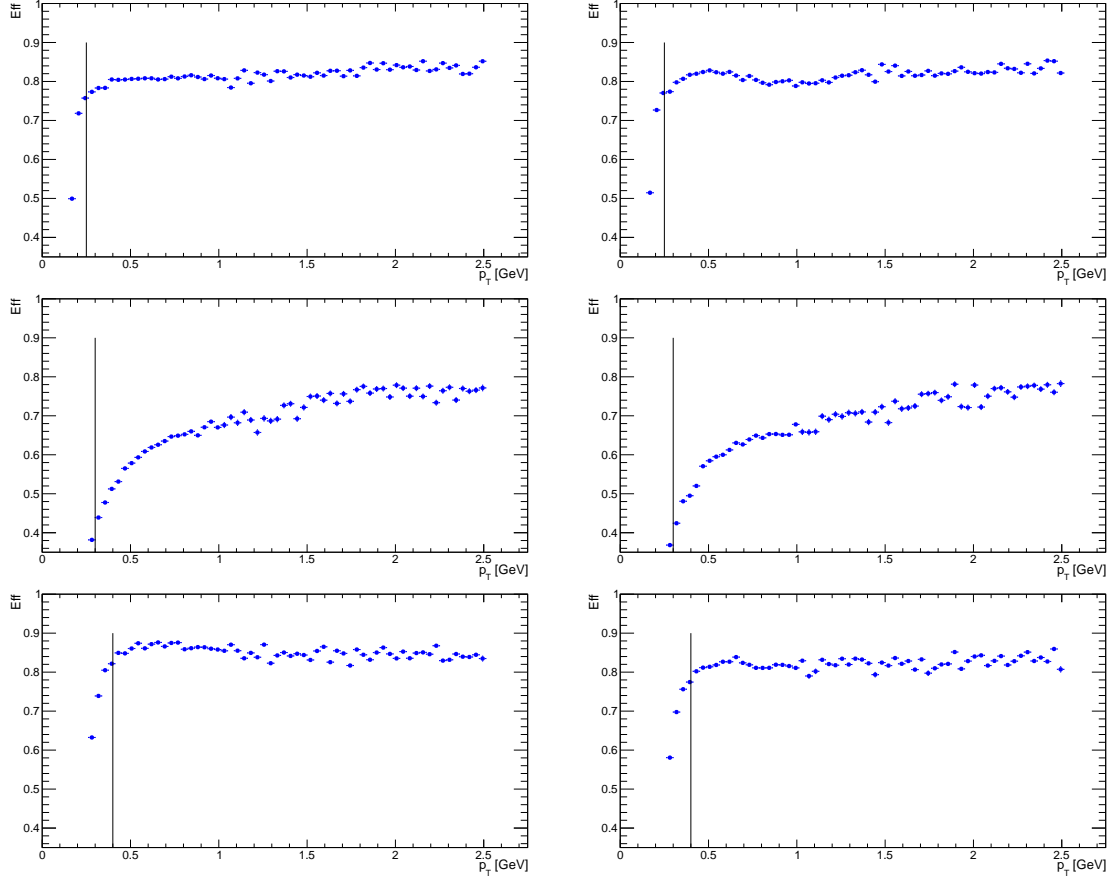


Figure G.4: The total TPC track efficiency for  $\pi^+$  (top left),  $\pi^-$  (top right),  $K^+$  (middle left),  $K^-$  (middle right), and  $p$  (bottom left), and  $\bar{p}$  (bottom right) as a function of the transverse momenta  $p_T$ .

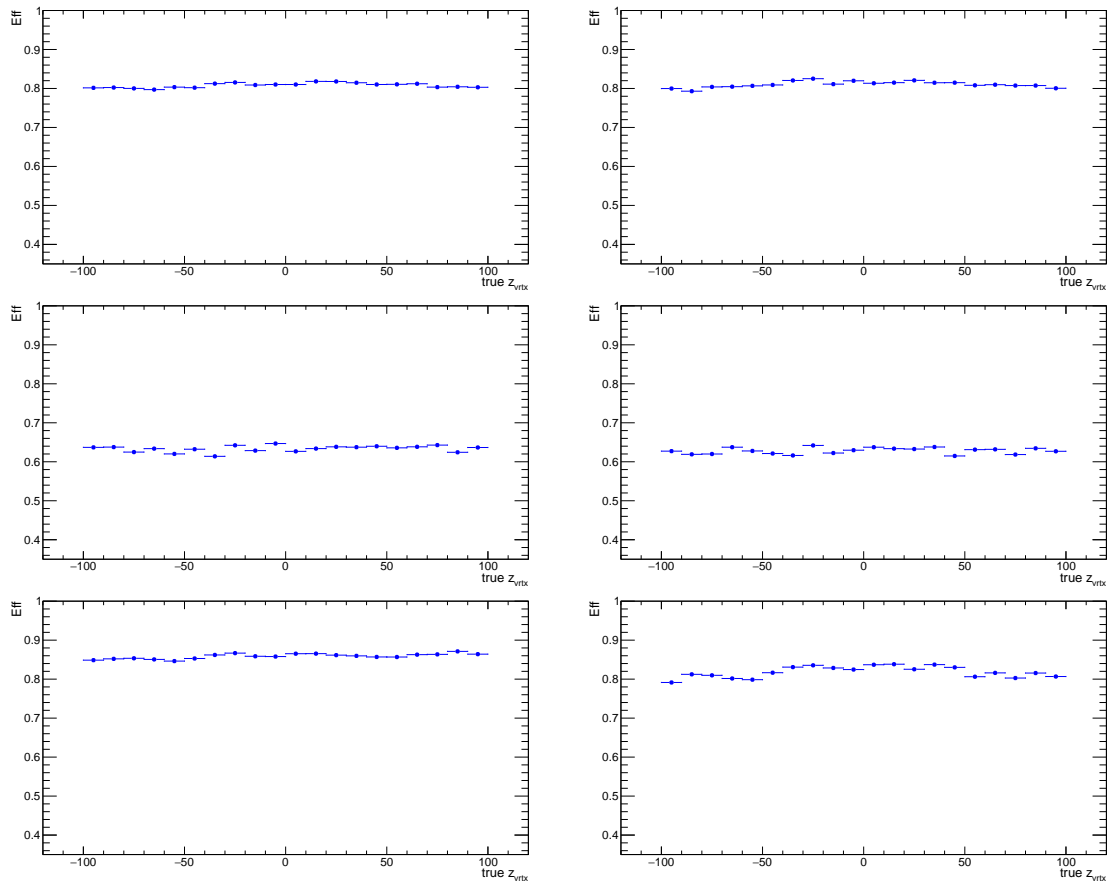


Figure G.5: The total TPC track efficiency for  $\pi^+$  (top left),  $\pi^-$  (top right),  $K^+$  (middle left),  $K^-$  (middle right), and  $p$  (bottom left), and  $\bar{p}$  (bottom right) as a function of the  $z$ -position of the primary vertex  $z_{\text{vtx}}$ .

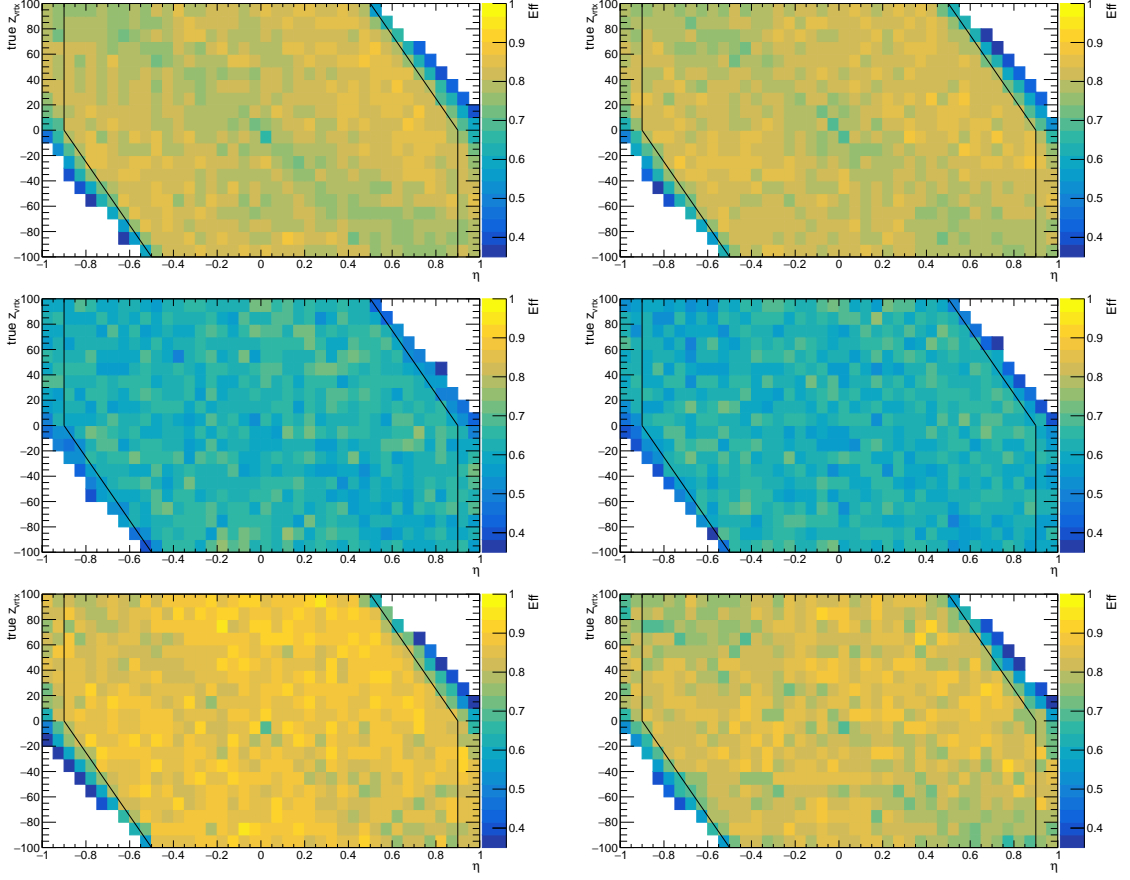


Figure G.6: The total TPC track efficiency for  $\pi^+$  (top left),  $\pi^-$  (top right),  $K^+$  (middle left),  $K^-$  (middle right), and  $p$  (bottom left), and  $\bar{p}$  (bottom right) as a function of the  $z$ -position of the primary vertex  $z_{\text{vtx}}$  and the pseudorapidity  $\eta$ .

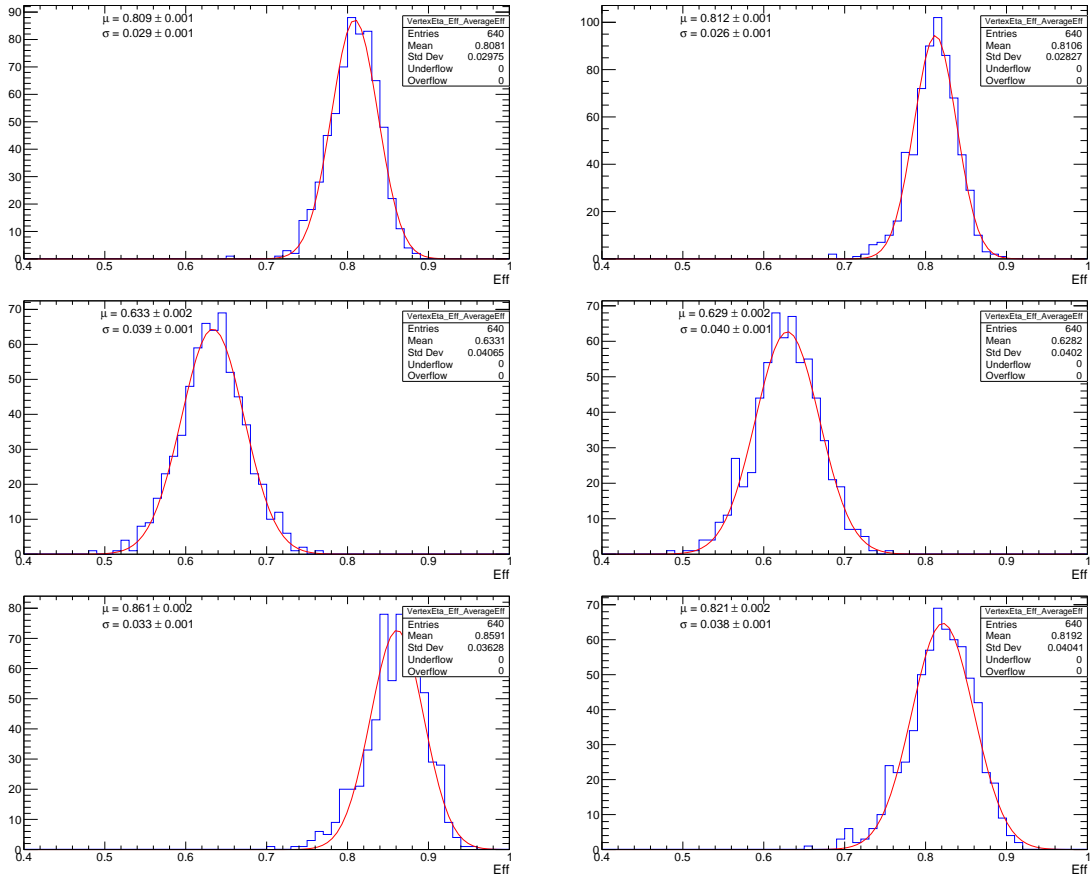


Figure G.7: The average total TPC track efficiency for  $\pi^+$  (top left),  $\pi^-$  (top right),  $K^+$  (middle left),  $K^-$  (middle right), and  $p$  (bottom left), and  $\bar{p}$  (bottom right) as a function of the  $z$ -position of the primary vertex  $z_{\text{vtx}}$  and the pseudorapidity  $\eta$ .



1924 **Appendix H**

1925 **The total TOF hit efficiency**

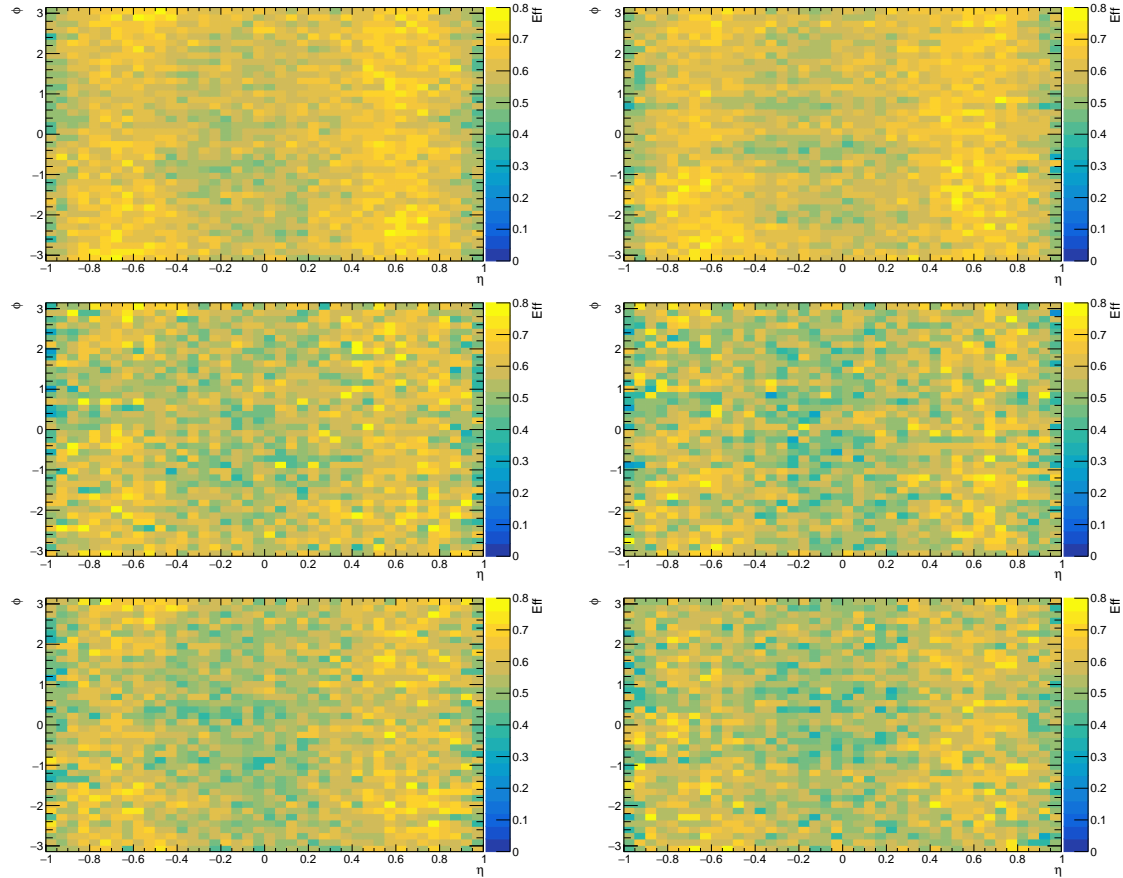


Figure H.1: The total TOF track efficiency for  $\pi^+$  (top left),  $\pi^-$  (top right),  $K^+$  (middle left),  $K^-$  (middle right), and  $p$  (bottom left), and  $\bar{p}$  (bottom right) as a function of the azimuthal angle  $\varphi$  and the pseudorapidity  $\eta$ .

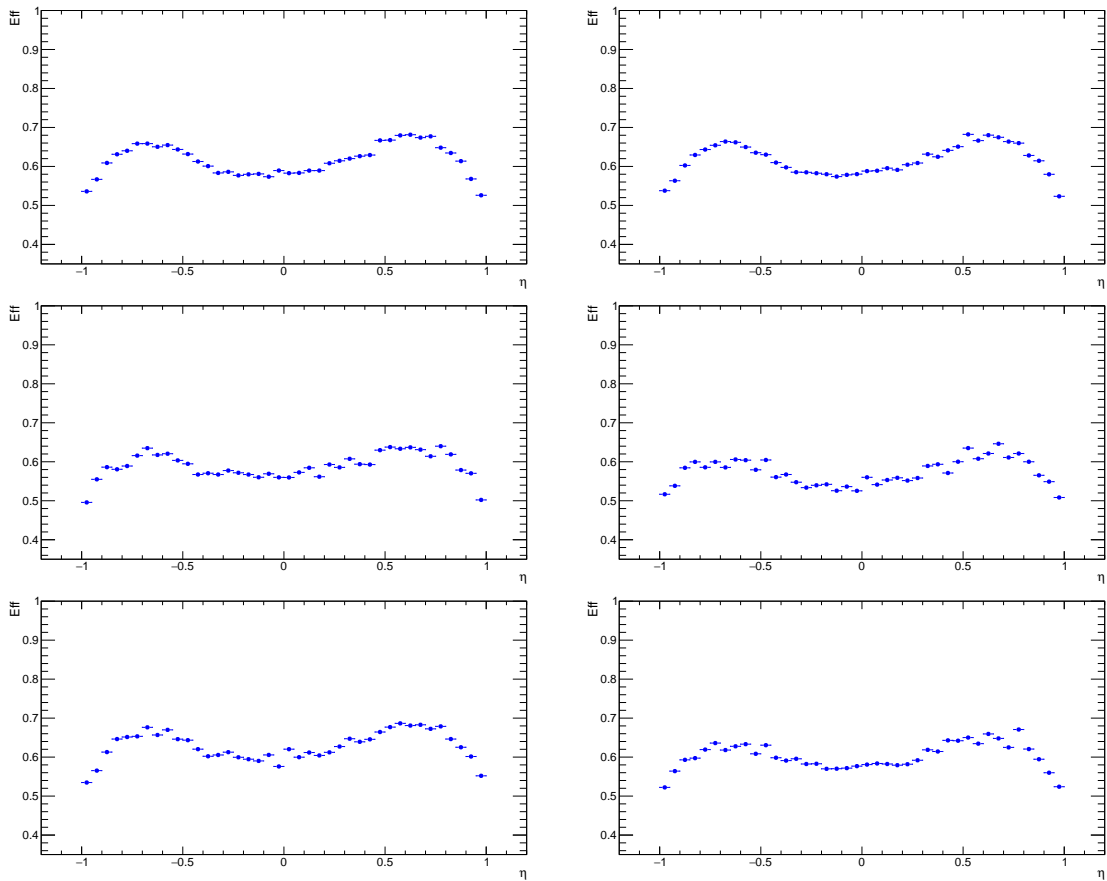


Figure H.2: The total TOF track efficiency for  $\pi^+$  (top left),  $\pi^-$  (top right),  $K^+$  (middle left),  $K^-$  (middle right), and  $p$  (bottom left), and  $\bar{p}$  (bottom right) as a function of the pseudorapidity  $\eta$ .

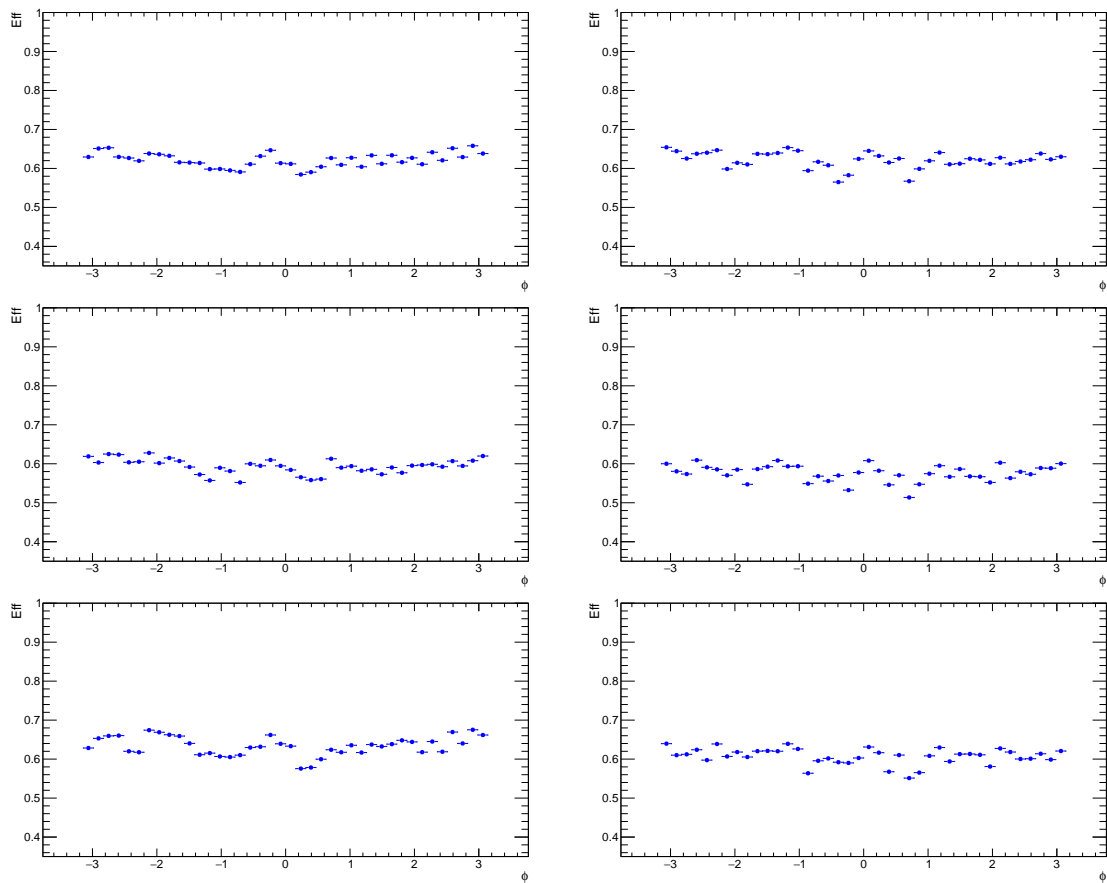


Figure H.3: The total TOF track efficiency for  $\pi^+$  (top left),  $\pi^-$  (top right),  $K^+$  (middle left),  $K^-$  (middle right), and  $p$  (bottom left), and  $\bar{p}$  (bottom right) as a function of the azimuthal angle  $\varphi$ .

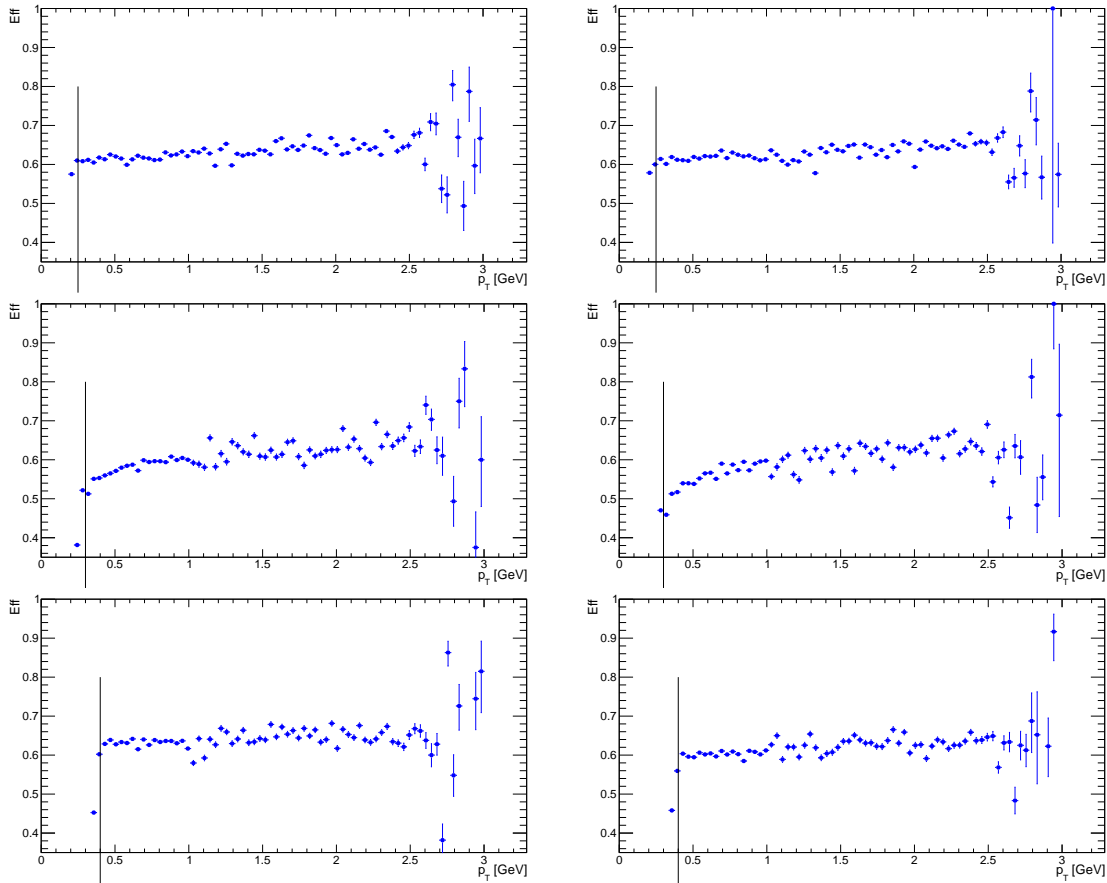


Figure H.4: The total TOF track efficiency for  $\pi^+$  (top left),  $\pi^-$  (top right),  $K^+$  (middle left),  $K^-$  (middle right), and  $p$  (bottom left), and  $\bar{p}$  (bottom right) as a function of the transverse momenta  $p_T$ .

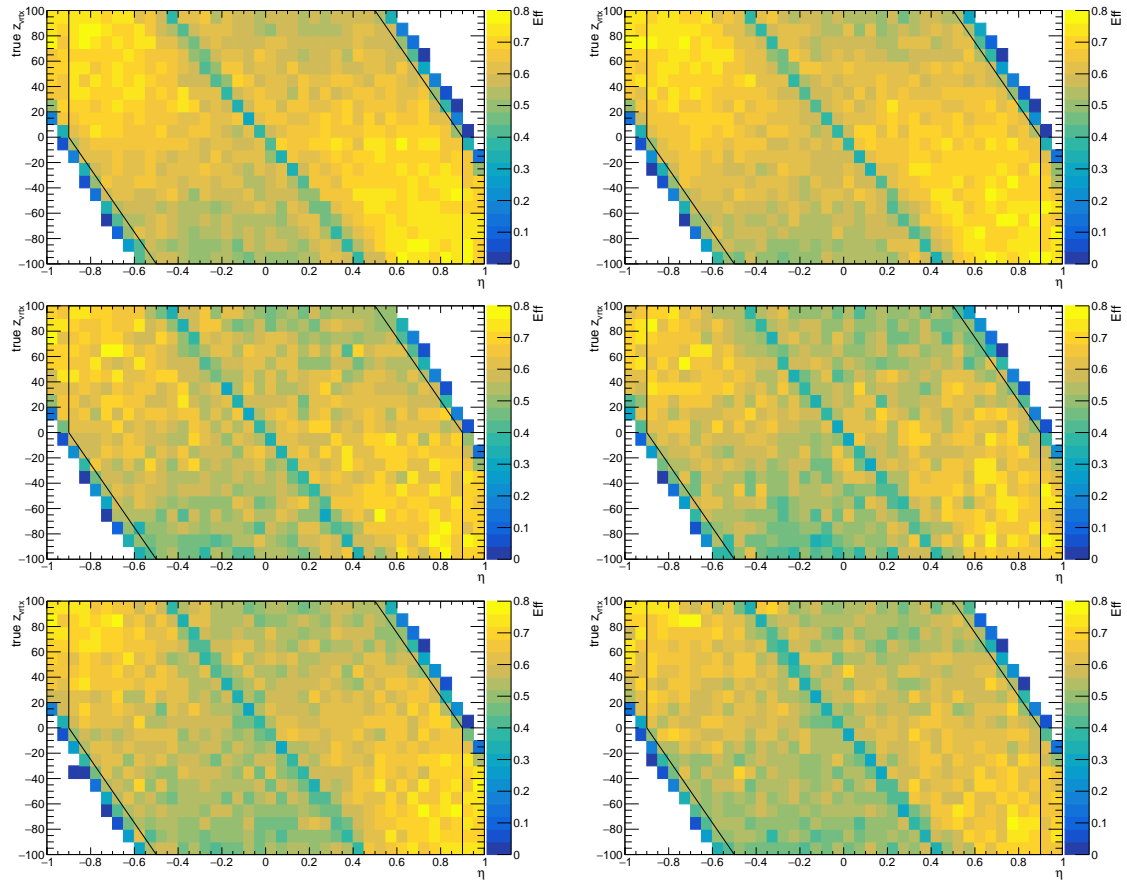


Figure H.5: The total TOF track efficiency for  $\pi^+$  (top left),  $\pi^-$  (top right),  $K^+$  (middle left),  $K^-$  (middle right), and  $p$  (bottom left), and  $\bar{p}$  (bottom right) as a function of the  $z$ -position of the primary vertex  $z_{\text{vtx}}$  and the pseudorapidity  $\eta$ .

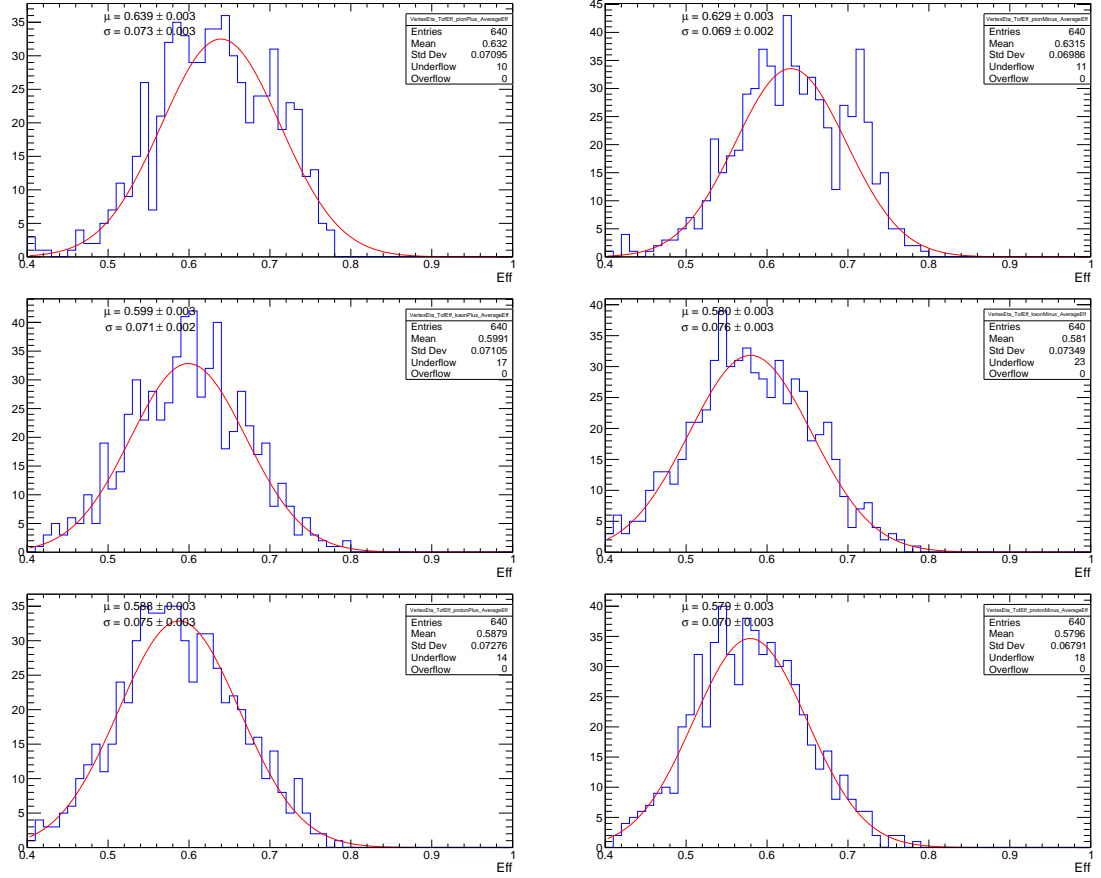


Figure H.6: The average total TOF track efficiency for  $\pi^+$  (top left),  $\pi^-$  (top right),  $K^+$  (middle left),  $K^-$  (middle right), and  $p$  (bottom left), and  $\bar{p}$  (bottom right) as a function of the  $z$ -position of the primary vertex  $z_{\text{vtx}}$  and the pseudorapidity  $\eta$ .

1926 **Appendix I**

1927 **Data driven method to TOF  
efficiency**  
1928

1929 The tag&probe method for data-driven analysis of TOF efficiency is discussed here. This  
1930 topic was mainly done by Michal Vranovsky, the CTU student.

1931 The method is based on a common procedure used in particle physics to measure  
1932 the probability of occurrence of a certain process. In this case, we use decays of  $K_S^0$  to  
1933 two daughter particles ( $\pi^+\pi^-$ ), each pair consists of a tag and a probe. A tag is a  
1934 particle that is detected by the detector, whereas the probe is the one under study. The  
1935 efficiency will therefore depend on two different yields of strange particles. The first case  
1936 is that both tracks in a pair have hits in TOF which represent only the probes that are  
1937 detected. The second case is when at least one of the tracks has a hit in TOF. This  
1938 represents all the different probes sent to the detector. The tag always has a hit in TOF  
1939 which is used as a control sample. The probe can but does not have to have a hit in  
1940 TOF. Because all corrections cancel when divided, the ratio of the two yields gives the  
1941 efficiency of the TOF. Due to the cancellation of all corrections, the final efficiency does  
1942 not depend on the event selection. However, event selection plays an important role in  
1943 decreasing background noise while maintaining a strong signal.

1944 **I.1 Pre-selection of candidates**

1945 The StUPCV0 class was developed by combining several loose conditions for the correct  
1946 selection of V0 candidates ( $K_S^0$  and  $\Lambda/\bar{\Lambda}$ ). The conditions are loose, so that several  
1947 different analyses can build upon the pre-selection. The reconstruction process relies  
1948 on StPicoHelix, a standard library implemented by the STAR Collaboration for particle  
1949 reconstruction. From a particle's charge, momentum, invariant mass, and a point of  
1950 origin, one can reconstruct the trajectory of a particle towards the beamline outside of  
1951 the TPC range.

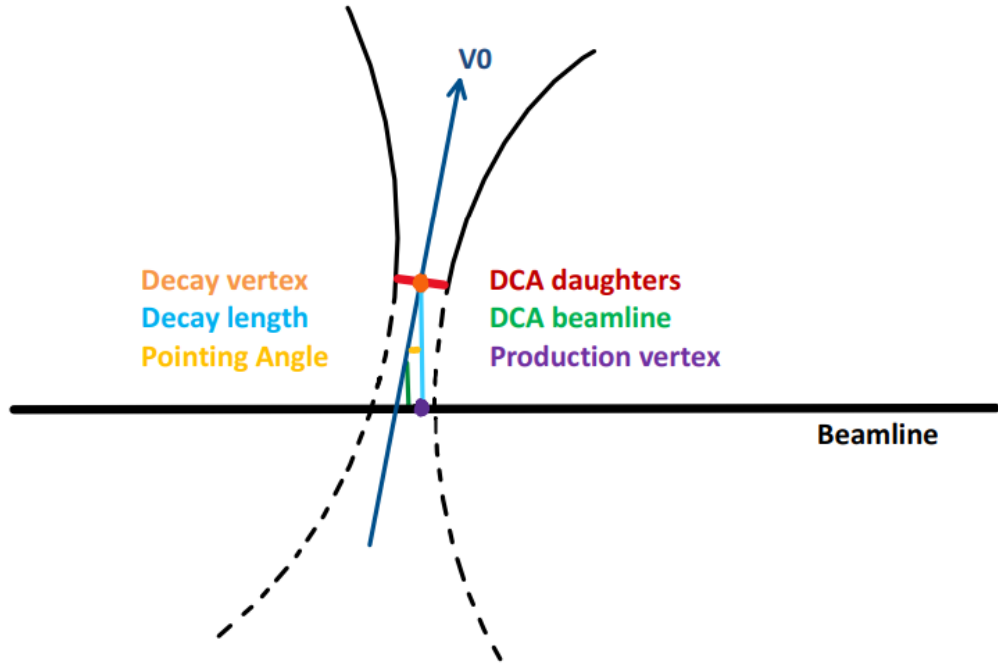


Figure I.1: An illustration of topological cuts used in the StUPCV0 class for V0 selection process.

- 1952     1. **Good quality track conditions:** before the process of reconstruction, one  
1953     confines the analysis to run only with tracks of good quality. This is done with several  
1954     lenient cuts on  $N_{hits}^{fit}$ , transverse momentum  $p_T$  and pseudorapidity  $\eta$ . These con-  
1955     ditions are described more closely in Sec. I.2.
- 1956     2. **DCA daughters < 3 cm:** the distance of closest approach (DCA) is the shortest  
1957     distance between trajectories of two different particles. This variable is represented  
1958     as the red line in Fig. I.1. The secondary vertex is determined as the middle point  
1959     between the points on the trajectories of the secondary particles. The 4-momentum  
1960     of the V0 candidate can also be obtained by the summation of 4-momenta of the  
1961     daughter particles. Its trajectory is not bent in the magnetic field, because its  
1962     charge is 0.
- 1963     3. **DCA beamline < 3 cm:** by inverting the direction of momentum of the V0  
1964     candidate, it is aimed towards the beamline. Variable DCA beamline is the shortest  
1965     distance between the beamline and the inverted trajectory of the V0 candidate.  
1966     The trajectory of the V0 candidate is in blue and the variable DCA beamline is in  
1967     green in Fig. I.1.
- 1968     4. **Decay length < 3 cm or  $\cos(\text{Pointing Angle}) > 0.9$ :** this is a combined  
1969     condition, the first one primarily for  $K_S^0$ , the second for  $\Lambda/\bar{\Lambda}$ . The decay length is  
1970     the distance between the hypothetical primary vertex and the secondary vertex.

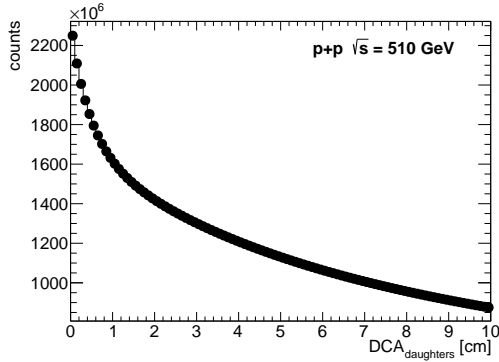


Figure I.2: Distribution of variable DCA between combinations of daughter particles from the pre-selection ran with *PicoDst* data.

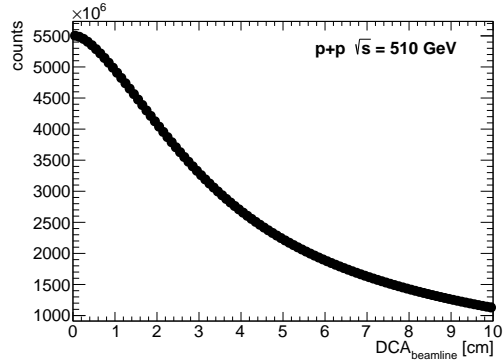


Figure I.3: Distribution of variable DCA from the inverted momentum of V0 candidate to the beamline in the pre-selection process ran over *PicoDst* data.

1971 The pointing angle is the angle between the direction of momentum of V0 candidate  
1972 and the vector from the primary vertex to the secondary vertex.

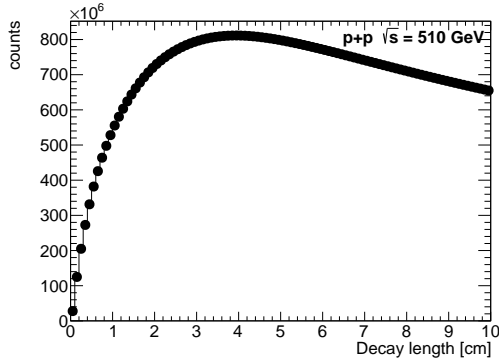


Figure I.4: Distribution of variable decay length in cm from pre-selection of candidates for TOF detector efficiency.

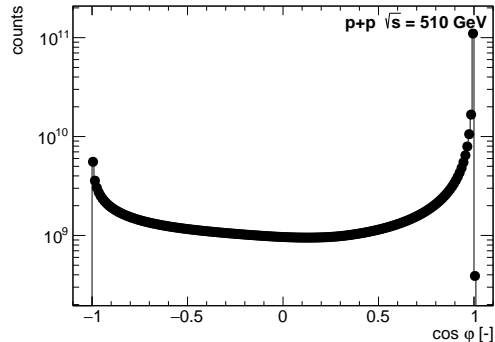


Figure I.5: Distribution of variable pointing angle which is the cosine of angle between reconstructed pair momentum and a vector between primary and secondary vertex.

1973  
1974 5.  $\mathbf{Q}_{\text{tot}} = \mathbf{0}$  : the sum of electromagnetic charge is to be equal to 0 for a neutral V0  
1975 candidate reconstruction. The non-zero pairs, also called like-sign pairs, usually  
1976 hint at the shape of the background.

1977 6.  $|\mathbf{m}_{V0} - \mathbf{m}_{K_S^0}| < 0.05 \text{ GeV}/c^2$  or  $|\mathbf{m}_{V0} - \mathbf{m}_\Lambda| < 0.05 \text{ GeV}/c^2$  : last condition of the pre-selection is on invariant mass of the reconstructed pair. This  
1978 condition is to limit the data size so that the *star-upcDst* format is still relatively  
1979 fast and at the same time that the peaks for  $K_S^0$  and  $\Lambda/\bar{\Lambda}$  can be easily fitted with  
1980 background.  
1981

---

## 1982 I.2 Selection criteria

1983 The following selection criteria are specifically created for the Tag&Probe method for  
 1984 the TOF detector efficiency. Due to much larger statistical significance, only particle  
 1985  $K_S^0$  is considered.

1986 The first five points are implemented to separate the good quality tracks from the  
 1987 rest. Then comes particle identification for pion selection. Then follow strict topological  
 1988 cuts. Lastly, there is a condition on the  $z$ -position of reconstructed vertex.

- 1989 1.  **$p_T > 200 \text{ MeV}$** : condition on the minimal transverse momentum of a particle.  
 1990 Particles with lower transverse momentum would not reach the outside diameter  
 1991 of the TPC, therefore the TOF detector.
- 1992 2.  **$N_{\text{hits}}^{\text{fit}} \geq 25$** : condition on the number of hits in TPC for track reconstruction  
 1993 which are used for establishment of a good quality trajectory reconstruction.
- 1994 3.  **$N_{\text{hits}}^{\text{dEdx}} \geq 15$** : condition on the number of hits in TPC for particle identification.
- 1995 4. **Particle identification:** is based on the information about energy loss from  
 1996 measurement in the TPC,  $n\sigma_\pi < 3$ . The reason why it is possible to have such  
 1997 loose condition is because the numbers of protons and kaons compared to pions  
 1998 in soft processes are significantly smaller. Therefore, the contamination is not  
 1999 significant. Correlation plot of particle momenta and energy loss after the PID  
 2000 condition can be seen in [Fig. I.6](#) and correlation plot of  $n\sigma_\pi$  and  $n\sigma_p$  is seen in  
[Fig. I.7](#).
- 2002 5.  **$V_{Z-\eta}$  condition:** the same combined condition on the  $z$  position of reconstructed  
 2003 hypothetical vertex and the pseudorapidity of both daughter particles as used in  
 2004 the main analysis a defined by [Eq. 3.3](#).
- 2005 6. **DCA daughters  $< 1.5 \text{ cm}$ :** condition on distance of closest approach explained  
 2006 in [Sec. I.1](#) is now set more rigidly.
- 2007 7. **DCA beamline  $< 1.5 \text{ cm}$ :** DCA to beamline is similarly to DCA daughters,  
 2008 constrained more strictly.
- 2009 8. **Decay length  $< 3 \text{ cm}$  or  $\cos(\text{Pointing Angle}) > 0.95$**  : this condition is also  
 2010 part of pre-selection criteria. Other than the fact that the condition on cosine of  
 2011 pointing angle is more restraint, the condition is the same.
- 2012 9.  **$Q_{\text{tot}} = 0$ :** opposite pairs of charged particles, also called unlike-sign pairs, form  
 2013 the signal.

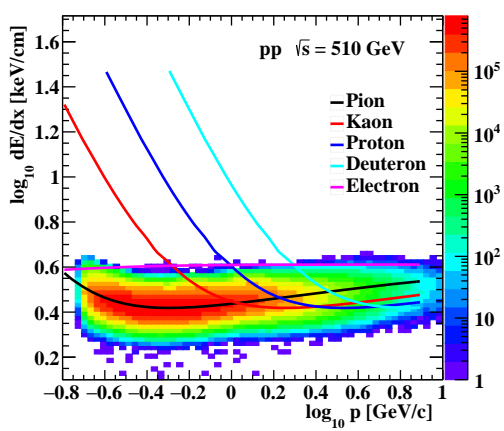


Figure I.6: Correlation plot of particle momentum and energy loss of particles that are chosen for  $K_S^0$  reconstruction. Both axes are logarithmic. The different colored lines represent the theoretical prediction for different particles.

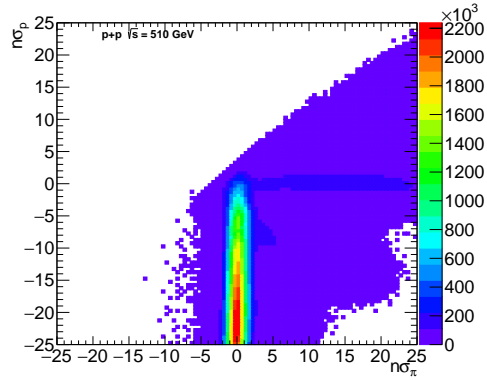


Figure I.7: Correlation plot of  $n\sigma$  plot for pions on the  $x$ -axis and protons on the  $y$ -axis. One can see the dominance of pions as a vertical line around  $n\sigma_\pi = 0$  and a narrow horizontal line going from the middle to the right, which represents protons. The small bulge on the right side of the pion line are the kaons.

2014 As in all other resonant particle analyses, the goal of the selection criteria is to reduce  
 2015 the background while preserving the signal. The signal that is being preserved is the  
 2016 invariant mass peak of particle  $K_S^0$ . The extraction of the yields and the results are  
 2017 described in the following section.

### 2018 I.3 Yield extraction and results

2019 This section calculates the joint TOF efficiency based on Run17 data and discusses the  
 2020 results.

2021 Firstly, the two yields, where at least one or both tracks have hits in TOF<sup>1</sup>, have  
 2022 to be extracted. The extraction is done using two different methods. The first method  
 2023 is based on fitting the signal and the background, then extracting the counts of  $K_S^0$  by  
 2024 subtracting the background from the signal. The signal is fitted with Crystal ball func-  
 2025 tion and background with a 1. degree polynomial. The second method is simpler. The  
 2026 background is assumed linear, therefore the same amount of background is in bins before  
 2027 the signal range and after, as can be seen in Fig. I.10. By subtracting the summation  
 2028 of bin contents outside the signal area from the sum in the signal area, one obtains the  
 2029  $K_S^0$  yield.

2030 These two methods are used to extract the yields in Fig. I.11, which is the invariant  
 2031 mass of pairs of pions when at least one of the tracks is matched with TOF and in

<sup>1</sup>A matched with TOF means that a track has a valid hit in the detector as well as having positive measurement of time and path length by the detector. In *star-upcDst* format, that translates to a track having `kTof` flag and that methods `tofTime()` and `tofPathLength()` return positive values.

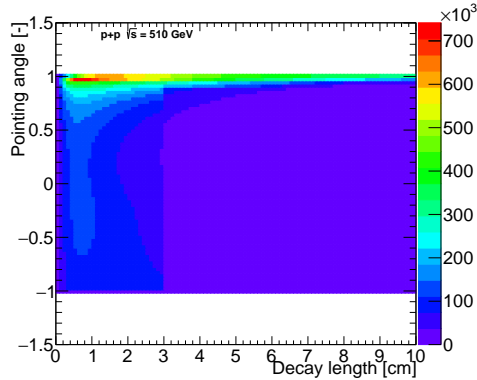


Figure I.8: Correlating distribution of decay length on the  $x$  axis and pointing angle on the  $y$  axis.

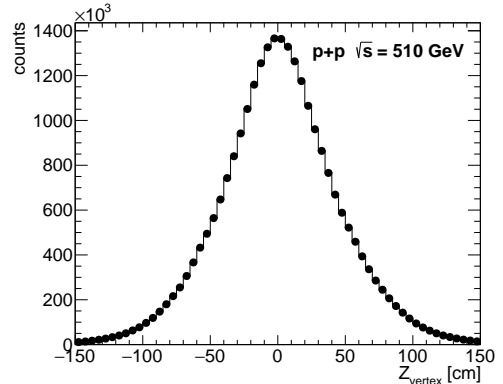


Figure I.9: Distribution of  $z$  coordinate position of vertex along the beamline before the condition is imposed.

2032 Fig. I.12 when both tracks are matched with TOF. The results of both methods for  
 2033 extracting yields and the final efficiencies are shown in Tab. I.1. The two methods  
 2034 are within statistical errors, therefore in agreement. For the following graphs, only the  
 2035 integration method is used.

	at least 1 ToF hit	2 ToF hits	efficiency [%]
Fitting	$100\ 773 \pm 1111(stat)$	$63\ 242 \pm 403(stat)$	$62.8 \pm 0.7(stat)$
Integration	$100\ 028 \pm 2646(stat)$	$62\ 107 \pm 827(stat)$	$62.0 \pm 1.0(stat)$

Table I.1: Table of results for yields of peaks for invariant mass peak of  $K_S^0$  and the Time of Flight detector efficiency.

2036 Furthermore, the efficiency is studied as a function of different variables of probes  
 2037 such as pseudorapidity  $\eta$ , azimuthal angle  $\varphi$ , transverse momentum  $p_T$  or  $z$ -coordinate of  
 2038 vertex  $V_Z$  see Figs. I.13–I.16. Obtained results from data are compared to two different  
 2039 Monte Carlo samples. The first sample, called "Efficiency (MC)", represents exclusive  
 2040 production of  $K_S^0$  pairs produced with DIME Monte Carlo generator and embedded into  
 2041 zero-bias data. The same Tag&probe method is used on the "Efficiency (MC)" sample.  
 2042 The second sample, called "true MC", comes from the official embedding discussed in  
 2043 Sec. 5.1. In this sample, the efficiency is studied by single particle approach, where the  
 2044 sample *total* is formed by true MC generated tracks that are reconstructed in TPC and  
 2045 the sample *passed* is formed by with the same tracks with a TOF hit.

## 2046 I.4 Systematic errors

2047 The previous plots of the TOF efficiencies are shown with statistical error bars only. This  
 2048 section evaluates the significance of systematic errors by comparing the reconstructed  
 2049 data with the "true MC" sample. For plots of variables  $\eta$ ,  $\varphi$ ,  $p_T$  and  $V_Z$ , the efficiency

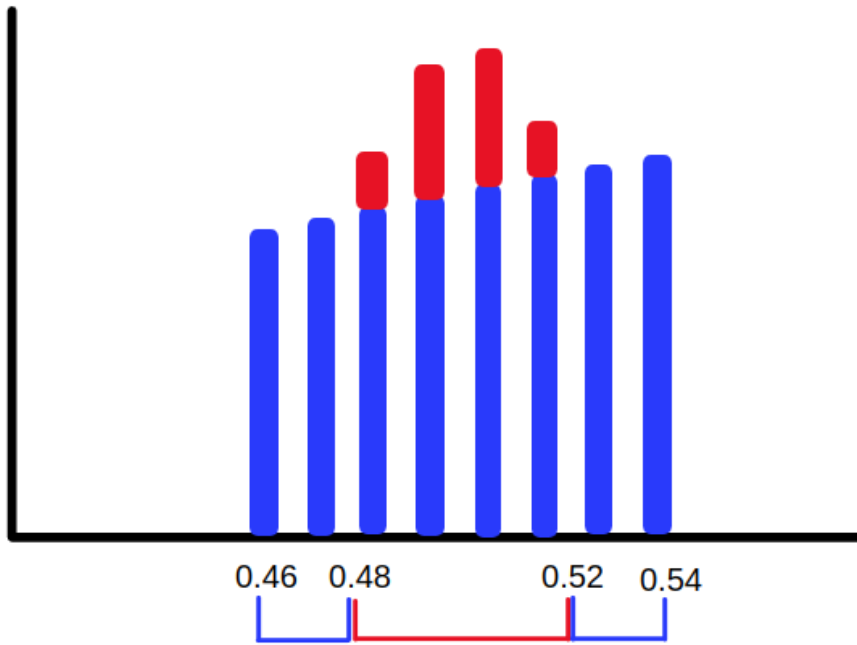


Figure I.10: Sketch of how  $K_S^0$  yield is extracted using integration method. Bin contents in the middle interval are added together, then the sum of intervals on the sides are subtracted from it.

of the data is divided by the MC sample. Then, the ratio plots are fitted with a constant function. The result of the fit shows the difference between the actual data and the Monte Carlo sample. To obtain systematic errors, one simply needs to recalculate the difference as a percentage of the efficiency. This is done by propagating the relative error to the absolute error of the final efficiency, which is taken as a weighted average of the two separate methods for yield extraction. The results of the systematic errors can be seen in Tab. I.2. All four different variables show a specific systematic error. The final systematic error has been taken as the average. Hence, the final calculated efficiency of TOF is  $(62.5 \pm 0.9(\text{stat}) \pm 1.0(\text{sys}))\%$ .

	Fit [%]	$\sigma_{\text{sys}} [\%]$
$\eta$	$97.6 \pm 1.8$	1.5
$\varphi$	$100.8 \pm 1.8$	0.5
$p_T$	$98.8 \pm 1.8$	0.8
$V_Z$	$98.4 \pm 1.6$	1.0

Table I.2: Table of systematic errors for different variables obtained by comparing data to true MC sample. The combined systematic error was estimated from all four variables at 1.0 %.

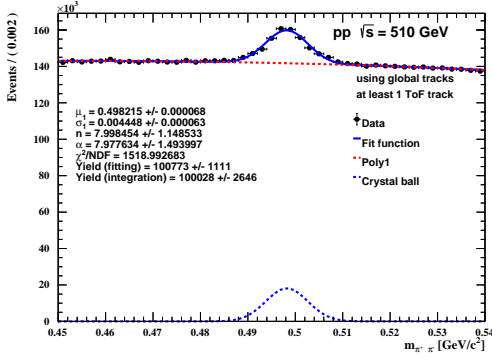


Figure I.11: Invariant mass of  $\pi^+\pi^-$  pairs where at least one of the tracks has a match with Time of Flight detector. Fitted with crystal ball function and a 1. degree polynomial.

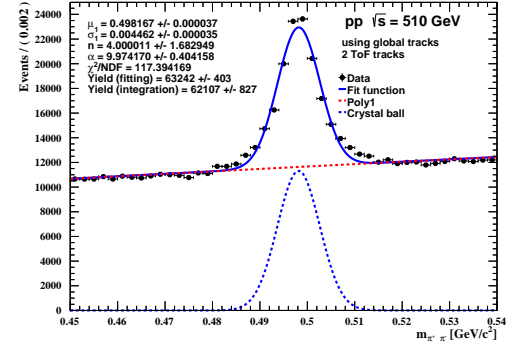


Figure I.12: Invariant mass of  $\pi^+\pi^-$  pairs where both tracks have a match with Time of Flight detector. Fitted with crystal ball function and a 1. degree polynomial.

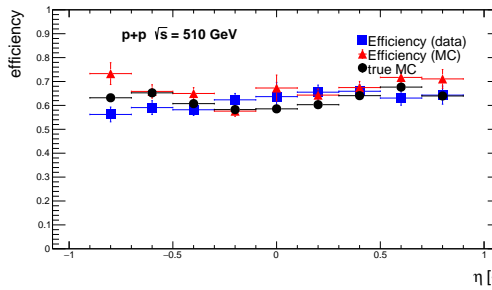


Figure I.13: Efficiency of TOF detector as a function of pseudorapidity. Blue is efficiency that comes from the data, red comes from the reconstructed MC sample.

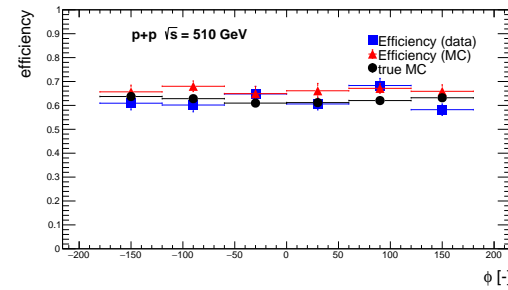


Figure I.14: Efficiency of TOF detector as a function of azimuthal angle  $\varphi$ . Blue is efficiency that comes from the data, red comes from the reconstructed MC sample.

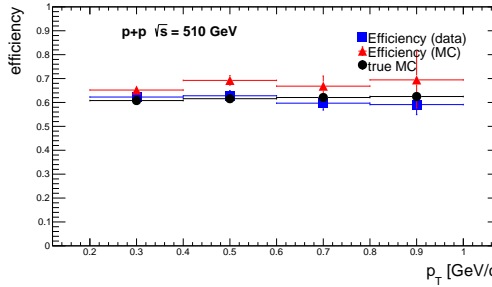


Figure I.15: Efficiency of TOF detector as a function of transverse momentum. Blue is efficiency that comes from the data, red comes from the reconstructed MC sample.

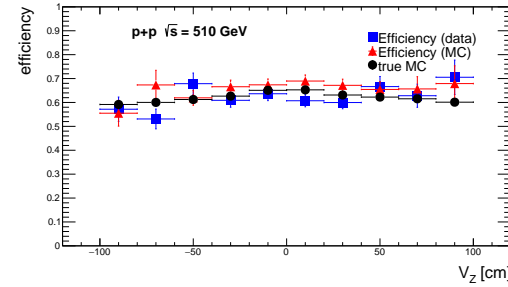


Figure I.16: Efficiency of TOF detector as a function of  $z$  coordinate of vertex. Blue is efficiency that comes from the data, red comes from the reconstructed MC sample.

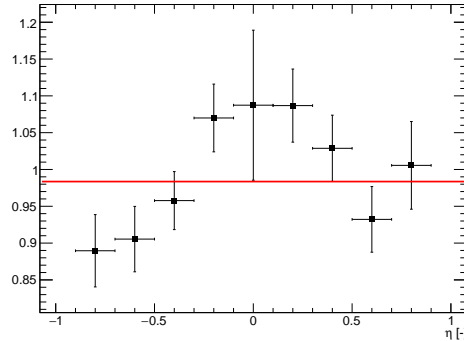


Figure I.17: Histogram of data efficiency divided by the true MC sample w.r.t. pseudorapidity for evaluation of systematic error. Fitted with a constant.

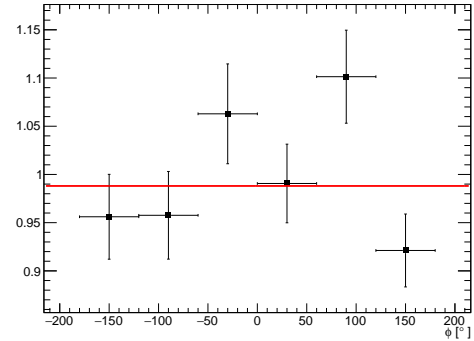


Figure I.18: Histogram of data efficiency divided by the true MC sample w.r.t. azimuthal angle for evaluation of systematic error. Fitted with a constant.

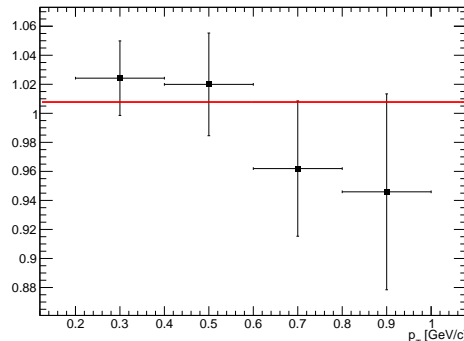


Figure I.19: Histogram of data efficiency divided by the true MC sample w.r.t. transverse momentum for evaluation of systematic error. Fitted with a constant.

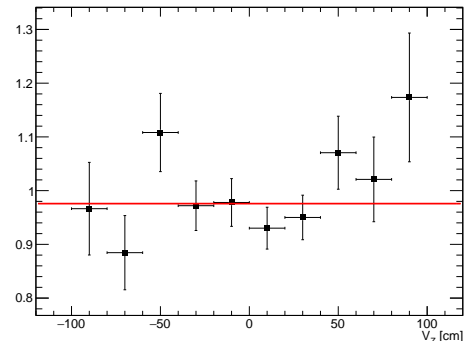


Figure I.20: Histogram of data efficiency divided by the true MC sample w.r.t. vertex  $z$  position for evaluation of systematic error. Fitted with a constant.



2059

# References

- 2060 [1] R. Sikora, et al. (STAR Collaboration), “Measurement of the central exclusive  
2061 production of charged particle pairs in proton-proton collisions at  $\sqrt{s} = 200$  GeV  
2062 with the STAR detector at RHIC,” *Journal of High Energy Physics*, vol. 2020,  
2063 no. 7, p. 46, 2020, ISSN: 1029-8479. DOI: [10.1007/JHEP07\(2020\)178](https://doi.org/10.1007/JHEP07(2020)178). [Online].  
2064 Available: [http://link.springer.com/10.1007/JHEP07\(2020\)178](http://link.springer.com/10.1007/JHEP07(2020)178).
- 2065 [2] K.H. Ackermann, et al. (STAR Collaboration), “STAR detector overview,” *Nuclear  
2066 Instruments and Methods in Physics Research Section A: Accelerators, Spectrometers,  
2067 Detectors and Associated Equipment*, vol. 499, no. 2, pp. 624–632, 2003,  
2068 ISSN: 0168-9002. DOI: [https://doi.org/10.1016/S0168-9002\(02\)01960-5](https://doi.org/10.1016/S0168-9002(02)01960-5).  
2069 [Online]. Available: <https://www.sciencedirect.com/science/article/pii/S0168900202019605>.
- 2070 [3] M. Harrison, et al., “THE RHIC ACCELERATOR,” *Annual Review of Nuclear  
2071 and Particle Science*, vol. 52, no. 1, pp. 425–469, 2002. DOI: [10.1146/annurev.nucl.52.050102.090650](https://doi.org/10.1146/annurev.nucl.52.050102.090650). eprint: <https://doi.org/10.1146/annurev.nucl.52.050102.090650>. [Online]. Available: <https://doi.org/10.1146/annurev.nucl.52.050102.090650>.
- 2072 [4] H. Hahn, et al., “The RHIC design overview,” *Nuclear Instruments and Methods in  
2073 Physics Research Section A: Accelerators, Spectrometers, Detectors and Associated  
2074 Equipment*, vol. 499, no. 2, pp. 245–263, 2003, ISSN: 0168-9002. DOI: [https://doi.org/10.1016/S0168-9002\(02\)01938-1](https://doi.org/10.1016/S0168-9002(02)01938-1). [Online]. Available: <https://www.sciencedirect.com/science/article/pii/S0168900202019381>.
- 2075 [5] M. Anderson, et al. (STAR Collaboration), “The STAR time projection chamber:  
2076 a unique tool for studying high multiplicity events at RHIC,” *Nuclear Instruments  
2077 and Methods in Physics Research Section A: Accelerators, Spectrometers, Detectors  
2078 and Associated Equipment*, vol. 499, no. 2-3, p. 20, 2003, ISSN: 01689002. DOI:  
2079 [10.1016/S0168-9002\(02\)01964-2](https://doi.org/10.1016/S0168-9002(02)01964-2).
- 2080 [6] J. Schambach, et al. (STAR Collaboration), “Proposed STAR Time of Flight Read-  
2081 out Electronics and DAQ,” *Computing in High Energy and Nuclear Physics, La-  
2082 Jolla, California*, vol. 2003, no. 1, p. 10, 2003.

- 2089 [7] C. A. Whitten (STAR Collaboration), “The Beam-Beam Counter: a local po-  
2090 larimeter at STAR,” *AIP Conference Proceedings*, vol. 2008, no. 1, pp. 390–396,  
2091 2008, ISSN: 0094243X. DOI: [10.1063/1.2888113](https://doi.org/10.1063/1.2888113). [Online]. Available: <http://aip.scitation.org/doi/abs/10.1063/1.2888113>.
- 2093 [8] C. Adler, et al., “The RHIC zero degree calorimeters,” *Nuclear Instruments and*  
2094 *Methods in Physics Research Section A: Accelerators, Spectrometers, Detectors*  
2095 *and Associated Equipment*, vol. 470, no. 3, pp. 488–499, 2001, ISSN: 01689002. DOI:  
2096 [10.1016/S0168-9002\(01\)00627-1](https://doi.org/10.1016/S0168-9002(01)00627-1). [Online]. Available: <https://linkinghub.elsevier.com/retrieve/pii/S0168900201006271>.
- 2098 [9] C. Adler, et al., “The RHIC zero degree calorimeters,” *Nuclear Instruments and*  
2099 *Methods in Physics Research Section A: Accelerators, Spectrometers, Detectors*  
2100 *and Associated Equipment*, vol. 499, no. 2-3, pp. 433–436, 2003, ISSN: 01689002.  
2101 DOI: [10.1016/j.nima.2003.08.112](https://doi.org/10.1016/j.nima.2003.08.112). [Online]. Available: <https://linkinghub.elsevier.com/retrieve/pii/S0168900203024069>.
- 2103 [10] S. Bültmann, et al. (PP2PP Collaboration), “The PP2PP experiment at RHIC: silicon detectors installed in Roman Pots for forward proton detection close to the beam,” *Nuclear Instruments and Methods in Physics Research Section A: Accelerators, Spectrometers, Detectors and Associated Equipment*, vol. 535, no. 1-2, p. 6, 2004, ISSN: 01689002. DOI: [10.1016/j.nima.2004.07.162](https://doi.org/10.1016/j.nima.2004.07.162).
- 2108 [11] J. Adam, “Results on total and elastic cross sections in proton–proton collisions at  $\sqrt{s} = 200$  GeV,” *Physics Letters B*, vol. 808, p. 135 663, 2020, ISSN: 0370-2693. DOI: <https://doi.org/10.1016/j.physletb.2020.135663>. [Online]. Available: <https://www.sciencedirect.com/science/article/pii/S0370269320304664>.
- 2112 [12] J. Adam. “STAR UPC+RP picoDsts.” (2022), [Online]. Available: <https://github.com/adamjaro/star-upcDst>.
- 2114 [13] G. V. Buren. “BTOF-matching in tracking and vertexing.” (2017), [Online]. Available: <https://drupal.star.bnl.gov/STAR/blog/genevb/btof-matching-tracking-and-vertexing>.
- 2117 [14] R. Reed, et al., “Vertex finding in pile-up rich events for p+p and d+Au collisions at STAR,” *Journal of Physics: Conference Series*, vol. 219, no. 3, p. 032 020, Apr. 2010. DOI: [10.1088/1742-6596/219/3/032020](https://doi.org/10.1088/1742-6596/219/3/032020). [Online]. Available: <https://doi.org/10.1088/1742-6596/219/3/032020>.
- 2121 [15] D. Smirnov, et al., “Vertex Reconstruction at STAR: Overview and Performance Evaluation,” *Journal of Physics: Conference Series*, vol. 898, p. 042 058, Oct. 2017. DOI: [10.1088/1742-6596/898/4/042058](https://doi.org/10.1088/1742-6596/898/4/042058). [Online]. Available: <https://doi.org/10.1088/1742-6596/898/4/042058>.

- 2125 [16] H. Bichsel, “A method to improve tracking and particle identification in TPCs  
2126 and silicon detectors,” *Nuclear Instruments and Methods in Physics Research Section A: Accelerators, Spectrometers, Detectors and Associated Equipment*, vol. 562,  
2127 no. 1, pp. 154–197, 2006, ISSN: 01689002. DOI: [10.1016/j.nima.2006.03.009](https://doi.org/10.1016/j.nima.2006.03.009). [Online]. Available: <https://linkinghub.elsevier.com/retrieve/pii/S0168900206005353>.
- 2131 [17] M.I. Abdulhamid (STAR Collaboration), “Results on elastic cross sections in  
2132 proton–proton collisions at  $\sqrt{s} = 510$  GeV with the STAR detector at RHIC,”  
2133 *Physics Letters B*, vol. 852, p. 138601, 2024, ISSN: 0370-2693. DOI: <https://doi.org/10.1016/j.physletb.2024.138601>. [Online]. Available: <https://www.sciencedirect.com/science/article/pii/S037026932400159X>.
- 2136 [18] M. Mieskolainen, “GRANIITTI: A Monte Carlo Event Generator for High Energy  
2137 Diffraction,” 2019. arXiv: [1910.06300 \[hep-ph\]](https://arxiv.org/abs/1910.06300).
- 2138 [19] V. Khoze, A. Martin, and M. Ryskin, “The rapidity gap Higgs signal at LHC,”  
2139 *Physics Letters B*, vol. 401, no. 3-4, pp. 330–336, 1997, ISSN: 03702693. DOI: [10.1016/S0370-2693\(97\)00426-7](https://doi.org/10.1016/S0370-2693(97)00426-7). [Online]. Available: <https://linkinghub.elsevier.com/retrieve/pii/S0370269397004267>.
- 2142 [20] C. Ewerz, M. Maniatis, and O. Nachtmann, “A model for soft high-energy scattering,  
2143 Tensor pomeron and vector odderon,” *Annals of Physics*, vol. 342, no. 1,  
2144 pp. 31–77, 2014, ISSN: 00034916. DOI: [10.1016/j.aop.2013.12.001](https://doi.org/10.1016/j.aop.2013.12.001). [Online].  
2145 Available: <https://linkinghub.elsevier.com/retrieve/pii/S0003491613002819>.
- 2146 [21] L. A. Harland-Lang, et al., “Central exclusive production within the Durham  
2147 model, A review,” *International Journal of Modern Physics A*, vol. 29, no. 17,  
2148 p. 1430031, 2014, ISSN: 0217-751X. DOI: [10.1142/S0217751X14300312](https://doi.org/10.1142/S0217751X14300312). [On-  
2149 line]. Available: <https://www.worldscientific.com/doi/abs/10.1142/S0217751X14300312>.
- 2151 [22] P. Lebiedowicz, et al., “Central exclusive diffractive production of the  $\pi^+\pi^-$  con-  
2152 tinuum, scalar, and tensor resonances in  $pp$  and  $p\bar{p}$  scattering within the tensor  
2153 Pomeron approach,” *Physical Review D*, vol. 93, no. 5, p. 054015, 2016, ISSN:  
2154 2470-0010. DOI: [10.1103/PhysRevD.93.054015](https://doi.org/10.1103/PhysRevD.93.054015). [Online]. Available: <https://link.aps.org/doi/10.1103/PhysRevD.93.054015>.
- 2156 [23] V. Khoze, A. Martin, and M. Ryskin, “Soft diffraction and the elastic slope at  
2157 Tevatron and LHC energies, A multi-pomeron approach,” *The European Physical  
2158 Journal C*, vol. 18, no. 1, pp. 167–179, 2000, ISSN: 1434-6044. DOI: [10.1007/s100520000494](https://doi.org/10.1007/s100520000494). [Online]. Available: <http://link.springer.com/10.1007/s100520000494>.

- 2161 [24] L. A. Harland-Lang, V. A. Khoze, and M. G. Ryskin, “Modelling exclusive meson  
2162 pair production at hadron colliders,” *The European Physical Journal C*, vol. 74,  
2163 no. 4, p. 2848, 2014, ISSN: 1434-6044. DOI: [10.1140/epjc/s10052-014-2848-9](https://doi.org/10.1140/epjc/s10052-014-2848-9).  
2164 [Online]. Available: <http://link.springer.com/10.1140/epjc/s10052-014-2848-9>.
- 2166 [25] L. A. Harland-Lang, V. A. Khoze, and M. G. Ryskin, “Exclusive LHC physics  
2167 with heavy ions, Superchic 3,” *The European Physical Journal C*, vol. 79, no. 1,  
2168 p. 39, 2019, ISSN: 1434-6044. DOI: [10.1140/epjc/s10052-018-6530-5](https://doi.org/10.1140/epjc/s10052-018-6530-5). [Online].  
2169 Available: <http://link.springer.com/10.1140/epjc/s10052-018-6530-5>.
- 2170 [26] P. Lebiedowicz and A. Szczurek, “Exclusive  $pp \rightarrow pp\pi^+\pi^-$  reaction, From the  
2171 threshold to LHC,” *Physical Review D*, vol. 81, no. 3, p. 036003, 2010, ISSN: 1550-  
2172 7998. DOI: [10.1103/PhysRevD.81.036003](https://doi.org/10.1103/PhysRevD.81.036003). [Online]. Available: <https://link.aps.org/doi/10.1103/PhysRevD.81.036003>.
- 2174 [27] A. B. Kaidalov, V. A. Khoze, A. D. Martin, and M. G. Ryskin, “Central exclusive  
2175 diffractive production as a spin-parity analyser, from hadrons to Higgs,” *The Eu-  
2176 ropean Physical Journal C*, vol. 31, no. 3, pp. 387–396, 2003, ISSN: 1434-6044. DOI:  
2177 [10.1140/epjc/s2003-01371-5](https://doi.org/10.1140/epjc/s2003-01371-5). [Online]. Available: <http://link.springer.com/10.1140/epjc/s2003-01371-5>.
- 2179 [28] G. Kallen, *Elementary Particle Physics*, 1st. Massachusetts: Addison-Wesley Ed-  
2180 ucational Publishers Inc, 1964, ISBN: 0201035758.
- 2181 [29] P. A. Zyla, et al. (Particle Data Group), “Review of particle physics,” *Progress of  
2182 Theoretical and Experimental Physics*, vol. 2020, no. 8, p. 2093, 2020, ISSN: 2050-  
2183 3911. DOI: [10.1093/ptep/ptaa104](https://doi.org/10.1093/ptep/ptaa104). [Online]. Available: <https://academic.oup.com/ptep/article/doi/10.1093/ptep/ptaa104/5891211>.
- 2185 [30] Xiaoxuan Chu, “ $Z^0$  cross section and transverse single spin asymmetry in  $\sqrt{s} =$   
2186 500(510) GeV p+p collisions at STAR,” *STAR Analysis Note*, Aug. 2023. [Online].  
2187 Available: [https://drupal.star.bnl.gov/STAR/system/files/Z0\\_analysis\\_note\\_v7.pdf](https://drupal.star.bnl.gov/STAR/system/files/Z0_analysis_note_v7.pdf).
- 2189 [31] M.I. Abdulhamid, et al. (STAR Collaboration), “Measurements of the  $Z^0/\gamma^*$   
2190 cross section and transverse single spin asymmetry in 510 GeV p+p collisions,”  
2191 *Physics Letters B*, vol. 854, p. 138715, 2024, ISSN: 0370-2693. DOI: <https://doi.org/10.1016/j.physletb.2024.138715>. [Online]. Available: <https://www.sciencedirect.com/science/article/pii/S0370269324002739>.
- 2194 [32] T. Akesson, et al. (AFS Collaboration), “A search for glueballs and a study of dou-  
2195 ble pomeron exchange at the CERN intersecting storage rings,” *Nuclear Physics B*,  
2196 vol. 1986, no. 264, pp. 154–184, 1986, ISSN: 05503213. DOI: [10.1016/0550-0545\(86\)90002-2](https://doi.org/10.1016/0550-0545(86)90002-2).

- 2197        3213(86) 90477 – 3. [Online]. Available: <http://www.sciencedirect.com/science/article/pii/0550321386904773>.
- 2198
- 2199 [33] A. Hayrapetyan, et al. (CMS and TOTEM Collaboration), “Nonresonant central exclusive production of charged-hadron pairs in proton-proton collisions at  $\sqrt{s} = 13$  TeV,” *Phys. Rev. D*, vol. 109, p. 112013, 11 Jun. 2024. DOI: [10.1103/PhysRevD.109.112013](https://doi.org/10.1103/PhysRevD.109.112013). [Online]. Available: <https://link.aps.org/doi/10.1103/PhysRevD.109.112013>.
- 2200
- 2201
- 2202
- 2203
- 2204 [34] T. Aaltonen and Albrow, “Measurement of central exclusive  $\pi^+\pi^-$  production in  $p\bar{p}$  collisions at  $\sqrt{s} = 0.9$  and 1.96 TeV at CDF,” *Phys. Rev. D*, vol. 91, p. 091101, 9 May 2015. DOI: [10.1103/PhysRevD.91.091101](https://doi.org/10.1103/PhysRevD.91.091101). [Online]. Available: <https://link.aps.org/doi/10.1103/PhysRevD.91.091101>.
- 2205
- 2206
- 2207
- 2208 [35] S. Dobbs, A. Tomaradze, T. Xiao, and K. K. Seth, “Comprehensive study of the radiative decays of  $J/\psi$  and  $\psi(2S)$  to pseudoscalar meson pairs, and search for glueballs,” *Phys. Rev. D*, vol. 91, p. 052006, 5 Mar. 2015. DOI: [10.1103/PhysRevD.91.052006](https://doi.org/10.1103/PhysRevD.91.052006). [Online]. Available: <https://link.aps.org/doi/10.1103/PhysRevD.91.052006>.
- 2209
- 2210
- 2211
- 2212

